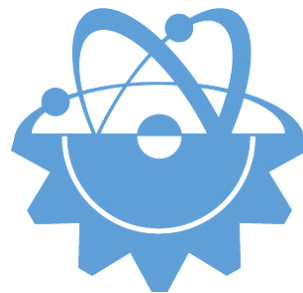


ISSN-Printed: 2536-5010
ISSN-Online: 2536-5134

Volume 11, No 1, 2021

EJT

EUROPEAN JOURNAL OF TECHNIC



Copyright © 2017

International Engineering, Science & Education Group

Email (for orders and customer services enquiries): info@ineseg.org, ejt@ineseg.org

Visit our home page on www.ineseg.org

All Rights Reserved. No part of this publication may be reproduced, stored in a retrieval system or transmitted in any form or by any means, electronic, mechanical, photocopying, recording, scanning or otherwise, except under the terms of the Copyright, under the terms of a license issued by the Copyright International Engineering, Science & Education Group (INESEG), without the permission in writing of the Publisher. Requests to the Publisher should be addressed to the Permissions Department, International Engineering, Science & Education Group (INESEG), or emailed to info@ineseg.org

Designations used by companies to distinguish their products are often claimed as trademarks. All brand names and product names used in this journal are trade names, service marks, trademarks or registered trademarks of their respective owners. The Publisher is not associated with any product or vendor mentioned in this journal.

This publication is designed to provide accurate and authoritative information in regard to the subject matter covered. It is sold on the understanding that the Publisher is not engaged in rendering professional services. If professional advice or other expert assistance is required, the services of a competent professional should be sought.



EUROPEAN JOURNAL OF TECHNIQUE (EJT)

ISSN-Printed: 2536-5010

ISSN-Online: 2536-5134

Scope: European Journal of Technique (EJT) established in 2010. It is a peer –reviewed international journal to be of interest and use to all those concerned with research in various fields of, or closely related to, Engineering disciplines. European Journal of Technique (EJT) aims to provide a highly readable and valuable addition to the literature which will serve as an indispensable reference tool for years to come. The coverage of the journal includes all new theoretical and experimental findings in the fields of Engineering or any closely related fields. The journal also encourages the submission of critical review articles covering advances in recent research of such fields as well as technical notes.

The scopes include:

- Mechanical Engineering
- Textile Engineering
- Electrical-Electronics Engineering
- Computer and Informatics Engineering
- Civil and Architecture Engineering
- Mining Engineering
- Chemical Engineering
- Metallurgical and Materials Engineering
- Environmental Engineering
- Food Engineering
- Geological Engineering
- Industrial Engineering
- Renewable Energy

EDITORIAL BOARD MEMBERS

Editor-in-Chief

- Musa YILMAZ

Publisher Of Journal

- Heybet KILIÇ

ETHICS and POLICIES

European Journal of Technique (EJT) is committed to following the Code of Conduct and Best Practice Guidelines of COPE (Committee on Publication Ethics). It is a duty of our editors to follow Cope Guidance for Editors and our peer-reviewers must follow COPE Ethical Guidelines for Peer Reviewers. We expect all prospective authors to read and understand our Ethics Policy before submitting any manuscripts to our journals.

Please note that submitted manuscripts may be subject to checks using the iThenticate service, in conjunction with CrossCheck, in order to detect instances of overlapping and similar text.

The [iThenticate](#) software checks submissions against millions of published research papers, documents on the web, and other relevant sources. If plagiarism or misconduct is found, consequences are detailed in the policy.

The chief goal of our policy is threefold: to provide advice for our authors, to maintain the scholarly integrity of our journals and their content, and to detail the ethical responsibilities of EJT, our editors and authors.

We expect all authors to read and understand our ethics policy before submitting to any of our journals. This is in accordance with our commitment to the prevention of ethical misconduct, which we recognise to be a growing problem in academic and professional publications. It is important to note that most incidents of plagiarism, redundant publication, copyright infringement or similar occur because of a lack of understanding, and not through fraudulent intent. Our policy is one of prevention and not persecution.

If you have any questions, please contact the relevant editorial office, or European Journal of Technique (EJT)' ethics representative: ejtineseg@gmail.com

Download a PDF version of the Ethics and Policies [PDF,392KB].

Authors' Responsibilities

Authors should:

- Ensure that all researched work submitted is original, fully referenced and that all authors are represented accurately. The submission must be exclusive and not under consideration elsewhere.
- Provide accurate contact details for a designated corresponding author, who shall be deemed by the publisher and editor as fully responsible for the authorship of the paper and all communications concerning the ethical status and originality of the paper. This includes any queries or investigations that may arise, pre- or post publication.
- Openly disclose the source of all data and third party material, including previously unpublished work by the authors themselves. Anything that could compromise the originality of the submission should be expressly avoided and/or discussed with the editorial office in the first instance.
- Identify any third party material that they intend to include in their article, and obtain written permission for re-use in each instance from the relevant copyright holders. Such permissions should be submitted once the manuscript is accepted, or requires small changes to be accepted. For further guidance on seeking permission to use 3rd party material please see the Rights and Permissions section.
- Openly disclose any conflict of interest - for example, if publication were to benefit a company or services in which the author(s) has a vested interest.

- Expect to formally agree publication terms which defines the author and the publishers rights for the work. Visit our website for further information.
- Expect the editor to scan submissions using plagiarism detection software at [iThenticate](#) to check a paper's originality before sending out for review.
- Fully correspond and comply with the editor and publisher in any requests for source data, proof of authorship or originality in a timely manner, providing reasonable explanation for discrepancies or failures to disclose vital information.
- Fully co-operate with any consequent investigations if the editor and/or publisher are dissatisfied with the evidence available or the explanations provided.
- Expect transparency, efficiency and respect from the publisher and the editor during the submissions process.
- Remain in good communication with both the publisher and the editor.
- When necessary, submit corrigenda in a timely and responsible fashion.
- Co-operate fully with the publication of errata and with the retraction of articles found to be unethical, misleading or damaging.
- Remain in good communication with the editor(s), the publisher and any co-authors.

Editors' Responsibilities

Editors should:

- Read and understand COPE guidelines as well as EJT's ethics policy, and follow them during all editorial processes.
- Protect the reputation of their journal(s) and published work by only publishing content of the highest quality and relevance in a timely and responsible manner.
- Carry out thorough, objective and confidential peer review for original article submissions that pass the initial quality check and editorial assessment, in adherence with COPE guidelines and EJT' ethics policy.
- Detail and justify any article types which will not be peer reviewed (e.g. editorials, opinion pieces etc.).
- Provide a transparent review and publication process as far as is possible, with full respect and care paid to the author(s).
- Provide advice and give reasonable explanation and updates to authors during the submissions process and once a decision has been made.
- Allow authors the right to appeal any editorial decision.
- Only accept papers based on the original merit, quality and relevance of their content.
- Support authors in queries concerning the originality of their submissions and request the support of EJT if necessary.
- Advise the publisher of any third party material which has been included for which they do not believe sufficient permission has been cleared.

- Be ready and prepared to publish corrections, corrigenda, errata when necessary, as well as retract articles that (the editor and EJT) deem unethical, misleading or damaging.
- Remain in good communication with both the publisher and the author(s).

Reviewers' Responsibilities

Reviewers should:

- Adhere to EJT's policy of confidential peer review of their journals. This includes, but is not restricted to, keeping their identity hidden from authors and not externally distributing any work that is passed to them for their eyes only.
- Only accept invitations to review work that is relevant to their own expertise and speciality.
- Review submitted work in a responsible, impartial and timely manner.
- Report any suspected ethical misconduct as part of a thorough and honest review of the work.
- Avoid the use of unnecessarily inflammatory or offensive language in their appraisal of the work.
- Accept the commitment to review future versions of the work and provide 'follow up' advice to the editor(s), if requested.
- Seek advice from the editor if anything is unclear at the time of invitation.
- Remain in good communication with both the publisher and the editor.

EJT's Responsibilities

EJT will:

- Protect the reputation of our journals and published work by only publishing content of the highest quality and relevance in a timely and responsible manner.
- Provide detailed information concerning both our understanding of publication ethics and our implementation of the same. Emphasise a desire for prevention, not eventual detection, of ethical misconduct.
- Uphold our COPE membership (or of such similar organisations) and keep our editorial offices, publishing staff and society partners up-to-date with their guidelines and policies, adapting our own where appropriate (and publicising any update).
- When necessary, request proof of originality/accuracy from the corresponding author of any work submitted to any of our journals.
- Use plagiarism detection software when necessary for any submission to any journal at any stage of the submissions and publication process.
- Provide a transparent submissions and publication process, with full respect and care paid to the author. This includes detailed and dedicated instructions to authors for each journal, outlining referencing style, accepted article types and submission processes.
- Investigate thoroughly any suggestion of ethical misconduct detected during any stage of the submissions process. This can include, but is not restricted to, the following: plagiarism, redundant publication, fabrication or misuse of data and authorial disputes.

- When necessary, retract articles that we deem to be unethical, misleading or damaging.
- When necessary, publish errata, corrigenda and retractions in a timely and responsible fashion, detailing the decision online in an open access format and publishing in print as soon as possible.
- Remain in good communication with editors, authors, reviewers and society partners (where applicable).

Further reading

- Authorship of the paper: Authorship should be limited to those who have made a significant contribution to the conception, design, execution, or interpretation of the reported study.
- Originality and plagiarism: The authors should ensure that they have written entirely original works, and if the authors have used the work and/or words of others that this has been appropriately cited or quoted.
- Data access and retention: Authors may be asked to provide the raw data in connection with a paper for editorial review, and should be prepared to provide public access to such data.
- Multiple, redundant or concurrent publication: An author should not in general publish manuscripts describing essentially the same research in more than one journal or primary publication. EJT do not view the following uses of a work as prior publication: publication in the form of an abstract; publication as an academic thesis; publication as an electronic preprint. Information on prior publication is included within each EJT and its journal Guideline for Authors.
- Acknowledgement of sources: Proper acknowledgment.
- Disclosure and conflicts of interest: All submissions must include disclosure of all relationships that could be viewed as presenting a potential conflict of interest.
- Fundamental errors in published works: When an author discovers a significant error or inaccuracy in his/her own published work, it is the author's obligation to promptly notify the journal editor or publisher and cooperate with the editor to retract or correct the paper.
- Reporting standards: Authors of reports of original research should present an accurate account of the work performed as well as an objective discussion of its significance.
- Hazards and human or animal subjects: Statements of compliance are required if the work involves chemicals, procedures or equipment that have any unusual hazards inherent in their use, or if it involves the use of animal or human subjects.
- Use of patient images or case details: Studies on patients or volunteers require ethics committee approval and informed consent, which should be documented in the paper.

EJT has also accessed and learned from the existing policies of other publishers and leading experts as well as open access articles that detail and define ethical misconduct.

- 'Plagiarism and the law', Joss Saunders, Learned Publishing, 23:279-202: <http://www.ingentaconnect.com/content/alpsp/lp/2010/00000023/00000004/art00002>
- iThenticate Plagiarism Resources: <http://www.ithenticate.com/resources/6-consequences-of-plagiarism>

EDITORIAL BOARD MEMBERS

Editor-in-Chief : Musa Yilmaz

International Editorial Board

Aayush Shrivastava	University of Petroleum and Energy Studies, Dehradun
Adelino Pereira	Engineering Institute of Coimbra, Portugal.
Ahmad Fakharian	Islamic Azad University, Qazvin, Iran
Ahmed Saber	Cairo University, Egypt
Arvind Kumar Jain	Rustam Ji Institute of Technology, India
Aydogan Ozdemir	Istanbul Technical University
Baseem Khan	Hawassa University, Hawassa, Ethiopia
Behnam Mohammadi-ivatloo	University of Tabriz, Tabriz, Iran
Bharti Dwivedi	Electrical Eng, Institute of Eng & Technology, Lucknow, UP, India
Carlos A. Castro	University of Campinas – UNICAMP
Deepak Kumar	University of Petroleum & Energy Studies (UPES)
Ernesto Vazquez	University of Nuevo Leon, Mexico
Faisal Khan	COMSATS Institute of Information Technology, Pakistan
Farhad Shahnia	Murdoch University, Perth, Australia
Farrokh Aminifar	University of Tehran
Fiaz Ahmad	National University of Computer and Emerging Sciences Pakistan
Gouthamkumar Nadakuditi	V R Siddhartha Engineering College Vijayawada, India
Hafiz Ahmed	Aerospace and Automotive Eng, Coventry Univ, United Kingdom.
Hamed Pourgharibshahi	Lamar University, USA
Hassan Bevrani	University of Kurdistan, Iran
Hemant Kumar Gianey	Thapar University, Patiala, Punjab, India
Hessam Golmohamadi	Semnan University, Semnan, Iran
Hilmy Awad	Helwan University, Cairo, Egypt.
Jamshed Ahmed Ansari	Sukkur IBA University Pakistan
José A. Dominguez-Navarro	University of Zaragoza, Spain.
Kalpana Chauhan	Galgotias College of Engineering and Technology Greater Noida, India
Khaled Ellithy	Qatar University, Doha, Qatar
Kim-Doang Nguyen	South Dakota State University, USA
Kundan Kumar	KIIT University, India
Lalit Kumar	GBPIET Pauri, India
Linquan Bai	ABB Inc. (USA)
Linquan Bai	Consulting Engineer at ABB Inc. (USA)
Md Shafiullah	King Fahd University of Petroleum & Minerals, SA
Mohammed Albadi	Sultan Qaboos University, Oman
Mohammed Albadi	Sultan Qaboos University, Oman
Mohd Tariq	Aligarh Muslim University
Mousa Marzband	Northumbria Univ, Newcastle upon Tyne, NE1 8ST, United Kingdom
Neeraj Kanwar	Manipal University Jaipur, India
Nishant Kumar	Indian Institute of Technology Delhi, New Delhi
Nitin Kumar Saxena	Wolaita Sodo University Ethiopia
Omar Hafez	Umm Al-Qura University, Makkah, Saudi Arabia
Omveer Singh	Gautam Buddha University, India
Payam Teimourzadeh Baboli	University of Mazandaran (UMZ), Iran
Payman Dehghanian	George Washington University, USA
Ragab A. El Sehiemy	Kafrelsheikh Univrsity, Egypt
Rajiv Singh	G.B. Pant University of Agriculture & Technology, Uttarakhand, India
Reza Sharifi	Amir Kabir university Tehran, Iran
Rudranarayan Senapati	Kalinga Institute of Industrial Technology, India
Saleh Y. Abujarad	Universiti Teknologi Malaysia
Sanjay Dambhare	Department of Electrical Engineering College of Engineering, INDIA
Saptarshi Roy	NIT Warangal, India
Shailendra Kumar	Indian Institute of Technology Delhi, India
Shailendra Kumar	Indian Institute of Technology Delhi
Shariq Riaz	The University of Sydney, Australia
Shengen Chen	University of Maine, USA
Syafaruddin	Universitas Hasanuddin, Indonesia
T. Sudhakar Babu	VIT University, Vellore, India
Thamer Alquthami	King Abdulaziz University
Theofilos Papadopoulos	Democritus University of Thrace, Greece
Uday P. Mhaskar	CSA Group, USA
Yogesh Rohilla	K Lakshmi Pat University, Jaipur, India
Yunfeng Wen	School of Electrical Engineering, Chongqing University, China
Zbigniew M. Leonowicz	Wroclaw University of Sci and Tech, Politechnika Wroclawska, Poland



CONTENTS

ENRICHMENT OF APATITE-BEARING IRON ORE BY MAGNETIC SEPARATION AND FLOTATION	1-6
INVESTIGATION OF HOME TYPE HELIOSTAT SYSTEMS DAYLIGHTING PERFORMANCE WITH LIGHTING SIMULATION METHOD	7-12
SOLUTIONS OF SOLID TIMBER AND GLULAM BRIDGE EXAMPLE WITH DIFFERENT APPROACHES IN TURKEY	13-18
PRODUCTION OF CURVED SURFACE COMPOSITES REINFORCED WITH RUBBER LAYER	19-22
DESIGN AND ANALYSIS OF QUADRATIC BOOST CONVERTER WITH INDUCTOR-CAPACITOR-DIODE VOLTAGE MULTIPLIER CIRCUIT	23-28
DE-ORBITING ELECTRO-MECHANICAL SYSTEM DESIGN FOR MICRO SPACECRAFT	29-33
DESIGN AND APPLICATION OF A SMART HOME SYSTEM BASED ON INTERNET OF THINGS	34-42
EXPERIMENTAL INVESTIGATION OF THE MECHANICAL AND MICROSTRUCTURE PROPERTIES OF S49 RAIL STEEL	43-46
EFFECTS OF SLIDING DISTANCE SPEED AND LOAD ON WEAR AND TEMPERATURE IN DIFFERENT MATRIX AND FIBER-REINFORCED COMPOSITE MATERIALS	47-52
COMPARISON BETWEEN MRAS AND SMO BASED SENSORLESS CONTROL METHODS OF PERMANENT MAGNET SYNCHRONOUS MOTOR	53-59
NUMERICAL INVESTIGATION OF FATIGUE BEHAVIOURS OF NON-PATCHED AND PATCHED ALUMINIUM PIPES	60-65
DYNAMIC INVESTIGATION OF A PERMANENT MAGNET SYNCHRONOUS MOTOR FOR FAULTY OPERATIONS	66-70
MODELING THE CA2+ CAMKII NETWORK OF LTP IN THE JIGCELL ENVIRONMENT	71-77
CLASSIFICATION OF ANALYZABLE METAPHASE IMAGES BY EXTREME LEARNING MACHINES	78-82
EFFECTS OF PARTIAL RCCI APPLICATION OF LPG ON PERFORMANCE, COMBUSTION AND EXHAUST EMISSIONS IN A DIESEL ENGINE POWERED GENERATOR	83-92
DESIGNING A CONTROL INTERFACE AND PID CONTROLLER OF CUK CONVERTER	93-100
MODELING AND ANALYSIS OF PITCH ANGLE CONTROL ON VARIABLE SPEED WIND TURBINES	101-106

Enrichment of Apatite-Bearing Iron Ore by Magnetic Separation and Flotation

M. Birinci 

İnönü University, Mining Engineering Department, 44280, Battalgazi, Malatya, Turkey. (e-mail: mustafa.birinci@inonu.edu.tr).

ARTICLE INFO

Received: Jan.,06.2021

Revised: Feb.,1.2021

Accepted: Feb.,19.2021

Keywords:

Magnetite
Apatite
Magnetic separation
Flotation
SEM-EDS

Corresponding author: M. Birinci

ISSN: 2536-5010 | e-ISSN: 2536-5134

DOI: <https://doi.org/10.36222/ejt.866718>

ABSTRACT

In this study, enrichment possibility of apatite-bearing iron ore sample was investigated to obtain iron and phosphate concentrate, separately. It was determined that the raw ore contains 35.75% Fe and 5.36 P₂O₅. Magnetite in the ore can be enriched with low-intensity magnetic separator, and apatite can be enriched from the non-magnetic product by flotation. For this purpose, the raw ore was ground below 106 m size and then subjected to magnetic separation (with two cleaner and one scavenger), and following flotation (with three cleaner and one scavenger).

According to the experimental result, a magnetic concentrate containing 63.55% Fe and 1.65% P₂O₅, and phosphate concentrate containing 25.33% P₂O₅ and 6.45%Fe were obtained. The results show that there are still difficulties to obtain plausible iron and phosphate concentrates in terms of phosphorus and iron impurities for iron and phosphate concentrate, respectively. It is concluded that it is hard to separate the iron and phosphorus phases from each other, possibly due to complex mineralogical composition and poor mineral liberation of the ore.

1. INTRODUCTION

With the developing industry and technology in the world, the demand for iron and steel is increasing continuously. Reserves of high-grade iron ore, that can be used directly in the iron and steel industry, are limited and are getting depleted very fast. In addition, it has become essential to prepare the iron concentrate to meet the specification of the steel industry. Physical methods such as gravity concentration, magnetic separation and flotation are standard practices to separate the gangue minerals from iron ores. However, the ores having ferromagnetic nature are suitable for being processed using magnetic separation methods [1]. For example, magnetite (Fe₃O₄) is the most ferromagnetic of all the naturally occurring minerals on earth, and therefore low-intensity magnetic separators are widely used to upgrade magnetite ores.

Phosphorus is an important impurity and almost all of the phosphorus in iron ore transferred directly into cast iron during metallurgical processes. It is well known that steel containing high phosphorus is brittle, and therefore dephosphorization of iron ore is an important research topic. The only option to control phosphorus in the metal is limiting the amount of phosphorus in the ore. It is generally recommended that the phosphorus content of iron ore should

be less than 0.1%, though phosphorus limits vary according to steel-producing countries. Removal of phosphorus from certain iron ores has proven difficult, especially when phosphorus phases are associated with the iron phases in a very complicated manner. However, phosphorus can be removed from iron ore by physical processes (magnetic separation, flotation and selective agglomeration), chemical (leaching), thermal and bioleaching processes, as reported in the literature [2-5].

On the other hand, phosphorus is the common element in the earth's crust and is found in all living organisms. It is known that there are more than 200 phosphate minerals in the earth's crust, and structurally all have a (PO₄) tetrahedral unit. Approximately 95% of the world phosphate rock production is consumed in fertilizer manufacturing. The primary phosphate mineral is apatite (Ca₅(PO₄)₃(F, Cl, OH, CO₃)), and found in phosphate rock as: (a) fluorapatite (Ca₅(PO₄)₃F), found mainly in igneous and metamorphic deposits, (b) chlorapatite (Ca₅(PO₄)₃Cl), found in igneous and metamorphic deposits, (c) hydroxylapatite (Ca₅(PO₄)₃(OH)), found in igneous and metamorphic deposits and, (d) carbonate-hydroxyl-apatite (Ca₅(PO₄,CO₃)₃(OH)), found mainly on islands as part of bird and bat excrements (e.g. guano phosphate formations) [6-8].

Beneficiation of phosphate ores is one of the important research subjects in mineral processing studies. After size reduction and classification, the enrichment processing of the phosphate ores may include washing, desliming, magnetic separation, and flotation depending on the types of gangue minerals present. However, flotation is the most common process among them as more than 60% of the marketable phosphate in the world is produced by flotation [9]. It was reported by Nanthakumar et al. [10] that the anionic flotation of phosphate ores generally relies on the use of fatty acid surfactant-type collectors, and in the case of high-iron phosphate ores, the depression of iron minerals is usually achieved using starch and the use of this polysaccharide in this role is based on the very successful application of various starches in beneficiating hematite-based iron ores [10]. However, the role of reagents utilised in igneous phosphate ores flotation was reviewed by Guimarães et al. [11].

The igneous and metamorphic phosphate deposits such as Bingöl-Genç (Avnik) and Bitlis-Ünaldı ores are very complex and contain mainly magnetite and apatite, and silicates such as amphibole, epidote, diopside and chlorite, carbonates, (calcite, dolomite, siderite, and ankerite), nepheline syenite, pyroxenite, foskorite, etc [12-16]. The major problem of Bingöl-Bitlis ores is the high phosphorus content. Obtaining, both, the iron and phosphate concentrate from these deposits will significantly contribute to the valuation of such ores.

In this study, it has been aimed to obtain both magnetite and apatite concentrates by using magnetic separation and flotation, respectively.

2. MATERIAL AND METHODS

2.1. Material

In this study, apatite-bearing iron ore sample from Bingöl region was used. The sample was initially crushed below 6.70 mm and then below 3.35 mm using laboratory jaw and roll crusher, respectively. The crushed product was ground by rod mill, and then magnetic separation and flotation tests were carried out according to the procedure shown in Fig. 1.

2.2. Methods

Magnetic separation: The magnetic separation experiments were performed using a drum type wet low-intensity magnetic separator. Drum rotation speed was selected as 25 rpm, pulp density in the mixing tank was adjusted to 10% of solids by weight. In the first magnetic separation circuit, a rougher magnetic and non-magnetic product were collected. And then, the magnetic product was subjected to two cleaner stages and a final magnetite concentrate was obtained (Fig.1).

Flotation tests: The direct anionic flotation of phosphate minerals was conducted in accordance with the flowsheet shown in Fig. 1. Flotation tests were carried out in a Denver type laboratory flotation machine with 1.5 L cell. 400 g of ground samples were used for each test. The conditioning and flotation steps were made at 45% and 27% solids concentrations by weight, respectively, while keeping the pulp stirring speed constant at 1500 rpm. An industrial-grade distilled tall oil type fatty acid was used as a collector to float phosphate minerals. Sodium metasilicate and corn starch were used as dispersant and depressant, respectively. But, it was demonstrated that sodium silicate could be used not only as a dispersant of slime but also as depressant and activator for

some minerals. MIBC was used as the frother and the dosage was fixed at 30 g/t. NaOH was used to regulate and control the pulp pH. According to the flowsheet in Fig. 1, in the first part of flotation tests, apatite was floated to obtain rougher apatite concentrate. The rough concentrate was subjected to further flotation process using three cleaner stages. The sink product from rougher flotation test was then transferred to the apatite scavenger stage. In the cleaner and scavenger stages, froth product was scraped for 5 and 3 min., respectively. After the flotation process, a final apatite concentrate and a tailing from scavenger stage, and a middling product attained by combining the middlings from scavenger and cleaner stages were obtained. After carrying out the flotation tests, all products (apatite concentrate, middling, and tailing) were filtered, dried, and weighed. Chemical assays of all products were determined using XRF analysis technique. The flotation recovery was calculated based on the grade and weight of flotation products.

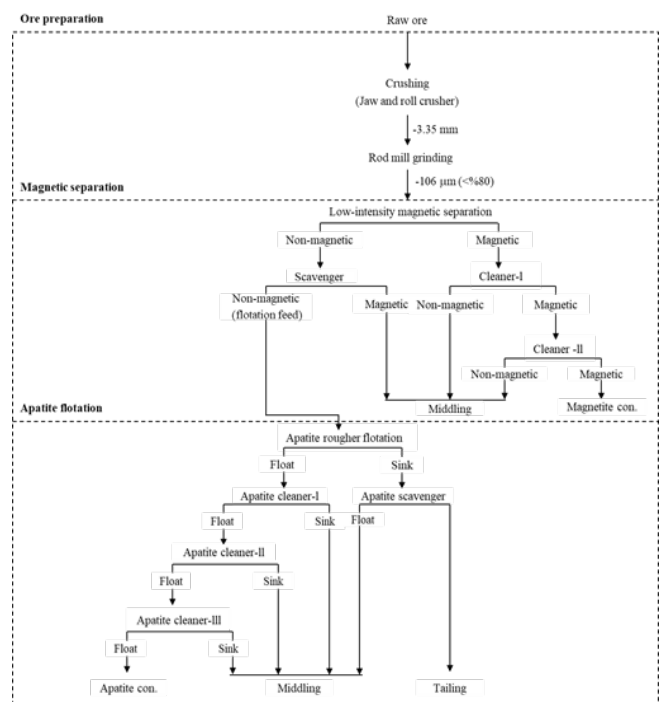


Figure 1. Flowchart of the ore preparation and beneficiation tests procedure.

Characterization techniques: Crystallinity of the samples was determined by X-ray diffraction analysis (XRD) using Rigaku RadB type diffractometer (at the Scientific and Technological Research Center, İnönü University, Malatya). The radiation applied was $\text{CuK}\alpha$ ($\lambda = 1.5405 \text{ \AA}$) from a long fine focus Cu tube, operating at 40 kV and 40 mA. The samples were measured in the range of 2-80 $^\circ$ with 0.02 $^\circ$ steps at a rate of 20 per min. Data collection and evaluation were performed with the International Centre for Diffraction Data (ICDD). The microstructure was observed by using an LEO Evo 40 model scanning electron microscope (SEM-EDS). The chemical composition of all sample was determined by X-ray fluorescence spectroscopy using the Thermo Scientific ARL ADVANT'X series XRF Spectrometers. The PSD analysis of the ground sample was determined using a Malvern Mastersizer 2000 particle analyser (Malvern Instruments Ltd., UK). The sample was stirred with distilled water at 2000 rpm in a 1-liter cell integrated with the device and in-situ

measurements were performed. Particle size distribution data were automatically obtained using Mastersizer 2000 software.

3. RESULTS AND DISCUSSION

3.1. Characterization of the ore

It is well known that the successful applicability of the physical beneficiation methods highly depends on the mineralogical characteristics of the iron ores [1] and the phosphate flotation is strongly influenced by the mineralogical composition of the phosphate ore [7,17]. Therefore, mineralogical and chemical characterization of raw ore was carried out before beneficiation tests.

Mineralogical analysis: XRD technique which may be coupled with chemical analysis is essential for characterization study, and applied for many purposes such as ore genesis, mineralization control and mineral processing, etc. In this study, XRD analysis was performed to determine the mineral phases of the raw ore, and the results are illustrated in Fig. 2. According to XRD analysis results, major mineral phases in the ore are apatite ($\text{Ca}_5(\text{PO}_4)_3(\text{F}, \text{Cl}, \text{OH}, \text{CO}_3)$) (but apatite type could not be distinguished), magnetite (Fe_3O_4), quartz (SiO_2), feldspar ($\text{NaAlSi}_3\text{O}_8$), calcite (CaCO_3), dolomite ($\text{CaMg}(\text{CO}_3)_2$), ilmenite (FeTiO_3), barite (BaSO_4), rectorite ($(\text{Na}, \text{Ca})\text{Al}_4(\text{Si}, \text{Al})_8\text{O}_{20}(\text{OH})_{4.2}(\text{H}_2\text{O})$), muscovite ($\text{KAl}_2(\text{AlSi}_3\text{O}_{10})(\text{F}, \text{OH})_2$). They are common minerals of phosphate bearing iron deposits, as reported in the literature [7,13].

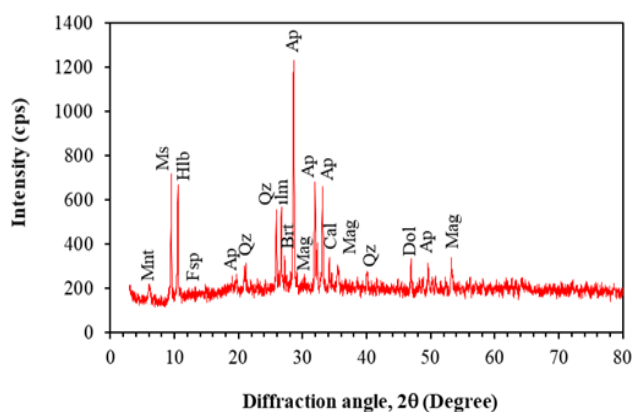


Figure 2. The XRD patterns of raw ore (Mnt: Montmorillonite, Ms: Muscovite, Ap: Apatite, Hlb: Hornblende, Fsp: Feldspar, Qz: Quartz, ilm: Ilmenite, Brt: Barite, Mag: Magnetite, Cal: Calcite, Dol: Dolomite).

Chemical analysis: Chemical analysis results of the raw ore is given in Tab. 1. The raw ore contains 35.75% Fe and 5.36% P_2O_5 . From the XRF results it can be seen that the ore sample is an iron rich ore containing phosphate and silicates as main gangue minerals. The raw ore can not be used directly in the iron-steel or fertilizer industries. Therefore, it must be enriched with suitable methods.

TABLE 1

CHEMICAL COMPOSITION OF THE ORE SAMPLE USED IN THE STUDY						
Compound	Fe	P_2O_5	SiO_2	Al_2O_3	CaO	MgO
Content (%)	35.75	5.36	27.25	6.12	10.18	0.68
	K_2O	Na_2O	TiO_2	MnO	LOI*	
	0.05	1.58	0.30	0.01	4.5	

* Loss on ignition (1000 °C)

3.2. Beneficiation tests

Magnetic separation test results: Phosphorous is a major contaminant for the vast majority of uses of iron ores, especially all related to iron making. It is found in a variety of forms from separate phosphate minerals to intimate association with iron hydroxide phases. When phosphate minerals can be traced as the major source of phosphorus, physical separation methods are feasible. The phosphorous removal of such ores can be normally carried through magnetic separation and flotation [18].

Magnetic separation test results are presented in Tab. 2. The results show that low-grade iron ore can be enriched by magnetic separation. It can be seen that the quality of magnetite product was improved in terms of chemical composition, especially for grades of Fe% and $\text{P}_2\text{O}_5\%$ compared to the content of the original ore. For example, Fe grade of raw ore increased from 35.75% to 63.55% with 80.40% Fe recovery.

TABLE 2

Product	Weight (%)	MAGNETIC SEPARATION TEST RESULTS			
		Grade %		Recovery %	
		Fe	P_2O_5	Fe	P_2O_5
Magnetite Conc.	45.23	63.55	1.65	80.40	13.92
Middling	15.68	24.06	3.42	7.19	10.00
Tailing/Non-mag	39.09	10.06	10.43	12.41	76.06
Feed	100	35.75	5.36	100	100

The full chemical analysis of the magnetite concentrate was also carried out and the results are given in Tab. 3. It can be concluded that a reasonable magnetite concentrate (can be used in iron and steel production and fed into the blast furnace) has been obtained by magnetic separation, except for the phosphate phase. However, the concentrate still contains a critical amount of phosphorus (1.65%).

TABLE 3

FULL CHEMICAL ANALYSIS OF MAGNETITE CONCENTRATE						
Compound	Fe	P_2O_5	SiO_2	Al_2O_3	CaO	MgO
Content (%)	64.73	1.62	6.36	2.22	1.94	2.16
	K_2O	Na_2O	TiO_2	MnO	S	
	0.11	0.68	0.25	0.05	0.5	

Chemical analysis results are also supported with XRD and SEM-EDS images given in Fig. 3 and Fig. 4. When XRD patterns of the magnetic product (or magnetite concentrate) from magnetic separation were examined, it was observed that the peak intensity of magnetite dramatically increased at around $35^\circ 2\theta$ (Fig. 3). The predominance of magnetite peaks indicates that magnetite is more abundant in magnetic concentrate. Although other peaks such as apatite are relatively declined, they are still present in the magnetic product.

As know, the combination of scanning electron microscopy-energy dispersive X-ray spectrometry (SEM-EDS) enable the chemical characterization of bulk and surface of individual particles. It can be observed from EDS spectrum of magnetic product that Fe exhibits very high distribution (95.95 wt.%).

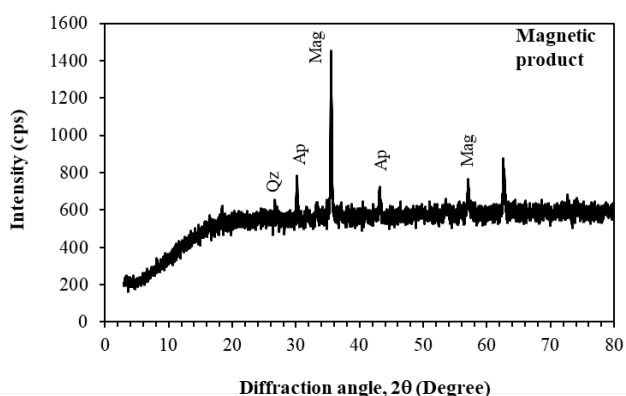


Figure 3. XRD patterns of the magnetic product obtained by low-intensity magnetic separation.

It indicates that main mineral phase in magnetic concentrate is magnetite, but, according to SEM observations, free particles consisting of single mineral phase in the mapping images are very rare, indicating poor mineral liberation as a result of intergrowth relationship with magnetite and phosphate mineral phases (Fig.4).

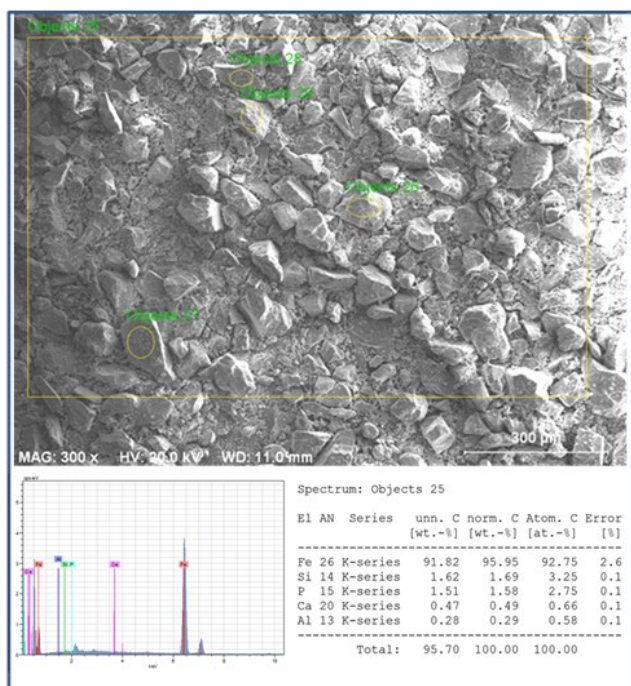


Figure 4. SEM-EDS images of the magnetite particles from magnetic separation.

Flotation test results: It is well known that the flotation performance strongly depends on particle size and liberation of the valuable mineral [19,20]. Also, previous studies have shown that the particle size distribution of milling ore has an essential effect on metallurgical results of phosphate flotation [21]. The particle size distribution of the flotation feed, the non-magnetic product of the magnetic separation, is shown in Fig. 5. As seen from the Fig. 5, d(50) value is about 80 mm. However, the slope of the curve becomes slightly steeper and indicates a narrow particle size distribution. According to the literature, narrow feed size distribution may have a positive effect on flotation process compared to large particle size distribution [22].

Magnetic separation tailing (i.e. non-magnetic product) was subjected to flotation process to obtain apatite

concentrate. An industrial-grade distilled tall oil type collector (tall oil+fuel oil, 800 g/t of dosage) was used as an apatite collector. As dispersant of slime, sodium metasilicate (Na₂SiO₃) solution (about 40%) was used to disperse silicate gangue minerals. Also, soluble corn starch ((C₆H₁₀O₅)_n) was used as depressant for iron minerals. The dosages of the sodium silicate and corn starches were 1200 and 1000 g/t, respectively. MIBC was used as the frother and the dosage was fixed at 30 g/t. NaOH was used to regulate and control the pulp pH at 9.5. Phosphate concentrate obtained by rougher flotation was subjected to three cleaning circuits to obtain high-grade phosphate concentrates.

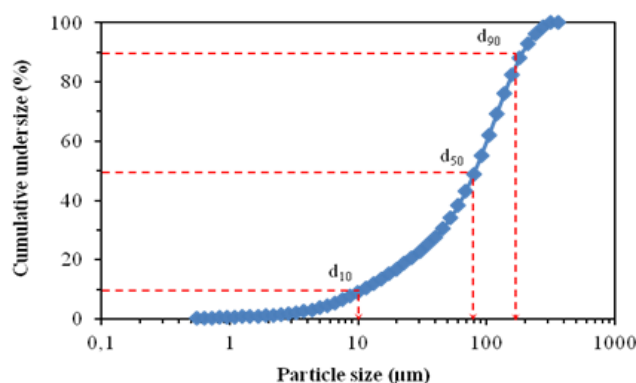


Figure 5. Particle size distribution of the flotation feed (i.e non-magnetic product from magnetic separator).

Flotation results presented in Tab. 4 clearly show that there is an improvement in P₂O₅ grade of the phosphate concentrate. It can be seen that the quality of concentrate was improved in terms of P₂O₅ and Fe grades, compared to the content of the original ore. A high-grade phosphate concentrate containing 25.33% P₂O₅ was obtained with 64.89% recovery. However, the relatively higher iron content (6.45% Fe) implies that Fe-bearing minerals may be present in concentrate. According to a recent study by Nakhaei and Irannajad [23], starch is a depressing and flocculating agent for various minerals but normally used as a depressant for iron oxides. However, it should be emphasized that the composition and interlocking of iron-bearing minerals are very critical in phosphate flotation. In cases where the magnetite is intimately intergrown with phosphate minerals (i.e. apatite), such particles tend to either float (i.e. going up to concentrate or middling) or sink (i.e. remaining to tailing) depending on the flotation conditions. As a result, interlocked mineral particles are the most important handicap to selective flotation, and it is very difficult to predict their behavior in flotation.

TABLE 4

Product	Weight (%)	DIRECT ANIONIC FLOTATION OF APATITE			
		Grade %		Recovery %	
		P ₂ O ₅	Fe	P ₂ O ₅	Fe
Apatite Conc.	26.72	25.33	6.45	64.89	17.13
Middling	18.39	9.47	8.49	16.70	15.52
Tailing	54.89	3.50	12.34	18.42	67.33
Feed	100	10.43	10.06	100	100

XRD pattern and SEM-EDS images of the apatite concentrate are shown in Fig. 6 and Fig. 7, respectively. Based on attrition-direct flotation, the results of XRD analysis confirmed that apatite minerals were enriched in flotation concentrate. In the apatite concentrate, the major crystalline

phase is apatite, XRD intensity of which is sharply increased by flotation. However, apatite flotation causes the intensity of magnetite reflection to decrease significantly, but never completely disappear (Fig. 6).

According to EDS spectrum of the flotation concentrate in Fig. 7, the total distribution of Ca and P elements is 83.89 wt.% and much higher than other elements. It indicates that the abundant mineral phase in flotation concentrate is phosphate minerals such as apatite, but also carries less amount of silica (e.g. quartz) and other mineral phases such as iron oxides (e.g. magnetite). Although the mineral source of fluor (F) in the ore is unrecognized, it may indicate fluorapatite ($Ca_5(PO_4)_3F$).

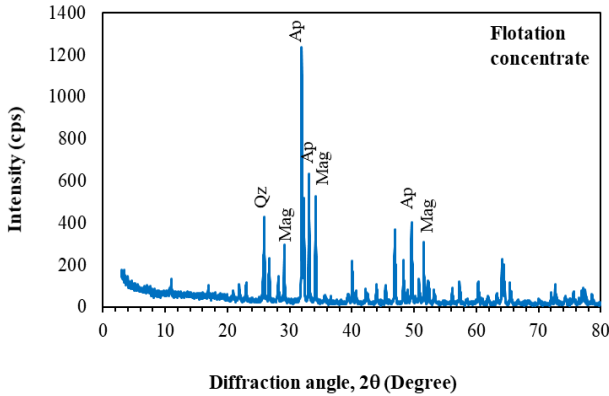


Figure 6. XRD patterns of flotation concentrate (i.e. apatite conc.).

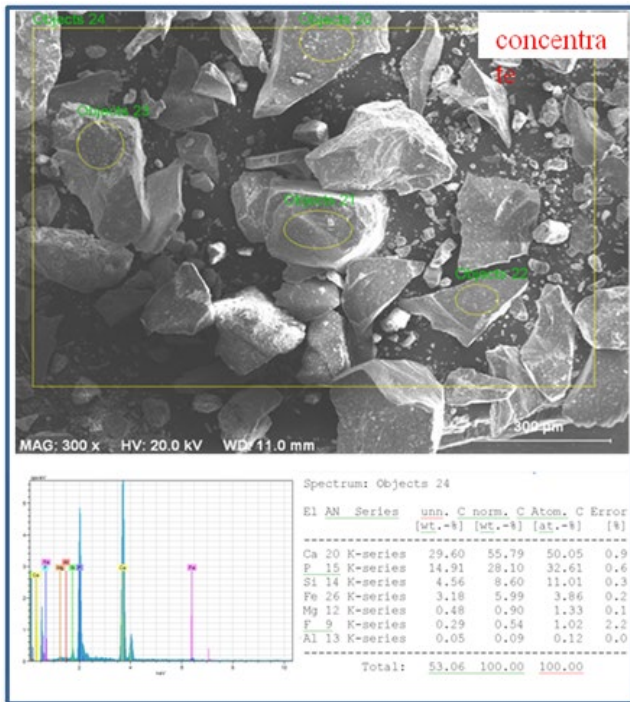


Figure 7. SEM-EDS images of flotation concentrate (i.e. apatite conc.).

As seen in the XRD pattern of flotation tailing in Fig. 8, the peak intensities of silicate minerals dramatically increased. The highest peak by appearing at around $26.5^\circ 2\theta$ is the typical peak of quartz. XRD results emphasize that the tailing is mostly composed of gangue minerals, but it also includes phosphate and iron phases.

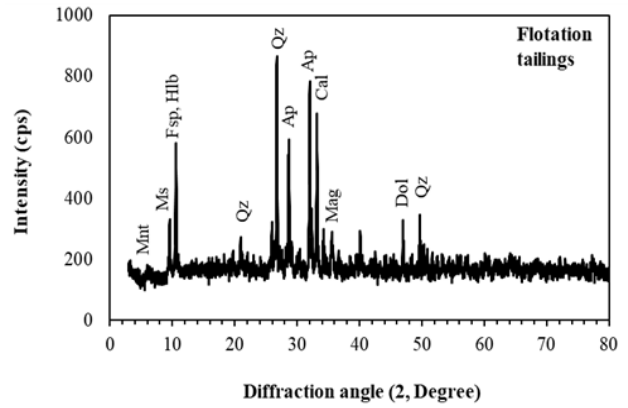


Figure 8. XRD patterns of flotation tailing.

The distribution of Fe and Si element in the EDS spectrum of tailing particles in Fig. 9 is 29.78 wt.% and 24.70 wt.%, respectively, implying that iron and silica mineral phases are more in tailings, as expected. Also, the tailing particle contains a significant amount of Ca (23.52 wt.%) and P (12.58 wt.%). Source of Ca in the flotation tailing comes from phosphate or largely carbonate minerals like calcite and dolomite.

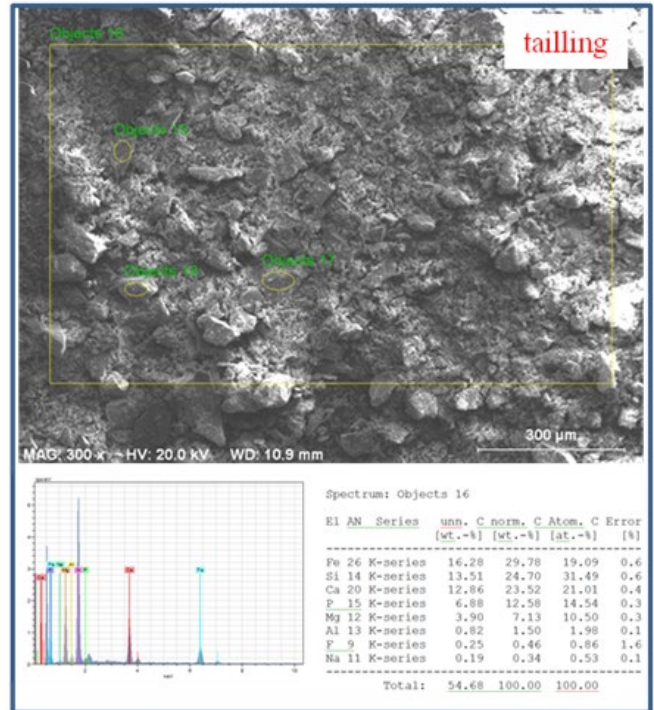


Figure 9. SEM-EDS images of flotation tailing.

4. CONCLUSION

In this study, the concentration of apatite-bearing iron ore from Bingöl region with low Fe and high P_2O_5 contents was investigated by utilizing consecutive magnetic separation and froth flotation. The following conclusions were drawn from this study:

- 1) As a result of magnetic separation processes, a concentrate having 63.55% Fe and 1.65% P_2O_5 grade was obtained with an 80.40% recovery from the raw ore containing 35.75% Fe and 5.36% P_2O_5 . However, the phosphorus content of the magnetite concentrate is critical for the iron and steel industry. Nevertheless, harmful impurities such as SiO_2 ,

Al_2O_3 , MgO , K_2O , and Na_2O have been reduced to the plausible level demanded by the iron and steel industry.

2) In order to obtain high-grade apatite concentrate with high apatite recovery, cleaning and scavenging stages are required. The batch flotation test with three cleaning stage increased the P_2O_5 content in the concentrate from 10.43% to 25.33% and decreased the Fe content from 10.06% to 6.45%. Unfortunately, P_2O_5 grade is still low for marketable phosphate concentrate, and Fe content in the concentrate was still high for the fertilizer industry.

3) The higher quality phosphate concentrate could not be obtained, probably due to mineralogical composition of the ore such as interlocking of Fe-oxides with phosphate minerals and the lack of mineral liberation.

5. ACKNOWLEDGEMENT

This study was carried out in the Mining Engineering Department of İnönü University, Mineral Processing Laboratories.

REFERENCES

- [1] S.K. Roy, D. Nayak, S.S. Rath, "A review on the enrichment of iron values of low-grade iron ore resources using reduction roasting-magnetic separation," *Powder Technology*, vol. 367, pp. 796-808, 2020.
- [2] A.C. Pereira, R.M. Papini, "Processes for phosphorus removal from iron ore-a review," *REM: Revista Escola de Minas*, vol. 68, no. 3, pp. 331-335, 2015.
- [3] Y. Mochizuki, N. Tsubouchi, "Removal of gangue components from low-grade iron ore by hydrothermal treatment," *Hydrometallurgy*, vol. 190, article no. 105159, 2019.
- [4] S.S. Rath, H. Sahoo, N. Dhawan, "Optimal recovery of iron values from a low grade iron ore using reduction roasting and magnetic separation," *Separation Science and Technology*, vol. 49, no. 12, pp. 1927-1936, 2014.
- [5] F.W. Su, K.H. Rao, K.S.E. Forsberg, P.O. Samskog, "The influence of temperature on the kinetics of apatite flotation from magnetite fines," *International Journal of Mineral Processing*, vol. 54, no. 3-4, pp. 131-145, 1998.
- [6] U.S.G.S. "Mineral Commodity Summaries, Phosphate Rock," U.S. Geological Survey, 2003.
- [7] A.M. Abouzeid, "Upgrading of Phosphate Ores-A Review," *The Journal of Ore Dressing*, vol. 9, no. 17, pp. 10-32, 2007.
- [8] P.V. Straaten, "Rocks for Crops: Agrominerals of sub-Saharan AfricaRocks for Crops," Department of Land Resource Science, Canada, 2002.
- [9] G. Baudet, "The Processing of Phosphate Ores," *Chron. Rch. Miner., Special Issue on Phosphates*, 1988.
- [10] B. Nanthakumar, D. Grimm, M. Pawlik, "Anionic flotation of high-iron phosphate ores-Control of process water chemistry and depression of iron minerals by starch and guar gum," *International Journal of Mineral Processing*, vol. 92, no. 1-2, pp. 49-57, 2009.
- [11] R.C. Guimarães, A.C. Araujo, A.E.C. Peres, "Reagents in igneous phosphate ores flotation," *Minerals Engineering*, vol. 18, no. 2, pp. 199-204, 2005.
- [12] D.P.T. "Madencilik ÖİK Endüstriyel Hammaddeler Alt Komisyonu, Gübre Sanayii Hammaddeleri Çalışma Grubu Raporu Fosfat, Kükürt, Potas," T.C. Başbakanlık Devlet Planlama Teşkilatı Müsteşarlığı, Yayın No: 2437, 1996.
- [13] B. Erdoğan, O.Ö. Dora, "Bitlis masifi apatitli demir yataklarının jeolojisi ve oluşumu," *Türkiye Jeoloji Kurumu Bülteni*, vol. 26, pp. 133-144, 1983.
- [14] C. Helvacı, "Apatite-Rich Iron Deposits of the Avnik (Bingöl) Region, Southeastern Turkey," *Economic Geology*, vol. 79, no. 2, pp. 354-371, 1984(a).
- [15] C. Helvacı, "Bitlis Masifi Avnik (Bingöl) yöresi apatitli demir yataklarının oluşumu," *Jeoloji Mühendisliği*, vol. 19, pp. 33-51, 1984(b).
- [16] H. Çelebi, "Türkiye Apatitli Manyetit Yatakları: Jeolojisi, Jeokimyası ve Ekonomik Potansiyeli," *İstanbul Yerbilimleri Dergisi*, vol. 22, no.1, pp. 67-83, 2009.
- [17] L.A.F. Barros, E.E. Ferreira, A.E.C. Peres, "Floatability of apatites and gangue minerals of an igneous phosphate ore," *Minerals Engineering*, vol. 21, pp. 994-999, 2008.
- [18] A.P.L. Nunes, A. C. Araujo, P. R. M. Viana, A. B. Henriques, "Revisiting phosphate separation from iron ores," *ANNALS - 3rd International Meeting on Ironmaking and 2nd International Symposium on Iron Ore*, Brazil, pp. 265-275, 2008.
- [19] W.J. Trahar, "A rational interpretation of the role of particle size in flotation," *International Journal of Mineral Processing*, vol. 8, pp. 289-327, 1981.
- [20] N.W. Johnson, "Existing methods for process analysis, Flotation Plant Optimisation A Metallurgical Guide to Identifying and Solving Problems in Flotation Plants," Edited by C.J. Greet. Spectrum Series No 16. The Australasian Institute of Mining and Metallurgy, Chapter 2, pp. 35-64, 2010.
- [21] D. Feng, C. Aldrich, "Influence of operating parameters on the flotation of apatite," *Minerals Engineering*, vol. 17, no. 3, pp. 453-455, 2004.
- [22] C.P. Massola, A. P. Chaves, J. R. B. Lima, C. F. Andrade, "Separation of silica from bauxite via froth flotation," *Minerals Engineering*, vol. 22, no. 4, pp. 315-318, 2009.
- [23] F. Nakhaei, M. Irannajad, "Reagents types in flotation of iron oxide minerals: A review," *Mineral Processing Extractive Metallurgy Review*, vol. 39, pp. 89-124, 2018.

BIOGRAPHIES

Mustafa Birinci obtained his BSc degree in mining engineering from Karadeniz Technical University (KTU) in 1997. He received the BSc., and MSc. diploma in Mining Engineering from the Karadeniz Technical University and İnönü University in 1997 and 2002 respectively, and PhD degrees in Graduate School of Naturel and Applied Science, Department of Mining Engineering of the same university in 2011. He was awarded a grant (2214-International Research Fellowship Programme for PhD Students) by The Scientific and Technological Research Council of Turkey (TUBITAK), and studied at The University of Utah, Metallurgical Engineering between 2009-2010 (9 months). His research interests are mineral processing and coal preparation, especially the concentration of metallic and industrial minerals by froth flotation. He has recently focused on hydrometallurgical processing of industrial minerals such as clay minerals. In 1998 he joined the Engineering Faculty, İnönü University as a research assistant, where he is presently an assistant professor. He is active in teaching and research in mineral processing.

Investigation of Home Type Heliostat Systems Daylighting Performance with Lighting Simulation Software

E. Uygun^{1*}  and, S. Görgülü² 

^{1*}Suleyman Demirel University, Department of Civil Engineering, 32260, Isparta, Turkey. (e-mail: mail@emreyugun.com).

²Burdur Mehmet Akif Ersoy University, Dep. of Electrical - Electronics Eng., Burdur, Turkey. (e-mail: sgorgulu@mehmetakif.edu.tr).

ARTICLE INFO

Received: March.,09.2021

Revised: Apr.,1.2021

Accepted: Apr.,12.2021

Keywords:

Sustainability
Daylighting
DIALux
Heliostat
Solar architecture

Corresponding author: *Emre Uygun*

ISSN: 2536-5010 | e-ISSN: 2536-5134

DOI: <https://doi.org/10.36222/ejt.893985>

ABSTRACT

Solar energy, which is an unlimited, costless and clean type of energy, is often preferred in architecture also as in all other areas. Today, all new technologies are made by focusing on solar energy. The main objective of lighting design in buildings is, to minimize energy consumption by keeping health and visual comfort at a high level. In this study, a home type heliostat system which is one of the modern and economic heliostat systems was introduced and its properties are listed. Based on the features of home type heliostat systems, all components of the system are modelled in a 3 Dimension stereolithography format. The daylighting performance of the home type heliostat systems was observed with the lighting simulation software. DIALux lighting design software was used in the study.

The results show that the home type heliostat systems can successfully transfer natural light into the building in a simulation environment created by modelling and contribute to illuminance.

1. INTRODUCTION

Like every other area, energy consumption continues to increase its importance every day in all interior design. Keeping building performance at the top level has become a primary objective when lowering energy consumption. With the research and the developing technology, sustainability has also been commemorated with other terms such as green, ecological, user, and environmentally friendly [1]. With these concepts desired in the field of lighting, energy optimization should be achieved by not reducing the comfort of the room but by creating the necessary illuminance without compromising building performance and user health [2]. Besides these, the efficiently designed natural lighting system supports the balancing of the space, the heat loads, the health, and the activities of the users [3]. Today, about 20% of the electricity consumed is on a large part of the lighting needs [4]. Daylight has a very important place among renewable energies in terms of reducing electricity consumption around the world [5, 6]. Daylight gain in buildings has a very important position in terms of both heating and lighting.

The natural lighting provides to the desired area by taking maximum advantage of daylight in daylight time and minimizes energy consumption by artificial lighting or even completely remove it. Besides, the positive effects of natural daylight on people have been discussed in previous studies [7, 8]. The vast majority of people who live in the city spend daylight hours under artificial lighting without seeing the daylight, and the harmful effects of this have been explored in previous studies [9]. 80% of human perception capacity is realized with the sense of sight [10]. Therefore, healthy sensing can be realized with natural and optimum illumination. In another study on lighting, results were obtained by neurobiological studies [11]. As a result of this comprehensive study, it has been mentioned that healthy lighting affects the regulation of brain activities and affects the regulation of the melatonin hormone secreted by the body [12, 13]. When designing living space, designers must account for the fact that lighting design affects autonomic reactions, hormones, and our nervous systems [14]. In a study conducted by Innovative Design, daylight schools were established through sensors, as result of this study, because of this space

which can use daylight in every area it was observed that the rate of children's coming to school was increased, there was a great reduction in library volume and children were much cheerful and they showed a rapid development [15]. In line with the work done, natural energy recovery and lighting design are at the forefront when the general methods are insufficient to provide the required lighting levels. In the design stage of the place, this situation should be determined and calculated by various simulation software. Alternative methods have emerged for current buildings and new buildings without energy-saving calculations at the design stage [16]. Because of the mini software and sensors, heliostat systems that collect and concentrate daylight are used in lighting systems from the past to the present [17]. Despite the rapid development of artificial lighting technologies designers are directed to the use of natural resources together with artificial lighting [18]. It has been realized that the energy-saving potential of the buildings can be subtracted to the upper levels with natural lighting [19]. With the correct use of a natural source such as the sun at our disposal, CIE lighting standards and optimum illuminance can be reached. Because of the building's north direction, it may not have access to daylight and environmental factors which block daylight can also cause this [20]. Home type heliostat systems can be used in these types of variations and even to remove frosted areas. The sun, which plays a major role in sustainable architecture in particular, plays a major role in optimizing energy use [21]. The importance of solar energy in energy-efficient buildings has been mentioned in earlier studies. In these studies, the importance of transferring daylight into living space and direct and indirect lighting methods are mentioned. It has been observed that energy consumption can be reduced between 30% and 70% by using natural lighting in addition to artificial lighting [22].

This study aimed to observe the value of daylight that home type heliostat systems can transfer into the building in a simulation environment, to present the obtained data with graphics, and to create a sample study with DIALux software for future studies.

2. MATERIAL AND METHODS

The home type heliostat system used in simulation has motors that provide 2-axis motion. Includes one sun sensor to detect and track the sun and it has one microprocessor that determines the motion by processing this data [23]. Provides the power of the movement with the solar energy collects by the solar panels located on it. Thus, there is no need for any external energy source to operate. It reflects daylight to the living space with its solar-powered motors and vinyl-coated reflectors. The light reflection area is about half a square meter and according to the manufacturer, the light stream is expected to correspond to 50,000 lumens or 500 watts [23]. This power is equivalent to approximately 60 standard light bulb luminous flux. First of all, the home type heliostat system has been detailed by plotting it as a technical drawing. The created a scaled format was transferred to the 3D modelling software by using the DXF (Drawing Interchange File) format. The 3D model of the home type heliostat system was created for the lighting design simulation process and visualization by utilizing the measurements on the picture. The modelled home type heliostat system is shown in Figure 1.

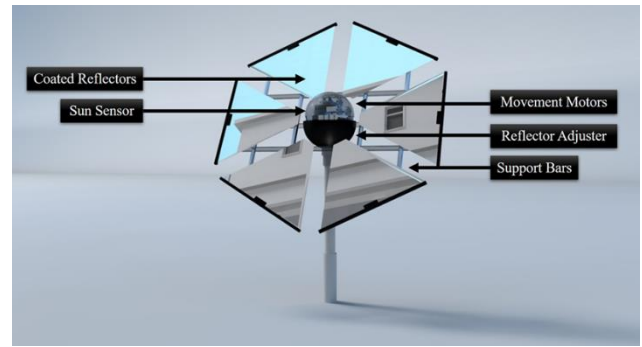


Figure 1. Home type heliostat system modelled for use in simulation

The modelling process was carried out by taking the basic information of the maximum height, the coating reflection rates, the axial rotation restrictions, and each component such as reflector number, reflector dimensions, electronic components, protection materials, axis support rods, sun sensor limits. A total of 160 m² 2-story villa has been modelled and prepared for the virtual simulation environment created. Illumination-focused windows are added and the entrance is positioned to be in the east direction. The model and simulation area view is shown in Figure 2. Coating, wall paints, window materials, reflecting rate information of the models has been entered in the DIALux software for the best results. Completed models were converted to 3D STL file format and exported from the 3D design software by object transfer to the lighting simulation area in DIALux. The distance of the home type heliostat system from its targeted space is planned as 9.1 m and the upper angle which it will make with vertical targeted as 160 and the lower angle targeted as 30. This angle determined in daylight design is very important and the ideal angle range to be used year-round is shown between +15 and -15 degrees [24]. The distance and angle values determined for the home type heliostat system were selected according to the maximum dimensions determined by the manufacturers such as Wikoda [23, 24].



Figure 2. Detailed villa model and position of home type heliostat system

Information of the region where the simulation will be performed is defined in the software as 29.00 longitudes 41.00 latitude location in Turkey / Istanbul. Turkey is a good location for this type of application [25]. To make regular measurements throughout the day and to obtain optimal results, the definition of the time zone is Istanbul (UTC + 02: 00).

Interior walls, texture coatings, and reflection rates have been set following the standards for an optimal simulation. At the same time, interior detailing models of the building and other parts were made transferable passing through a structural arrangement in STL format as separate files. The transferred interior detail models were placed in the space.

Texture coatings and reflection rates of the locally organized internal detail models were entered. Daylight calculation is performed using the three different sky models described in CIE 110-1994 in the DIALux lighting simulation software. These occur with the formation of sun position and light stage following the time zone and region of the software according to cloudy sky, average sky, and clear sky conditions. In the study conducted, modelling and daylight staging was performed using open sky conditions without a heliostat system and with a heliostat system at 1-hour intervals throughout the day. The open sky condition is chosen as the condition that can best measure heliostat efficiency from natural lighting methods. This system and similar ones have shown their true abilities when they are placed properly in the upper part of a window opening to capture the sky beam in open sky conditions and to direct their direct component to the part near the ceiling window [26, 27]. Polygon constructions of the used design materials were transferred to the DIALux software without distortion in their structural details by keeping their polygon structures at a detailed level and by maintaining scales while importing interior design models. Thus, in the daylight lighting simulations which will be made although the simulation and calculation times are extended, it is aimed to get the most accurate results from the simulation. Reflection rates of textures (wall, floor, furniture) are presented in Figure 3.

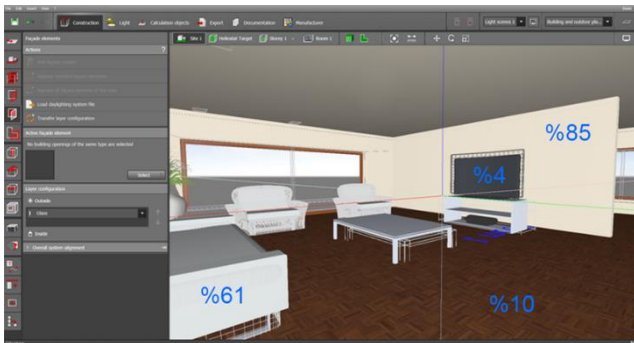


Figure 3. Reflection rates of textures

Calculation area 1 (daylight transfer area which is the primary target of the home type heliostat system), calculation area 2 (Interior zone at the working plane defined by the DIALux software) were defined. Then the two defined areas were simulated model together with the open sky by measurements made at intervals of one hour per day. In the DIALux lighting simulation software, according to sun position, the home type heliostat system repositioned with hourly metrics by calculating angle with measurement horizontally for best results. Solar track sensor section, support section, and reflective surfaces were separately defined to DIALux lighting simulation software and therefore this positioning was made possible. The angular adjustment of the reflective surfaces is shown in Figure 4. Defined angular movement and the angle required for the home type heliostat system to the specified targets are determined by the NOAA (Earth System Research Laboratory) solar calculator. Angular changes of less than 1° were entered by using object position in the DIALux software [28]. The working plane and window, defined as the target for the home type heliostat system, were used as virtual computing fields to obtain daylight illumination values.

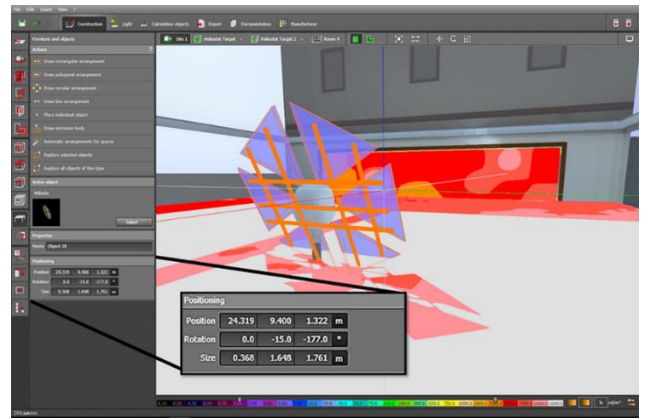


Figure 4. Defining the angular motion for the home type heliostat system reflective surfaces

When the amount of solar energy transfer used in the windows decreases, the light transmission also decreases [29]. The window glasses used in the modelled space were defined in standard single glass properties at a rate of 90% permeability. The preliminary comparison image of the home type heliostat system position calculations at the same time and conditions is presented in Figure 5. Afterwards, results were obtained with the home type heliostat system at intervals of one hour throughout the day and the contribution rate of the heliostat model to illuminance was calculated to be compared with the tables.

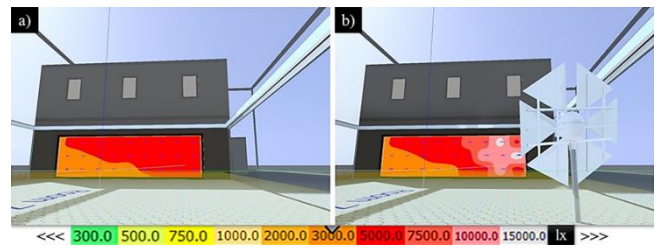


Figure 5. Sample images are taken from daylighting simulation under equal conditions (a) Without home type heliostat (b) With home type heliostat

3. RESULTS AND DISCUSSION

For the measurement which its modelling and simulation preliminary information is completed, the indoor working plane which was defined by DIALux software has two different virtual measurement surfaces as indicated in Figure 7, windows are set as light zones of brightness levels. These zones were established for taking a total of 12 results hourly in open sky conditions between 07:00 a.m. and 06:00 p.m. on 01.06.2017. The graph of the colour information graph values based on DIALux software data is shown in Figure 6. According to this data, the first contact points of the daylight are measured at 15,000 lux and more. These points are represented by a white tissue sample. The daylight-gathering criterion is distributed in the hot-cold colour range.

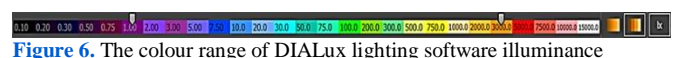


Figure 6. The colour range of DIALux lighting software illuminance

Daylight transferring element (window) and working plane (living space) which are 2 calculation areas was specified in DIALux software. The measurements taken from these areas are presented in comparison tables. The images of these 2 calculation areas are shown in Figure 7.

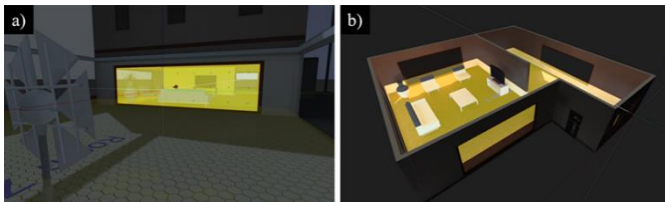


Figure 7. Virtual sensor areas (a) Sensor area 1 (b) Sensor area 2

Virtual illumination level sensors are placed on the window (virtual sensor area 1) and the work plane (virtual sensor area 2). Dimensions of the measuring areas serving as sensors were determined as 6.1 x 2.2 m and 8.4 x 9.5 m, respectively. Measurements were taken on equal conditions, every 1-hour interval in the 2 defined calculation areas, and binary comparison tables were generated from the obtained data. Based on the results of the calculation area data comparison given in Tables 1 and 2, comparisons were made by drawing a table of illumination intensity change charts.

TABLE 1

MAXIMUM ILLUMINANCE OBTAINED THROUGH THE WINDOW (AREA 1)

Clear sky Date / Time (01.06.2017)	Calculation area 1	
	Heliostat passive	Heliostat active
07:00	22,378 lx	22,631 lx
08:00	47,196 lx	47,456 lx
09:00	57,417 lx	57,706 lx
10:00	56,197 lx	56,531 lx
11:00	46,298 lx	46,625 lx
12:00	30,768 lx	30,913 lx
13:00	11,835 lx	12,727 lx
14:00	7,646 lx	8,784 lx
15:00	5,411 lx	7,074 lx
16:00	4,325 lx	5,735 lx
17:00	3,216 lx	3,970 lx
18:00	3,076 lx	3,432 lx

TABLE 2

MAXIMUM ILLUMINANCE OBTAINED OVER THE WORKING PLANE (AREA 2)

Clear sky Date / Time (01.06.2017)	Calculation area 2	
	Heliostat passive	Heliostat active
07:00	4,238 lx	4,303 lx
08:00	6,953 lx	7,028 lx
09:00	7,765 lx	7,854 lx
10:00	7,240 lx	7,335 lx
11:00	5,840 lx	5,945 lx
12:00	4,048 lx	4,162 lx
13:00	2,845 lx	2,984 lx
14:00	2,258 lx	2,420 lx
15:00	1,971 lx	2,158 lx
16:00	1,844 lx	2,040 lx
17:00	1,741 lx	1,955 lx
18:00	1,589 lx	1,799 lx

According to the data taken for these zones, it is seen that the average home type heliostat system effect for the working plane is around an average of 150 lux. A gain zone chart was given for workspace values in the direction of the data which is obtained with DIALux software and presented in Table 2. Figure 8 shows a graph of the average value of the gain for the working plane (Area 2) generated from the obtained data.

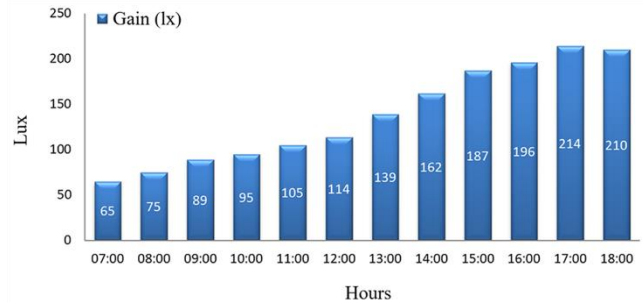


Figure 8. Working plane average lighting gain chart with home type heliostat system

Observed that in the simulation area created, home type heliostat system has been observed that it contributes totally up to 1,000 lux between 12:00 p.m. - 06:00 p.m. It was observed that the home type heliostat systems had a contribution of 3.41% in total to the working plane luminous intensity when the daylight is active. The visualization of these values as a color distribution in the DIALux software is presented in Figure 9.

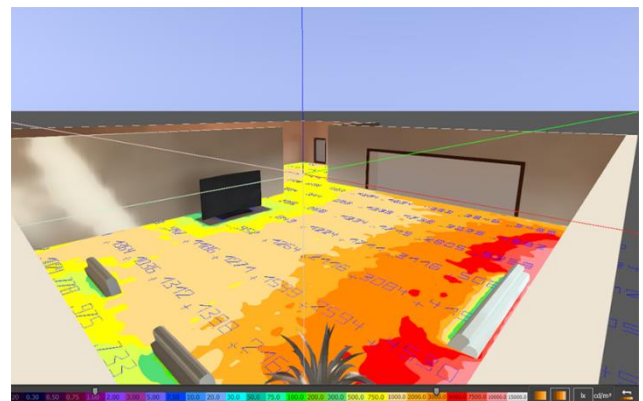


Figure 9. Illuminance colour distribution at the working plane (area 2)

Luminous distribution and brightness values at the 15 m² walls where daylight is projected by using the home type heliostat system are presented in Figure 10.

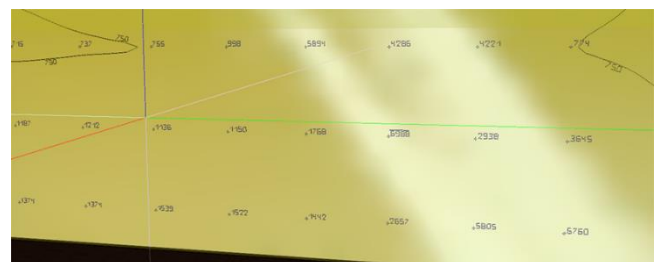


Figure 10. Image of the luminous distribution and brightness values from wall

According to the measurements taken from the working plane (Area 2), it has been observed that the home type heliostat system can instantaneously add up to 200 lx value to the average illuminance. The positioning of these systems in

the design phase of the challenging spaces can provide great advantages to the designer. At the same time, this will help to create sustainable buildings that conserve energy. The use of such natural energy resources, which can create a visual unity with space, will become an indispensable part of modern architecture and eco-friendly places. The architectural visualization of the system modeled as a simulation area is given in Figure 11.



Figure 11. Visualization of the generated simulation environment

Thanks to the reflective ratio coating feature of the DIALux software, the positive effect of home type heliostat systems on sustainable structures can be observed in the simulation environment. This observation will also give an advantage to the designer and with the use of preliminary calculations of such systems in further studies, will be reflected as positive effects on nature, humans, space, and the environment. Because of the easy-to-use feature of home type heliostat systems, more efficient hybrid systems can be found by investigating the possibility of simultaneous operation with other systems which are difficult to integrate into living areas [30]. As we know it, such systems use the sun as a light source, that's why it will be beneficial to use them for the areas which have high daylight-taking time. With the use of the north facade of the place, the heating problem caused by the transfer can be overcome. Regions such as Turkey have an effective geographical settlement with their location for lighting systems that utilize natural energy [31]. The natural daylight reaching indoors will be beneficial to our physique balance system in the first place. This type of natural lighting application will help people to improve their health and productivity levels by reducing stress levels. Thanks to daylight transmitted by natural lighting systems, they will provide physiologically positive effects to us. Also, in geographically disadvantaged areas, for example, it has been observed that in deep valleys, there is a system that can contribute to lighting values in shaded facades of places located on steep slopes. The use of such systems in conjunction with artificial lighting systems may provide maximum electricity savings by reducing the duration of artificial lighting devices. This study will be a reference to future research in terms of simulation and measurement methods for home type heliostat systems.

4. CONCLUSION

According to the manufacturers, light stream from home type heliostats is expected to correspond to 50,000 lumens and the illuminance for a 0.5 m² area transmitted from the recommended 9.1 m distance is an average of 15,000 lx and above [23, 24, 32]. This value was observed and visualized in

the lighting simulation. In the measurements taken from the working plane, it has been observed that the home type heliostat system can instantaneously add up to 200 lx to the average illuminance. These systems, which are practical for installation and application, are introduced for the alternative lighting methods, and simulation data was generated for the home type heliostat systems in the name of sustainable buildings.

5. ACKNOWLEDGEMENT

This study has been produced from the master's degree dissertation of Emre UYGUN.

REFERENCES

- [1] B. Edwards, E. Naboni. "Green buildings pay: Design, productivity and ecology", London, 2013.
- [2] V. Loftness, B. Hakkinen, O. Adan, A. Nevalainen. "Elements that contribute to healthy building design", Environmental Health Perspectives, vol. 115, pp. 965-970, 2007. <https://doi.org/10.1289/ehp.8988>.
- [3] I.G. Capeluto. "The influence of the urban environment on the availability of daylighting in office buildings in Israel", Building and Environment, vol. 38, pp. 745-752, 2010. [https://doi.org/10.1016/S0360-1323\(02\)00238-X](https://doi.org/10.1016/S0360-1323(02)00238-X).
- [4] T. Rubeis, M. Muttillio, L. Pantoli, I. Nardi, I. Leone, V. Stornelli, D. Ambrosini. "A first approach to universal daylight and occupancy control system for any lamps: Simulated case in an academic classroom", Energy Buildings, vol. 152, pp. 24-39, 2017. <https://doi.org/10.1016/j.enbuild.2017.07.025>.
- [5] U.S. Energy Information Administration (EIA), "Annual Energy Outlook", USA, 2012.
- [6] N. Nasrollahi, E. Shokri. "Daylight illuminance in urban environments for visual comfort and energy performance", Renewable and Sustainable Energy Reviews, vol. 66, pp. 861-874, 2016. <https://doi.org/10.1016/j.rser.2016.08.052>.
- [7] F. M. Marks. "Letter to the Editors: Lighting for Different Healthcare Settings", Health Environments Research and Design Journal, vol. 6, no. 3, pp. 166-168, 2013. <https://doi.org/10.1177%2F193758671300600314>.
- [8] G.H. Lim, M.B. Hirning, N. Keumala, N.A. Ghafar. "Daylight performance and user's visual appraisal for green building offices in Malaysia", Energy and Building, vol. 141, pp. 175-185, 2017. <https://doi.org/10.1016/j.enbuild.2017.02.028>.
- [9] E. Uygun, S. Görgülü. "Daylight simulation performance comparison of DIALux and RELUX illumination simulation programs", The Journal of Graduate School of Natural and Applied Sciences of Mehmet Akif Ersoy University, vol. special no. 1, pp. 1-8, 2016.
- [10] F. Çetin, B. Gümüş, Y. Özbudak. "Ergonomic evaluation of lighting characteristics", 2nd National Lighting Symposium and Exhibition, Diyarbakır, pp. 20-23, 2003.
- [11] M.S. Rea. "Light-much more than vision, proceedings of light and human health: EPRI/LRO", 5th International Lighting Symposium, Palo Alto, CA, pp. 1-15, 2002.
- [12] P. Badia, B. Myers, M. Boecker, J. Culpepper, J.R. Harsh. "Bright light effects on body temperature, alertness, EEG and behavior", Physiology and Behavior, vol. 50, no. 3, pp. 583-588, 1991. [https://doi.org/10.1016/0031-9384\(91\)90549-4](https://doi.org/10.1016/0031-9384(91)90549-4).
- [13] A.J. Lewy, T.A. Wehr, F.K. Goodwin, D.A. Newsome, S.P. Markey. "Light suppresses melatonin secretion in humans", Science, vol. 210, 1267-1269, 1980. <https://doi.org/10.1126/science.7434030>.
- [14] W. Bommel. "CIE and the way of putting 'lighting and health' into daily lighting practice, Proceeding Book of Lux Europa", 10th European Lighting Conference, Berlin, pp. 25-26, 2005.
- [15] B. Matusiak. "Daylight design for healthy learning environments", Professional Lighting Design, Turkey, vol. 33, pp. 72-76, 2010.
- [16] U.S., Green Building Council, <https://www.usgbc.org/credits/healthcare/v4-draft/eqc-0>.
- [17] S. Aydınlı, A. Rosemann. "A new lighting scheme that combines natural and artificial lights with heliostats and light transmitters", 3rd National Lighting Congress, Istanbul, pp. 36-43, 2000.
- [18] T. Yapar. "Energy Saving with Lighting Automation", Master Thesis, Yıldız Teknik University, Istanbul, 2007.

- [19] W.M. Lam. "Sunlighting as formgiver for architecture", New York, 1986.
- [20] C. Willis. "Form Follows Finance: Skyscrapers and Skylines in New York and Chicago", Princeton Architectural Press, New York, 1995.
- [21] M. Guzowski. "Daylighting for Sustainable Design", McGraw-Hill, USA, 2010
- [22] İ. Yüksek, T.T. Karadayı. "Energy-Efficient building design in the context of building life cycle", Energy Efficient Buildings, 2017. <https://doi.org/10.5772/66670>.
- [23] Wikoda, Natural sunlight to your home, <http://wikoda.com>.
- [24] eSolar energy news, Wikoda, <http://www.esolarenergynews.com/p/wikodas-sunflower.html>.
- [25] G. Z. Brown, M. Dekay. "Sun, Wind and Light: Architectural Design Strategies", John Wiley and Sons Inc., USA, 222-223, 2001.
- [26] Building Physics Expertise Applications, <http://www.yfu.com/yazilar/mim65-mayis.pdf>.
- [27] B. Erel. "A research on new technologies developed in the field of lighting with natural daylight", Master Thesis, Istanbul Teknik University, Istanbul, 2004.
- [28] NOAA, Solar Position Calculator, <https://www.esrl.noaa.gov/gmd/grad/solcalc>.
- [29] G. E. Weidman. "Considerations in the selection of solar energy controlled reflected glass in curtain wall", Flachglas A. G. 1999.
- [30] Z. Wang, Y.K. Tan. "Illumination control of LED systems based on neural network model and energy optimization algorithm", Energy and Buildings, vol. 62, pp. 514-521, 2013. <https://doi.org/10.1016/j.enbuild.2013.03.029>.
- [31] A. Sozen, E. Arcaklioglu, M. Ozalp, E. Kani. "Solar-energy potential in Turkey", Applied Energy, vol. 80, no. 4, 367-381, 2005. <https://doi.org/10.1016/j.apenergy.2004.06.001>.
- [32] Heliostat Design Concepts, <http://www.redrok.com/concept.htm>

BIOGRAPHIES

Emre Uygun received his bachelor's degree in Construction Education from Süleyman Demirel University in 2015. He received his master's degree in Spatial Planning and Design (Interdisciplinary) at Burdur Mehmet Akif Ersoy University in 2018. During his undergraduate and graduate studies, he worked at Süleyman Demirel Technopark for 5 years and actively took a part in TÜBİTAK projects covering the fields of health, nanotechnology, fiber lasers, materials and design. Moreover, he is studying another bachelor degree at the Isparta University of Applied Sciences, Department of Civil Engineering. Currently, he is a Ph.D. student in the Department of Sustainable Building Materials and Technologies within the scope of priority areas in the Civil Engineering Department of Süleyman Demirel University. He is awarded by scholarships of YÖK 100/2000 doctoral program and TUBITAK 2211-C program for his Ph.D. thesis subject.

He has been involved in international studies in the fields of artificial intelligence, lighting design, sustainable building materials and technologies, nanotechnology, laboratory measurement and analysis techniques, transportation engineering. He has a patent submission for his Ph.D. project which focused on the application of artificial intelligence on a transportation system. He is currently working on a project developed in the field of smart railways and continues his doctorate education.

Sertaç Görgülü obtained his B.Sc. degree from Marmara University in 2001. In 2002, he started to work as a research assistant at Marmara University. He received his M.Sc. and Ph.D. degrees from Marmara University in 2004 and 2011 respectively. Between 2009 and 2013, he worked at Kırklareli University in various titles. He has been working at Burdur Mehmet Akif Ersoy University since 2013.

He works in the fields of natural and artificial lighting and design, renewable energy.

Solutions of Solid Timber and Glulam Bridge Example with Different Approaches in Turkey

Gökhan Şakar^{1*}, Hüseyin Kürşat Çelik²

¹Dokuz Eylül University, Department of Civil Engineering, Izmir, Turkey, (gokhan.sakar@deu.edu.tr)

²Dokuz Eylül University, The Graduate School of Natural and Applied Science, Izmir, Turkey, (hkursadcelik@gmail.com)

ARTICLE INFO

Received: April., 01. 2020

Revised: Dec., 05. 2020

Accepted: April, 13. 2021

Keywords:

Solid timber

Glulam

Timber bridge

EN5

NDS

Corresponding author: *Gökhan Şakar*

ISSN: 2536-5010 / e-ISSN: 2536-5134

DOI: <https://doi.org/10.36222/ejt.712893>

ABSTRACT

In this paper, the properties of solid timber and glulam materials are investigated. An existing steel bridge in Turkey is resized and reanalyzed with the SAP2000 analysis programme using solid timber and glulam. In this way, the potential of timber as an alternative to steel is examined. Solid timber and glulam solutions are realized with EN5 norms used in Europe and NDS norms used in America. Structural analysis results and quantities take-off are compared. As a result of the analysis, it was seen that internal forces and quantities take-off in EN5 solutions were higher than NDS. It is expressed that the reason for this is the resistance factors in EN5 are different and the solution parameters are more general expressions.

1. INTRODUCTION

Various building materials have been used throughout the history in order to form a structural system, and steel and reinforced concrete materials are still widely used today. Research of alternative structural materials has increased for the get solution of topics like limited resource, sustainable structure, energy efficiency and environmental pollution. Therefore, potential of timber, the oldest construction materials of mankind, takes attention day by day, especially with the developing industrial facilities and technologies.

Since the millennium, the variety and frequency of research on wood has increased. General topics of studies about solid timber and glued laminated timber can be summarized like potential of timber according to physical and mechanical properties, positive and negative effects on environmental, energy efficiency etc.

Örs and Togay [1], investigated to production, cost and employment condition of timber industries in Turkey. They explained that the unit cost of timber buildings is not expensive comparisons between alternative materials and will be cheaper in future with the developments of production techniques. Doğangün et al [2] examined the earthquake performance of traditional wooden structures. They stated that the performance of timber structures was good in the past earthquakes in Turkey and they underlined that these

structures should be encouraged. There is a similarity on results of studies about timber structures seismic performance around the world. Investigation of casualties in huge earthquake general in the world showed that platform framed timber structures had a little part in entire losses [3]. In addition, studies show that wood will make a major contribution to the reduction of CO₂ emissions in the world and thus have a positive impact on the environment [4]. Moreover, using of timber could be preferred than concrete for large-scale highway bridges because of CO₂ emissions and environmental friendly, resulting from life cycle assessments [5].

It is the fact that if there is a requirement to resisting the bigger loads and the long spans, solution can be more resistant materials. That is why the developments of glued laminated timbers (glulam). Glulam is produced by lamination of a few timber layers. Production phase can be summarized like; timbers taking from logs, drying, and lamination with hydraulic press [6]. In Fig. 1, producing of glulam beams can be seen.

There isn't significantly difference between solid timber and glulam. But, through the production techniques of glulam has important advantages against to solid timber. For example, different tree species can be used together in lamination process. Thus, with variety of layer dimension and layer numbers, glued laminated timber can be solution for

engineering or architectural requirements. Possibility of using timber purified from defects while taking timber from logs ensure glulam more quality than solid timber. Also, it can be obtaining same dimension of solid timber with using of small timber pieces. So, amounts of wastage materials can be reduced. Glued laminated timber had used first time in 1893 for auditorium construction in Basel, and today, bridges, houses, mosques, cinemas, theatres are being built with this material. Moreover, wide range of structures has been constructed with glulam beams [7].

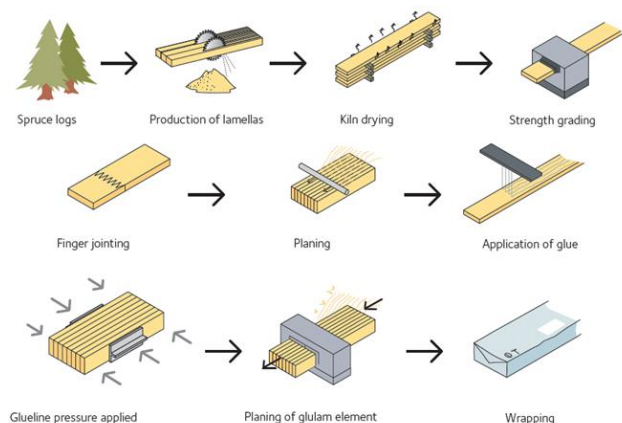


Figure 1. Producing Scheme of Glulam Beams [6]

Glulam is often used construction of pedestrian bridges and vehicle bridges. Crocetti enounce that timber becomes alternative choice for bridge construction in European countries because of developments of engineering wood products like glued laminated timber [8]. Fragiacomio et al focused on timber-concrete composite bridges. They explained that timber-concrete composite bridges have the same compression and tension strengths compared with concrete bridges. In addition, composite bridges are lighter and more environmental than concrete one [9]. Additionally, studies about cost comparison between timber, steel and prestressed concrete bridges showed the timber bridges initial costs cheaper than other alternatives, due to timber weight to strength ratio [10]. Similarly, glulam girder bridge cost cheaper than prestressed concrete bridge, including of full-scale fatigue and strength tests [11].

2. PROPERTIES OF TIMBER

Physical and mechanical properties have significant effects on structural durability, safety and costs. Strength properties of structural timber elements must be adjusted according to climate condition, role in structural system and etc. Therefore, in this part of paper, physical and mechanical properties of timber will be mentioned.

In generally, timber is fibrous, heterogenic and anisotropic structural materials taken from trees. Timber occurs with longitudinal living cells. Widths of this structure like tubules are bigger than a few hundred times of its heights. These tubules made the basis of structural system of timber and it has lignocelluloses chemical form. Jelly formed pectoselulose is resin that keep it together this tubules [12].

2.1. Weight per volume

Weight per volume of timber is ratio of sample weight to the volume at a given humidity. This value can change 0,1 t/m³ to 1,5 t/m³ according to timber varieties [13].

With the relatively low weight to strength, timber has some advantages comparison between steel and reinforced concrete. Total consumed energy amounts including production of timber, construction of timber structures and service life will be low levels against to reinforced concrete and steel structures [4]. Also, thanks to its low weight to resistant, seismic performance of platform frame timber structures can provide to keep casualties low. For example, life loss in earthquakes can show in Tab. 1 [4].

Table 1

CASUALTIES IN EARTHQUAKES [4]

Earthquakes	Richter Magnitude	Number of Person Killed	Number of Platform Frame Wood House Strongly Shaken (Estimated)	
			Total	Wood House
Alaska, 1964	8.4	13	<	
San Fernando	6.7	63	4	100000
CA, 1971				
Edgecumbe, NZ 1987	6.3	0	0	7000
Saguenay QC, 1988	5.7	0	0	10000
Loma Pieta CA, 1989	7.1	66	0	50000
Northridge CA, 1994	6.7	60	2	200000
Kobe Japan, 1995	6.8	63	0	8000

2.2. Thermal expansion and conductivity

Thermal expansion coefficient of timber can be assumed 1,7 to 2,5*10⁻⁶/°F⁻¹ at parallel to grain and coefficient for across the grain are generally five or ten times greater than parallel to grain coefficient. Timber is not good at thermal conductivity because of its nature that cellular and made by cellulose [13]. Timber is flammable, even exposed low fire temperature; it loses too much capacity of resistant parameters comparisons between reinforced concrete and steel [14]. But still it has got an advantage. Timber layers that exposing to fire will be charred and it covers the timber inner section from fire penetration. Also, timber has lower thermal expansion coefficient than steel and reinforced concrete [13, 14].

2.3. Moisture

Timbers mechanical properties is effecting too much with moisture ratio. As the moisture content of timber increases, pressure, tensile and bending strengths decrease. But this decreasing is stopped at the certain level of moisture saturation point [15].

2.4. Mechanical properties

It is not easy to investigate timber's mechanical properties because of its heterogenic and anisotropic nature. Timbers resistance against mechanical effects may be changeable by different species and same species's different samples. Timber's mechanical properties change with its anatomy, density, moisture content, applied force direction [16]. In Tab. 2, can be seen some resistance values of timber.

Table 2

THE VALUES OF STRETCHING ACCORDING TO ITS CLASS OF GENUS AND SPECIES OF TIMBER MATERIALS [17].

Strength	Allowable Stress Values According To Material Type And Class			
	Classes of Needle Leaf Trees			Oak and Beech
	1	2	3	
1 Bending	130	100	70	110
2 Tensile	105	85	0	100
3 Compression*	110	85	60	100
4 Compression**	20	20	20	30
5 Compression*	25 ¹	25 ¹	25 ¹	40 ¹
6 Compression**	9	9	9	10

¹ It can be usable only if consider to gently crushing of materials, *: Parallel To Grain; **: Perpendicular To Grain, values given in kg/cm²

Timber modulus of elasticity change with fiber direction. For example, elasticity modulus of pine is 10 000 MPa at parallel to grain, 3 000 MPa perpendicular to grain [17].

Because of timber's anisotropic material, design methods little more complicated than steel and reinforced concrete design methods. Also, the fact that the strength parameters perpendicular to the fibers are lower than the strength parameters parallel to the fibers is disadvantages of timber.

2.4. Load duration

Flexural strength of timber is inversely related with load duration. Deformation of timbers has direct proportion with load duration [16].

3. TIMBER AND GLUED LAMINATED TIMBER DESIGN PRINCIPLES

Today, various materials based on wood can be used in structure. Solid timber, glued laminated timber, plywood, OSB and other wood-based panels are entered in scope of Turkey Seismic Code-2018 [18]. Many countries, published codes or standards for structural timber design. According to Turkey Seismic Code-2018 timber structures design with 'Eurocode 5-Design of Timber Structures [19]. But, TS647-Building code for Timber Structures still exists. So, this paper aimed on TS647-Building Code for Timber Structures [17], Eurocode 5-Design of Timber Structures [19], National Design Specification for Wood Construction [20]. These codes based on same principles and may show some differences about application of strength adjustments, load and resistance factors and load values [21]. So, these codes and standards are investigated and shortly explained of their design philosophies.

3.1. TS 647-Building Code for Timber Structures

In this code, timber is identified as solid timber and plywood that is used in construction of timber structures. The code includes different types of timber building construction

and allowable stress design. According to TS647, mechanical properties of timber must be correlated with some factors given by different environmental conditions.

3.2. Eurocode 5-Design of Timber Structures

The code includes solid timber, solid timber, glued laminated timber and other wood based structural products and wood based panels. It takes into account of some requirements such as mechanical resistance, serviceability, durability and fire resistance.

This code depends on limit state design requirements. While designing with different limit states, materials mechanical properties, time dependent behaviour, climate conditions and situations like stages of construction must be notice.

According to EN5, materials characteristic properties must be adjust appropriate to various environmental conditions. These conditions is load duration, moisture content and changes of moisture. Load duration class is given with a table and samples. Service classes are characterized by moisture content in the materials corresponding to temperature of 20°C and the relative humidity of the surrounding air. Adjustment of characteristic values is made by given modification coefficient (k_{mod}) and deformation coefficient (k_{def}). Resistance factors are listed as a table for different wood materials. For instance, factor of solid timber and glued laminated timber is 1,30 and 1,25 respectively. Design values of mechanical properties are calculated characteristic values divided by partial factors and multiplied with k_{mod} . Stiffness properties such as modulus of elasticity and shear modulus are modified for serviceable limits states or ultimate limit states. Stiffness properties adjust with moisture conditions in serviceable limit states calculations. In ultimate limit states design, corrections are made considering load durations, service conditions and load factors [19].

3.3. National Design Specifications for Wood Construction (NDS)

Specification includes lumber, glued laminated timber, piles, poles, prefabricated wood I-joist, lumber composites, and wood based panels and cross laminated timber. It contents allowable stress design (ASD) methods and load and resistance factor design (LRFD) methods.

Similar to EN5, characteristic value of wood materials must be adjusted due to moisture, load duration and other requirements. Corrections are made by several coefficients. Some of this coefficient is only used in allowable stress design and some used in load and resistance factor design. So that, coefficients given in parentheses indicate which design method it belongs to. Also, adjustment of characteristic values is not applied for all resistance parameters. The application of coefficients is explained in the related sections of the specification and the table shows which coefficient will affect which parameters according to the type of material.

Some coefficients in the specification are common to all wood materials. These coefficients are load duration factor, temperature factor, resistance factor and time effect factor. Load duration factor (ASD) is used for loads with different periods than normal loading conditions (ten years period). Temperature factor values are given in tables considering moisture conditions and temperature values. It is used in cases where the limit value 37,78 °C is exceeded. Resistance factors

(LRFD) are given in table in accordance with timber materials types and resistance values. Time effect factor (LRFD) is given in tables according to load combination and for earthquake combinations, this value is taken 1. Properties of solid timber material are corrected depending on load duration, moisture and temperature conditions, dimension, direction of load and grain, defects of timber, usage of combined elements, bearing area and time effects. Some coefficients decrease characteristic values while others increase. Also, some strength effects like stability of column-beam and buckling are taking into account with adjustment coefficient. Similar to solid timber, properties of glued laminated timber are adjusted conditional on load duration, moisture, temperature, dimension, load direction, curvature, layer numbers, bearing area and time effects. Besides, several effects like stability of column-beam and buckling are considering to adjustment coefficient like solid timber. Resistance factor changes with different strength parameters [20].

4. NUMERICAL ANALYSIS

In order to examine the potential of timber as an alternative, analysis and design of an existing steel bridge was reanalyzed and redesigned using with timber and glued laminated timber. The existing steel bridge is a pedestrian bridge and was completed in 2015. The steel pedestrian bridge was reanalyzed with TSC-18 [18] and TSDC-17 [21] which are existing codes in Turkey. Although NDS includes LRFD and ASD methods, EN5 includes only LRFD methods. So, LRFD design methods were applied in calculation of bridge design for timber bridge and glulam bridge. Also, as a result of the calculation, the sections found by LRFD method were smaller than those found by ASD method [23].

Steel bridge structural system can be showed in Fig. 2. The bridge consists of S275JR build up main beams and IPE180 profile joists. Build up main beams has made by steel plate, which is welded body and flanges of the profile. Metal decks are placed on the beams and bridge platform is obtained from reinforced concrete slab. Total span of the bridge is 44 m, width is 11 m. The height of the bridge rises 2.35 m inwards 19 m from the start and end points. Bridge geometry, restrain and build up section properties are given in Fig. 3.

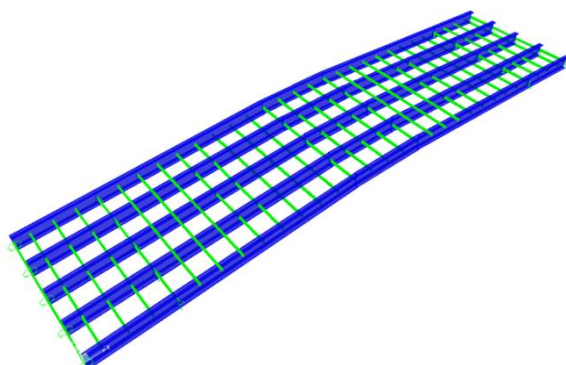


Figure 2. Steel structural system design model (blue for main beam, green for joists)

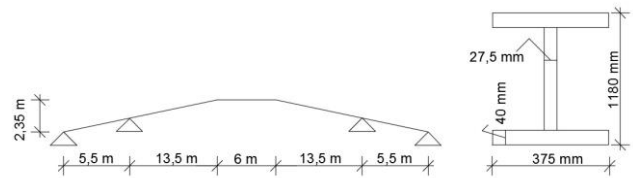


Figure 2. Bridge geometry and built up section dimensions

Structural system of the timber bridge is given in Fig. 4 and it contains main truss beams, joists solid beams and braces located on secondary direction. Cross section dimensions of timber structural system are given in Tab. 3. Easily available cross-sectional dimensions were selected and used. Timber bridges are designed with EN5 and NDS separately. In design, C24h and C50h solid timber and GL24h glued laminated timber beam was used. Load and resistance factors were taken from ASCE 7-16 for NDS, also taken from EN0 for EN5. Common loads used in bridge designs are given in Tab. 4.

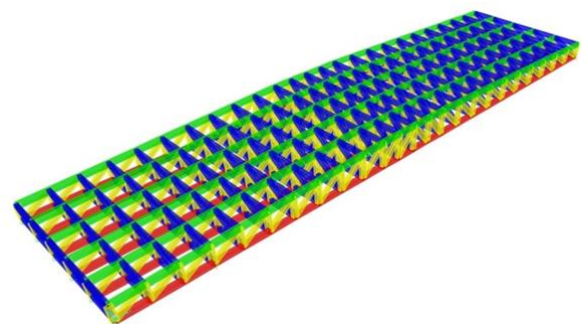


Figure 2. Timber load bearing system design model (the model used in all timber bridge design. Red and green represents the chords, yellow represents webs, blue represents the lateral stability element obtained the joists and bracing member.)

Table 3
DIMENSION OF TIMBER STRUCTURAL SYSTEM ELEMENTS SECTION

Element	NDS (cm)	Eurocode 5 (cm)
C24h Timber Truss Chords	50*25	60*30
C24h Timber Posts and Diagonals	40*20	50*25
C24h Timber Lateral Stability Elements	40*25	40*25
C50h Timber Truss Chords	45*20	50*20
C50h Timber Posts and Diagonals	30*15	40*20
C50h Timber Lateral Stability Elements	30*20	30*15
GL24h Glued Laminated Timber Truss Chords	50*20	60*25
GL24h Glued Laminated Post and Diagonals	40*20	50*25
GL24h Glued Laminated Timber Lateral Stability Elements	40*25	40*25

Table 4
SAME LOAD VALUES TAKING INTO ACCOUNT

Slabs load= 15 cm concrete + mosaic-adhesive + metal deck = 515 kg/m ²
Live load = 500 kg/m ²
Snow load = 75 kg/m ²
Railing load = 50 kg/m
Wind Load = 50 kg/m ²

Span/800 was chosen as displacement limit at steel and timber bridge design. All bridge calculations were performed with SAP2000 v20 structural analysis program [24]. Maximum displacement of steel bridge was calculated as 3,94 cm. Maximum displacement values of solid timber and glued laminated timber bridges are given in Tab. 5.

Table 5

TIMBER BRIDGES MAXIMUM DISPLACEMENTS FROM ANALYSIS RESULTS

Bearing System Types	NDS(cm)	Eurocode 5(cm)
C24h Solid Timber	3,92	3,91
C50h Solid Timber	4,07	4,09
GL24h Glulam	4,04	4,06

Largest stress ratio (requirements/capacity) showed from results is given below in Tab. 6 and quantities of structural elements given below in Tab. 7.

Table 6

CAPACITY RATIO OF LOAD BEARING ELEMENTS

Bearing System Types	ELEMENT TYPES	STRESS RATIO
S275	Main beam	0,47
S275	Joists	0,41
C24h NDS	Main beam	0,77
C24h NDS	Joists	0,94
C50h NDS	Main beam	0,78
C50h NDS	Joists	0,86
GL24h NDS	Main beam	0,78
GL24h NDS	Joists	0,91
C24h EN5	Main beam	0,67
C24h EN5	Joists	0,95
C50h EN5	Main beam	0,53
C50h EN5	Joists	0,85
GL24h EN5	Main beam	0,66
GL24h EN5	Joists	0,95

Table 7

QUANTITIES TAKING FROM SAP2000

Bearing System Types	Quantities
S275	110,074 ton
C24h NDS	211,742 m ³
C50h NDS	132,94 m ³
GL24h NDS	180,22 m ³
C24h EN5	271,255 m ³
C50h EN5	134,44 m ³
GL24h EN5	255,41 m ³

5. Results

Timber based materials have been found to be used in structural system for satisfying to lots of engineering or architectural requirements because of their positive characteristic properties. The most important reasons for this are its high strength to weight ratio and being a sustainable material.

There are codes and standards of various countries in the design of timber structures. In this paper, commonly used codes namely NDS and EN5 were used in analyzes. According to these codes, characteristic values of timber material must be adjusted depending on different reasons for structural design. This regulation is based on similar philosophy and may comprise some differences.

In this paper, the existing steel pedestrian bridge redesigned and reanalyzed with solid timber and glued laminated timber materials. The steel bridge was controlled with TSC-18 and TSDC-17. Vertical displacements were effective in the design of the steel bridge. While vertical displacement was dominant in main beams stress was dominant in lateral stability elements in solid timber and glued laminated timber design. Quantities, capacity ratios and vertical displacement results are given in the tables in related topics. According to the stress ratios given in Tab. 6, it is seen that the capacities of solid timber and glued laminated timber materials can be used more efficiently than steel. Since the vertical displacement criterion is dominant in stress in steel bridge solution, the use of material capacity remains low. In addition, since the weight of the bridge made of wood materials is less than that of the steel bridge, less earthquake force comes into the system and loads and stresses remain at lower levels. Therefore, timber structural system has more capacity ratio than steel structural system.

As a result of the analyses made with GL24h glued laminated timber and C24h solid timber, the structural system could be solved with approximately similar sections. On the other hand, it is difficult to obtain the required sections with solid timber and the material loss is considerable. In the use of glued laminated timber, the necessary elements can be preferred because they are easily produced and protection procedures are not required [25].

The materials GL24h and C24h were chosen because they are readily available from the manufacturers. However, as can be seen from the values given in Tab. 7, the use of more strength timber material had a positive effect on the results. But, since the C50h solid timber is special production and difficult to supply, the unit cost is high. Thus, it has expensive cost than GL24h and C24h materials. This paper not includes the cost analysis because of the cost is variable depends on many factor. As the costs are variable and depend on many factors, cost analysis is not performed in the study.

Analysis results from NDS and EN5 have some differences. The main reason for this is diversity of resistance factors. The strength coefficients of NDS in timber material corrections are taken different for tenacity parameter. In contrast, all parameters in EN5 are reduced by the same parameter. This result in higher quantities in the solutions made with EN5 than in NDS. This result is similar with literature knowledge [22].

REFERENCES

- [1] Y. Örs and A. Togay, "Production, price and employment in Turkish wood construction industries", *Journal of Polytechnic*, vol. 7, no. 1, pp. 53-61, 2004.
- [2] A. Doğangün, R. Livaoglu, Ö. İ. Tuluk and R. Acar, "Earthquake performances of traditional timber structures", presented at Deprem Sempozyumu, Kocaeli, Turkey, pp. 797-799, 23-25 March 2005.
- [3] J. H. Rainer and E. Karacabeyli, "Ensuring good seismic performance with platform-frame wood housing", National Research Council of Canada, Institute for Research in Canada, Construction Technology Update No.45, 2000. <https://doi.org/10.4224/20327963>
- [4] A. H. Buchanan, "Can timber buildings help reduce global CO₂ emission", presented at 9th World Conference on Timber Engineering, Portland, USA, 1, pp. 2204-221, 2006.
- [5] R. O'Born, "Life cycle assessment of large scale timber bridges: a case study from the World's largest timber bridge design in Norway", *Transportation Research Part D: Transport and Environment*, vol. 59, pp. 301-312, March, 2018. <https://doi.org/10.1016/j.trd.2018.01.018>
- [6] E. Borgström, "Design of Timber Structures", 2nd ed., vol. 1, Stockholm, Sweden, Swedish Forest Industries Federation, 2016.
- [7] R. C. Moody and R. Hernandez, "Glued-Laminated Timber", in *Engineering wood products-a guide for specifiers, designers and users*, S. Smulski, Ed., Madison, Wisconsin, USA, PFS Research Foundation, 1997, pp. 1-1-1-39.
- [8] R. Crocetti, "Timber bridges: general issues, with particular emphasis on Swedish typologies", presented at 20. Internationales Holzbau-Forum IHF, Garmish, Germany, 3-5 December 2014.
- [9] M. Fragiaco et al, "Timber-concrete composite bridges: three case studies", *Journal of Traffic and Transportation Engineering*, vol. 5., no. 6, pp. 429-438, 2018. <https://doi.org/10.1016/j.jtte.2018.09.001>
- [10] R. A. Behr et al, "Cost comparison of timber, steel and prestressed concrete bridges", *Journal of Structural Engineering*, vol. 116, no. 12, pp. 3448-3457, 1990.
- [11] M. Tazarv et al, "Glulam timber bridges for local roads", *Engineering Structures*, vol. 118, pp. 11-23, 2019. <https://doi.org/10.1016/j.engstruct.2019.03.012>
- [12] J. T. Ricketts and S. F. Merrit, "Building design and construction handbook", 6th ed., New York, USA, McGraw-Hill Companies, 2001.
- [13] R. J. Ross, "Wood handbook: wood as an engineering material", Wisconsin, USA, United States Department of Agriculture Forest Service, 2010.
- [14] M. H. Ramage et al, "The wood from the trees: the use of timber in construction", *Renewable and Sustainable Energy Reviews*, vol. 68, pp. 333-359, February, 2017. <https://doi.org/10.1016/j.rser.2016.09.107>
- [15] S. K. Duggal, "Building materials", 3rd ed., Daryaganj, New Delhi, New Age International, 2008.
- [16] J. M. Dinwoodie, "Timber: its nature and behaviour", 2nd ed., London, United Kingdom, Taylor&Francis, 2004.
- [17] TS 647-Building Codes for Timber Structures, Ankara, Turkey, Turkish Standards Institution, november, 1979.
- [18] TSC-18-Turkish Seismic Design Code, Ankara, Turkey, Ministry of Environment and Urbanization, 2018.
- [19] Eurocode 5-Design of Timber Structures, European Committee for Standardization, 2004.
- [20] NDS, National Design Specifications for Wood Construction, USA, American National Standards Institute, 2018.
- [21] TSDC-17, Turkish Steel Design Code, Ankara, Turkey, Ministry of Environment and Urbanization, 2017.
- [22] J. P. Wacker and J. S. Groenier, "Comparative analysis of design codes for timber bridges in Canada, the United States, and Europe", *Transportation research record*, no. 2200, pp. 163-168, 2010. <https://doi.org/10.3141/2202-19>.
- [23] J. Showalter, H. B. Manbeck and D. Pollock, "LRFD versus ASD for wood design", presented at ASAE Annual International Meeting, Orlando, Florida, USA, July 12-16, 1998.
- [24] SAP2000, Structural Analysis Program-Integrated Finite Element Analysis and Design of Structures, Analysis Reference, Berkeley, California, USA, 2019.
- [25] A. Çekiç et al, "Properties of timber and glulam beams, usage and design of structures and strengthening of glulam beams with FRP", BSc graduation thesis, Department of Civil Engineering, Dokuz Eylül University, Izmir, Turkey, 2019.

BIOGRAPHIES

Gökhan Şakar is an associate professor in the Department of Civil Engineering at the Dokuz Eylül University where he has been a faculty member since 1997. He also completed his PhD at Dokuz Eylül University. His main research interest is strengthening of reinforced concrete structures especially with fiber-reinforced polymer materials. He has been involved in experimental research on the behavior of reinforced concrete structures. He has many papers on this subject. He is also interested in steel and timber structures. He currently has several master and PhD students and continues to experiment in the field of structural mechanics.

Hüseyin Kürşat Çelik received his BSc degree in civil engineering from Dokuz Eylül University (DEU) in 2019. Currently, he is an MSc student in Structural Engineering at The Graduate School of Natural and Applied Science, Dokuz Eylül University. His main research interest is timber structures.

Production of Curved Surface Composites Reinforced with Rubber Layer

Mustafa Albayrak^{1*}  and Mete Onur Kaman² 

^{1*} Inonu University, Department of Machine and Metallurgy Technologies, Malatya, Turkey, (mustafaalbayrak@inonu.com)

² Firat University, Mechanical Engineering Department, Elazığ, Turkey. (mkaman@firat.edu.tr).

ARTICLE INFO

Received: Nov., 11. 2020

Revised: May., 19. 2021

Accepted: Jun, 20. 2021

Keywords:

Glass fiber
EPDM rubber
Vacuum infusion
Curing
Delamination.

Corresponding author: A. Albayrak

ISSN: 2536-5010 / e-ISSN: 2536-5134

DOI: <https://doi.org/10.17694/ejt.824761>

ABSTRACT

In this study, laminated composites reinforced with rubber layers were produced under vacuum infusion method for different curved surface geometries. For this purpose, EPDM rubber interlayers, known for their impact-absorbing feature, were laid on curved-surface metal molds processed on computer numerical control (CNC) benches together with woven glass fiber woven fabrics. Thus, sandwich plates with an array of [0 °] 6 glass fiber / EPDM rubber / [0 °] 6 glass fiber were obtained. It has been evaluated how the interface adhesion pr

operties of the structure, which is formed by combining different types of materials under vacuum, depending on the temperature curing. For this reason, composites were produced by curing under high temperature and room temperature. As a result, it was determined that in composites produced by curing at room temperature, separation occurred between layers and the desired interface toughness could not be achieved. However, no delamination defects were observed in the structure of sandwich plates obtained for 100 ° C curing, and it was observed that the adhesion tendency of rubbers with hyper-elastic material structure increased with temperature. A good harmony was achieved between fabrics and rubbers with the effect of temperature together with vacuum and very smooth geometries were obtained

1. INTRODUCTION

With the development of production techniques, a significant part of the elements that make up the machine and building system can be produced from composite materials. Fiber reinforced composites are manufactured in thin section, ie plate form, due to their high mechanical properties. Considering the usage areas and locations of the plates, the most used ones are the plates with curved surfaces. These composite plates can be produced by combining a single type of fiber and matrix, or by combining several fibers with different properties [1]. It is understood from experimental studies in the literature that rubber reinforcement provides improvements in the mechanical, acoustic and ballistic performance of composites [2-14].

As with every element that makes up the machinery and structures, plates are also exposed to impacts and strains depending on where they are used, and as a result, different stresses occur. These stresses can damage the plates and prevent them from fulfilling their essential function. Fiber reinforced composites are mostly orthotropic materials that exhibit elastic behavior. Especially, fiber reinforced composites are materials that exhibit brittle fracture behavior and damage occurs due to fiber breakage as a result of impact.

These breaks also cause the onset and spread of the damage on the surfaces outside the impact contact area, and sometimes even invisible delamination (separation between layers) damages. Rubbers are the most effective impact absorbing materials today. Thanks to the rubber layer to be used as an intermediate layer in fiber-reinforced composite materials, large fiber breaks and irreparable structural damage can be prevented. When the studies on this subject are examined; Sabah et al. [5] obtained sandwich samples using rubber and aluminum honeycomb as core material between carbon fiber reinforced plastic shells. Repeated impact tests were carried out on these samples with hemispherical steel strikers at different energy levels. Khodadadi et al. [6] studied the impact absorption energies of composite materials consisting of kevlar fibers and polymer matrix under high speed impact test. Using two different matrix materials, rubber and thermoset (epoxy), they examined the effect of the composite on the impact absorption energy. Therefore, rubber layers have been added between thin composite plates with curved surfaces in order to make the structure more ductile and flexible, to increase the damped impact energy and to distribute the impact load better [5, 6]. Composites with the same alignment and curved surface geometries were produced under room temperature and 100 ° C curing temperature. As a result of the

productions made by vacuum infusion method, rubber and fiber interface adhesion properties were examined and compared.

2. MATERIAL AND METHOD

In the study, firstly, molds with flat and curved surface geometries were produced on CNC machines for composite production. For these molds, 600x150 mm cold work tool steel molds are preferred. Metal molds are preferred because curing process will be performed under the effect of temperature in the production to be made by vacuum infusion method. In order to make CNC workmanship less costly, these molds are not emptied. The geometries and dimensions of the curved surface molds to be used for composite production are given in Figures 1 and 4.

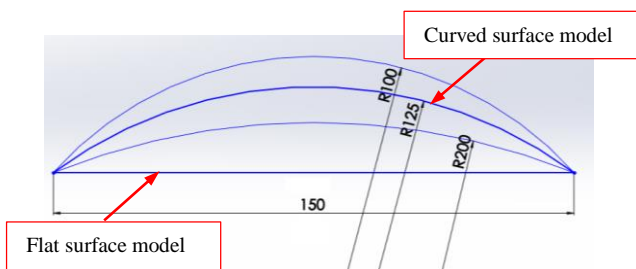


Figure 1. Sandwich plate models with fixed width and different curved surface (3 models)

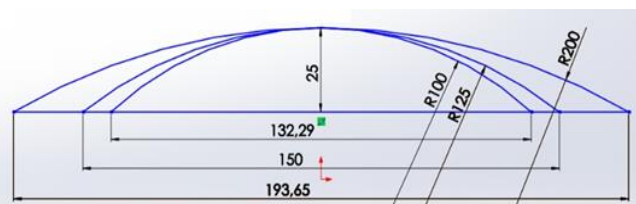


Figure 2. Sandwich plate models with different curved surfaces with fixed height (3 different models)

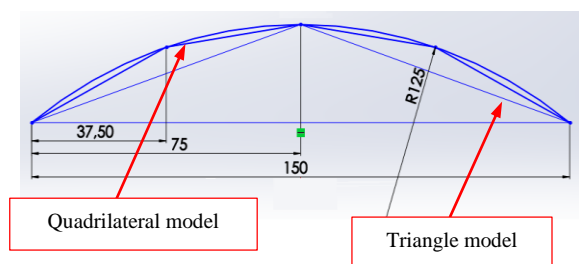


Figure 3. Sandwich plate models with different geometries tangential to the curved surface from inside

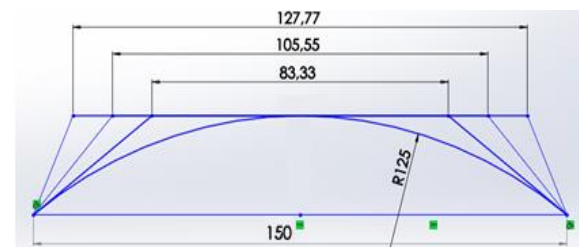


Figure 4. Sandwich plate models tangent to the curved surface from outside (3 different models).

In the production of sandwich plates, woven glass fiber fabrics with a weight of 300 g / m² are used as fiber material and epoxy resin suitable for 100 ° C curing is used as matrix material. Lineflex EPDM membrane with a thickness of 0.5 mm was preferred as an intermediate layer. In the vacuum

infusion method; First, a release film is laid to allow the mold to separate. Then, a flow net was laid on the curved surface where the fabrics will be spread, so that the resin can also wet the lower fabrics. Afterwards, the plate was affixed around the mold surface with double-sided tape that would leave the fabrics within its boundaries and provide sealing. After cutting the appropriate fabric and rubber for the size of the plate to be produced, how many layers and which fiber orientation is desired, the fabric is laid on top of each other and rubber layers are added between them. After the stripping layer is added to the fabrics to scrape the bag and the flow net, the flow net is laid on the peeling layer and closed with vacuum nylon. Finally, resin transfer was achieved by connecting one end of the mold to the resin and the other to the vacuum pump with a hose. After the vacuum process was completed, the fabric and rubber layers were left to dry and removed from the mold as a curved surface plate.

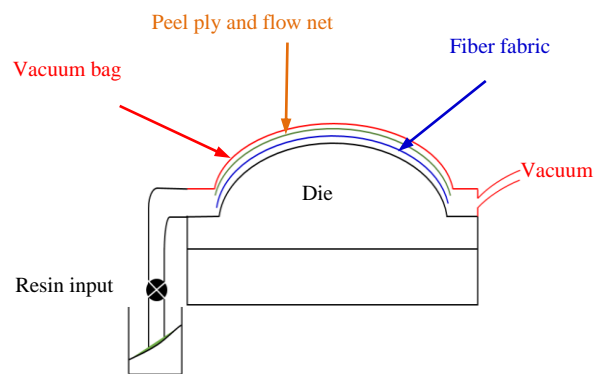


Figure 5. Vacuum infusion method schematic representation

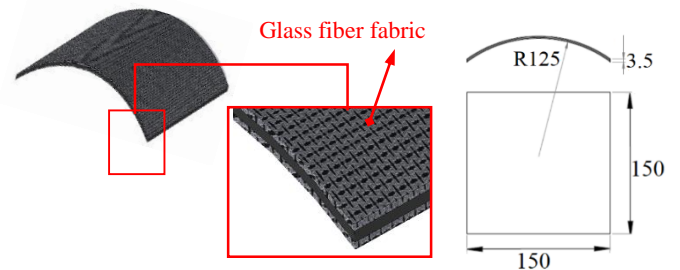


Figure 6. Vacuum infusion method schematic representation

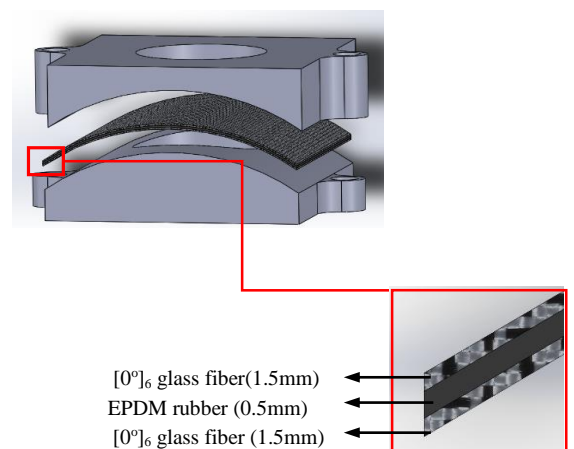


Figure 7. Solid model and alignment of the sandwich plate.

The schematic view of the vacuum infusion method is shown in Figure 5. In addition, the surface geometry and layer (rubber and glass) arrangement for the plate with common

geometry in all sandwich groups to be produced are given in Figures 6 and 7. The graph of the curing process over time is presented in Figure 8.

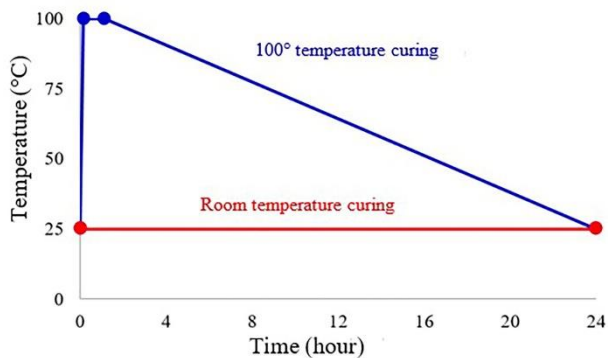


Figure 8. Curing process change over time [15].

Production stages of triangular, rectangular and common model composites from curved surface composites are presented in Figure 9. These samples have an array of $[0^\circ]_6$ glass fiber / EPDM (Ethylene Propylene Diene Monomer) rubber / $[0^\circ]_6$ glass fiber. It is also produced separately at room temperature and under 100°C curing. Later, these composite plate samples were prepared by cutting along the mold boundaries. Wet marble cutting machine is used for cutting. It was preferred to use the wet cutting method because the glass dust that will occur during the cutting of the glass composite is harmful to health.

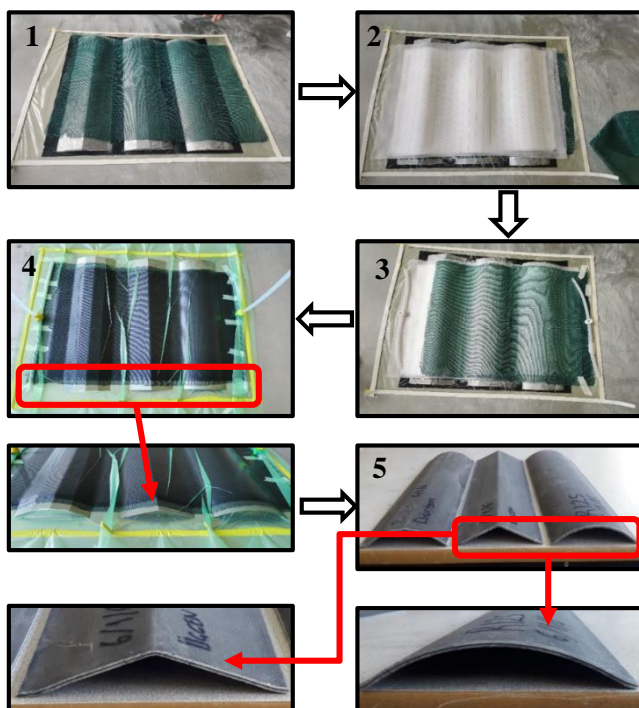


Figure 9. Sandwich composite production stages; 1) laying a flow net on the molds, 2) lining up fabric and rubbers between two peeling layers, 3) adding a flow net to the top for the resin to flow easily, 4) laying vacuum nylon to check its tightness under vacuum, 5) the samples obtained.

3. RESULTS

The interface adhesion properties of the samples obtained under different curing temperatures were checked and

evaluated. In the examinations, it has been observed that especially rubber materials with hyperplastic material properties have a good compatibility with the fabrics under temperature and their adhesion properties increase. In addition, it has been determined that temperature is a highly influential parameter on glass fiber / rubber interface adhesion properties. Pictures of the products obtained at two different temperatures are shown in Figure 10.

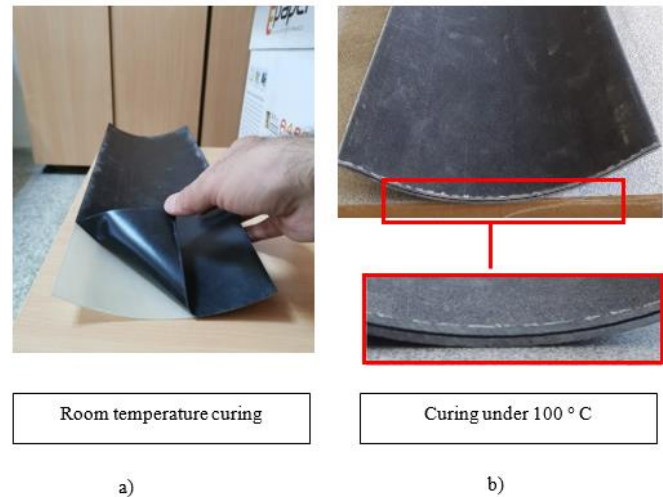


Figure 10. Interface properties of the samples produced; a) Sample obtained by curing at room temperature b) Sample obtained by curing at 100°C .

As can be seen in Figure 6, it has been observed that as a result of curing at room temperature, a sufficient adhesion surface has not been formed between EPDM rubber and glass fiber layer and it can be easily peeled off the glass fiber surface by hand. Sivaraman et al. [10] performed the curing of carbon fiber / rubber composites at room temperature and observed delamination damage at the fiber / rubber interface in the bending test. In addition, in the curved surface samples obtained by curing under high temperature, the interface strength between the fabric and the rubber was clearly seen and smooth geometries were obtained with vacuum. As a result of the study, it has been revealed that ductile materials such as rubber, which have the feature of hyper elastic material, must be cured under high temperatures in order to be used with fiber fabrics. It has been determined that only this way the desired adhesion surfaces can be obtained. Stelldinger et al. [16] produced sandwiches with a rubber interface layer of Krabion® EPDM using carbon fiber / epoxy prepreg layers at 135 degrees Celsius, and they did not find any delamination damage in impact tests. Similar situation Taherzadeh-Farda et al. It is also valid in the study by [17].

4. CONCLUSION

In this study, sandwich plates with rubber interlayer with different curved surface geometries were produced under different curing temperatures. The results obtained can be briefly summarized as follows;

- With the increase of temperature, the melting rubber layer surface adhered to the glass fiber surface and created a high bond strength. However, it should not be forgotten that the melting event is at a partial level at this point.
- Since rubber does not melt in production at room temperature, the internal force that holds the rubber and fiber interface together is only the strength of the epoxy. This force

is insufficient to hold the rubber and glass fiber interface together.

- The next step is to examine the impact behavior of sandwiches produced by curing at 100 ° C. In addition, in order to understand the damage mechanisms as a result of the impact, numerical analysis based on the appropriate damage model should be done. For this, the fracture toughness of the rubber / glass fiber interface Mod-I and Mode-II should be determined.

ACKNOWLEDGEMENT

This study was supported by Firat University Scientific Research Projects (FÜBAP) Unit with the project numbered MF.20.10.

REFERENCES

- [1] S. L. Valença, S. Griza, V. G. de Oliveira, E. M. Sussuchi, F. G. C. de Cunha, "Evaluation of the mechanical behavior of epoxy composite reinforced with Kevlar plain fabric and glass/Kevlar hybrid fabric," Composites Part B: Engineering., vol. 70, pp.1-8, 2015.
- [2] K. S. Ravishankar and S. M. Kulkarni, "Ballistic impact study on jute-epoxy and natural rubber sandwich composites," Materials Today: Proceedings., vol. 5 no. 2, pp. 6916-6923, 2018.
- [3] M. Vishwas, S. Joladarashi, S. M. Kulkarni, "Behaviour of natural rubber in comparison with structural steel, aluminium and glass epoxy composite under low velocity impact loading," Materials Today: Proceedings, vol. 4, no. 10, pp.10721-10728, 2017.
- [4] T. Adachi, T. Ozawa, H. Witono, S. Onishi, Y. Ishii, "Energy absorption of thin-walled cylinders filled with silicone rubber subjected to low-velocity impact," Mechanical Engineering Journal, vol. 4, no. 5, 17-00052, 2017.
- [5] S. A. Sabah, A. B. H. Kueh, M. Y. Al-Fasih, "Bio-inspired vs. conventional sandwich beams: A low-velocity repeated impact behavior exploration," Construction and Building Materials, vol. 169, pp.193-204, 2018.
- [6] A. Khodadadi, G. Liaghat, A. R. Bahramian, H. Ahmadi, Y. Anani, S. Asemani, O. Razmkhah, "High velocity impact behavior of Kevlar/rubber and Kevlar/epoxy composites: A comparative study", Composite Structures, vol. 216, pp.159-167, 2019.
- [7] H. Park, H. Jung, J. Yu, M. Park, S. Y. Kim, "Carbon fiber-reinforced plastics based on epoxy resin toughened with core shell rubber impact modifiers. e-Polymers," vol. 15 no. 6, pp. 369-375, 2015.
- [8] W. Li, R. Li, C. Li, Z. R. Chen, L. Zhang, "Mechanical properties of surface-modified ultra-high molecular weight polyethylene fiber reinforced natural rubber composites," Polymer Composites, vol. 38 no. 6, pp.1215-1220, 2017.
- [9] B. Haworth, D. Chadwick, L. Chen, Y. J. Ang, "Thermoplastic composite beam structures from mixtures of recycled HDPE and rubber crumb for acoustic energy absorption," Journal of Thermoplastic Composite Materials, vol.31, no.1, pp.119-142, 2018.
- [10] R. Sivaraman, T. A. Roseenid, S. Siddanth, "Reinforcement of elastomeric rubber using carbon fiber laminates," International Journal of Innovative Research in Science, Engineering and Technology, vol.2, no.7, pp.3123-3130, 2013.
- [11] D. Düring, L. Weiß, D. Stefaniak, N. Jordan, C. Hühne, "Low-velocity impact response of composite laminates with steel and elastomer protective layer," Composite Structures, vol.134, pp.18-26, 2015.
- [12] V. Mahesh, S. Joladarashi, S. M. Kulkarni, "An experimental investigation on low-velocity impact response of novel jute/rubber flexible bio-composite," Composite Structures, vol.225, 111190, 2019.
- [13] R. Gokuldass, R. Ramesh, "Mechanical and low velocity impact behaviour of intra-ply glass/kevlar fibre reinforced nano-silica and micro-rubber modified epoxy resin hybrid composite," Materials Research Express, vol. 6, no. 5, 055302, 2019.
- [14] E. Sarlin, M. Lindroos, M. Apostol, V. T. Kuokkala, J. Vuorinen, T., Lepistö, M. Vippola, "The effect of test parameters on the impact resistance of a stainless steel/rubber/composite hybrid structure," Composite structures, vol. 113, pp.469-475, 2014.
- [15] S. Erdem, "Nonlinear buckling analysis in patched hybrid composite plates by vacuum infusion method", Ph. D. thesis, Firat University, Elazığ, Turkey, 2020.
- [16] E. Stelldinger, A. Kühhorn, M. Kober, "Experimental evaluation of the low-velocity impact damage resistance of CFRP tubes with integrated rubber layer," Composite Structures, vol.139, pp.30-35, 2016.
- [17] A. Taherzadeh-Fard, G. Liaghat, H., Ahmadi, O. Razmkhah, S. C. Charandabi, M. A. Zarezadeh-mehrzi, A. Khodadadi, "Experimental and numerical investigation of the impact response of elastomer layered fiber metal laminates (EFMLs)," Composite Structures, vol. 245, 112264, 2020.

BIOGRAPHIES

Mustafa ALBAYRAK obtained his BSc degree in mechanical engineering from Firat University in 2010. He received MSc. in Mechanical Engineering from the Firat University in 2013. He is still PhD student in Mechanical Engineering department of the same university. His research interests are composite materials, finite elements methods, impact and failure analysis. In 2013 he joined the Department of Machine and Metallurgy Technologies, Cumhuriyet University as a teaching assistant, but he is working now in Machine and Metallurgy Technologies Department, Malatya Organized Industrial Vocational School . He is active in teaching and research in the finite element modeling, analysis.

Mete Onur KAMAN obtained his BSc degree in mechanical engineering from Firat University in 1997. He received MSc. in Mechanical Engineering from the Firat University in 2000. and PhD degrees in Graduate School of Science, Mechanical Engineering of the same university in 2006. His research interests are composite materials, finite elements methods, and fracture mechanics In 2006 he joined the Faculty of Mechanical Engineering, Firat University as a research assistant, where he is presently a professor. He is active in teaching and research in the finite element modeling, analysis.

Design and Analysis of Quadratic Boost Converter with Inductor-Capacitor-Diode Voltage Multiplier Circuit

Mustafa İnci^{1*} 

^{1*}İskenderun Technical University, Mechatronics Engineering Department, 31200, Hatay, Turkey. (e-mail: Mustafa.inci@iste.edu.tr).

ARTICLE INFO

Received: May., 11 2021

Revised: May., 31. 2021

Accepted: Jun, 01. 2021

Keywords:

Dc-dc converters

High gain

Quadratic boost converter

Voltage multiplier circuit

Corresponding author: *Mustafa İnci*

ISSN: 2536-5010 / e-ISSN: 2536-5134

DOI: <https://doi.org/10.36222/ejt.936097>.

ABSTRACT

In the current study, design and analysis of quadratic boost dc-dc converter with a voltage multiplier are presented. An additional inductor-capacitor-diode circuit is implemented as a voltage multiplier in the designed converter. In comparison with conventional boost converter, the designed quadratic boost converter based on additional multiplier circuit provides high gain voltage conversion with high efficiency. These properties make the designed converter practicable for sustainable energy implementations. The proposed converter is used to obtain higher output voltages employing equal input voltages in comparison with traditional boost converter, two-level cascade boost converter and traditional quadratic boost dc-dc converter. In the current study, operational principles of quadratic boost dc-dc converter with voltage multiplier circuit are clarified in detail. The relationship between input voltage and output voltage is formulized analytically and mathematical analysis of quadratic boost converter with voltage multiplier circuit is comprehensively given for smooth dc-dc converter operation. Subsequently, a controller scheme based on proportional-integral (PI) is presented for quadratic boost converter integrated with multiplier circuit. In the performance results, the operational waveforms of the designed converter are performed by using Simulink simulation program. Voltage gain analysis of designed converter versus conventional boost converters is compared to show the voltage conversion rates for different duty cycle values. In the designed converter, the input voltage is selected as a 24 V dc voltage source. At load side, the resistive load in the rating of 80 Ω consumes 720 W active power. In addition, input/output voltages, power waveforms and current waveforms are introduced.

1. INTRODUCTION

Applications in areas such as electric vehicles, grid integration of renewable energy systems, transmission, and portable electronic devices have increased the need of dc-dc power converters with high voltage gain power supplies in recent years [1]. Also, applications in photovoltaic systems, wind turbines, fuel cell stacks, lightning, switched-mode power supplies, robotics, televisions, personal computers, transportation, battery charger topologies can be given as examples of devices using high conversion dc-dc converters [2, 3]. High efficiency, high gain, and low cost dc-dc step-up converters are power circuits that increase the voltage to a higher value make them significant for optimum operation and design of electronic devices [4, 5]. The conventional boost converters increase the dc voltages at limited conversion rates. For this, advanced high-boost dc-dc converters are implemented to obtain better voltage conversion gain capability in several applications.

Various dc-dc boost converter structures with isolated and non-isolated are used to obtain higher voltage gain than conventional boost converters [6, 7] for different implementations, including renewable energy. Figure 1 shows several application areas of high-gain dc-dc converters. As shown in the figure, these converters can be used for photovoltaic, fuel cell applications, grid integration, electric vehicle interface, and residential usage [8, 9]. Some isolated topologies are bridge [10], flyback [11], and forward [12] dc-dc converters. But, in these topologies, using a step-up transformer induces higher volume and losses together with a high cost. Instead of isolated topologies, the most common boost topologies are interleaved [13], cascaded [14], and quadratic [15] dc-dc converters. In interleaved topology, the voltage gain is constant like a conventional boost converter. This converter is preferred to reduce the current ripples. The cascade converter, the combination of two or more boost converters, is the simple method to obtain a higher voltage conversion rate than the conventional boost power circuits

[16]. However, this converter causes high switching losses and supplementary elements. Quadratic converters use a single switch to obtain better voltage conversion in comparison with interleaved and cascaded boost converters [17, 18].

In the current study, a quadratic boost dc-dc power conversion circuit with an additional inductor-capacitor-diode voltage multiplier circuit is presented. Its performance is compared to conventional boost, cascade

boost (two-level) and conventional quadratic converters. The quadratic boost power circuit based on voltage multiplier circuit is a single switching element-based power electronic converter like conventional boost and quadratic topologies. The presented topology consists of a transistor, three inductors, four capacitors, and four diodes. It aims to obtain higher output voltage values than the conventional boost, cascade boost, and conventional quadratic converter with the same switching ratio.

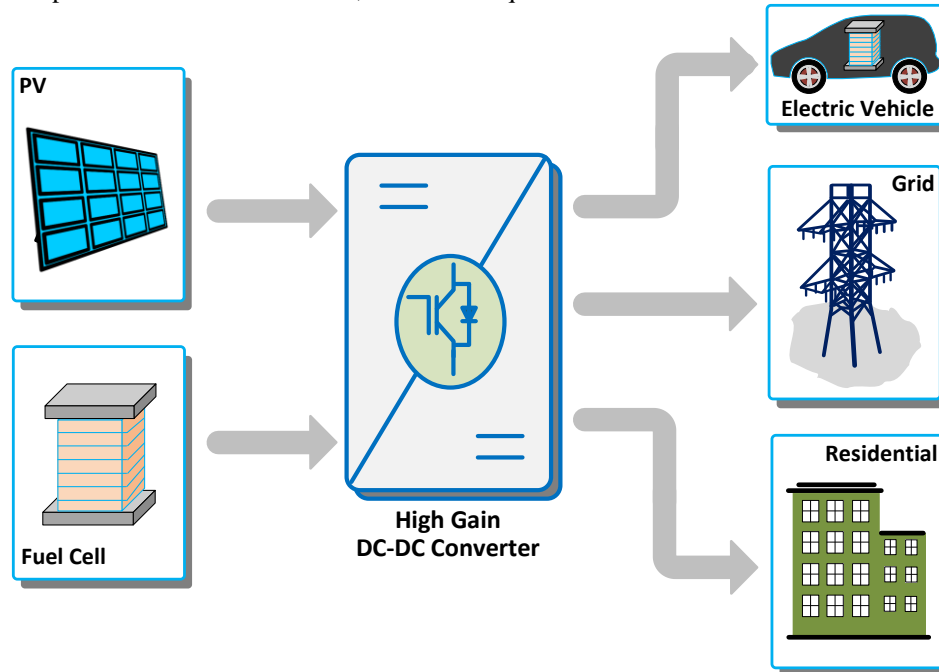


Figure 1. A typical scheme of high gain dc-dc converters for various applications

The rest of the current study is organized as follows: operating principles and analytical behavior of the quadratic boost power circuit with voltage multiplier circuit is given in Section II. The control scheme of the designed converter is given in Section III. The performance evaluation of the presented dc-dc converter topology is introduced in Section IV. And finally, the conclusions are summarized in Section V.

2. QUADRATIC BOOST CONVERTER INTEGRATED WITH VOLTAGE MULTIPLIER

A dc-dc converter is a power electronic circuit that step-up a dc voltage from a level to a different level [19]. In the current study, a quadratic boost power circuit is integrated with a voltage multiplier circuit. The scheme of a quadratic boost converter with a voltage multiplier circuit is presented in Figure 2. It is used to increase the output voltage, and to diminish voltage stress on transistor and diodes. As shown in the electrical scheme, it consists of 3 inductive elements, 4 capacitive elements, 4 diodes and 1 transistor [20]. It is demonstrated that V_{in} symbolizes input voltage while output voltage is defined as V_o .

In the analysis of quadratic boost converter with additional multiplier circuit, all the components are assumed as ideal. We presume that the power circuit works in continuous conduction mode. Furthermore, the values of capacitance voltages and inductance currents are supposed as fixed with minimal ripple [20]. As presented in Figure 3, the

designed quadratic boost converter with an additional voltage multiplier circuit has two switching states. Figure 4 shows the quadratic boost converter's electrical waveforms with additional voltage multiplier circuit.

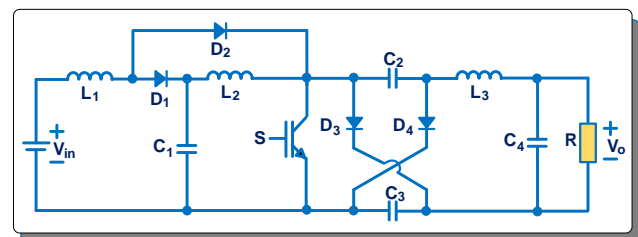


Figure 2. Quadratic boost converter connected with an additional inductive-capacitive-diode multiplier circuit

State 1: In the first state, the switching element is 'closed', and its state is defined as ON state. The inductors (L_1 , L_2 and L_3) store the energy through the input voltage source. All diodes are open, and this state is defined as a reversing state. C_1 capacitor supplies its stored energy to inductor L_2 . The capacitors, C_2 and C_3 , discharge in this state, and their energy are stored in output inductance (L_3). As a result, all inductors' currents increase linearly in the switching ON state [21]. As shown in the waveforms (given in Figure 4), the inductor currents are linearly reduced between $t=0$ and $t=T$.

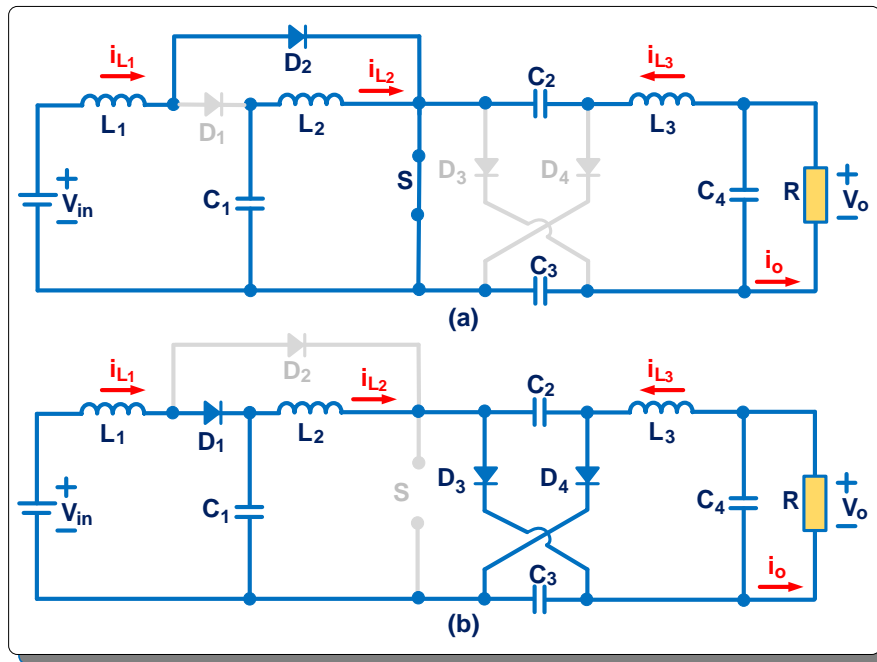


Figure 3. The states of converter (a) switch is ON, (b) switch is OFF

In state 1, the changes in inductors are defined as follows:

$$\left\{ \begin{array}{l} \frac{di_{L1}}{dt} = \frac{V_{in}}{L_1} \\ \frac{di_{L2}}{dt} = \frac{V_{C1}}{L_2} \\ \frac{di_{L3}}{dt} = \frac{2V_{C2} - V_o}{L_2} \end{array} \right\} \quad (1)$$

State 2: In the second state, the switching element is 'open', and it is said as OFF state. When the switching is in OFF state, the inductor L1 supplied its stored energy to capacitance C1, and the inductor L2 supplies its energy to capacitances C2, C3, and load resistance R. The inductor L3 delivers its stored energy into the load resistance. Thus, all inductors' currents decrease linearly in the switching OFF state [21]. As shown in the waveforms (given in Figure 4), the inductor currents are linearly reduced between $t=DT$ and $t=T$.

In state 2, the changes in inductors are expressed as follows:

$$\left\{ \begin{array}{l} \frac{di_{L1}}{dt} = \frac{V_{in} - V_{C1}}{L_1} \\ \frac{di_{L2}}{dt} = \frac{V_{C1} - V_{C2}}{L_2} \\ \frac{di_{L3}}{dt} = \frac{V_{C2} - V_o}{L_2} \end{array} \right\} \quad (2)$$

In Eqs. (1-2), $\frac{di_{L1}}{dt}$, $\frac{di_{L2}}{dt}$, $\frac{di_{L3}}{dt}$ indicate the changes in inductor current versus time. V_{in} and V_o express input voltage and output voltage in dc-dc converter, respectively. V_{C1} and V_{C2} are capacitance voltages in the converter.

Solving V_o , the net change in inductor currents must be zero for a periodic operation. Using Eqs. (1)-(2), we can arrange the equations to obtain the output voltage [21].

$$L_1 \rightarrow V_{in}DT_s + (V_{in} - V_{C1})(1-D)T_s = 0 \quad (3)$$

$$L_2 \rightarrow V_{C1}DT_s + (V_{C1} - V_{C2})(1-D)T_s = 0 \quad (4)$$

$$L_3 \rightarrow (2V_{C2} - V_o)DT_s + (V_{C2} - V_o)(1-D)T_s = 0 \quad (5)$$

Solving the Eqs. (3-5), the output voltage is obtained as:

$$V_o = V_{in} \frac{1+D}{(1-D)^2} \quad (6)$$

By using Eq. (3-5), the voltage stresses of capacitive elements are computed as:

$$V_{C1} = \frac{V_{in}}{(1-D)} \quad (7)$$

$$V_{C2} = V_{C1}(1-D) = \frac{V_o}{1+D} \quad (8)$$

The voltage stress of the switching element is given as below:

$$V_{S-stress} = V_{C2} \quad (9)$$

The voltage stresses of the diodes (D1, D2 and D3) are defined as follows:

$$V_{D1-stress} = \frac{(1-D)V_o}{1+D} \quad (10)$$

$$V_{D2-stress} = \frac{DV_o}{1+D} \tag{11}$$

$$V_{D3-stress} = V_{C2} \tag{12}$$

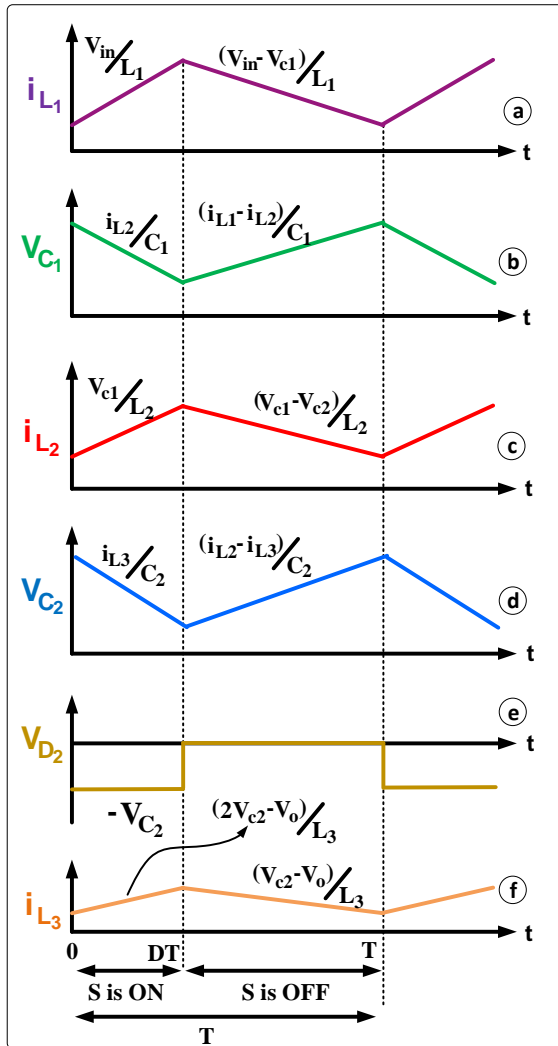


Figure 4. The significant waveforms (a) inductor current i_{L1} , (b) capacitor voltage V_{c1} , (c) inductor current i_{L2} , (d) capacitor voltage V_{c2} , (e) diode voltage V_{D2} , and (f) inductor current i_{L3}

3. CONTROL

In order to supervise the output voltage of quadratic boost converter connected with an extra voltage multiplier circuit, a PI controller is used. In PI control method, both proportional and integral gains are used together [22], as shown in Figure 5.

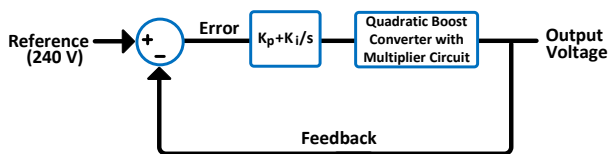


Figure 5. PI controller for quadratic boost converter integrated with additional multiplier circuit

In the controller, an error signal is produced with dc-link voltage at the output. The obtained voltage is measured and compared to the reference voltage value [23]. In the

designed system, the reference voltage value is selected as 240 V.

4. RESULTS

The quadratic boost power circuit integrated with an additional voltage multiplier circuit is tested with an input voltage of 24 V (dc) for a 720 W resistive load. The proposed converter has been built and analyzed through Simulink software. The parameter values of the designed power circuit are also given in Table 1. The component values are selected according to the design criteria in Ref. [20].

TABLE 1
PARAMETERS OF THE DESIGNED CONVERTER

Parameters	Value	Unit
Input Voltage	V_{in}	24 [V]
Inductances	L_1	0.1 [mH]
	L_2	1 [mH]
	L_3	1 [mH]
Capacitances	C_1	100 [uF]
	C_2	47 [uF]
	C_3	47 [uF]
	C_4	100 [uF]
Resistance	R	80 [Ω]
Switching	f	5000 [Hz]
Duty cycle	D	0.6 [-]

Figure 6 exhibits the voltage gain waveforms of the converters tested in the simulation program. When the results are examined, it is seen that the voltage conversion gain of the quadratic boost converter connected with voltage multiplier circuit is higher than other topologies. At $D=0.6$, the voltage gain of the quadratic boost converter with the voltage multiplier circuit is 10. The gain values of quadratic boost, cascade boost, and conventional boost are 6.25, 6.25, and 2.5, respectively.

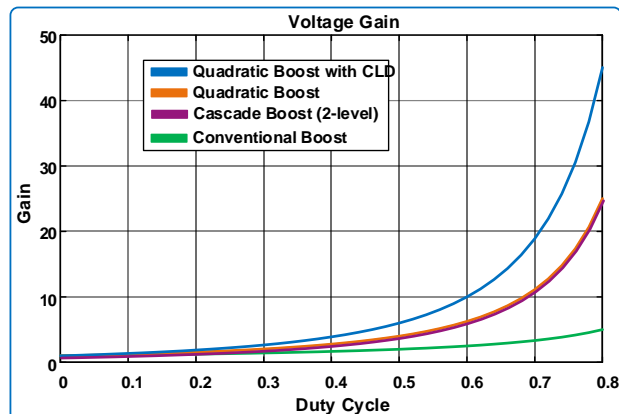


Figure 6. Voltage gain analysis of the converters tested in the simulation environment

The input/output voltages and switching signals are presented in Figure 7. The dc-dc converter is performed at 5000 Hz and 250 W load rating. As shown in waveforms, the magnitude of the input voltage is 24 V. The switching process is achieved with 0.6 duty cycle and 5 kHz. The

quadratic boost power circuit's output voltage with inductive-capacitive-diode structure is measured as 240 V, which is appropriate with the theoretical analysis. Figure 8 introduces inductor currents $IL1$, $IL2$, and $IL3$, and output current I_o , respectively. As shown in the results, the net change in the inductor current is zero. Also, the value of the output load current is fixed, and it equals to 3 A.

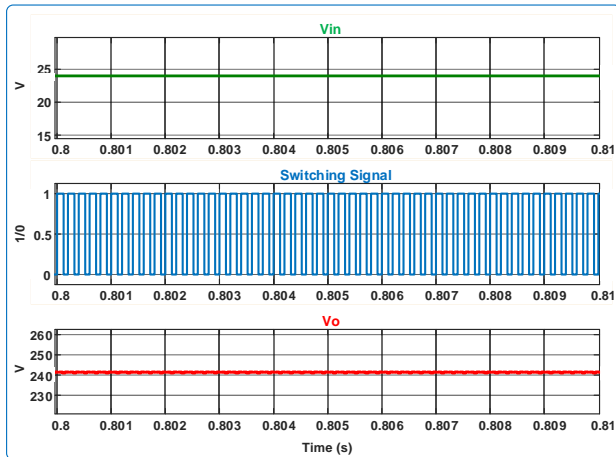


Figure 7. The input voltage, switching, and output voltage

The power waveform at the output load is presented in Figure 9. At the steady-state situation, the stepped-up voltage of the converter is equal to 240 V. In this way, a current in the rating of 3 A flows through the resistive load (80Ω). For this, the consumed power by the resistive load is calculated as 720 W. As shown in the waveform, the output power value is equal to 720 W for steady-state situation.

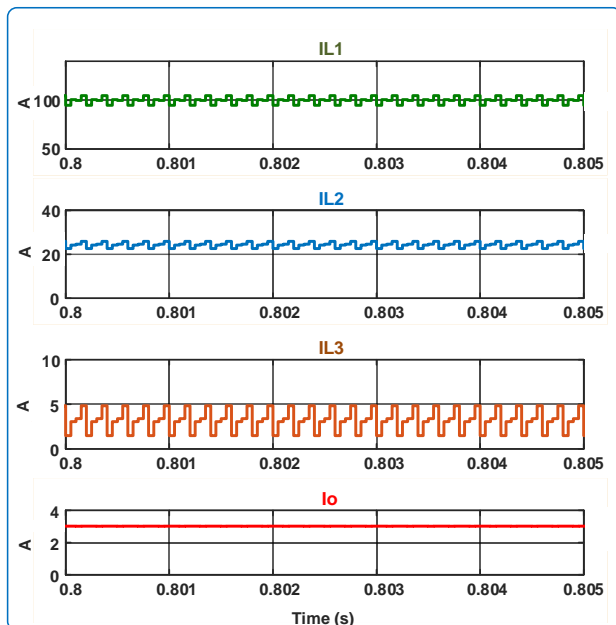


Figure 8. Inductor currents and output current

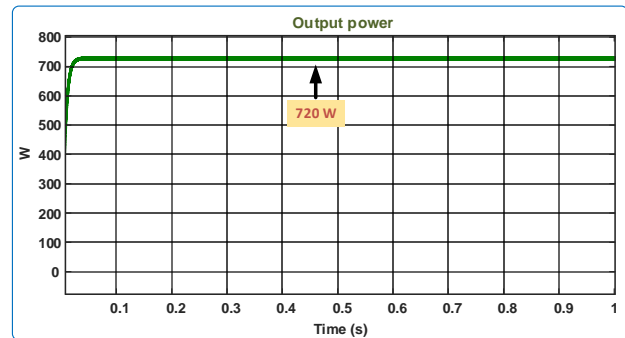


Figure 9. Output power waveform

5. CONCLUSION

In this study, the performance evaluations of the quadratic boost converter integrated with inductive-capacitive-diode structure are presented. This converter is a single switch-based dc-dc converter similar to conventional boost, cascade boost, and quadratic topologies. It consists of a transistor, three inductors, four capacitors, and four diodes to convert low voltage into higher voltages. In the current study, it is also mentioned that this converter, which has high gain and high efficiency, is important in energy applications. Using this converter aims to obtain higher output voltage values compared to conventional boost, cascade boost, and conventional quadratic converter with the same switching and input voltage ratings. The quadratic boost power circuit with voltage multiplier structure is performed for low voltage low power in the performance results. Also, the voltage conversion superiority of the converter is supported through voltage gain analysis compared to the aforementioned dc-dc converters. Besides, the input/output waveforms are given to verify the operation of quadratic boost converter with inductive-capacitive-diode circuit.

DECLARATION

The author(s) declared no potential conflicts of interest with respect to the research, authorship, and/or publication of this article. The abstract of this study was presented at International Conference on Engineering Technologies (ICENTE'20).

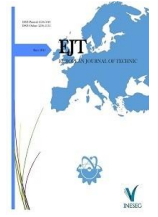
REFERENCES

- [1] A. Affam, Y. M. Buswig, A.-K. B. H. Othman, N. B. Julai, and O. Qays, "A review of multiple input DC-DC converter topologies linked with hybrid electric vehicles and renewable energy systems," *Renewable and Sustainable Energy Reviews*, vol. 135, p. 110186, 2021.
- [2] M. Rezvanyardom and A. Mirzaei, "High gain configuration of modified ZVT SEPIC-Boost DC-DC converter with coupled inductors for photovoltaic applications," *Solar Energy*, vol. 208, pp. 357-367, 2020.
- [3] H. Wang, A. Gaillard, and D. Hissel, "A review of DC/DC converter-based electrochemical impedance spectroscopy for fuel cell electric vehicles," *Renewable Energy*, vol. 141, pp. 124-138, 2019.
- [4] Q. Qi, D. Ghaderi, and J. M. Guerrero, "Sliding mode controller-based switched-capacitor-based high DC gain and low voltage stress DC-DC boost converter for photovoltaic applications," *International Journal of Electrical Power & Energy Systems*, vol. 125, p. 106496, 2021.

- [5] M. M. Savrun and M. İnci, "Adaptive neuro-fuzzy inference system combined with genetic algorithm to improve power extraction capability in fuel cell applications," *Journal of Cleaner Production*, vol. 299, p. 126944, 2021.
- [6] F. L. Tofoli, D. d. C. Pereira, W. J. d. Paula, and D. d. S. O. Júnior, "Survey on non-isolated high-voltage step-up dc-dc topologies based on the boost converter," *IET Power Electronics*, vol. 8, pp. 2044-2057, 2015.
- [7] M. İnci, "Interline fuel cell (I-FC) system with dual-functional control capability," *International Journal of Hydrogen Energy*, vol. 45, pp. 891-903, 2020.
- [8] M. İnci, M. Büyük, M. M. Savrun, and M. H. Demir, "Design and Analysis of Fuel Cell Vehicle-to-Grid (FCV2G) System with High Voltage Conversion Interface for Sustainable Energy Production," *Sustainable Cities and Society*, vol. 67, p. 102753, 2021.
- [9] M. İnci, M. Büyük, M. H. Demir, and G. İlbey, "A review and research on fuel cell electric vehicles: Topologies, power electronic converters, energy management methods, technical challenges, marketing and future aspects," *Renewable and Sustainable Energy Reviews*, vol. 137, p. 110648, 2021.
- [10] J. Voss, J. Henn, and R. W. D. Doncker, "Control techniques of the auxiliary-resonant commutated pole with special regards on the dual-active bridge DC-DC converter," *CPSS Transactions on Power Electronics and Applications*, vol. 3, pp. 352-361, 2018.
- [11] Ö. Çelik, A. Tan, M. İnci, and A. Teke, "Improvement of energy harvesting capability in grid-connected photovoltaic micro-inverters," *Energy Sources, Part A: Recovery, Utilization, and Environmental Effects*, pp. 1-25, 2020.
- [12] D. López del Moral, A. Barrado, M. Sanz, A. Lázaro, C. Fernández, and P. Zumel, "Analysis and implementation of the Autotransformer Forward-Flyback converter applied to photovoltaic systems," *Solar Energy*, vol. 194, pp. 995-1012, 2019.
- [13] H. Wu, T. Mu, H. Ge, and Y. Xing, "Full-Range Soft-Switching-Isolated Buck-Boost Converters With Integrated Interleaved Boost Converter and Phase-Shifted Control," *IEEE Transactions on Power Electronics*, vol. 31, pp. 987-999, 2016.
- [14] F. Jian, Z. Bo, Q. Dongyuan, and X. Wenxun, "A novel single-switch cascaded DC-DC converter of Boost and Buck-boost converters," in *2014 16th European Conference on Power Electronics and Applications*, 2014, pp. 1-9.
- [15] A. Sferlazza, C. Albea-Sanchez, and G. Garcia, "A hybrid control strategy for quadratic boost converters with inductor currents estimation," *Control Engineering Practice*, vol. 103, p. 104602, 2020.
- [16] S. Shoja-Majidabad and A. Hajizadeh, "Decentralized adaptive neural network control of cascaded DC-DC converters with high voltage conversion ratio," *Applied Soft Computing*, vol. 86, p. 105878, 2020.
- [17] R. Reshma Gopi and S. Sreejith, "Converter topologies in photovoltaic applications – A review," *Renewable and Sustainable Energy Reviews*, vol. 94, pp. 1-14, 2018.
- [18] B. Sri Revathi and M. Prabhakar, "Non isolated high gain DC-DC converter topologies for PV applications – A comprehensive review," *Renewable and Sustainable Energy Reviews*, vol. 66, pp. 920-933, 2016.
- [19] M. İnci, K. Ç. Bayindir, and M. Tümay, "The performance improvement of dynamic voltage restorer based on bidirectional dc-dc converter," *Electrical Engineering*, vol. 99, pp. 285-300, 2017.
- [20] J. Leyva-Ramos, R. Mota-Varona, M. G. Ortiz-Lopez, L. H. Diaz-Saldierna, and D. Langarica-Cordoba, "Control Strategy of a Quadratic Boost Converter With Voltage Multiplier Cell for High-Voltage Gain," *IEEE Journal of Emerging and Selected Topics in Power Electronics*, vol. 5, pp. 1761-1770, 2017.
- [21] Y. Ping, X. Jianping, Z. Guohua, and Z. Shiyu, "A new quadratic boost converter with high voltage step-up ratio and reduced voltage stress," in *Proceedings of The 7th International Power Electronics and Motion Control Conference*, 2012, pp. 1164-1168.
- [22] I. Laoprom, S. Tunyasirirut, W. Permpoonsinsup, and D. Puangdownreong, "Voltage Control with PI Controller for Four Phase Interleaved Boost Converter," in *16th International Conference on Electrical Engineering/Electronics, Computer, Telecommunications and Information Technology (ECTI-CON)*, 2019, pp. 278-281.
- [23] M. İnci, "Active/reactive energy control scheme for grid-connected fuel cell system with local inductive loads," *Energy*, vol. 197, p. 117191, 2020.

BIOGRAPHY

Mustafa İNCİ received the BSc and MSc degrees in Electrical-Electronics Engineering from Çukurova University, in 2011 and 2013. He received the PhD degree in Electrical-Electronics Engineering from Çukurova University, in 2017. He is currently Associate Professor at the department of Mechatronics Engineering, İskenderun Technical University. His research areas are advanced multilevel inverters, renewable energy systems, vehicle-to-grid (V2G) systems and custom power devices. He is a member of IEEE since 2015 and reviewer for IEEE, IET and Elsevier journals.



De-Orbiting Electro-Mechanical System Design for Micro Spacecraft

Uğur Kesen^{1*}

^{1*}Marmara University, Technology Faculty, Mechatronics Engineering Department, 34722, Goztepe, Istanbul, Turkey. (e-mail: ukesen@marmara.edu.tr).

ARTICLE INFO

Received: Apr., 04. 2021
Revised: May., 24. 2021
Accepted: May, 31. 2021

Keywords:

De-orbiting
Electro mechanic
Nano-micro spacecraft
Satellite

Corresponding author: *Uğur Kesen*

ISSN: 2536-5010 / e-ISSN: 2536-5134

DOI: <https://doi.org/10.36222/ejt.942123>

ABSTRACT

The number of small and micro satellites in Low Earth Orbit (LEO) is rapidly increasing. There is a risk of collision due to the lack of active orbital control of these satellites which also raises concerns about the debris. Existing low-orbit satellites pose dangers for new low-orbit satellites to be sent into orbit. A de-orbiting system to be activated at the end of the lifetime of the satellites is seen as the most effective solution to this danger. In this study, an electromagnetic satellite de-orbiting system is designed using aerodynamic principle. This system has been developed for a micro satellite with maximum edge dimensions of 100 cm. When the satellite lifetime is over, the system will be activated and will drop the satellite at the latest of 11 years. This system can de-orbit a micro satellite with a maximum weight of 50 kilograms. This system is activated with a command from the earth after the lifetime of the satellite is over. In this study, a de-orbiting electromechanical system (DES) is designed with an assumption of 750 km of satellite altitude and 98.4 degrees of orbital slope.

1. INTRODUCTION

In recent years, industry groups and universities all around the world launch an increasing number of micro satellites. Small satellites like CubeSat allow low-cost access to space. Several companies have proposed global broadband Internet networks provided by vast constellations of thousands of small satellites. [1]. A small spacecraft produced in accordance with the standards significantly reduces the development process and cost. At this stage, the most important problem is the pollution caused by expired satellites and the destruction of them. The existence of satellites, which have completed their lifetime and are now waste, poses a collision hazard for newly sent and active satellites. Out of 34,000 objects larger than 10 cm in orbit, only 20,000 have been cataloged [2, 3]. These cataloged objects include about 2000 active satellites, among which less than 1500 are maneuverable. These numbers are indicated in figure 1.

Everything else consists of orbital debris, large moons of the launch vehicles upper stages, mission-related objects, immobile parts from non-maneuverable fragmentation or collisions [4]. Non-trackable debris population is the primary risk and danger to successful operations in space. Objects that are too small to be cataloged in an orbital debris environment could cause a collision large enough to disable a satellite [5].

In a recent study, the authors propose establishing a new initiative called space environment management (SEM), consisting of both debris mitigation and debris remediation to reduce the risk of collision [6]. Another possible system used to avoid collisions is a sounding rocket system that will drag down the satellite and cause a deviation from the orbit [7]. Some technologies exist to increase the surface area of a CubeSat and accelerate orbit due to aerodynamic drag in low Earth orbit [8, 9]. There are also other studies that focus on use of lasers to re-orbit large orbital debris and spacecraft [10, 11]. Also, some other studies consider basic technologies of active removal of space debris from the geostationary orbit. This concept designed to take advantage of service spacecrafts by coupling them to a rigid arm to capture debris and tow them to graveyard orbit [12]. In another study, a solar sail was deployed to low Earth orbit and the sail membrane was used as a drag-sail to perform de-orbiting [13].

In this study, an electromagnetic satellite de-orbiting system is designed using aerodynamic principle. The electronic system operates a mechanical sailing module with the Sail module codes it receives from the earth. This electromechanical system will bring the micro satellite, with the maximum edge dimensions of 100 cm and a maximum weight of 50 kilograms, back to the earth at the latest of 11 years. In this study, a de-orbiting electromechanical system

(DES) is designed with an assumption of 750 km of satellite altitude and 98.4 degrees of orbital slope.

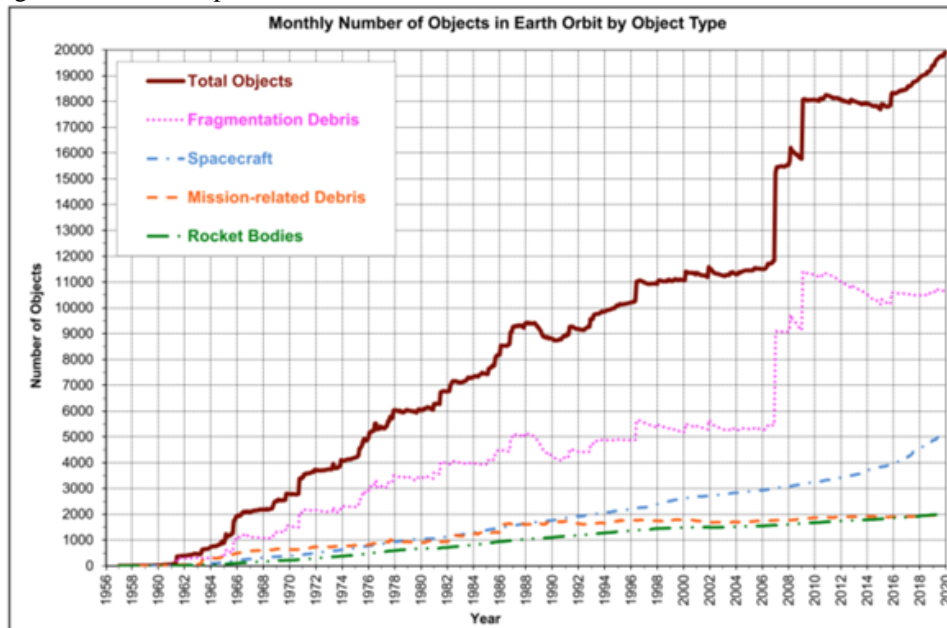


Figure 1. Number of cataloged objects in earth orbit by object type [4]

2. MATERIALS AND METHOD

The designed de-orbiting system uses aerodynamic principle. The system model block diagram is shown in Figure 2. The electronic circuit system breaks the line that will enable the operation of the mechanical system with the signal coming from the Earth to the micro satellite microprocessor. 4 different arms in the mechanical system are opened to activate a wide drop sail which will increase the dragging area. Each arm contains 3 different opening mechanism.

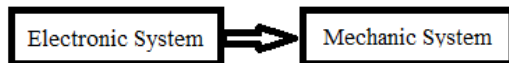


Figure 2. Electromechanical system model

The first opening mechanism opens a separate arm at 90 degrees from the satellite's body. After the first opening is completed, the second and third opening mechanisms begin to open simultaneously. After the opening is completed, the total surface area reaches 10.804 m².

2.1. Design Equipments

The system is a design formed by the cooperation of many different equipment.

Torsion Spring: Torsion spring generates a force that will open the system 180 degrees. There are 2 torsion springs for each fan which sums up to a total of 8 torsion springs.

Compression Springs: After the fan is turned on, the compression springs push the fan, creating an additional 0.4 m² drag area for each fan.

Sail Hinge: Sail hinge is used to open the sail arm.

Body Hinge: Body hinge joins the satellite and the fan system. The first opening occurs through the body hinges. It opens the main arm. Here, a spring with a wire thickness of 1.5 mm is used. The system contains a total of 4 hinges.

Sail Wing: It is used to open the arms in different directions. A torsion spring is also used here. Sail wing is connected to the body hinge.

Arm and Arm Slot: This area contains the compression springs. The compression spring pushes the inner lever which expands the sail area.

2.2. The Sail

The sail are the core components of the design. They increase the total aerodynamic drag area, increasing the satellite's fall time. The springs release the sails by moving the levers where the sails are connected. The unfolded sail is shown in figure 3. Sail will be turned off using origami techniques.

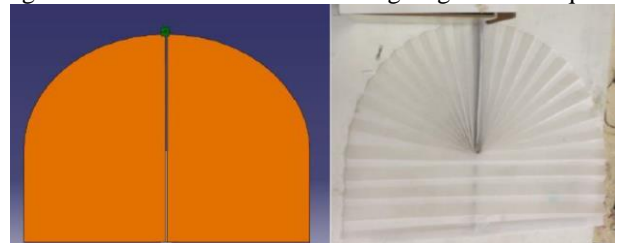


Figure 3. Sail and CAD design

2.2.1. Sailing Material Kapton HN Film

Kapton HN general-purpose film has been successfully used in applications with temperatures ranging from -269°C (-452°F) to 400°C (752°F). Kapton HN film can be laminated, metallized, punched, formed or adhesive coated. For applications requiring an all-polyimide film with excellent property balance over a broad temperature range, Kapton HN is the preferred alternative. Kapton HN Film is shown in Figure 4. Physical and thermal properties of Kapton HN Film is shown table 1 and table 2 [14].

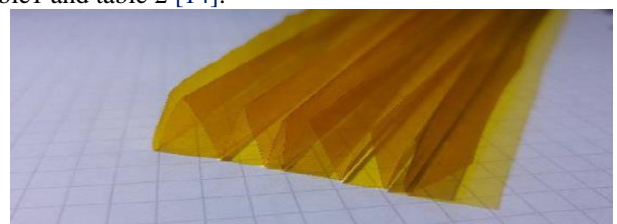


Figure 4. Kapton HN film

TABLE 1. Physical properties of Kapton HN film [14]

Property	Unit	75µm	125µm
Ultimate Tensile Strength At 23°C (73°F) At 200°C (392°F)	psi (MPa)	33,5 (231) 20,0 (138)	33,5 (231) 20,0 (138)
Density	g/cc	1.42	1.42
Tear Strength, Initial (Graves)	N (lbf)	26.3 (1.6)	46.9 (1.6)

TABLE 2. Thermal properties of Kapton HN film [14]

Property	Typical Value	Test Conditions
Thermal Coefficient of Linear Expansion	20 ppm/°C (11 ppm/°F)	-14 to 38°C (7 to 100°F)
Specific Heat, J/g.K (cal/g.°C)	1.09 (0.261)	
Shrinkage, % 30 min at 150°C 120 min at 400°C	0.17 1.25	

2.2.2. Sailing Material Mylar Film

Mylar films are rugged, all-purpose films that are translucent in heavier gauges and clear in 48 through 92 gauges. They have a rough surface that allows for easy handling, adhesion, and processing. They're used in a wide variety of industrial settings. Physical and thermal properties of Mylar Film is shown table 3 and table 4. Mylar film is shown in Figure 5 [15].

TABLE 3. Physical properties of Mylar film [15]

Property	Unit	Thickness (µm)
Tensile Strength MD	kpsi	28
Tensile Strength TD	kpsi	34
Elongation at Break MD	%	125
Elongation at Break TD	%	100

TABLE 4. Thermal properties of Mylar film [15]

Property	Unit	Thickness (µm)
Shrinkage MD (150°C) 30 min	%	1.5
Shrinkage TD (150°C) 30 min	%	1.0

The system is completely switched to open conformation with the opening of the compression springs which activates DES. The steps of DES activation are shown in Figure 6.



Figure 5. Mylar film

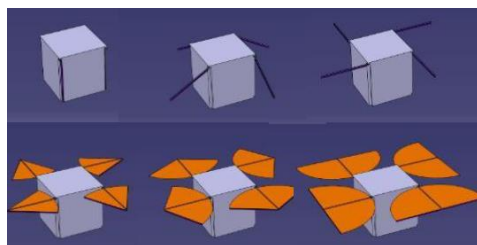


Figure 6. The steps of DES activation

2.3. Mechanism Design

During the lifetime of the satellite, the system will stay in a closed conformation. After the completion of its lifetime, the first part of the unfolding starts with the release of the torsion

spring. The lines that keep the torsion spring taut are connected to a resistor which when heated burns the line causing the release of the torsion spring. After release, the torsion spring opens the main lever 90 degrees. The completion of first opening starts the second opening. The fan mechanism starts moving after the lines are burned. With this step, the sails start to unfold.

2.3.1 Mass Budget

It is important to keep the additional weight that DES will bring on the micro satellite as small as possible. Therefore, the mass budget of DES was calculated in table 5 and it was observed to be low.

Area Calculation: $((0.5 \times 0.5 \times 3.14) / 2 + 0.4) \times 4 + (0.5 \times 0.5) = 3,42m^2$

TABLE 5. Mass budget

Components	Mass (gr)	% 20 Tolrance (gr)	Estimated Mass (gr)
Long spring (steel)	7.47	1.49	8.96
Tube (aluminum)	74.61	14.92	89.53
Inner lever (aluminum)	49.15	9.83	58.99
Wings x 2 (aluminum)	48.17	9.63	57.81
180 degree opening hinge piece (aluminum)	2.35	0.47	2.82
180 degree opening spring (steel)	1.10	0.22	1.32
First hinge (steel)	53.12	10.62	63.75
Kapton Film	2.22	0.07	1.85
Total x4 pieces			1140.2 (gr)

Because of its flexibility, low cost, and positive results at the end of its project life, the proposed design framework is favored. In order to develop an efficient DES system, we must consider whether it would work in space. At the end of its mission life, it must have an acceptable atmospheric re-entry period. The aerodynamic drag force concept is used to reduce the satellite's atmospheric re-entry period. This necessitates lowering the satellite's ballistic coefficient. The ballistic coefficient (BC) is used to describe spacecraft orbital decay, integrating the mass of the spacecraft, m , the region of its line-of-flight cross section, A , and the related drag coefficient, C_d , where:

$$BC = \frac{m}{A \cdot C_d} \quad (1)$$

Atmospheric drag is a major perturbing force for objects in Low-Earth Orbit. The drag force experienced by a spacecraft is determined by;

$$F_{aero} = -\frac{1}{2} \cdot C_d \cdot S \parallel V_{rel} \parallel V_{rel} \quad (2)$$

S is the spacecraft area projected along the direction of motion, C_d is a dimensionless drag coefficient, q is the local atmospheric density, and V_{rel} is the relative velocity of the spacecraft with respect to the atmosphere.

By lowering the ballistic coefficient (BC), which is inversely proportional to $C_d \cdot A$, we can reduce satellite atmospheric re-entry time. Therefore, C_d or satellite projected area along the direction of motion (A) must be increased. We create a DES concept based on a satellite in order to increase the projected area by using sail.

Advantages/Disadvantages of Kapton Film over Mylar Film;

- The tensile strength is higher than that of Mylar Film

- Elongation at break rate is less than Mylar
- It shrinks with less heat than Mylar

2.3.2 Operating System

The sail unfolding occurs through the heated resistors. For each sail to be unfolded, 4 resistors and 2 separate lines are required. In case one of the resistors malfunctions, the others will complete the operation. In case of a problem in the circuit and early heating of the resistors, one of the 2 lines will remain intact and prevent early unfolding. This way, the early unfolding of the sails is prevented, and the safety of the satellite is prolonged. The line system is shown in figure 7.

The line that holds the sails can resist a total of 37 kg of force. During the test, since real time waiting is not possible, the test was carried out by applying 37 kg of force to the line for 7 days. At the end of the test, no disintegration or expansion was observed on the line. This method was designed in the Istanbul Technical University Space Systems Design and Test Laboratory and was used in itüpsat, Türksat3Usat, BeEagleSat, Havelsat and Ubakusat satellites. And this line system has worked successfully in all satellites [16-18].

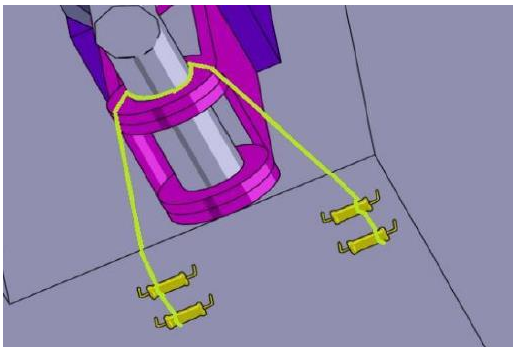


Figure 7. The line system

At room temperature, the 10-ohm resistor connected to the line was burned and disconnected in 7 seconds with 5V, 0.48A. Here, Nickel chrome wire, which can withstand higher temperatures, can be considered as a replacement for the resistor. Electronic circuit controlling the sailing system is shown in Figure 8.

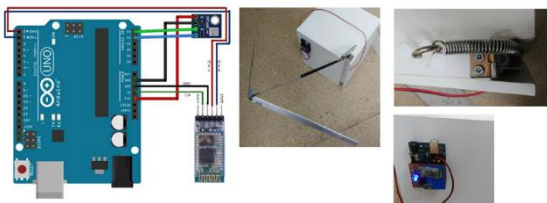


Figure 8. Electronic circuit controlling the sailing system

2.3.3 Lifetime Analysis

Satellite lifespan analysis was made with the analysis parameters given in Table 6. The results of the drop analysis for some scenarios are shown in Figure 9.

TABLE 6. Analysis parameters

Semi-major axis	7128 km
Orbital inclination	98.4 degree
R.A.A.N	30 degree
Argument pf Perigee	210 degree
Mean Anomaly	190 degree
Atmosphere model	
Cd	2.2
Cr	1
Solar Flux Estimates	CSSI

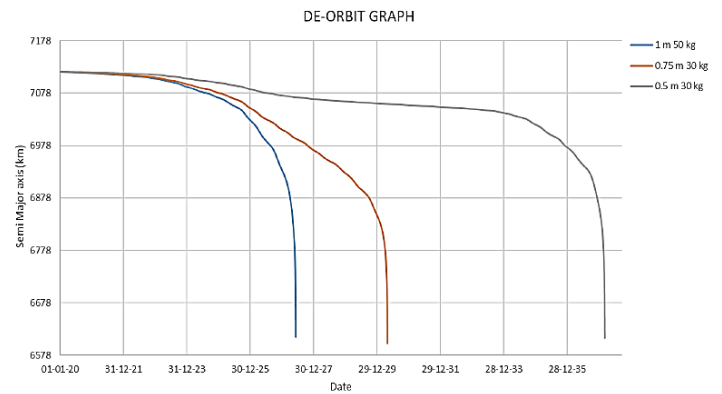


Figure 9. Drop Analysis for some scenarios

TABLE 7. Analysis results

Scenario	Satellite Height (m)	Satellite Mass (kg)	Total Drag Area (m ²)	Total Drag Area Of The Satellite (m ²)	Life time (day)	Life time (year)
1	1	50	10.804	11.804	2716	7.4
2	1	52	10.804	11.804	2875	7.9
3	1	40	10.804	11.804	2281	6.2
4	0.75	30	6.077	7.077	3772	10.3
5	0.75	50	6.077	7.077	6313	17.3
6	0.5	50	2.701	3.701	16496	45.2
7	0.5	40	2.701	3.701	7524	20.6
8	0.5	30	2.701	3.701	6276	17.2
9	1	50	0	1		340

According to the results indicated in Table 7, the system we designed can drop a 1 cubic meter satellite of 50-kilogram mass in 7.4 years. The analysis was repeated with different satellite sizes and masses and a comparison was made. As can be seen from the table, If the length of one edge of the satellite is reduced to 0.5 meters, the time required to drop the satellite from an altitude of 750 km increases to 17 years. If a square satellite is designed with 1-meter edge length and the mass kept as 50 kg, the system meets the required conditions and drops the satellite before 11 years.

2.4 Sail Electronics Module

A simple electronic circuit that allows the sails to be unfolded was designed. The electronic circuit consists of Arduino microcontroller, pressure and height sensors. At a certain height and pressure value, the circuit enables the lines to break by heating the resistors. Thus, the release mechanism actuators work. The satellite's command receiver will interpret the sail module commands sent from the ground. It will send these commands to the sail electronics module over the bus. When the lifetime of the satellite ends or the satellite becomes unusable by any means, the command sent from the ground station to set the sails and de-orbit the satellite. The release mechanism and actuators have been tested with this circuit assembly. The electronic circuit controlling the sail opening system is shown in figure 8.

3. CONCLUSION

As a conclusion of this study, the system we designed can drop a 1 cubic meter satellite with 50 kilograms' mass in 7.4 years. The analysis was repeated for varying sizes and masses

of satellites. The results suggest that this system can drop a micro satellite in a solar cycle. Also, altitude information data has been transferred successfully. The results vary for satellites with different sizes and masses. In addition, solar flux value is another important parameter that determines the life of the satellite. The system is applicable for various sizes of satellites. It is cheap and simple. At very high altitudes, the system is not effective enough due to low atmospheric density. Since the system is simple, inexpensive and has low mass, it can be preferred at altitudes such as 750 km. The drag area can be increased with minor improvements to the system.

REFERENCES

- [1] V. Braun, "Small Satellite Constellations and End-of-Life Deorbit Considerations." Handbook of Small Satellites: Technology, Design, Manufacture, Applications, Economics and Regulation, 2019, pp 1-23.
- [2] C. Bonnal, D. McKnight, C. Phipps, C. Dupont, S. Missonnier, L. Lequette, M. Merle, S. Rommelaere, "Just in Time Collision Avoidance – a Review". Acta Astronautica, 170, 2020, pp 637-651.
- [3] A. Chandra, J. Thangavelautham, "De-Orbiting Small Satellites Using Inflatables", in The 19th Advanced Maui Optical and Space Surveillance Technologies Conference. vol. 1 Maui, Hawaii, 2018, pp 1-11.
- [4] "Https://Orbitaldebris.Jsc.Nasa.Gov", (Last access: 25th September 2020)
- [5] D. J. Kessler, B. G. Cour-Palais, "Collision Frequency of Artificial Satellites: The Creation of a Debris Belt." Journal of Geophysical Research: Space Physics, 83, 1978, pp 2637-2646.
- [6] D. McKnight, T. Maclay, "Space Environment Management: A Common Sense Framework for Controlling Orbital." Debris Risk. Proc. AMOS, 2019.
- [7] A. Jarry, C. Bonnal, C. Dupont, S. Missonnier, L. Lequette, F. Masson, "Srm Plume: A Candidate as Space Debris Braking System for Just-in-Time Collision Avoidance Maneuver." Acta Astronautica, 158, 2019, pp 185-197.
- [8] D. Guglielmo, S. Omar, R. Bevilacqua, L. Fineberg, J. Treptow, B. Poffenberger, Y. Johnson, "Drag Deorbit Device: A New Standard Reentry Actuator for Cubesats." Journal of Spacecraft and Rockets, 56, 2019, pp 129-145.
- [9] D. Turse, P. Keller, R. Taylor, M. Reavis, M. Tupper, C. Koehler, "Flight Testing of a Low Cost De-Orbiting Device for Small Satellites.", in The 42nd Aerospace Mechanism Symposium. vol. 1 Greenbelt, Maryland, 2014, pp 183-188.
- [10] C. R. Phipps, C. Bonnal, "A Spaceborne, Pulsed Uv Laser System for Re-Entering or Nudging Leo Debris, and Re-Orbiting Geo Debris." Acta Astronautica, 118, 2016, pp 224-236.
- [11] C. R. Phipps, "L'Adroit – a Spaceborne Ultraviolet Laser System for Space Debris Clearing." Acta Astronautica, 104, 2014, pp 243-255.
- [12] A. Vnukov, T. Balandina, "Effectiveness Analysis of Active Space Debris Removal Technologies for the Geostationary Orbit." International Conference Aviamechanical engineering and transport (AVENT), 2018.
- [13] S. A. Song, Y. Yoo, C. G. Han, S. Koo, J. Suk, S. Kim, "System Design of Solar Sail Deployment and Its Effect on Attitude Dynamics for Cube Satellite Cnusat-1", The Asia-Pacific International Symposium on Aerospace Technology (APISAT-2014), Shanghai, China, 2014, pp 24-26.
- [14] "Https://Www.Dupont.Com/Content/Dam/Dupont/Amer/Us/En/Products/Ei-Transformation/Documents/Dec-Kapton-Hn-Datasheet.Pdf", (Last access: 25th September 2020)
- [15] "Https://Laminatedplastics.Com/Mylar.Pdf", (Last access: 25th September 2020)
- [16] A. R. Aslan, M. E. Bas, M. S. Uludag, S. Turkoglu, I. E. Akyol, M. D. Aksulu, E. Yakut, M. Suer, B. Karabulut, A. Sofyali, "The Integration and Testing of Beeaglesat", The 6th Nano-Satellite Symposium (NSAT), Kobe, Japan, 2015, pp 1-7.
- [17] P. Acar, M. Nikbay, A. R. Aslan, "Design Optimization of a 3-Unit Satellite De-Orbiting Mechanism", ESA Small Satellites Systems and Services the 4S Symposium, 2012, pp 4-8.
- [18] M. Cihan, O. O. Haktanir, I. Akbulut, A. R. Aslan, "Flight Dynamic Analysis of Itupsat1", International Workshop on small satellites, new missions and new technologies, 2008.

BIOGRAPHIES

Uğur KESEN He received the BSc., and MSc. diploma in Electronic and Telecommunication Engineering from the Yıldız Technical University in 1990 and 1993 respectively, and PhD degrees in Graduate School of Science from Marmara University in 2001. He was engaged in research and project on the optical fibers telecommunication and artificial neural networks.



Design and Application of a Smart Home System Based on Internet of Things

Resul Daş^{1*} , Taha Ababaker² 

¹Firat University, Software Engineering Department, 23119, Elazig, Turkey. (resuldas@gmail.com).

²Zakho University, Computer Science Department, Duhok, Iraq. (taha88eng@gmail.com).

ARTICLE INFO

Received: May., 01. 2021

Revised: July., 03. 2021

Accepted: July, 11. 2021

Keywords:

Smart home

IoT

AES

NodeMCU ESP8266

Arduino Uno

Corresponding author: *Name Surname*

ISSN: 2536-5010 / e-ISSN: 2536-5134

DOI: <https://doi.org/10.36222/ejt.931161>

ABSTRACT

The Internet of Things plays a critical role in smart home systems techniques. A smart home system provides a major change in the life of humans that gives home appliances intelligent operation. This encouraged us to create a solution for controlling certain home appliances, such as door and lights. This system is used to monitor the status of the door, window, temperature, humidity, and measuring distance by using various sensors such as IR, DHT22, and ultrasonic sensors. NodeMCU ESP8266, Relay module, and Arduino Uno have been used as the main parts in this paper. The system presented in this paper able to monitor and control home appliances from any corner of the world at any time and efficiently utilize the power by properly controlling the appliances. Ubidots IoT platform and Blynk application were used to check and read data from sensor modules placed in the home and, also to control home appliances by turning ON/OFF relay switches such as door and lights. The paper also focused on protecting user's data by using the AES method to ensure that a system encrypts and encodes Wi-Fi information before sending it to a destination, eventually, to restore the original data, it decrypts and decodes the data.

1. INTRODUCTION

The Internet of Things (IoT) has recently turned into a human lifestyle of great potential. Due to the development of modern wireless communication technology, the IoT concept is a revolutionary concept that has gained popularity. In different areas, comprehensive IoT-related research and applications are currently underway. The fundamental formation of this concept is to create applications that allow human life to interact with each other through the objects in the world [1]. One of the more prevalent IoT technologies is a smart home. Both digital and mechanical devices are interconnected in a smart home to create a network that interacts and creates collaborative space between the user and others [2]. This involves everything from smartphones, lamps, washing machines, coffee makers, sensors, actuators, and computers to the internet, where devices are intelligently connected to allow new ways of communication between people and almost everything else between them. These can be controlled and accessed at any time remotely from any computer, smartphone, or tablet [3]. With the increasing amount of devices connected to the IoT, security and privacy problems are being noticed and more pronounced [4]. Since IoT devices are expected to make their data available to stakeholders, doing so in a managed manner has become the key problem [5]. The data transmitted can include sensitive information relating to behaviors, privacy,

activities, and relationships of users, all of which relate to the privacy of individuals [6]. Therefore, IoT systems must ensure data integrity and confidentiality and also user's anonymity and privacy [7]. This paper explores how a framework for the monitoring and controlling of home appliances using Arduino Uno, NodeMCU, and relay module as the main hardware parts. Also, the Ubidots IoT platform and Blynk application have been introduced in this paper to allow the use of IoT. The various sensor modules data in the home environment are sent through the Arduino Uno and Arduino exchange the data with NodeMCU. The NodeMCU is coded via Arduino Integrated Development Environment (IDE) with the USB to tell the NodeMCU what to do. NodeMCU controls three channels of relay kit and receives instructions to show the temperature, humidity, door status, window status, and distance measurements from Blynk mobile application and Ubidots IoT platform web application and processes them to monitor the sensors and control actuator circuit of home appliances. Also, implementing an Advanced Encryption Standard (AES) is needed to increase confidentiality in data security. All the information in the system will be encrypted and decrypted by the AES method. The remainder of this article is structured as follows, the related work in this area is mentioned briefly in section two. The system design is described in section three. Section four presents the implementation of the performed method. Section five discusses and shows the application

results. This paper is concluded in section six and describes future work.

2. RELATED WORK

To thoroughly understand the definition of smart home and IoT technologies, we have gone through many articles, studies, conference papers, and project reports. The following are some of the suggested and current smart home systems.

The design and implementation of a smart home for the elderly and disabled were proposed by Das et al. [8], the presented system was a sample of smart home technology applications consisting of a variety of networked sensors. While it was just a very clear example of smart homes, it illustrates that smart homes can impact the elderly and disabled in all aspects of everyday life. Mandula et al. [9], suggested a home automation based on IoT using an android mobile application. Two kinds of home automation Bluetooth-based and Ethernet-based were used in their article. The custom mobile android application was used to control home appliances such as air-conditioning, TV, fan, etc. however, the prototype data sources were not transparent, leading to an impasse when several android phones attempt to access the same website. Tuna [10], proposed a secure smart home systems web-based communication frame for elderly and disabled people. To ensure safe internet communication first, the RSA algorithm was used to encrypt the data and then transmit and sent the encrypted data to the receiver. For security purposes, signs of contact should be removed after the receiver reads the encrypted content. The proposed system was able to allow confidential messaging between smart home residents and individuals they want to communicate with. The platform can also be conveniently built into clever home control panels or web-based smart home systems. Reddy et al. [11], have presented a home automation based on IoT using an android application. The authors used android mobile via the Wi-Fi module to send commands to the Arduino and Arduino processes all the home devices to be monitored and controlled. The voltage levels of electrical appliances were regulated in their framework such as lamps, fans, etc. On their android cell phone, they get the status of their home appliances. A smart automated home framework using IoT with the Blynk application was developed by Durani et al. [12], their study included the functionality of NodeMCU ESP8266 that is connected with the house appliances such as lights, water pump, fan, etc. with the help of online coding and hosting using a web server. The entire functionality was handled by a mobile application created in the android

application from which house applications were managed with the support of the internet. The focus of their study was also on wireless control of circuit devices by NodeMCU and the Blynk application.

A smart incubator with IoT has been proposed by Sivamani et al. [13], their paper explores the cost-effective existence of an embedded incubator baby monitoring system in real-time. All the information and data were stored in the Ubidots user's account and then a message of parameters value send as a notification to the signed user when Arduino has Wi-Fi access. Every second the values can be verified. It gives precise values, which are synchronized every second. A smart home automation system based on IoT with a sensor node was proposed by Singh et al. [14], in their paper, a smart home integrated various electrical appliances in the house and automated them without human intervention. Their system was able to monitor the various environmental variables and directs devices to function according to the user's requirements. By using IoT technology they achieved the development of smart homes. Imam [15], have proposed a simple smart home based on IoT using NodeMCU and Blynk. Based on the results of the review of all data obtained by testing a smart home with an IoT-based NodeMCU, it showed that it can be built with different hardware and software support components so that it can be incorporated into a smart home system that is functioned by the Blynk android application according to what is intended to control some of the performance of home electronics, such as lights, fan, early warning system, etc. A healthcare monitoring system based on IoT by using NodeMCU and Arduino was introduced by Wai et al. [16], the proposed patient monitoring system was designed to minimize the time. Results demonstrated that the doctor can test his/her patient anytime and anywhere. The nurses or doctors could conveniently use the computer to search and store them in the database. Also, the doctors were able to use mobile phones and with the help of NodeMCU can be incorporated into a global network. Data security and challenges in smart cities have been presented by Farahat et al. [17], the suggested system prevents attackers from attacking citizen data by encoding and then encrypting them through the AES technique when they are transmitted wirelessly from any source to any destination. The destination decrypts and decodes the data for the approved user to recover the original sensor data. A mechanism of authentication was used to avoid others from accessing the data of the person. Table I introduce a comparative summary from the previous studies and compared with our work:

TABLE I
Comparative summary for the literature studies

Ref.	Purpose	Technology	Application	Results
[8]	Design a smart air conditioning application for smart home services	Raspberry Pi, M2M	Control of an air conditioner	Successfully design a smart air conditioner
[9]	To implement an IoT based home automation system through data processing	Arduino Uno, NodeMCU ESP8266 and Arduino Nano, IoT	Home control and monitoring system detect the presence of harmful gas and measure temperature and humidity	Successfully can control the proposed system remotely by android smart phone via internet
[10]	To eliminate potential information security threats	Web-based smart home interfaces	Secure smart home for the elderly and disabled	The system is capable of using confidential messaging between smart home inhabitants and people they would like to communicate

[11]	To control and monitor home appliances using android application over internet	Arduino Mega, IoT, Wi-Fi	Home control and monitoring system	The system capable solution has proved to be controlled remotely, provide home security and it is low cost as compared to the previous systems
[12]	To present a small IoT system designed and created by utilizing a WLAN network based on Node MCU ESP8266	NodeMCU ESP8266, IoT	Real-time home security, automation, monitoring, and controlling of remote systems	Successfully implemented an intelligent, comfortable, and energy-efficient system
[13]	To design a cost-worthy of an embedded device for real-time monitoring of newborn babies in the incubator	IoT, Arduino, NodeMCU, Wi-Fi	Monitor's oxygen supplementation and pressure levels, monitors the temperature, radiation, pulse activity, and air humidity, gas around the environment	Successfully monitor and maintain environmental conditions suitable for a newborn baby, store data, and check the values every second
[14]	To develop a new solution which controls some home appliances	NodeMCU ESP8266, IoT Arduino UNO	Provides information about the energy consumed, check the level of gas detects the human object	The system achieved the development of smart home by using the IoT
[15]	To presents a simple prototype of smart home, or the easy way and low cost to control loads by Wi-Fi connection generally	NodeMCU ESP8266, IoT	Home control and monitoring system	Based on the results of analysis of all data obtained by testing the smart home, the system accomplished successfully
[16]	To constantly monitor the patient's physiological parameters	NodeMCU ESP8266, IoT Arduino UNO	Healthcare monitoring system	The system achieved the desired result
[17]	To secure the WiFi-based data transmission system that encrypts and encodes data	IoT	Smart sensors data encoding, Smart cities, Real time data security	The system successfully avoids any attackers to attack the citizen's personal data when it is wirelessly transmitted from any source to any destination
[18]	Provide essential security to homes and associate control operations	Raspberry Pi	Home control and monitoring system	The smart home system successfully designed and implemented
[19]	To design and implement a cost-effective IoT based autonomous alarm and access control system	Ethernet module, IoT	Control the states of the alarm, set an alarm, lock, and unlock the door, monitor the state of the door	The aim of developing a cost-effective IoT based autonomous alarm and access control system is accomplished
[20]	To give ease in everyday life, provide comfort, authentication and security, and additionally spare power and human endeavor	Arduino Mega 2560, Arduino UNO, GPRS, ESP8266, Ethernet Shield, Router	Controlling and indicating electrical and electronic devices in houses and buildings	The implementation of the system was managed successfully, the system can work with all its pieces through the internet properly
[21]	To provide secure data transmission among several associated sensor nodes in the network	Intel Galileo Board, Wi-Fi Module (N-2320), IoT	Secure data transmission, facilitate energy-efficient data encryption	The proposed TBSA algorithm consumed less energy in comparison with some existing methods
[22]	To study and evaluate a suitable set to develop a smart door lock which is intended to offer high security, easy access, and control	IoT, Microcontroller, Bluetooth beacons	Smart door lock	A fully functional smart door application was accomplished, and the result of security implementation of the product was an overall, more robust
[23]	To explores the Android OS as a medium to manage and operate different sensors embedded within smartphones	IoT	Extract the data from sensors, data in the local database, Transfer data via HTTPS to Ubidots	The Android application completed successfully all the tasks that were programmed
[24]	To solve the problem of the popularity of smart homes due to high costs in real life	NodeMCU ESP8266	Smart home control system	The system worked normally, and the monitoring data can be reflected in the monitoring interface in real-time
[25]	To optimize performance and saves unnecessary wastage of power	NodeMCU	Home control and monitor	Proposed a user-friendly system that can be used for benefiting the mass. Also, the cost of the system is within reach
[26]	To present a cost reduced and flexible home control and monitoring system	Raspberry Pi, IoT	Accessing and controlling devices and appliances remotely	The projects achieved desired results and can be said to be done successfully
[27]	To monitor the status of the door, controlling the door, and increasing security in a house	ESP32, IoT	Door security system	The motion detection sensor can detect movement accurately up to 1.6 meters ahead, and messages published encrypted properly
[28]	To switch to automated state controlling the appliances automatically as per the sensors' readings	IoT, NodeMCU, Raspberry Pi	Home control and monitoring system	The project was designed and implemented successfully

[29]	To design a system to help reduce the energy consumption	Arduino, IoT	Monitor electricity consumption and trace the history of electricity consumption data	The system successfully worked to control the monitoring of the amount of electrical energy usage through IoT
Our work	To create a prototype for an IoT-based smart home system to monitor and control electrical equipment and to protect the system's data from hackers and intruders while connecting with the internet	Arduino Uno, NodeMCU ESP8266, IoT	Home control and monitor remotely from a smartphone application and web application, Door unlock, Door status, Window status, system encryption, and decryption	Our work accomplished to designs a smart home system that enables homeowners to control and monitor appliances remotely, and also the data of the system was encrypted and decrypted properly

Based on Table I, we can analyze that every author comes with different technology and concept for the smart home system. With these different technologies, designs, and algorithms. The common purpose of every author's work was to smoothen the lives of homeowners, the old aged, and disabled people, save electricity, provide comfort, authentication, and security, a cost-reduced and flexible home control and monitoring system, and additionally spare power and human endeavor. Compared to the above smart home system applications, our system can be more secure with the AES technique by encrypting and decrypting the entire system parts and being more protected and more secure from hackers and intruders connecting with the internet. Furthermore, our system can be monitored and controlled remotely from anywhere and anytime by mobile application and web application.

3. SYSTEM DESIGN

The designed system has two main parts: hardware design and software design. The hardware part is constructed by arranging microcontrollers, actuators, and sensors while programming written and uploaded into the microcontrollers is included in the software part. The system performed in this paper displays microcontrollers connected to household devices for monitoring and controlling sensor modules and actuator modules. The general block diagram of the performed system is shown in Figure 1. This design section demonstrates how various components of the hardware are set up. The system uses an IoT platform and mobile application to control three loads and to monitor four sensor modules.

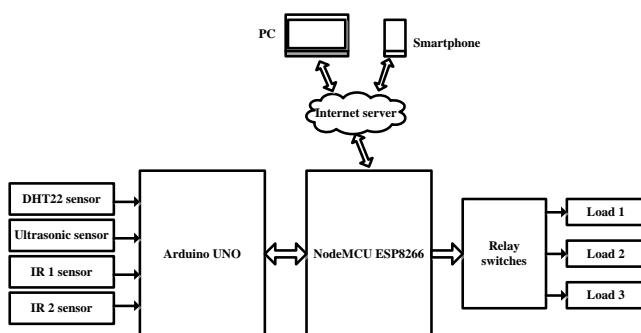


Figure 1. The general block diagram of the performed system

The requirements, data relating to different components and different functional units used in the performed system are listed below:

3.1. Arduino Uno

Arduino is an open source hardware and software platform that encourages ease of use. It has an electronic circuit board (Known as a microcontroller), and a ready to use a program

called Arduino IDE to write a program code and upload it to the physical platform. Arduino boards can read and transform analog or digital input signals from various sensors into outputs such as triggering a motor, turning ON/OFF LED, connecting to the cloud, and several other activities. Using Arduino IDE, you can control your board functions by sending a series of instructions to the board microcontroller [30]. In this system, Arduino reads the sensor modules data and send them via serial communication UART protocol to NodeMCU.

3.2. NodeMCU ESP8266

NodeMCU is a Lua-based open-source firmware and development board specifically designed for IoT-based applications. It includes firmware running on Espressif Systems' ESP8266 Wi-Fi SoC, and ESP-12-based hardware. By connecting it to any microcontroller using the serial UART or directly as a Wi-Fi enabled microcontroller by programming a new firmware using the SDK, the ESP8266 can be used as an external Wi-Fi module. This microcontroller has built-in Wi-Fi networking support to send and receive mobile data via a web server [31]. In this paper, it receives sensor data from Arduino Uno and sends them to the Blynk mobile application and Ubidots IoT platform, and then receives instructions to control home appliances from them. It then drives the relay module to power the appliances.

3.3. Sensor modules

The sensor modules gather their information about the current state of the environment in the home and submit that in turn to the Arduino board and then Arduino transfer the data by UART serial communication protocol to NodeMCU. Three types of sensor modules are used in the project, the HC-SR04 ultrasonic sensor for distance measurements, DHT22 temperature and humidity sensor to detect room ambient temperature and humidity, and IR1 and IR2 obstacle avoidance sensor to monitor the status of the door and window respectively.

3.4. Relay module

It is a 5V relay interface board, it has a standard interface that a microcontroller can control directly. In this study, three switches are used, two are used to turn ON/OFF the lights and the other one is used for unlocking/opening the solenoid door lock. The NodeMCU output signal activates and deactivates the relay for switching.

3.5. Solenoid electric door lock 12V

The solenoid is electromagnets. As electricity is applied, the coil of copper wire inside is energized and magnetized. In the performed system the solenoid is used to unlock/open the door.

3.6. Blynk

Blynk is an IoT platform that enables remote control of electronic devices using android and IOS software. It offers a dashboard that allows the user to build a graphical interface with various widgets. Sensor data can also be stored and displayed by Blynk [32]. Blynk provides libraries to the most common hardware platforms like SparkFun, Arduino, Raspberry Pi, ESP8266, etc. Libraries, server, and application are the three most significant components in the Blynk. The application can assist to construct the GUI. All the communication between the hardware and application is the server's responsibility. And libraries use the commands to enable the communication between the server with hardware. NodeMCU is the main component of this project. It is connected with an external power source with cable and also receives sensor module data from Arduino. Relay is the next critical component. The door and lights are connected with NodeMCU through the relay. We can run all devices via the Blynk server using the Blynk application. Different buttons are added in the Blynk application, using certain buttons that can turn ON/OFF the switches.

3.7. Ubidots

Ubidots platform is also used in this paper which is a cloud storage system that uses IoT to store a vast amount of information and record several values for every second. Each Ubidots user has the API credential to be included in the code. Then Ubidots are linked to the hardware, and hardware-measured data is sent to the IoT platform. The device in Ubidots is a virtual representation of data sources [33]. It transmits data from the sensor to the cloud of Ubidots through a connection protocol. When the device is built, it receives hardware data and is displayed inside the device in a variable. This is achieved in the code by using variable names. It is applied to the dashboards as a widget to visualize the data after data is presented in a variable. Users may display data as a table, indicator or graph, etc.

3.8. Advanced Encryption Standard

The AES is a symmetric key algorithm. AES used a 128, 192, 256-bit block length. AES is centered at the top of the network of permutations and substations. AES used a block size that was set. AES acts on a 4x4 bytes column-major order matrix. It is fast to implement hardware and software in equal measure. AES offers high and fast security [34]. Low power consumption is used by AES.

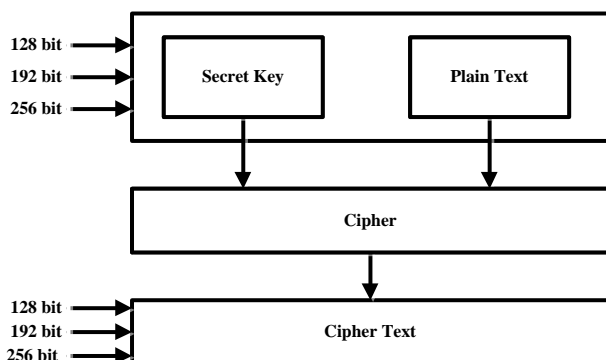


Figure 2. AES design

The AES conducts byte-based computations. 128 bits of a plaintext block is used as 16 bytes by AES. These 16 bytes are divided into four rows and four columns. AES is a variable depending on the key length. The AES cipher specifies the number of conversions round repeats that the input exchange is called plaintext, and the cipher text is called the final output [35]. In this study, we provide a secure data mechanism, using the AES method to improve data security. The AES technique encrypts and decrypts data before sending it from one device to another. Figure 2 shows the AES technique design.

4. SYSTEM IMPLEMENTATION

The performed system allows users to monitor and control their home appliances remotely at any time, using smartphones, tablets, and PCs. Using a mobile application and IoT platform, the user is able to control his or her home appliances easily through the internet by reading sensor data in their mobile application and IoT platform webpage. Figure 3 shows the schematic diagram of the performed system.

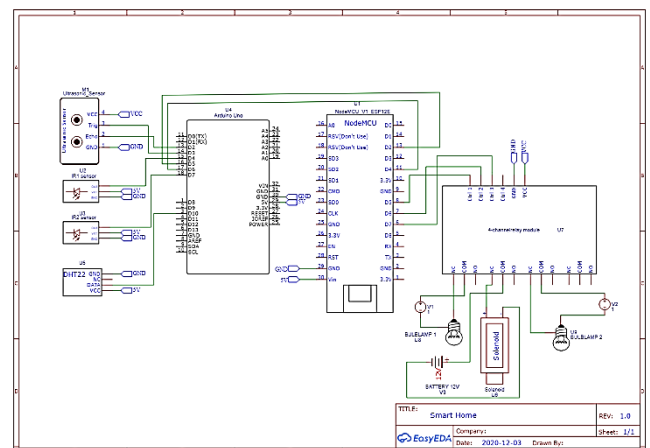


Figure 3. Schematic diagram of the performed system

NodeMCU needs to be identified to the SSID, the password, and token code letting the server of Blynk and Ubidots connects them. Sensors send variable data to Arduino Uno regarding environmental conditions and then Arduino Uno transfer the data to the NodeMCU via serial communication UART protocol. The user receives this information from the internet server in his/her mobile application and IoT platform and then decides on his/her behavior to control the appliances. NodeMCU ESP8266 receives the instruction from the internet server when pressing the required button in the application and platform and provides the actuator circuits with an output signal. When the relay is switched high, the power from the source is obtained by the devices. The switching circuit is used for turning lights ON/OFF and unlocks the door. Furthermore, the Blynk application and Ubidots IoT platform webpage show the temperature and humidity so the user can read the information on the DHT22 sensor, monitor the status of door and window by IR1 and IR2 sensors and, also the ultrasonic sensor displays the distance measurements of an object in the house. In order to achieve the desired performance, the encryption part involved, it consists of several processes and techniques. Encrypting all the data through the server and ESP8266 is the main concept. The processes that were involved in this project are encrypting and decrypting using AES-128

and also encoding and decoding the encrypted data to make it more secure. The process starts by ESP8266 at first gets the original sensor modules data from the Arduino with the original load's data connected with NodeMCU. This data will be encrypted into a string by the AES algorithm, only the system knows what are these generated data means and after the data are encrypted, it will be encoded until it is sent to the server for the session to start. By decrypting and encoding, the server processes the data. The connection between the ESP8266 and the server must be authenticated. After all, data is encrypted and encoded, the strings will be sent to the server. The strings obtained by the server will be decrypted and decoded and the relation authentication will be recognized as a credential between the server and ESP8266. The complete flowchart that gives the entire performed system operation is shown in Fig 4.

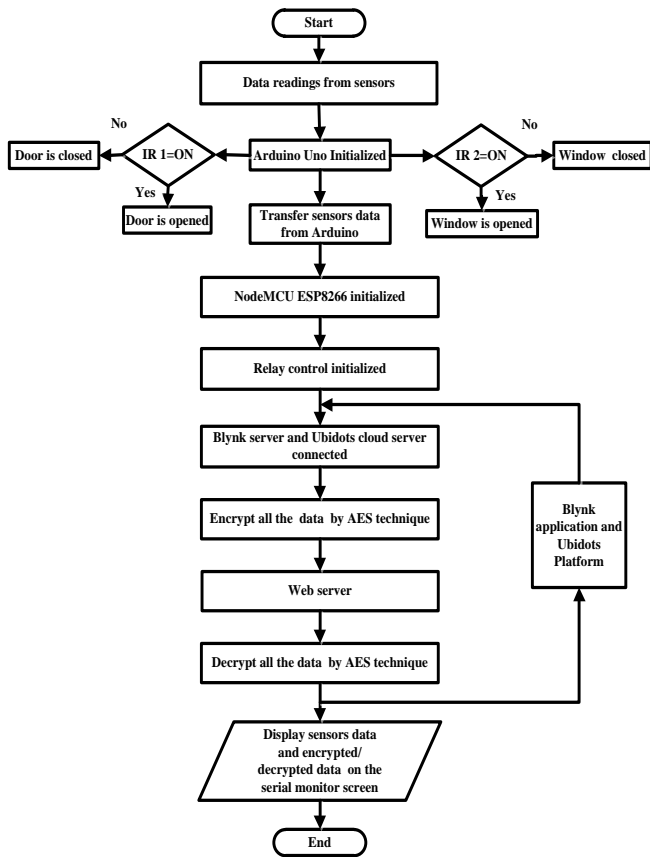


Figure 4. Flowchart diagram of the performed system

To display the value of sensor modules on the Blynk application and Ubidots IoT cloud platform, NodeMCU ESP8266 returns the output values of the sensor modules to the Blynk application and Ubidots platform, the remaining process are only commands send from ESP8266 to the mobile application and web application to control the appliances. Figure 5 and Figure 6 show and explain the Blynk and Ubidots operations respectively.

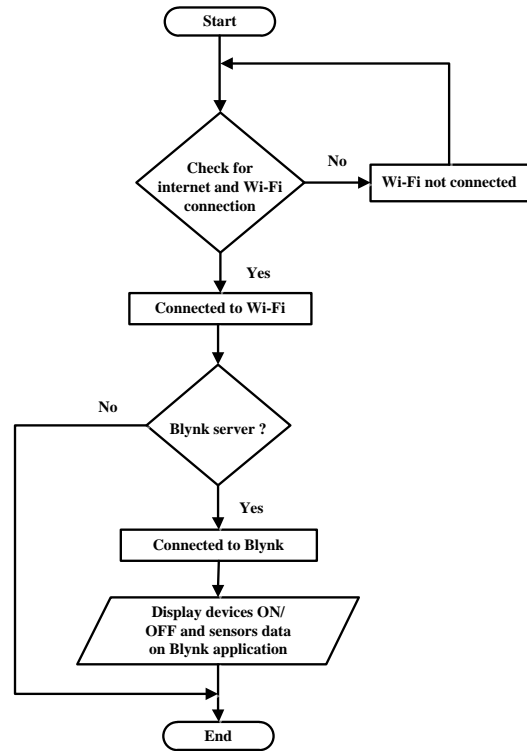


Figure 5. Flowchart diagram of Blynk operation

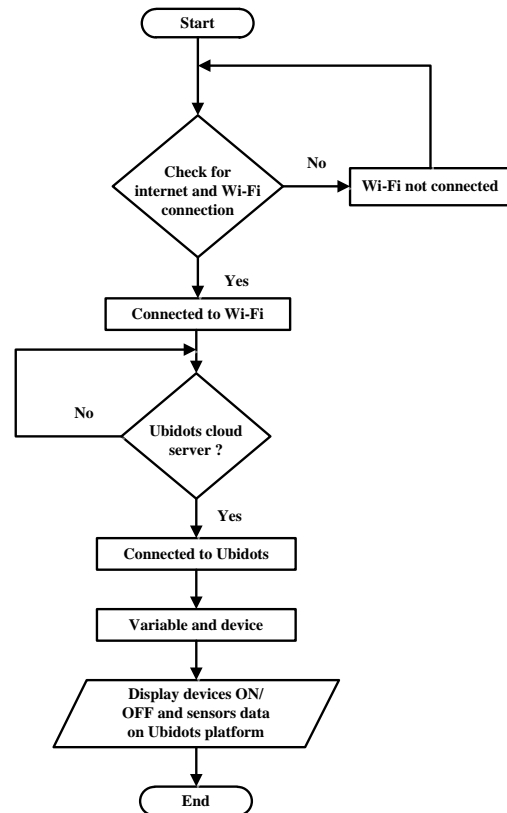


Figure 6. Flowchart diagram of Ubidots operation

5. APPLICATION RESULT

In the performed system, all hardware components were first verified and tested to ensure that all systems operate properly. Also, the key important parts of the system were tested to see

if they worked properly such as the connection between Arduino and NodeMCU for exchanging sensors data. Figure 7 shows the entire setup of the performed system.

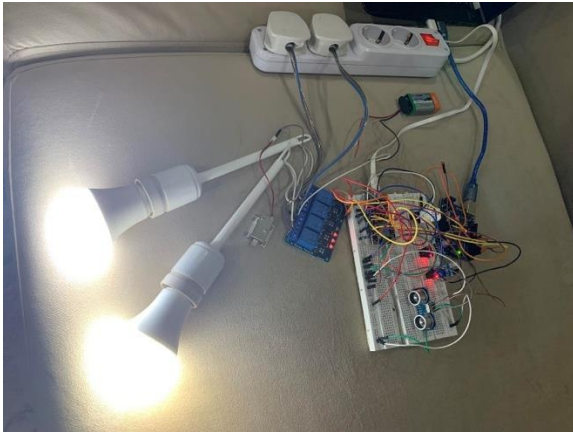


Figure 7. The entire setup of the performed system

Besides, the connectivity of the ESP8266 Wi-Fi module with the internet was tested to ensure that the connection was properly made. Figure 8 illustrates the sensor readings data on the serial monitor.

```

COM7
..WiFi connected
IP address:
192.168.43.232
entra
Attempting MQTT connection...connected
Subscribed to:
/v1.6/devices/management/Bulb1/lv
Subscribed to:
/v1.6/devices/management/Solenoid/lv
Subscribed to:
/v1.6/devices/management/Bulb2/lv
Subscribed to:
/v1.6/devices/management/light4/lv
Encryption has started (newline):
JSON received and parsed
{
  "temp": 26.1,
  "hum": 27.5,
  "len": 2330,
  "win": 1,
  "door": 1
}Temperature: 26.10
Humidity: 27.50
Length: 2330
Window: 1
Door: 1

```

Figure 8. Sensors reading data on the serial monitor

The results on the serial monitor screen, shows that the Wi-Fi ESP8266 is connected to the internet and the IP address has been obtained. And also, the figure shows the data readings of the sensors, which read the temperature and humidity degrees in real time and their incoming data comes from the sensor DHT22, the ultrasonic sensor which is known as the "length" in the Arduino IDE code to measures the distance of an object, and the status of the door and window is called "win" and "door", which indicates their status if the door and window are closed, "0" will be displayed, and "1" will be displayed if it is open and their data comes from IR1 and IR2 sensors respectively. Results are acquired after the system hardware and software implementation and can be viewed on the internet

created by the Blynk android application and Ubidots IoT cloud platform webpage.

The Blynk application provides the facility for easy monitoring, reading of sensor data, and controlling appliances. There are three different tabs for the three appliances namely solenoid, light 1, and light 2 also, there are display widgets that show sensor modules readings from Arduino Uno to NodeMCU via the Blynk server which is named length, temperature, humidity, door status, and window status. On the button widget, the current ON/OFF status of the system is displayed. The home appliances can be operated from any remote location by pressing the virtual button on the smartphone. The results of the designed system obtained on the Blynk android applications are shown in Figure 9.

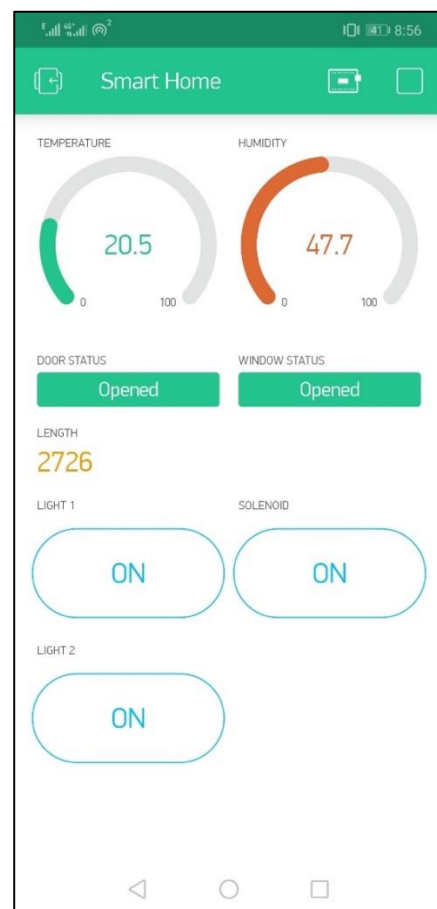


Figure 9. Screenshot of the Blynk application

The Ubidots IoT cloud platform is the best connection for the IoT. Ubidots provides developers with a platform that allows them to quickly capture sensor data and convert it into helpful information and also control appliances in an easy way. Using the Ubidots platform to send data to the cloud from any web-enabled device. The dashboards use widgets such as metrics, indicators, tanks, thermometers, and button switches to display the data. The dashboard generated in the platform uses thermometer and tank widgets to visually show the temperature and humidity degrees reading in real-time, and their incoming data comes from the DHT22 sensor. The indicators used on the IoT platform dashboard named door status and window status to show and monitor the status of the door and window if it's open or closed and their data comes from IR1 and IR2 sensors. The distance of an object measured by the ultrasonic sensor

using a metric widget identified as a length on the dashboard and finally, three button switches generated on Ubidots platform dashboard to switch ON/OFF relay board which is connected to bulb1, bulb2, and solenoid to unlock the door. Figure 10 illustrated all the widget used in Ubidots platform webpage.

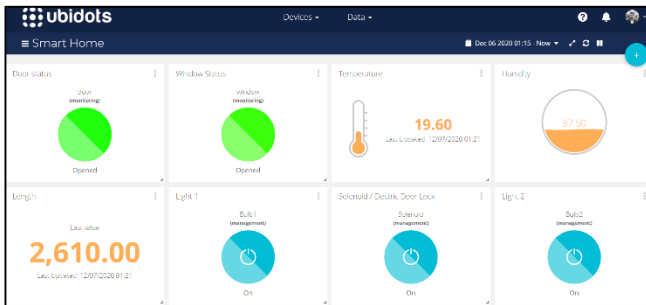


Figure 10. The system web page of Ubidots IoT platform

```
COM7
INPUT:18.3999996185
encrypted = Tr64jDgx168gERS605uikFd6g9iLsIXxpq1XUZ5aLc4=
Ciphertext: Tr64jDgx168gERS605uikFd6g9iLsIXxpq1XUZ5aLc4=
Temperature: 18.3999996185
SUCCES
INPUT:49.6000022888
encrypted = GcDnCXQXejVj07wpWwG8mAa5z28AF+KJ3Z8hRYgow/ew=
Ciphertext: GcDnCXQXejVj07wpWwG8mAa5z28AF+KJ3Z8hRYgow/ew=
Humidity: 49.6000022888
SUCCES
INPUT:2600
encrypted = r5ALnoPqFQL1zxvFx3a01Q==
Ciphertext: r5ALnoPqFQL1zxvFx3a01Q==
Length: 2600
SUCCES
INPUT:1
encrypted = 5Sh1Yww+8dVewKk8uwCDYw==
Ciphertext: 5Sh1Yww+8dVewKk8uwCDYw==
Door: 1
SUCCES
INPUT:1
encrypted = 5Sh1Yww+8dVewKk8uwCDYw==
Ciphertext: 5Sh1Yww+8dVewKk8uwCDYw==
Window: 1
SUCCES
INPUT:solenoid
encrypted = FXWM3XExkru1l6EON1n3sw==
Ciphertext: FXWM3XExkru1l6EON1n3sw==
Door is decrypted INPUT:Bulb1
encrypted = GAqtcJl3qKIiOLvXz00khg==
Ciphertext: GAqtcJl3qKIiOLvXz00khg==
Bulb1 is decrypted INPUT:Bulb2
encrypted = L3Q2Noah0z29NNbRZUew/w==
Ciphertext: L3Q2Noah0z29NNbRZUew/w==
Bulb2 is decrypted publishing to TOPIC:
```

Figure 11. Data encrypted and decrypted by AES displays on the serial monitor

Encryption is a mechanism that transforms the actual information into an encrypted data. The results are shown on the serial monitors in Figure 11, in the beginning, all the incoming data from ESP8266 are encrypted into a string by the AES algorithm, only the system knows that what is this generated data means. And, it also relies on the size of the information which requires to be processed. After that, this information is sent to the ciphertext. Finally, all the encrypted data are encoded and sent to the server.

Decryption is a mechanism for converting encrypted information returns to their original data. When the server receives encrypted and encoded data, the server decrypts the

data first and then go through the decoding process to get back to the original data.

6. CONCLUSION

The performed system in this paper is a simple design of an IoT-based smart home system. The performed system is designed and successfully implemented. In this project, all sensor modules data are sent to NodeMCU by Arduino Uno, and home devices are connected to NodeMCU by relay module which then sends to the Blynk server and cloud server of Ubidots by ESP8266 Wi-Fi. The data can be monitored and controlled on the Blynk application and Ubidots platform webpage. Also, all the data are encrypted through ESP8266 and the server by using the AES method. The process that was involved to secure the data is encrypt/decrypt using AES-128. To prevent others from accessing the user's data, an authentication method is used. This system refers to the real-time automation, monitoring, and control of remote systems.

Future studies will concentrate on incorporating the proposed system into essential smart home services. By using various sensors and various home appliances, this work can also be further improved.

REFERENCES

- [1] J. Y. Kim, H.-J. Lee, J.-Y. Son, and J.-H. Park, "Smart home web of objects-based IoT management model and methods for home data mining," in *2015 17th Asia-Pacific Network Operations and Management Symposium (APNOMS)*, 2015, pp. 327-331.
- [2] K. Agarwal, A. Agarwal, and G. Misra, "Review and Performance Analysis on Wireless Smart Home and Home Automation using IoT," in *2019 Third International conference on I-SMAC (IoT in Social, Mobile, Analytics and Cloud) (I-SMAC)*, 2019, pp. 629-633.
- [3] L. Salman, S. Salman, S. Jahangirian, M. Abraham, F. German, C. Blair, et al., "Energy efficient IoT-based smart home," in *2016 IEEE 3rd World Forum on Internet of Things (WF-IoT)*, 2016, pp. 526-529.
- [4] R. Sarmah, M. Bhuyan, and M. H. Bhuyan, "SURE-H: A Secure IoT Enabled Smart Home System," in *2019 IEEE 5th World Forum on Internet of Things (WF-IoT)*, 2019, pp. 59-63.
- [5] V. D. Vaidya and P. Vishwakarma, "A comparative analysis on smart home system to control, monitor and secure home, based on technologies like GSM, IOT, Bluetooth and PIC Microcontroller with ZigBee Modulation," in *2018 International Conference on Smart City and Emerging Technology (ICSCET)*, 2018, pp. 1-4.
- [6] M. Baykara and S. Abdullah, "Designing a Securable Smart Home Access Control System using RFID Cards," *Journal of Network Communications and Emerging Technologies (JNCET)*, vol. 10, 2020.
- [7] T. Alaswad, "An Investigation into the Security Challenges and Implications Surrounding Smart Home Technologies," *Cardiff Metropolitan University*, 2017.
- [8] R. Das, G. Tuna, and A. Tuna, "Design and Implementation of a Smart Home for the Elderly and Disabled," *International Journal of Computer Networks and Applications (IJCA)*, 2(6), p.242-246, 2015.
- [9] K. Mandula, R. Parupalli, C. A. Murty, E. Magesh, and R. Lunagariya, "Mobile based home automation using Internet of Things (IoT)," in *2015 International Conference on Control, Instrumentation, Communication and Computational Technologies (ICCICCT)*, 2015, pp. 340-343.
- [10] G. Tuna, "Secure Web-Based Communication Framework For Smart Home Systems Designed For The Elderly And Disabled," in *Proceedings of International Academic Conferences*, 2016.
- [11] P. S. N. Reddy, K. T. K. Reddy, P. A. K. Reddy, G. K. Ramaiah, and S. N. Kishor, "An IoT based home automation using android application," in *2016 International conference on signal processing, communication, power and embedded system (SCOPES)*, 2016, pp. 285-290.
- [12] H. Durani, M. Sheth, M. Vagharia, and S. Kotech, "Smart automated home application using IoT with Blynk app," in *2018 Second International Conference on Inventive Communication and Computational Technologies (ICICCT)*, 2018, pp. 393-397.

- [13] D. Sivamani, R. Sagayaraj, R. J. Ganesh, and A. N. Ali, "Smart incubator using internet of things," *International Journal for Modern Trends in Science and Technology*, vol. 4, pp. 23-27, 2018.
- [14] H. Singh, V. Pallagani, V. Khandelwal, and U. Venkanna, "IoT based smart home automation system using sensor node," in *2018 4th International Conference on Recent Advances in Information Technology (RAIT)*, 2018, pp. 1-5.
- [15] A. H. Imam, "A Simple Smart Home based on Iot Using Nodemcu and Blynk," *Universitas Muhammadiyah Surakarta*, 2019.
- [16] K. T. Wai, N. P. Aung, and L. L. Htay, "Internet of Things (IoT) Based Healthcare Monitoring System using NodeMCU and Arduino UNO," 2019.
- [17] I. Farahat, A. Tolba, M. Elhoseny, and W. Eladrosy, "Data security and challenges in smart cities," in *Security in smart cities: Models, applications, and challenges*, ed: Springer, 2019, pp. 117-142.
- [18] A. H. Hassan, A.-f. Y. Awad, and A. H. El-Amin, "Smart Home: Home Monitoring & control System using Simple Mobile App," *Sudan University of Science and Technology*, 2015.
- [19] L. P. Akhtar, "IoT based autonomous office alarm and access control system," *Master's Thesis, Technical University of Denmark*, 2017.
- [20] I. Mohammed and E. Duman, "Implementation of a smart house application using wireless sensor networks," in *9th International Conference on Networks & Communications. Computer Science & Information Technology*, 2017, pp. 53-70.
- [21] S. Pirbhulal, H. Zhang, M. E. E. Alahi, H. Ghayvat, S. C. Mukhopadhyay, Y.-T. Zhang, et al., "A novel secure IoT-based smart home automation system using a wireless sensor network," *Sensors*, vol. 17, p. 69, 2017.
- [22] M. Almosawi and K. Djupsjö, "IoT Security Applied on a Smart Door Lock Application," ed, 2018.
- [23] J. Alonso, C. Bayona, O. Rojas, M. Terán, J. Aranda, H. Carrillo, et al., "Iot solution for data sensing in a smart campus using smartphone sensors," in *2018 IEEE Colombian Conference on Communications and Computing (COLCOM)*, 2018, pp. 1-6.
- [24] T. Qiang, G. Guangling, C. Lina, and W. Han, "Nodemcu-based Low-cost Smart Home Node Design," in *IOP Conference Series: Materials Science and Engineering*, 2018, p. 012013.
- [25] R. Mahindar, M. Prakash, S. Ghosh, S. Mukherjee, and R. Ghosh, "IoT-based home appliances control system using NodeMCU and Blynk server," *International Advanced Research Journal in Science, Engineering and Technology*, vol. 5, pp. 16-22, 2018.
- [26] R. Majhi, "IoT: Home Automation," 2019.
- [27] C. R. Aldawira, H. W. Putra, N. Hanafiah, S. Surjarwo, and A. Wibisurya, "Door security system for home monitoring based on ESP32," *Procedia Computer Science*, vol. 157, pp. 673-682, 2019.
- [28] B. Bohara, S. Maharjan, and B. R. Shrestha, "IoT based smart home using Blynk framework," *arXiv preprint arXiv:2007.13714*, 2020.
- [29] A. Surriani, A. Pradana, M. Arrofiq, J. Putra, M. Budiyanto, and L. FSubekti, "Design of Power Monitoring Application," in *IOP Conference Series: Materials Science and Engineering*, 2020, p. 012069.
- [30] S. A. Arduino, "Arduino," *Arduino LLC*, vol. 372, 2015.
- [31] D. A. Aziz, "Webserver based smart monitoring system using ESP8266 node MCU module," *International Journal of Scientific & Engineering Research*, vol. 9, pp. 801-808, 2018.
- [32] M. S. Osman, "Smart home meter reading using IoT with Blynk app," in *AIP Conference Proceedings*, 2019, p. 020109.
- [33] L. Enciso and A. Vargas, "Interface with Ubidots for a fire alarm system using WiFi," in *2018 13th Iberian Conference on Information Systems and Technologies (CISTI)*, 2018, pp. 1-6.
- [34] R. Daş and G. Tuna, "Design and implementation of a simple, AES-based secure messaging platform," in *The International Conference on Engineering and Natural Sciences (ICENS) 2016*, Sarajevo, May 2016, pp. 47-52. [Online]. Available: <https://www.icens.eu/album/icens-2016>
- [35] S. Heron, "Advanced encryption standard (AES)," *Network Security*, vol. 2009, pp. 8-12, 2009.

BIOGRAPHIES

Resul Das received his B.Sc. and M.Sc. in Computer Science from Firat University in 1999, 2002 respectively. Dr. Das received his Ph.D. degree from the Electrical and Electronics Engineering Department at the same university in 2008. He is currently a Professor and Chair of the Software Engineering Department at Firat University, Turkey. He has authored several papers in international conference proceedings and refereed journals and has been actively serving as a reviewer for international journals and conferences. His current research interests include complex networks, computer networks, web mining, knowledge discovery, information and network security, software design and architecture, and IoT/M2M applications.

Taha Ababaker received his B.Sc. in Electrical and Computer Engineering from the University of Duhok, Iraq in 2011. He is currently an M.Sc. student at Firat University, Turkey department of software engineering. He has interests in Computer Networking, Computer Programming, IoT, Computer Organization, and Digital Image Processing. He can fluently speak English and Arabic.

Experimental Investigation of the Mechanical and Microstructure Properties of S49 Rail Steel

Anıl Rıdvanoğulları^{1*}, Tayfun Çetin² and Mehmet Akkaş³

^{1*}Muş Alparslan University, Department of Motor Vehicles and Transport Technologies, 49250, Güzeltepe, Muş, Turkey. (e-mail: a.ridvanoğullari@alparslan.edu.tr).

²Hakkari University, Department of Electricity and Energy, 30000, Hakkari, Turkey. (e-mail: tayfuncetin@hakkari.edu.tr).

³Kastamonu University, Department of Mechanical Engineering, 37150, Kastamonu, Turkey. (e-mail: mehmetakkas@kastamonu.edu.tr).

ARTICLE INFO

Received: Oct., 18. 2020

Revised: May., 19. 2021

Accepted: Jun, 20. 2021

Keywords:

S49 rail steel
Mechanical properties
Three-point bending
Microstructure
Hardness

Corresponding author: Anıl Rıdvanoğulları

ISSN: 2536-5010 / e-ISSN: 2536-5134

DOI: <https://doi.org/10.17694/ejt.812142>

ABSTRACT

This study was carried out to determine the microstructure and mechanical properties of S49 rail steel. For this purpose, firstly, three samples of S49 rail steel material were prepared by cutting by wire erosion method for three-point bending test. Microstructural analyses of S49 rail steel were examined by scanning electron microscopy (SEM). Energy dispersion spectrometer (EDS) analysis was performed to determine the chemical composition of the S49 rail steel material. Hardness test and three-point bending test were performed to determine the mechanical properties of the samples. SEM and EDS analyses of fractured surfaces were performed from the broken samples after the three point bending test.

1. INTRODUCTION

Railway transport has an important place in both freight and passenger transport. Railway transportation, which is in the safe class in the field of logistics, consists of three main parameters as railway, vehicles and facilities [1]. Railway is divided into two main components as infrastructure and superstructure. Railway infrastructure is known as all kinds of excavation work (ground consolidation) to be able to build a superstructure on the railway whose route is determined. The superstructure, on the other hand, is the part consisting of rails, sleepers, ballasts and fasteners that enable the movement of railway vehicles and transfer the loads on them to the platform [2-4].

The rail, which is one of the elements that make up the railway superstructure, is a very important element for the superstructure that enables the railway vehicles to roll (move) on it and is responsible for transferring the weight and forces from the vehicles to the ballast and sleeper. The rail is specially manufactured because it must be resistant to weight and other forces from railway vehicles. A standard rail; It consists of three parts: cork, body and base (Figure 1) [5].

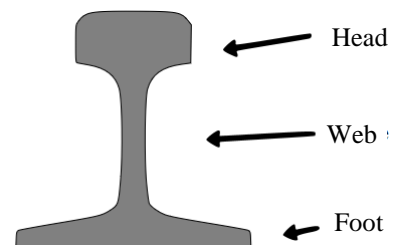


Figure 1. Sections of a standard rail

Rails are divided into classes in terms of shape and weight. S49 (49E1), UIC60 (60E1), which are divided into corrugated, single mushroom, double mushroom. such as the rail's weight per kilogram per meter (Figure 2).

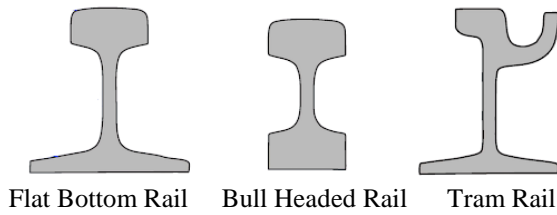


Figure 2. Rail shapes

Rails should be rigid enough not to wear but flexible enough not to break [6]. As the train speed increases, security problems occur. Therefore, material properties and shape are important in the railway line [7].

S49 (49E1) type rails, which are known to be approximately 49 kg per meter, are an important type of rail used in rail superstructure for both freight and passenger transportation. It is especially preferred in conventional railway lines. Since conventional lines generally operate under intense operation, the rails are broken, cracked, deteriorated over time. such defects occur.

Due to fatigue damage, which is one of the most common damage to the rails, increase in train operating speeds, higher axle loads and higher traffic density, train logistics will continue and will continue to be important. The contact pressure between the wheel and the rail, which can increase up to 1 GPa, and the surface shear stresses that can reach MPa at high levels can cause plastic deformations in the rails [8]. The surface, microstructural and mechanical properties of the rail have a significant effect on the mechanism of damage that may occur in the rail material during train operating conditions and on the wear resistance of the rail [9]. High and repetitive loads that occur during service conditions cause micro and macro cracks or rail breaks on the surface where the rail contacts the wheel [9]. When these defects cannot be detected within maintenance intervals, they may cause delay events to occur.

2. EXPERIMENTAL STUDIES

Standard metallographic processes were applied to obtain images of the samples with scanning electron microscopy (SEM). These applied metallographic processes were applied as sanding, polishing and etching respectively. Scanning electron microscopy (SEM) analysis was taken from the "FEI QUANTA 250 FEG" brand device in Kastamonu University Central Research Laboratory. Energy dispersion spectrometer (EDS) analyzes were taken from the "FEI QUANTA 250 FEG" brand device in Kastamonu University Central Research Laboratory. Hardness measurements were made to determine the mechanical properties of the samples. Hardness measurements were made by DIGIROCK brand macro hardness tester with Rockwell-C hardness measurement method. Since the strength of the test specimens is not in the shape and size of the tensile test specimen, it was measured by the three-point bending test. The bending tests were carried out with a SCHIMATZU type universal test machine according to the ASTM B 528-83 standard. By making a special apparatus shown in Figure 3, the flexural strength of the samples was measured using the TRAPEZIUMX software.

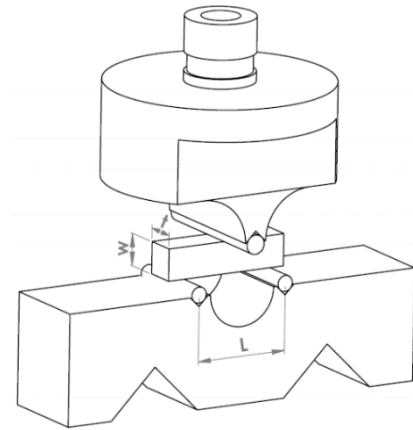


Figure 3. Schematic view of the three-point bending test [10].

In Figure 3, the graphics obtained as a result of the three-point bending tests for all three sample series are given.

3. EXPERIMENTAL RESULTS AND DISCUSSION

SEM image and EDS analysis results taken from S49 rail steel are given in Figure 4.

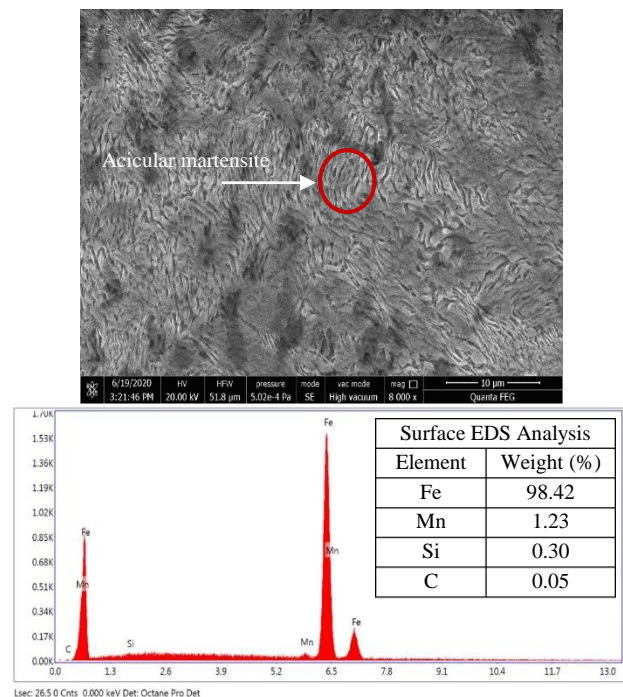


Figure 4. SEM image and EDS analysis of S49 rail steel

When Figure 4 is examined, scattered cementite grains are observed in martensite blocks. In addition, the microstructure is thought to be composed of acicular martensite. When the EDS analysis results given in Figure 4 are examined, it is understood that the material is S49 rail steel material. In addition, when the analysis results are examined, the Fe, Mn, Si and C peaks present in the S49 rail steel material can be seen clearly [11, 2, 12].

TABLE I
HARDNESS VALUES OF S49 RAIL STEEL.

	1.	2.	3.	Average
	Measurem	Measure	Measure	Measurement
	ent	ment	ment	Value
HRC				
Hardness Value	22.2	25.4	26.7	24.76

In order to determine the hardness exactly, hardness values were measured from various parts of the sample and at least five hardness values were taken from all surfaces of each sample. By taking the average of the hardness values measured, the average hardness values of the samples were found (Table 1). Macro hardness measurement values were determined by applying HRC test method and diamond cone tip by applying 10 kgf preload and 150 kgf total load.

In Figure 5, macro images of S49 rail steel after three-point bending are given.

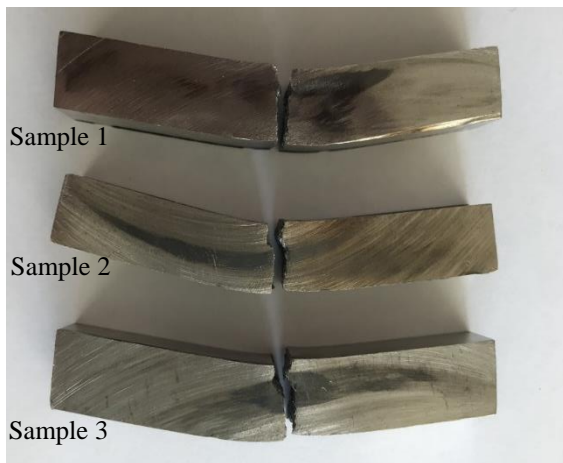


Figure 5. Macro images of S49 rail steel after the three-point bending test

When the sample images given in Figure 5 are examined, it is clearly seen that the samples are broken in the same regions and in the same shapes after the three-point bending test.

Three-point bending strengths of the samples are given in Figure 6 graphically.

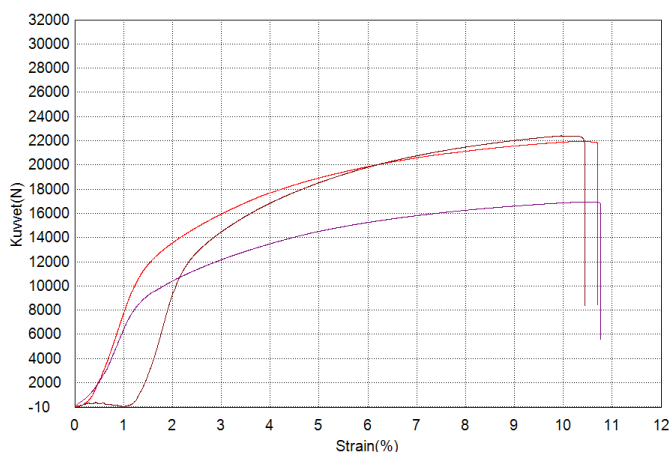


Figure 6. Three-point bending strength graphs of the samples

When the graphic given in Figure 6 is examined, the bending strength of S49 rail steel can be seen clearly. Three-point bending tests were carried out with three samples. It was measured as 1776 MPa in the first measurement, 2251 MPa in the second measurement and 1301 MPa in the last measurement. The average of three measurements was calculated as 1776 MPa [8,13].

In Figure 7, broken surface SEM and EDS analysis images and results are given after the three-point bending test of S49 rail steel.

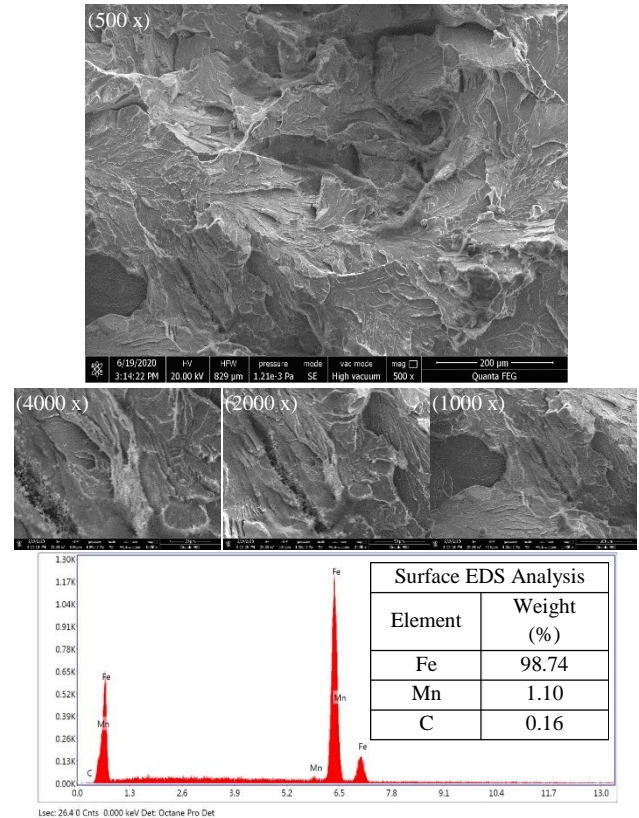


Figure 7. Broken surface SEM and EDS analysis of S49 rail steel after three-point bending test

When the SEM images given in Figure 7 are examined, it is seen that the S49 rail steel material is broken in a brittle way. Because, when looking at the SEM images of the sample, it is seen that there is too much roughness on the surface and the materials that make up the composition are broken from the grain boundaries. In addition, Fe, Mn and C peaks were detected in the internal structure of the sample as a result of the broken surface EDS analysis [10,14].

4. CONCLUSION

In this study, the microstructure and mechanical properties of S49 rail steel were successfully performed. Scanning electron microscopy (SEM), Energy dispersion spectrometer (EDS), hardness, three-point bending test and SEM and EDS analyzes of fractured surfaces were successfully applied to the samples. The report of the experimental results can be summarized as below:

- ✓ Fe, Mn, Si and C peaks present in S49 rail steel material were determined.

- ✓ In the inner structure, scattered cementite grains were found in martensite blocks.
- ✓ Macro hardness measurement values were measured by HRC test method using a diamond cone tip by applying 10 kgf preload and 150 kgf total load and the hardness value was measured as 24.76.
- ✓ The average of the three-point bending test measurement was calculated as 1776 MPa.
- ✓ It was found that the S49 rail steel material broke brittle after the broken surface.
- ✓ As a result of the broken surface EDS analysis, Fe, Mn and C peaks were detected in the internal structure of the sample.

REFERENCES

- [1] Vural, D., Gencer, C. and Karadoğan, D. (2014). Ulaştırma uygulamalarına yönelik çok modlu model önerisi. Savunma Bilimleri Dergisi, 13(1), pp. 75-105.
- [2] Kaewunruen, S., Ngamkhanong, C. and Lim, C. H. (2018). Damage and failure modes of railway prestressed concrete sleepers with holes/web openings subject to impact loading conditions. Engineering Structures, 176, pp. 840-848.
- [3] Kozak, M. (2011). Demiryolunda Rayların Birleşim Noktaları ve Özelliklerinin Araştırılması. Electronic Journal of Construction Technologies/Yapı Teknolojileri Elektronik Dergisi, 7(2).
- [4] Kozak, M. and Ünal, O. (2014). Bazalt Agregası ile Üretilen Beton Travers de Çelik Lifin Kullanılabilirliğinin Araştırılması. Journal of Natural & Applied Sciences, 18(3).
- [5] Özkul, F. (2014). Demiryollarında Ray Birleştirme Yöntemlerinin İncelenmesi, Alüminotermid Ve Yakma Alın Kaynak Yöntemlerinin Karşılaştırılması (Doctoral dissertation, Fen Bilimleri Enstitüsü).
- [6] Uzbaşı, B. (2013). Demir Yolu İltisak Hatlarında Aşınma Kayıpları. Mühendis ve Makine, cilt 54, sayı 638, pp. 39-45.
- [7] Eroğlu, M., Esen, İ., Ahlatçı, H., Özçelik, S., Sun, Y. and Pamuk, S. (2016). TCDD Karabük-Bolkuş Bölgesindeki 49E1 Raylarda Ondülasyon Ölçümleri Ve Değerlendirilmesi. ISERSE'16, pp. 445-451.
- [8] Pal, S., Valente, C., Daniel, W. and Farjoo, M. (2012). Metallurgical and physical understanding of rail squat initiation and propagation. Wear, vol. 284-285, pp. 30-42.
- [9] Çöl, M., Koç, F.G. and Yamanoğlu, R. (2013). H. Wendel S40 Ray Çeliğinde Yorulma Çatlaklarının Mikroyapısal Karakterizasyonu. ISERSE'13, pp. 251-256.
- [10] Çelik E. (2009). Elmaslı kesici takımlarda alternatif bağlayıcılar. Doktora Tezi, F.Ü. Fen Bilimleri Enstitüsü, Elâzığ.
- [11] Çetin, T. and Akkaş, M. (2020). Effect of WC Reinforced on Microstructure and Mechanical Properties of CuAlMn Alloys Produced by Hot Pressing Method. European Journal of Technique, 10(1), pp. 173-183.
- [12] Sharma, S., Sangal, S. and Mondal, K. (2016). Wear behaviour of bainitic rail and wheel steels. Materials Science and Technology, 32(4), pp. 266-274.
- [13] Meriç, C., Atık, E. Şahin, S. (2002). Mechanical and metallurgical properties of welding zone in rail welded via thermite process. Science and technology of welding and joining, 7(3), pp. 172-176.
- [14] Kuziak, R. and Zygmunt, T. (2013). A New Method of Rail Head Hardening of Standard-Gauge Rails for Improved Wear and Damage Resistance. steel research international, 84(1), pp. 13-19.

BIOGRAPHIES

Anıl Rıdvanogulları obtained his BSc degree in railway system engineering from Karabük University (KBU) in 2016. He received his MSc from the Mechanical Engineering Department of the same university, Institute of Science, Department of Mechanical Engineering in 2018. Research areas, railway vehicles and equipment. Recently, he focused on rail system superstructure construction and materials. Between 2016 and 2019, he worked as a part-time instructor at Karabük University Railway Systems Engineering. In 2019, he joined Muş Alparslan University Vocational School of Technical Sciences Rail Systems Road Technology program as a lecturer and is still working as a lecturer.

Tayfun Çetin obtained his B.Sc. degree from Fırat University in 2010. In 2010, He received his M.Sc. and Ph.D. degrees from Fırat University and Karabük University in 2014 and 2019 respectively. He started to work as a lecturer at Hakkari University in 2019. He has been working at Hakkari University since 2019. He works in the fields of powder metallurgy and material science.

Mehmet Akkaş obtained his BSc degree in Metal Teaching Program from Fırat University in 2010. He received the MSc. Diploma in Metallurgy Education from Fırat University in 2013. He received the Ph.D. diploma in Manufacturing Engineering Department from the Karabük University in 2017. His research interests are powder metallurgy, powder production, gas atomization and composite materials. In 2018 he joined the Department of Mechanical Engineering, Faculty of Engineering and Architecture, Kastamonu University as an assistant professor, where he is presently an assistant professor.

Effects of Sliding Distance Speed and Load on Wear and Temperature in Different Matrix and Fiber-Reinforced Composite Materials

H.Pihitli 

Department of Mechanical Engineering, Engineering Faculty, Firat University, 23279 Elazığ, Turkey, (e-mail: hpihtili@firat.edu.tr)

ARTICLE INFO

Received: Oct., 20. 2020

Revised: Apr., 14. 2021

Accepted: Jun., 10. 2021

Keywords:

Wear
Glass Fibers
Woven Fabric Polyester Resin
Epoxy Resin
Composite Materials

Corresponding author: *H.Pihitli*

ISSN: 2536-5010 / e-ISSN: 2536-5134

DOI: <https://doi.org/10.17694/ejt.813718>

ABSTRACT

In this study, wear behaviours of fiber-reinforced and matrix composite materials are experimentally investigated under different speeds, loads and temperature. Composite materials were made of Kevlar-epoxy resin, glass fibre-epoxy resin and glass fibre-polyester resin materials. Tests were conducted for speeds of 0,390 and 0,557 m/s , at two different loads of 5N and 10N, respectively. Wear in the experiments was determined as lost in mass. In addition, the photographs of specimens were taken under the SEM and wear behaviours on these photographs were investigated. As a result of this study, it is shown that the applied load on the specimens has more effect on the wear than that of speed. The surface temperature plays an important role in the friction and wear of polymers and increases at higher sliding speeds and loads. The temperature of the specimens increased more with the increasing sliding speed and applied load, so the wear increases more with the temperature.

1. INTRODUCTION

In industry applications, increase in using composite materials causes that it is necessary to know behaviour of working conditions, so that wear is the most important parameter and its experimental behaviour must be known. The kind of composite material used in production technology and their usage areas have been increased every day. Fiber-reinforced polymer composite, due to good combination of properties, are used particularly in automobile and airplane industries, the manufacturing of spaceship and sea vehicles. Composite materials are ideal for structural applications where high strength-to- mass ratio and specific stiffness of GFRP is not extraordinarily high. Especially woven fabrics have rather low specific strength and stiffness is required. Aircraft and spacecraft are typical mass-sensitive structures in which composite materials are cost effective. To gain full advantages of composite materials, both aircraft and spacecraft are being designed in a manner much different designing with composites is state of the art [1]. The increase in the usage of composite materials means that it is necessary to know their behaviour under working conditions. The wear resistance is an important parameter and its experimental behaviour must be known. Composite materials are being used more and more instead of steels and other metals because of their high strength at low specific mass. Besides, wider choices of materials and

manufacturing of GFRP still require a lot of handworks and are rather expensive make them an ideal case for engineering applications [2, 3, 4]. On account of their good combinations of properties, fibre reinforced polymer composites are used particularly in the automotive and aircraft industries, the manufacturing of spaceships and sea vehicles [5, 6]. Nowadays, non-metal composite materials are being widely used as an alternative to steel and other materials. There are two main characteristics which make these materials attractive comparing conventional metallic designs. They are of relatively low density and they can be tailored to have stacking sequences to provide high strength and stiffness in the direction of high loadings [8]. Composite materials consist of a resin and reinforcement chosen according to desired mechanical properties and the application [9, 10]. Among the fibre reinforcements, glass, carbon and aramid fibres are the most likely candidates and are widely employed. Polymer composites reinforced with these fibres are usually one to four times stronger and stiffer than their unfilled equivalents [11]. Among the resins, polyester, epoxy, phenolic and silicon resins are the most likely candidates and are widely employed. The ever-increasing demand for reliability and long life of machines are one of the main problems of contemporary engineering [12]. In industry, particularly materials working in places where wear properties are desired to be wear resisting.

For this reason, the wear resistance of the materials must be known [7]. Wear (DIN 50320) is called as occurring non-desired modifications with deviation of little pieces due to a mechanical cause or energy on surface of material [13]. Many studies reported that the wear resistance with polymer sliding against steel improved when the polymers are reinforced with glass or aramid fibres. However, the behaviour is affected by factors such as the type, amount, size, shape and orientation of the fibres, the matrix composition and the test conditions such as load, speed and temperature [11, 13, and 19]. The wear resistance of materials is determined in the result of laboratory experiments. In this study, the wear behaviours of woven glass fibre, composite materials are investigated under different loads, speeds, temperature and sliding distances.

2. Experimental Procedure

In this work, composite materials were made of Kevlar-epoxy resin, glass fibre-epoxy resin and glass fibre -polyester resin material. They had a quasi-isotropic stacking sequence, 90^0 , with the surface ply, which is contact with friction during experiments having a 90^0 fibre orientation direction. Wear behaviour of the glass fibre-polyester resin (provided by Fiber Cag, Turkey) and glass fibre-epoxy matrix resin (CYCOM7701) provided by TAI, Turkey are experimentally investigated. The woven glass fibre-reinforced composites made of 425 gm^{-2} and 500 gm^{-2} (yarns can be produced from a wide range of fibers and whiskers. In the case of short fibers and whiskers, the yarn must be spun (or twisted) to hold the fibers together. Continuous fibers require no spinning, but it is often advantageous to do so. Fabrics are produced from these yarns by normal weaving processes). If the fibres are not spun the fabrics are usually denser and involve quite less fibre flexure. Plain wave glass fibre-polyester matrixes contain E glass fibres of diameter $10\text{-}24 \text{ }\mu\text{m}$. Woven fabrics should be used when high shear strengths are required in the plane of the reinforcing sheet. The more unidirectional weaves generally have lower shear strengths than conventional weaves. The glass fibre composites have been reinforced with the volume of fibers $V_f = 30 \text{ vol } \%$ and with the volume of matrix $V_m = 70 \text{ vol } \%$. Matrix material used in these composites is polyester resin (Neoxil CE92). It is often desirable to add mineral filler to polyester resins. In addition to lowering the cost of resins, filler materials also improve the surface appearance, resistance to water and reduce shrinkage. Polyesters are also commonly used as matrix materials, particularly with glass fibre reinforcement. Polyester is an economic material that has high chemical resistance and resistance to environmental effects. It has high dimensional stability and low moisture absorption. Low volume-fraction glass fibre-polyester composites with a wide range of colours have been in use for a long time. The production technologies for glass and thermoset glass-polyester composites are easier and cheaper than those for other glass-resin materials [5, 6, and 15].

Glass-fibre reinforced polymer with thermoset polyester resin is an attractive material that is economically desired. Its applications at low temperatures and under service terms are easy, when this material is compared to advanced polymer composites with complex molecule structure, high strength and working under terms of difficult service [5, 6, 12]. This material is preferred due to the superiority of polymer mixed material, because it is easy to produce and at low cost, more than advanced engineering applications. It is being questioned

the developed and improved properties of this material in present [9]. Epoxy resins of several families are now available ranging from viscous liquids to high-melting solids. Among them, the conventional epoxy resins manufactured from epichlorohydrin and bisphenol remain the major type used. Epoxy resins are also modified with plasticizers [5, 6]. They are generally known as products used in structural component, adhesives, and protective plating due to their very good mechanical properties, chemical resistant and electrical characteristics. The shrinkage of epoxy is less than 2 % and there is no water or volatile by-products generated during curing. When these epoxy resins are reinforced with high-strengthened fiberglass, the obtained product is used in structural applications to resolve need of high hardness and lightness [9, 18].

2.1. Wear Test Details

The woven glassfiber-epoxy matrix resin, the woven glassfiber-polyester matrix resin and Kevlar-epoxy resin composite materials were provided in the dimension of $310 \times 290 \times 3 \text{ mm}^3$. The experiment specimens of size $47 \times 27 \times 3 \text{ mm}^3$ were cut from the sheets Fig.1. The wear of composite materials was performed using a block on shaft test method Fig. 2. The abrasive used at the wear of specimens is SAE 1030 (DIN 22) steel ground whose surface ground and the diameter of 15mm. The hardness and surface roughness (R_a) of the deprecator shaft are 150 HB30 and $1.25 \text{ }\mu\text{m}$, respectively. The wear tests were performed on a specially prepared experimental set-up by using a lathe. The actual loads were placed on the pan of the load arm of this apparatus. The schematic view of wear set-up is shown in Fig.2. The role of experimental conditions is very important in experimental studies.

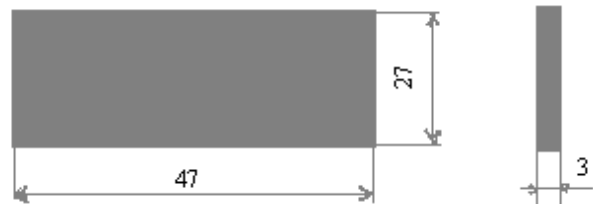


Figure 1. Dimensions of the plate used for the wear experiment

First, ambient conditions should not be changed during the experiment sets for the accuracy. The experiments were repeated till if any change of the experiment conditions had been observed.

First, ambient conditions should not be changed during the experiment sets for the accuracy. The experiments were repeated till if any change of the experiment conditions had been observed. The amount of wear will able to increase with the effect of temperature. Because it is determined that the deprecator shaft was heating in the results of a performed experiment; a new experiment was performed after the shaft was completely cooled in all experiments.

All the experiments were conducted at the room temperature (20^0C). The temperature of the specimens was measured with a Cole-Palmer H-08406-46 infrared temperature measurement device. The glassfiber-epoxy resin, glassfiber-polyester resin and the Kevlar-epoxy resin composite materials specimens were tested under the different experiment conditions. Tests

were conducted for 0,390 and 0,557 m/s speeds, at two different loads of 5N and 10N. The mass losses were measured at each different sliding distances. Wear in the experiments was determined as mass loss. For each experiment, one of the specimens was used. The amount of wear was measured before the experiment and after the experiment with the apparatus of balance scales with an accuracy of 10^{-3} g.

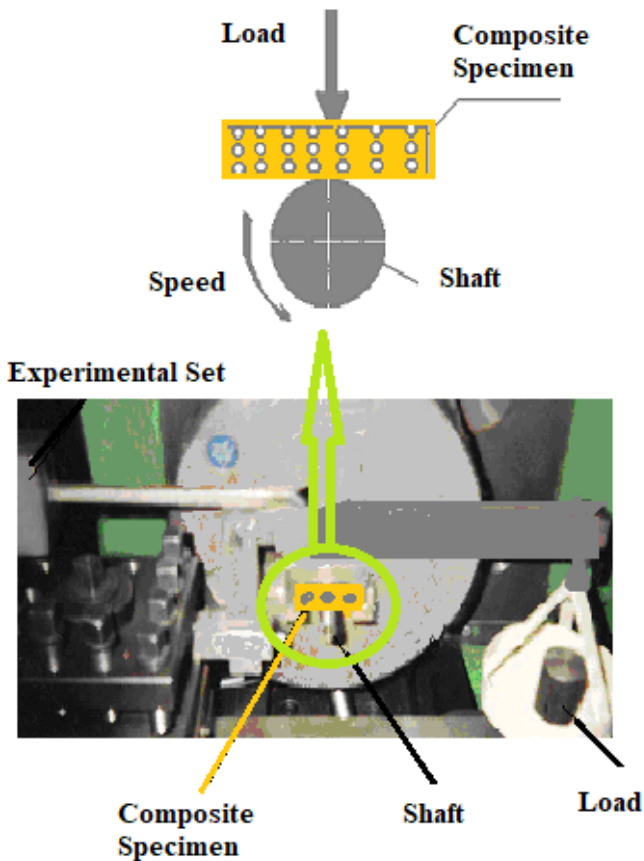


Figure 2. Photograph of the experimental setup and schematic view of a block-on-shaft wear test.

3. The experimental results and discussion

The wear and friction behaviour of polymeric composites have to be considered as a function of load, sliding speed and distance or temperature. The surface temperature plays an important role in the friction and wear of polymers. An increase in wear intensity can occur thermal softening. Effects of the normal load and the sliding speed on the mass loss of woven glass fibre, glass fibre-epoxy resin and glass fibre-polyester resin composite specimens are shown in Figs. 3-13, respectively. The mass loss of the glass fibre-polyester resin composite specimens did not change below the sliding distance of 942m, as shown in Fig. 3.

However, the mass loss of the plain polyester resin increased after the sliding distance 942 m. This result may be explained as the increase of the temperature occurred at the experiments. The wear on the glass-fiber polyester composite decreases due to the effect of increasing temperature removal from the surface as illustrated. The epoxy-based composite exhibits lower wear loss than that of polyester-based composite [18, 20]. The mass loss is lower in glass fiber-epoxy resin composite specimens than in fiberglass-polyester resin composite under 0,390 m/s

speed and 5N load according to the sliding distance in Fig. 3. SEM photograph shows the features of worn surface at 0,39 m/s speed and 5 N load in Fig.4. The results also show that the wear did not occur in Kevlar fibre-reinforced composite specimens at 0,390 m/s speed and 5N load. From Figs. 3–5, it is seen that the wear increased with the increasing sliding distance. The mass loss of all the composite specimens generally increased with the sliding distance at the constant sliding speed 0,390 m/s when the applied load was increased from 5 to 10N (compare Fig. 3 with Fig. 5 and in Fig. 6). Because the fiberglass-epoxy resin has a low friction coefficient and high wear resistance; the mass loss of the fiberglass epoxy resin is lower than that of fiberglass-polyester composite [5, 6, 12].

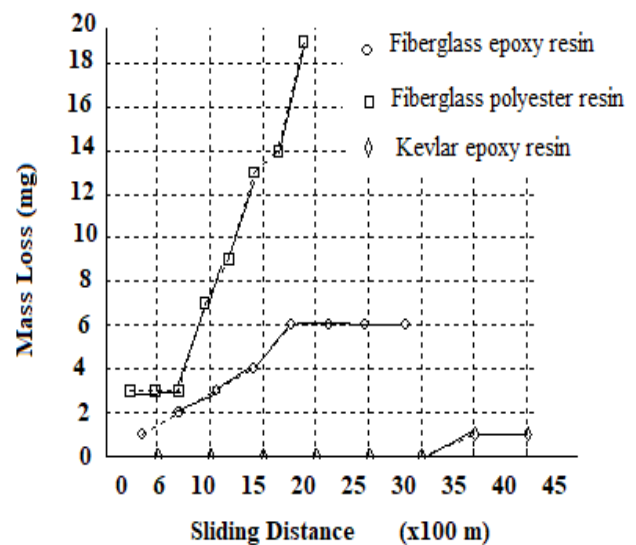


Figure 3. Variation of mass loss with respect to sliding distance at 0,390 m/s speed and 5N load.

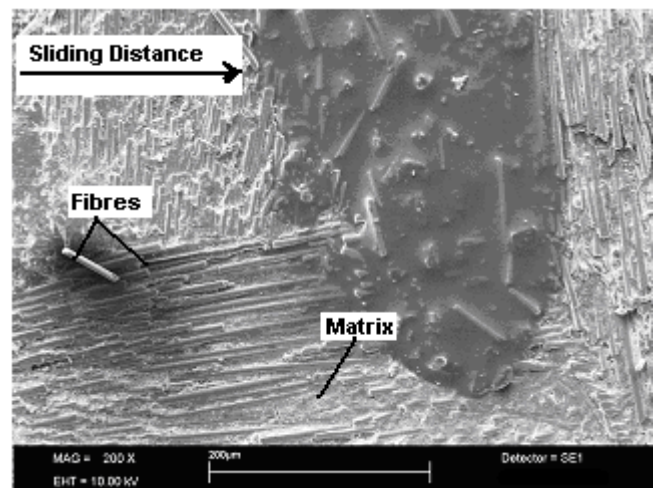


Figure 4. SEM photograph showing the worn surface of glass fiber-epoxy resin Composite at 0,390 m/s speed and 5N load.

Because of the low friction coefficient of epoxy resin, the temperature is increased. For this reason, the mass loss becomes less depending on the sliding distance as shown in Fig. 5.

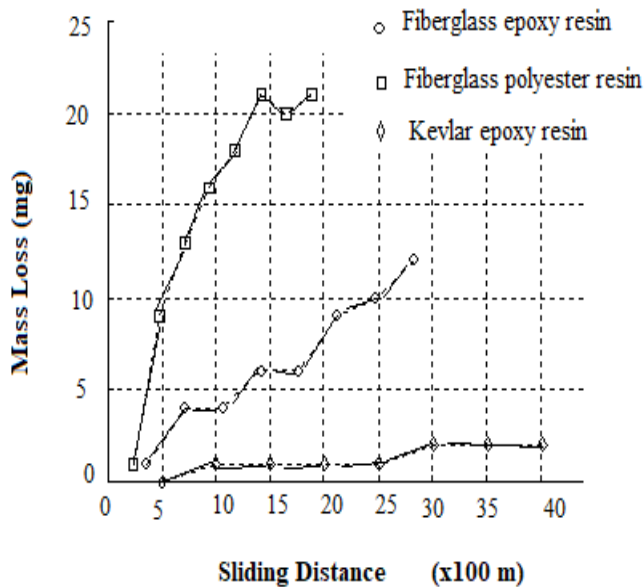


Figure 5. Variation of mass lost with respect to the sliding distance for 0,390 m/s speed and 10N load.

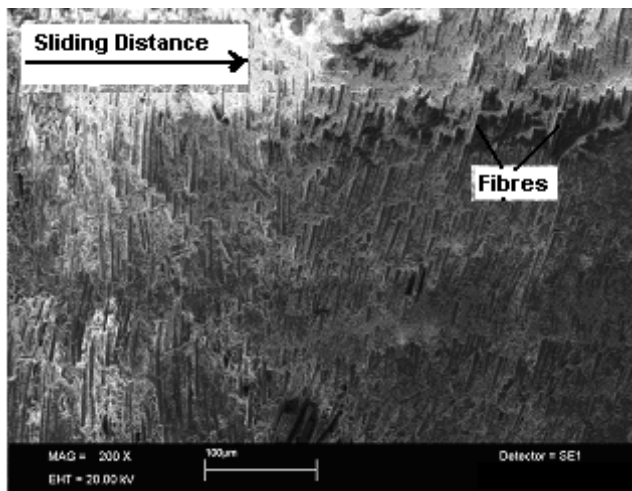


Figure 6. SEM photograph showing the worn surface of glass fiber-epoxy resin composite at 0,390 m/s speed and 10N load.

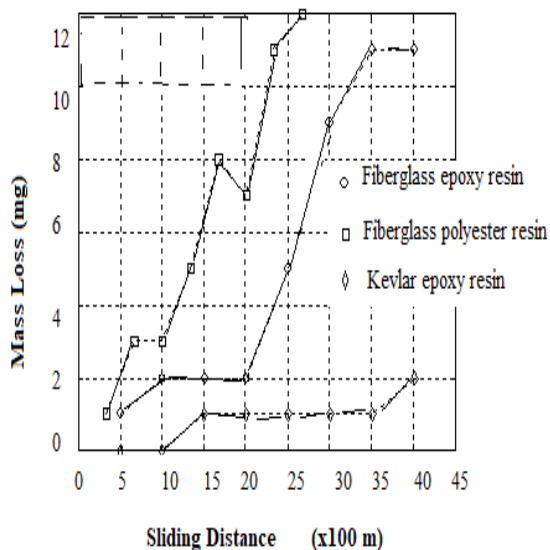


Figure 7. Variation of mass lost with respect to the sliding distance for 0,557 m/s speed and 5N load.

A little increase in temperature depends on sliding distance at 0,557 m/s speed and 5N load. The wear will occur in the polyester resin rather than the reinforcement. SEM photograph in Fig. 8. Shows the features of worn surface at 0,557 m/s speed and 5N load. As the earlier mentioned, epoxy-based composites exhibit lower wear loss than polyester-based composites. In addition, kevlar fibres usually exhibit much higher wear resistance than glass fibres [8, 14] and kevlar fibres exhibit lower friction than glass fibres. The low friction coefficient is prevented to increase of the temperature. For this reason, the mass loss of the kevlar fibre-reinforced composite material becomes less than that exhibited by the woven glass fabric-reinforced composites. The woven glass fabric-reinforced composites were subjected to a larger mass loss depending on sliding distance, when both the sliding speed and the applied load are increased as it can be seen in Fig. 8.

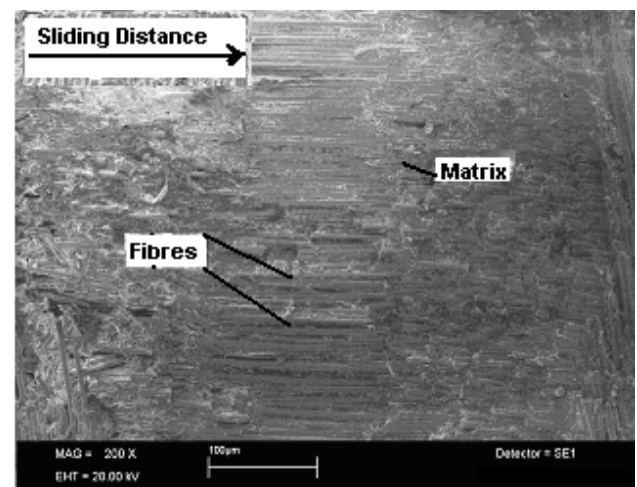


Figure 8. SEM photograph showing the worn surface of fiberglass-epoxy resin composite at 0,557 m/s speed and 5N load.

It is well-known that the surface temperature plays an important role in the friction and wear of polymers and thus it increases at higher sliding speeds and loads [5, 6, 18]. The applied load on the specimens has more effect on the wear than the sliding speed according to the data given in Figs. 3–11. SEM photographs in Figs. 4 and 6 depict the features of worn surface in sample subjected to increasing distance of sliding. In Fig. 7, the wear of matrix material due to larger sliding distance compared to Fig. 5 is noticeable comparing Fig. 9 with Fig. 10, it is possible to highlight the effect of increasing load application on the wear surface features. As seen in Fig. 13, when load is increased, causes to rise of temperature up to a point, the ends of fibers are broken due to matrix detachment. composite for all the speeds and loads according to sliding distances (Figure 3, 5, 6, 8 and 9). Glass fibre-epoxy resin composites generally showed higher resistance and minimum wear if we compare with the glass fibre-polyester matrix resin composites materials. The glass fibre-epoxy resin composites have a low friction coefficient and high wear strength, which prevents the increase of temperature. For this reason, the mass loss of glass fibre-epoxy resin composites is low depending on the sliding distance. The study also showed that higher loads and sliding velocities bring about changes in worn surface features such as interface separation, inclined fracture of fibres, loss of matrix as well as the appearance of debris with the two

different. The wear occurs in the matrix rather than the reinforcement.

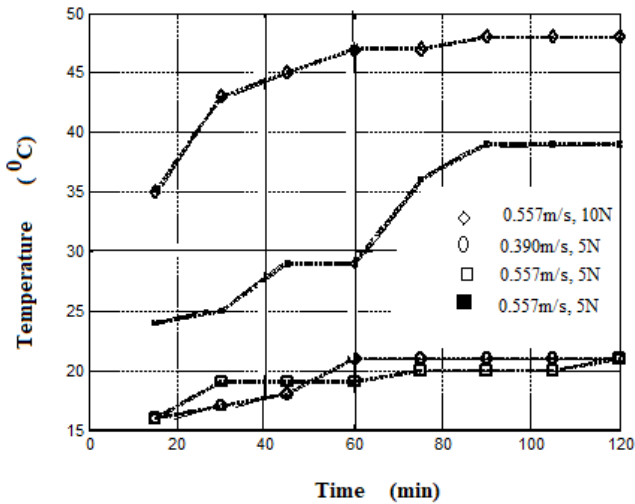


Figure 9. Effect of speed and load on temperature (20 °C) and time of fiberglass–polyester resin composite.

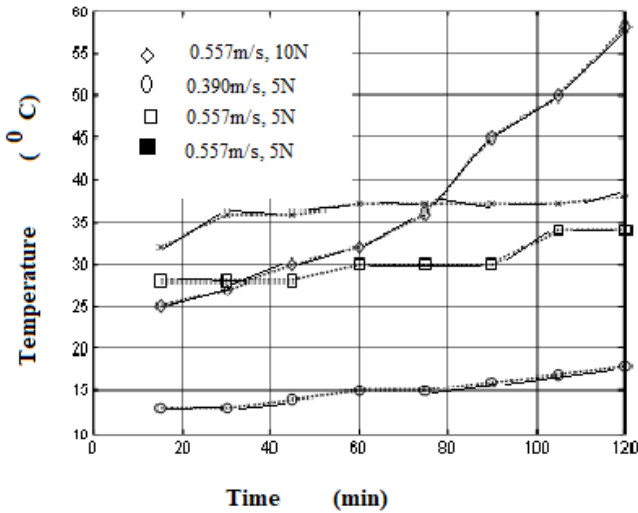


Figure 10. Effect of speed and load on temperature(20 °C) of fiberglass–epoxy resin composite.

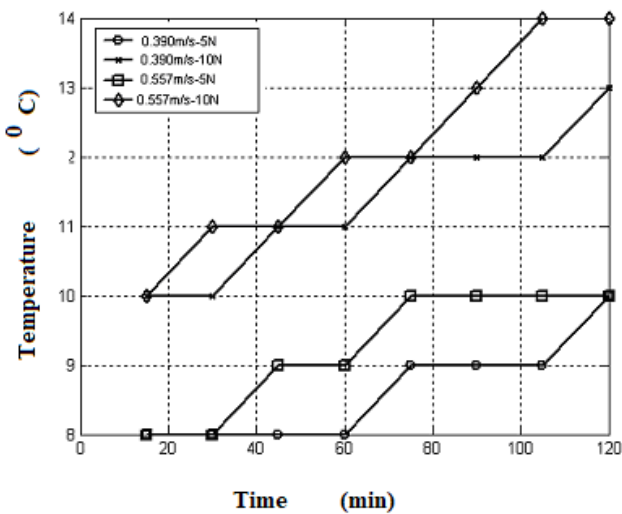


Figure 11. Effect of speed and load on temperature (20 °C) of kevlar-epoxy resin composite.

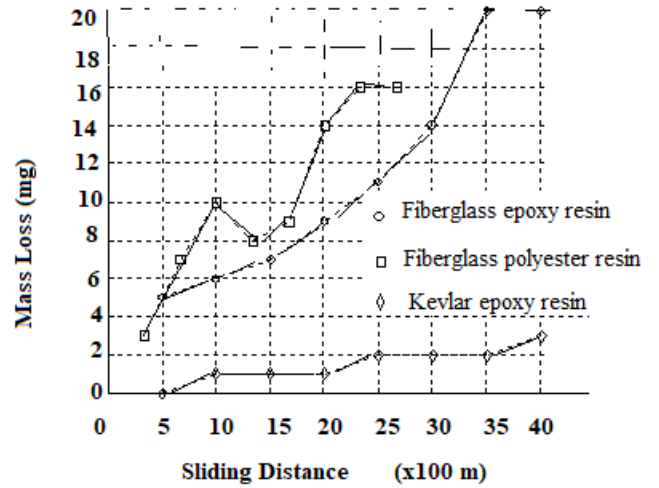


Figure 12. Variation of mass loss with respect to the sliding velocity for 0,557 m/s speed and 10N load.

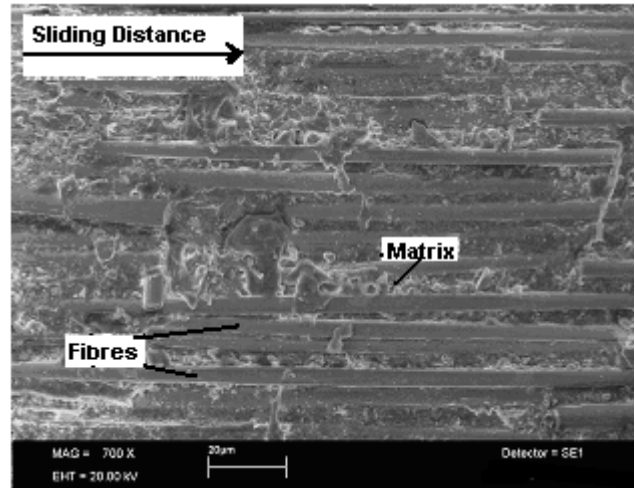


Figure 13. SEM photograph showing the worn surface of glass fibre–epoxy resin composite at 0,557 m/s speed and 10N load.

3. Conclusion

The mass loss of the woven glass fibre-epoxy resin composite increases with increasing of load and speed. Because the temperature raised with increasing of load and speed. The mass loss of all composite specimens generally increased with the sliding distance at the constant sliding speed of 0,390m/s when the applied load was increased from 5N to 10N (compare Fig. 3 with Fig. 5, and Fig. 6).

The wear in the woven glass fibre-epoxy resin composite specimens is lower than the woven glass fibre-polyester resin. Therefore, the wear in the woven 425 gm² glass fabric-reinforced composite is lower than the woven 500 gm² glass fabric-reinforced composite keeping all test parameters constant. Due to the kevlar fibres having a low friction coefficient and high wear strength, and epoxy-based composite exhibit lower wear loss than polyester-based composite, the wear of the kevlar fibre-reinforced composite is lower than the woven glass fabric-reinforced composites.

REFERENCES

- [1] Vinson, J.R., Chou, T., Composite Materials and their use in structures, London, (1975).
- [2] Kishore, Sampathkumaran P., Seetharamu S., Murali A. and Kumar R.K. Journal of Reinforced Plastics and Composites.; 18(1):55–62,(1999).
- [3] Kishore, Sampathkumaran P., Seetharamu S., Vynatheya S., Murali A. and Kumar R.K., SEM Observations of The Effects Of Velocity and Load on The Sliding Wear Characteristics of Glass Fabric–Epoxy Composites with Different Fillers”, Wear,237: 20–27, (2000).
- [4] A.A. Collyer, “Rubber Toughened Engineering Materials”, Chapman & Hall, London, (1994).
- [5] Pihtili, H., Tosun,N., “Effect of load and speed on the wear behaviour of woven glass fabrics and aramid fibre-reinforced composites” , Wear 252 , 979 -984, (2002).
- [6] Pihtili, H., Tosun,N “Investigation of the wear behaviour of a glass-fibre-reinforced composite and polyester resin Composites”, Science and Technology 62; 367–370,(2002).
- [7] N.S. El-Tayeb, R.M. Gadelrap, “Friction and wear properties of E-glass fiber reinforced epoksi composites under different sliding contact conditions”, Wear 192,; 112-117,(1996).
- [8] N. Chand, A. Naik, S. Neogi “Three-body abrasive wear of short glass fibre polyester composite”, Wear 242; 38–46,(2000).
- [9] T. Kunishima, T. Kurokawa, H. Arai, V. Fridrici, P. Kapsa, Reactive extrusion mechanism, mechanical and tribological behavior of fiber reinforced polyamide 66 with added carbodiimide Mater. Des., 188 Article 108447, (2020).
- [10] J.S.N. Kukureka, C.J. Hooke, M. Rao, P. Liao, Y.K. Chen, “The effect of fibre reinforcement on the friction and wear of polyamide 66 under dry rolling–sliding contact”, Tribol. Int. 32,; 107–116,(1999).
- [11] V.K. Srivastava, J.P. Pathak, “Friction and wear properties of bushing bearing of graphite filled short glass fibre composite in dry sliding”, Wear 197 ,; 145–150,(1996).
- [12] ASM Handbook, ASM International. Materials Park. USA. 1992.
- [13] R.Ramesh, Kishore, Rao R.M.V.G.K, “Dry sliding wear studies in glass fiber reinforced epoxy composites”, Wear, 89: 131, (1983).
- [14] Bolvari AE, Gleen SB. Eng Plast, 9:205 –15. (1996).
- [15] T. Kunishima, S. Nagai, T. Kurokawa, J. Galipaud, G. Guillonneau, G. Bouvard, J.-Ch Abry, C. Minfray, V. Fridrici, Kapsa effects of temperature and addition of zinc carboxylate to grease on the tribological properties of PA66 in contact with carbon steel Tribol. Int. p. 106578, (2020).
- [16] D. Zhao, H. Hamada, Y. Yang Influence of polyurethane dispersion as surface treatment on mechanical, thermal and dynamic mechanical properties of laminated woven carbon-fiber-reinforced polyamide 6 composites Compos. B Eng., 160 pp. 535-545,(2019).
- [17] T. Kunishima, K. Miyake, T. Kurokawa, H., Arai Clarification of tribological behavior on tooth surface of resin worm gear for electric power steering, JTEKT Eng. J. English Edition, 1013E pp. 27-33, (2016).
- [18] B.Vishwanath, A.P. Verma, C.V.S. (Kameswara Rao, Composite Sci. Technol. 44 (1),77–86,(1992).
- [19] J. Chen, H. Xu, C. Liu, L. Mi, CShen The effect of double grafted interface layer on the properties of carbon fiber reinforced polyamide 66 composites Compos. Sci. Technol., 168 pp. 20-27,(2018).
- [20] J D.W. Gebretsadik, J. Hardell, B. Prakash Friction and wear characteristics of PA 66 polymer composite/316L stainless steel tribopair in aqueous solution with different salt levels Tribol. Int., 141, Article 105917, ,(2020).
- [21] M.T. Lates, R. Velicu, C.C. Gavrila Temperature, pressure, and velocity influence on the ribological properties of PA66 and PA46 Polyamides, Materials, 12 (20) p. 3452. (2019).
- [22] Y.K. Chen, O.P. Modi, A.S. Mhay, A. Chrysanthou, J.M. O’Sullivan, (2003). The effect of different metallic counterface materials and different surface treatments on the wear and friction of polyamide 66 and its composite in rolling-sliding contact Wear, 255, pp. 714-721.
- [23] T. Kunishima, Y. Nagai, T. Kurokawa, G. Bouvard, J.- C. Abry, V. Fridrici, P. Kapsa, Tribological behavior of glass fiber reinforced-PA66 in contact with carbon steel under high contact pressure, sliding and grease lubricated conditions Wear. (2020).
- [24] N.G. Karsli, T. Yilmaz, O. Gul, Effects of coupling agent addition on the adhesive wear, frictional and thermal properties of glass fiber-reinforced polyamide 6,6 composites Polym. Bull., 75 pp. 4429-4444. (2018).
- [25] N.G. Karsli, S. Demirkol, T. Yilmaz, Thermal aging and reinforcement type effects on the tribological, thermal, thermomechanical, physical

and morphological properties of poly (ether ether ketone) composites, Compos. Part B, 88 pp. 253-263 (2016).

BIOGRAPHIES

Haşim Pihtili was graduated from Fırat University the department of Mechanical Engineering in 1986. Then he started his master science study and became research assistant in the same university. He completed his master study in 1988. He was completed PhD study in 1991 and promoted to assistant professor in 1993. He has been Associate Professor in 2015. He has taught the lectures of machine elements, composite materials and laboratory courses related to construction and manufacturing since 1988. He has numerous publications in national and international journals. Particularly, they are mainly about wear, composite materials and construction of machines. He has a chapter in the book namely Woven fabric engineering. He has also edited the book ‘Tribology in Engineering’. He is still reviewer in various journals, a member of Turkish Composites Manufacturers Association (TCMA) and he has five patent at the same time.

Comparison Between MRAS and SMO Based Sensorless Control Methods of Permanent Magnet Synchronous Motor

Çağlar Aydın^{1*} , Sencer Ünal² , Mehmet Özdemir³ 

¹Firat University, Electrical and Electronics Engineering Department, Elazığ, Turkey. (e-mail: caglaraydin217@gmail.com).

²Firat University, Electrical and Electronics Engineering Department, Elazığ, Turkey. (e-mail: sencerunal@firat.edu.tr).

³ Firat University, Electrical and Electronics Engineering Department, Elazığ, Turkey. (e-mail: mozdemir@firat.edu.tr).

ARTICLE INFO

Received: Oct., 16, 2020

Revised: May., 22, 2021

Accepted: May, 23, 2021

Keywords:

Pmsm

Mras

Smo

Sensorless

Corresponding author: Çağlar Aydın

ISSN: 2536-5010 / e-ISSN: 2536-5134

DOI: <https://doi.org/10.36222/ejt.811569>

ABSTRACT

This paper presents a comparison between sliding mode observer and model reference adaptive system based sensorless position and speed control of permanent magnet synchronous motor. In traditional sliding mode observers, signum function, which is used as switching function, causes chattering effect. To reduce chattering effect, low pass filter is used but this filter introduces a phase delay. In order to eliminate these problems, a sigmoid function is used instead of signum function in sliding mode observer based control method. In model reference adaptive system based control method, it is purposed to make error zero between the reference model and adjustable model. Popov's super stability theorem is used for the stability of model reference adaptive system control method. Both of the control methods are simulated with Matlab/Simulink.

1. INTRODUCTION

Permanent magnet synchronous motors (PMSM) are widely used in high performance applications for their advantages such as high power density, high efficiency, high torque to inertia ratio and robustness. In earlier control applications, direct current (DC) machines were used because of that flux and torque of DC machines could be controlled separately. But DC machines increase operation and maintenance cost due to the presence of commutator and brushes and they can not operate in explosive and hazard conditions due to sparking occurs at brushes. In last decades, applying vector control [1-2] and developments in power electronic devices allowed induction machines as an important alternative to the DC machines. However in comparison with induction machine, PMSM, which is another alternative current (AC) machine, has some advantages such as high power factor, high efficiency and decreased rotor losses [3-4].

In order to use PMSM with high efficiency, absolute position and speed information have to be obtained. For this purpose, position and speed sensors such as tachogenerator, resolver and encoder are generally used. Due to disadvantages of these sensors such as bigger motor size, higher cost and

complexity, sensorless control method has recently attracted an important attention.

In Fig. 1, sensorless field oriented control (FOC) is used to control the torque and magnetic flux of the motor separately. Flux and torque are controlled respectively by i_d and i_q currents. In this control, the error signal is obtained from the difference between the reference and estimated values and then the error is processed through a PI controller.

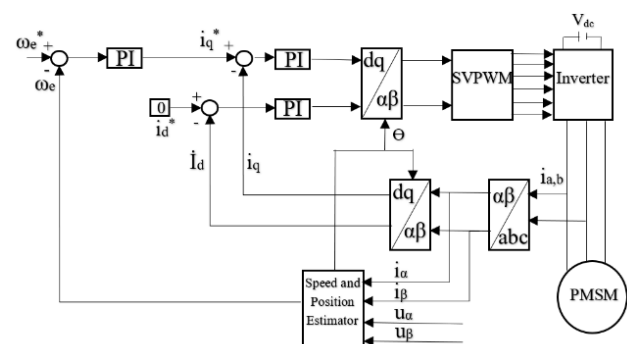


Figure 1. Block diagram of sensorless FOC of PMSM

Sensorless control methods of PMSM can be divided into two main categories:

- Model based sensorless methods
- High frequency (HF) signal injection based methods

Model based control methods require measurement of stator voltages and currents to estimate the back electromotive force (EMF) for position and speed information. Model based methods are generally used in medium and high speed operations. In these methods, position and speed information is contained by the back EMF and so in low speed operations, in which back EMF magnitude is not sufficiently large to measure, position and speed information can not measure accurately. Main techniques of the model based control methods are; sliding mode observer (SMO), model reference adaptive system (MRAS) and extended Kalman filter (EKF) [5-6].

HF signal injection methods use magnetic saliency (anisotropy) of the machine, which is a result of saturation and geometric construction, for position and speed information. In signal injection methods generally two techniques are used: high frequency signal injection method and pulse injection method. In surfaced mounted PMSM, rotor position does not change according to the stator inductances and so HF signal injection can not be used in these motors. HF signal injection methods are used in standstill and low speed operations; because in high speed operation they need very high frequency [7-9].

In this paper SMO and MRAS based control methods are compared. In order to eliminate chattering effect caused by signum switching function in SMO based control method, without using a low pass filter, a sigmoid function is used to get accurate position and speed information. Owing to sigmoid function, it has also been observed a decrease in noise and ripple of the system. In MRAS based method, PMSM itself is chosen as reference model and current model as adjustable model. Adjustable model variables are adjusted through adaption mechanism to estimate accurate position and speed information. According to results, it is observed that a decrease in the noise and ripple of the torque and speed curves.

2. MODELLING OF PMSM

d-q axis equivalent circuit models are as in Fig. 2:

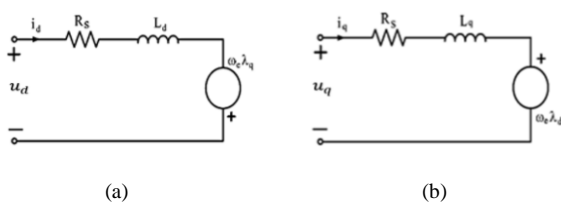


Figure 2. Equivalent circuit models of PMSM in rotor reference frame (a) d-axis and (b) q-axis

Flux equations in rotor reference frame (1), (2):

$$\lambda_q = L_q i_q \quad (1)$$

$$\lambda_d = L_d i_d + \lambda_m \quad (2)$$

Voltage equations in (3), (4):

$$u_d = R_s i_d + p \lambda_d - \omega_e \lambda_q \quad (3)$$

$$u_q = R_s i_q + p \lambda_q + \omega_e \lambda_d \quad (4)$$

In equation (3), (4); u_d and u_q are the d-q axis voltages, p is the derivative operator, i_d and i_q are the d-q axis currents, λ_d and λ_q are the d-q axis fluxes and λ_m is the permanent magnet flux.

Electromagnetic torque produced by PMSM is (5):

$$T_e = \frac{3p}{2} [\lambda_m i_q + (L_d - L_q) i_d i_q] \quad (5)$$

First part of the Eq. 5 shows the torque produced by permanent magnets and second part of the Eq. 5 shows the reluctance torque. In surfaced mounted PMSM, reluctance torque is equal to zero because d and q axis inductance have the same value. Mechanical torque is as in Eq. 6;

$$T_m = j p \omega_m + B \omega_m + T_L \quad (6)$$

In Eq. 6, ω_m is mechanical speed, j is moment of inertia and T_L is load torque.

3. SENSORLESS CONTROL METHODS OF PMSM

3.1. Sliding mode observer

Sliding mode control is a control method that changes dynamics of nonlinear systems using HF switching functions [10-11]. For estimation of speed and position information of a PMSM, sliding mode control is used as an observer. SMO is one of the back EMF based estimation methods.

Fig. 3 shows the behaviour of the system states in SMO:

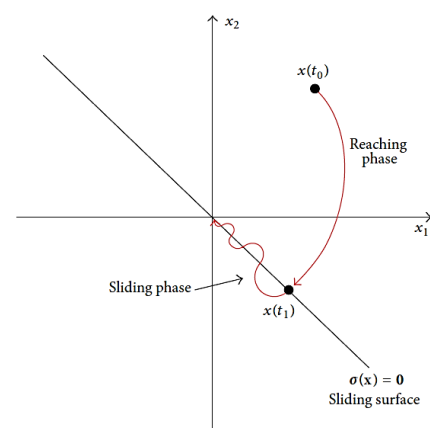


Figure 3. The behaviour of the system states in SMO [13]

Fig. 3 shows that SMO forces state variables to the sliding surface and then controls the system to maintain position of the state variables on the sliding surface. The main purpose of this control is to make the sliding surface variable ($\sigma(x)$) zero. The first step for controller is to choose a sliding surface. Then a reaching phase and a sliding phase occur. Reaching phase begins with the initial state and continues to end of the

switching state. During the reaching phase, state variables are led to sliding phase. In sliding phase state variables are hold on sliding surface and led to equilibrium point [12].

In SMO based control to reach the sliding surface, an infinite switching frequency is needed. But it is not possible to use an infinite switching frequency. This situation is called as chattering effect and causes estimation errors. Chattering effect also causes noise and oscillation in the system. To eliminate this effect, a low pass filter is used but filters cause a phase delay [14]. To keep up phase delay at minimum level, filter designing has an important effect. Another solution to eliminate chattering effect is to use a sigmoid function instead of signum function.

Current equations ($a - \beta$ coordinates) in stationary reference frame in (7), (8):

$$\frac{d}{dt} i_\alpha = -\frac{R_S}{L_S} i_\alpha + \frac{1}{L_S} u_\alpha - \frac{\lambda_m}{L_S} \omega_r \sin \theta_r \quad (7)$$

$$\frac{d}{dt} i_\beta = -\frac{R_S}{L_S} i_\beta + \frac{1}{L_S} u_\beta - \frac{\lambda_m}{L_S} \omega_r \cos \theta_r \quad (8)$$

Back EMF equations in (9), (10):

$$e_\alpha = -\lambda_m \omega_r \cos \theta_r \quad (9)$$

$$e_\beta = \lambda_m \omega_r \sin \theta_r \quad (10)$$

Using stationary reference frame equations of PMSM, Eq. (11) and (12) is obtained:

$$\frac{d}{dt} \hat{i}_\alpha = -\frac{R_S}{L_S} \hat{i}_\alpha + \frac{1}{L_S} u_\alpha - K_{sw} \frac{1}{L_S} H(\hat{i}_\alpha - i_\alpha) \quad (11)$$

$$\frac{d}{dt} \hat{i}_\beta = -\frac{R_S}{L_S} \hat{i}_\beta + \frac{1}{L_S} u_\beta - K_{sw} \frac{1}{L_S} H(\hat{i}_\beta - i_\beta) \quad (12)$$

The error between reference and estimated values is

$$\tilde{i}_s = \hat{i}_s - i_s$$

$$H(\tilde{i}_\alpha) = \left(\frac{2}{1 + \exp(-a\tilde{i}_\alpha)} \right) - 1 \quad (13)$$

$$H(\tilde{i}_\beta) = \left(\frac{2}{1 + \exp(-a\tilde{i}_\beta)} \right) - 1 \quad (14)$$

Lyupanov function is used for stability of the observer.

$$V = \frac{1}{2} (\tilde{i}_\alpha^2 + \tilde{i}_\beta^2) \quad (15)$$

$$\begin{aligned} \frac{d}{dt} V = & -\frac{R_S}{L_S} (\tilde{i}_\alpha^2 + \tilde{i}_\beta^2) + \frac{1}{L_S} (e_\alpha \tilde{i}_\alpha + e_\beta \tilde{i}_\beta \\ & - \frac{K_{sw}}{L_S} (|\tilde{i}_\alpha| + |\tilde{i}_\beta|)) \end{aligned} \quad (16)$$

When observer reached the sliding surface, estimated current values turn into reference frame. Then current equations are $\tilde{i}_\alpha = 0$ and $\tilde{i}_\beta = 0$.

$$\hat{e}_\alpha = K_{sw} H(\tilde{i}_\alpha) \quad (17)$$

$$\hat{e}_\beta = K_{sw} H(\tilde{i}_\beta) \quad (18)$$

Fig. 4 shows block diagram of SMO with sigmoid function:

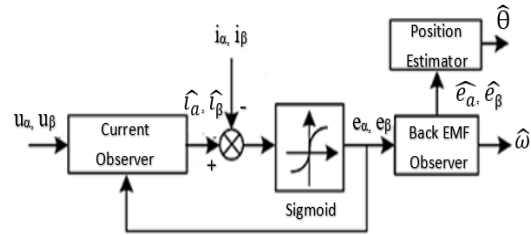


Figure 4. Block diagram of SMO with sigmoid function

In Eq. (19) rotor position:

$$\hat{\theta} = -\tan^{-1} \left(\frac{\hat{e}_\alpha}{\hat{e}_\beta} \right) \quad (19)$$

In Eq. (20) rotor speed:

$$\hat{\omega}_r = \frac{d\hat{\theta}}{dt} \quad (20)$$

Fig. 5 shows Matlab/Simulink model of SMO.

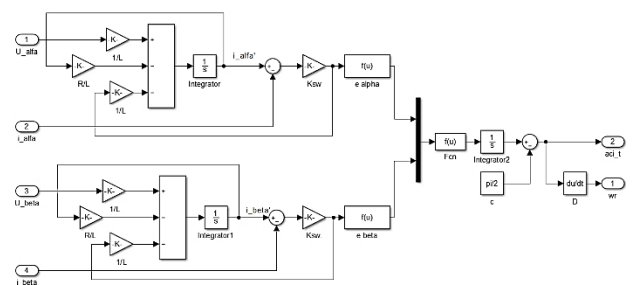


Figure 5. Matlab/Simulink model of SMO

3.2. Model reference adaptive system

MRAS is a closed loop control method to estimate position and speed of PMSM. MRAS has three main models: reference model, adjustable model and adaption mechanism. Reference model is independently of the variable and it does not contain unknown parameters. Adjustable model is dependent on variable being estimated. The adaption mechanism uses the difference between the two models to tune the estimated

variable and feed it back to the adjustable model [14]. Adaption mechanism controls adjustable model through a PI controller [15-17]. In this paper PMSM itself is chosen as reference model and current model of PMSM is chosen as adjustable model. Fig. 6 shows structure of MRAS.

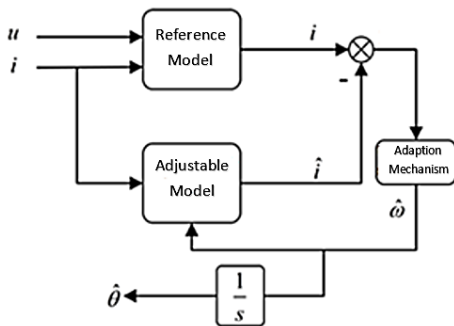


Figure 6. Structure of MRAS

According to the mathematical model of PMSM in the d-q coordinate system, the current model of the stator can be described as [17]:

$$\frac{d}{dt} \begin{bmatrix} i_d + \frac{\lambda_m}{L} \\ i_q \end{bmatrix} = \begin{bmatrix} -\frac{R_s}{L} & \omega_e \\ -\omega_e & -\frac{R_s}{L} \end{bmatrix} \begin{bmatrix} i_d + \frac{\lambda_m}{L} \\ i_q \end{bmatrix} + \frac{1}{L} \begin{bmatrix} u_d + \frac{R_s \lambda_m}{L} \\ u_q \end{bmatrix} \quad (21)$$

$$i_d^* = i_d + \frac{\lambda_m}{L}, \quad i_q^* = i_q \quad (22)$$

$$u_d^* = u_d + \frac{R_s \lambda_m}{L}, \quad u_q^* = u_q \quad (23)$$

MRAS reference model can be described:

$$\frac{d}{dt} \begin{bmatrix} i_d^* \\ i_q^* \end{bmatrix} = \begin{bmatrix} -\frac{R_s}{L} & \omega_e \\ -\omega_e & -\frac{R_s}{L} \end{bmatrix} \begin{bmatrix} i_d^* \\ i_q^* \end{bmatrix} + \frac{1}{L} \begin{bmatrix} u_d^* \\ u_q^* \end{bmatrix} \quad (24)$$

MRAS adjustable model can be described as:

$$\frac{d}{dt} \begin{bmatrix} i_d^{\wedge} \\ i_q^{\wedge} \end{bmatrix} = \begin{bmatrix} -\frac{R_s}{L} & \omega_e \\ -\omega_e & -\frac{R_s}{L} \end{bmatrix} \begin{bmatrix} i_d^{\wedge} \\ i_q^{\wedge} \end{bmatrix} + \frac{1}{L} \begin{bmatrix} u_d^* \\ u_q^* \end{bmatrix} \quad (25)$$

The error between the reference model and adjustable model can be written as: $e = i^* - i^{\wedge}$

$$pe = Ae - WI \quad (26)$$

$$v = De \quad (27)$$

$$D = I \quad \text{and then} \quad v = e \quad (28)$$

According to Popov Super Stability Theory:

- (1) Transfer matrix $H(s) = D(sI - A)^{-1}$ must be positive real matrix,
- (2) $\int_0^{t_0} v^T W dt \geq -\gamma_0^2, \quad \forall t_0 \geq 0, \quad \gamma_0^2 > 0$ is any finite positive number.

Then, $\lim_{t \rightarrow \infty} e(t) = 0$, the MRAS is asymptotically stable.

$\hat{\omega}$ can be obtained as:

$$\hat{\omega} = \int_0^{t_0} k_1 (i_d^* i_q^{\wedge} - i_q^* i_d^{\wedge}) dt + k_2 (i_d^* i_q^{\wedge} - i_q^* i_d^{\wedge}) + \hat{\omega}(0) \quad (29)$$

When k_1 and $k_2 \geq 0$:

$$\hat{\omega} = k_1 \int_0^{t_0} [i_d^* i_q^{\wedge} - i_q^* i_d^{\wedge} - \frac{\lambda_f}{L} (i_q^* - i_q^{\wedge})] dt + k_2 [i_d^* i_q^{\wedge} - i_q^* i_d^{\wedge} - \frac{\lambda_f}{L} (i_q^* - i_q^{\wedge})] + \hat{\omega}(0) \quad (30)$$

Rotor position is defined as integral of speed (Eq. 31):

$$\theta_e = \int_0^{t_0} \hat{\omega} dt \quad (31)$$

Fig. 7 shows Simulink model of adjustable model:

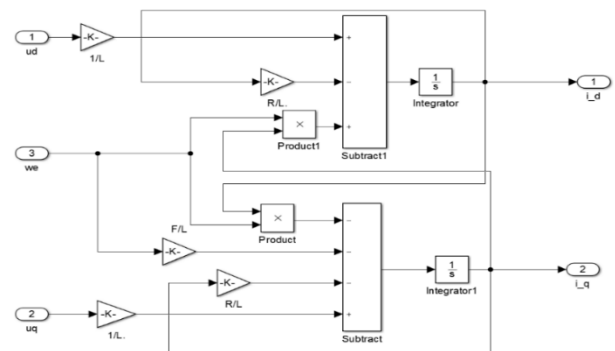


Figure 7. Adjustable Model

Fig. 8 shows Simulink model of adaption mechanism:

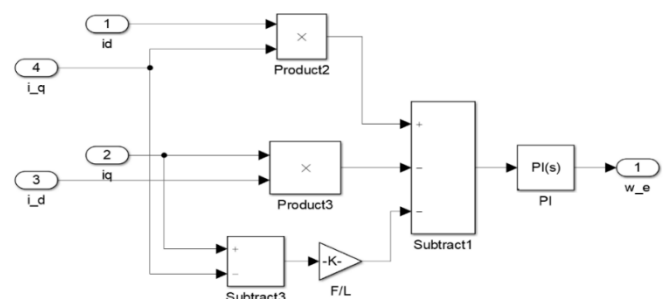


Figure 8. Adaption Mechanism

4. SIMULATION RESULTS

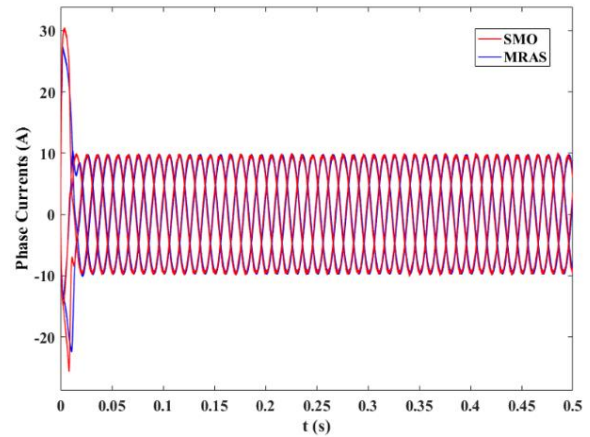
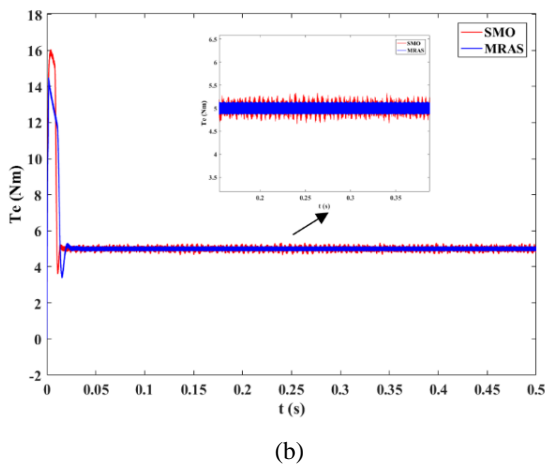
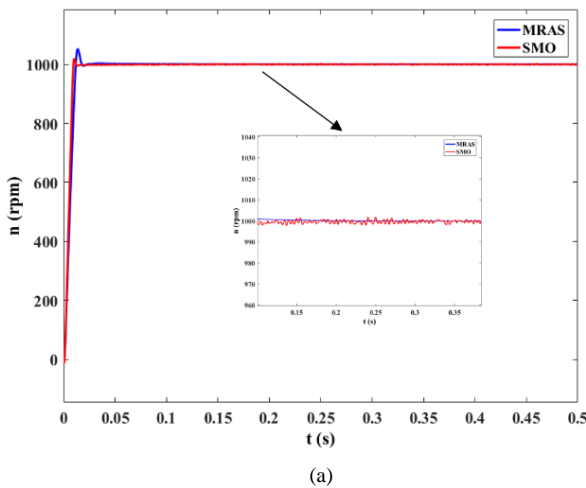
Table 1 shows simulation parameters of the PMSM model:

TABLE I

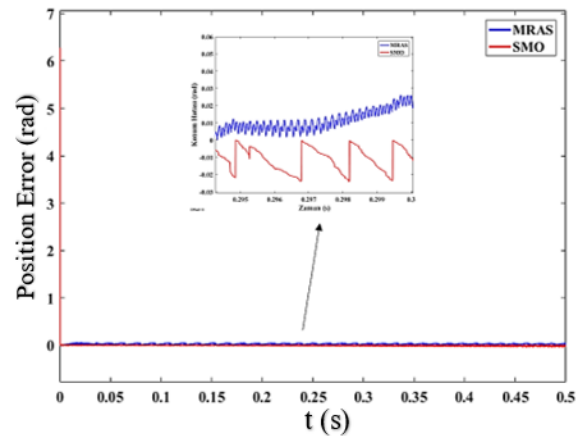
PARAMETERS	VALUES
Stator resistance (R_s)	2.8175 Ω
Pole Pairs (p)	2
d-axis inductance (L_d)	0.0085 H
q-axis inductance (L_q)	0.0085 H
Rotor flux linkage (λ_m)	0.175 Wb
Moment of inertia (J)	0.0008 kgm^2

PARAMETERS of PMSM

In Fig. 9, reference speed is 1000 rpm and load torque is 5 Nm for 0-0,5 s and it is shown that speed, torque, phase currents and position error simulation results of SMO and MRAS based models and their comparison.



(c)

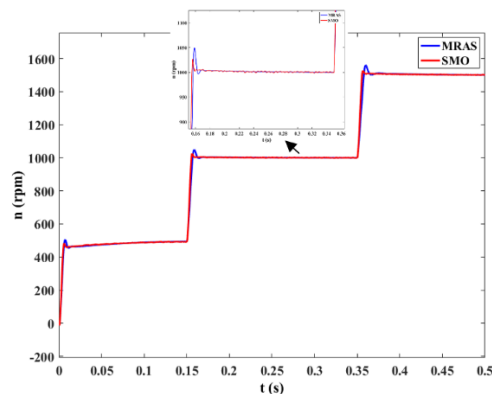


(d)

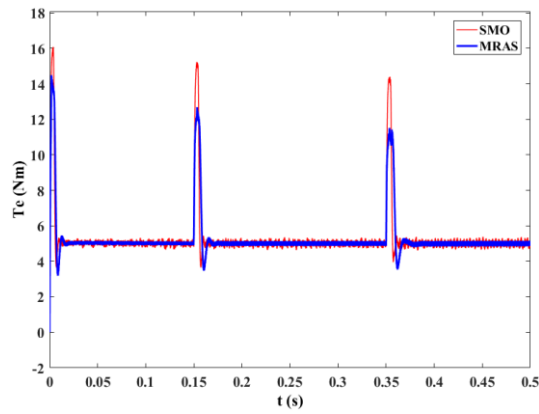
Figure 9. Speed, torque, phase currents and position error graphics of PMSM for 1000 rpm and 5 Nm

In Fig. 9.a, MRAS based control method speed response has 5% overshoot and 0.03 s settling time while SMO based control method has 2% overshoot and 0.09 s settling time. In Fig 9.d, position error in MRAS based control is 0.039 rad while in SMO based is 0.035 rad.

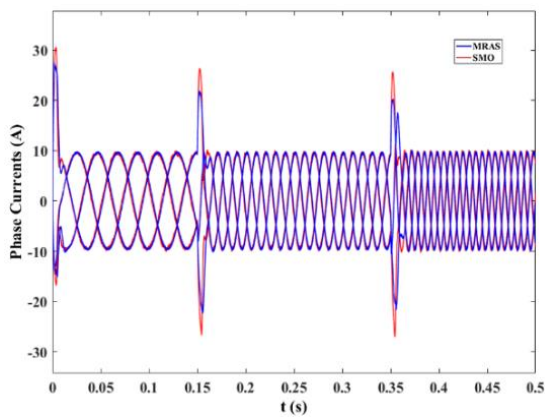
In Fig. 10 shows the speed of PMSM as the reference is changed 500-1000-1500 rpm at 0-0.15-0.35 s and load torque is 5 Nm at 0-0,5 s. In Fig. 10, it is shown that speed, torque, phase currents and position error simulation results of SMO and MRAS based models and their comparison.



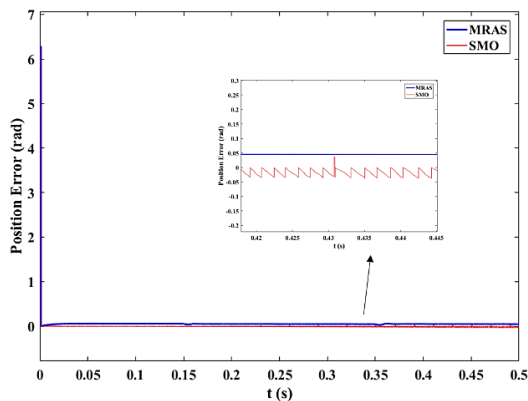
(a)



(b)



(c)

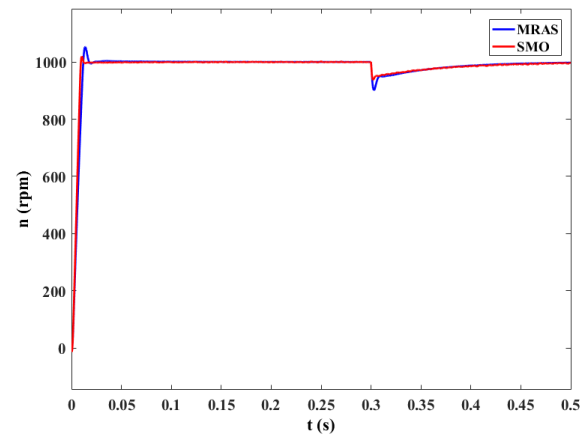


(d)

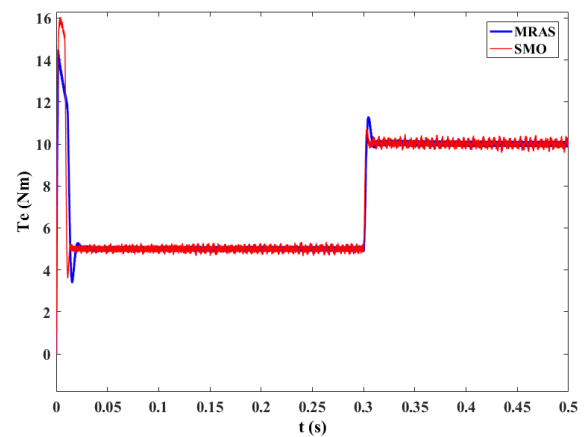
Figure 10. Speed, torque, phase currents and position error graphics of PMSM for 500-1000-1500 rpm and 5 Nm

In Fig. 10.a, when speed is increased from 500 rpm to 1000 rpm at 0.15 s, MRAS based control method speed response has 5% overshoot and SMO based control method has 3% overshoot. In Fig. 10.a and b, it is shown that in speed and torque curves SMO based model has more ripple than MRAS based model. As can be seen in Fig. 10.c, initial phase currents' values of MRAS is smaller than SMO. In Fig 10.d, position error in MRAS based control is 0.045 rad while in SMO based is 0.035 rad. SMO based model achieves fast response to load and speed variations but its settling time is more than MRAS model.

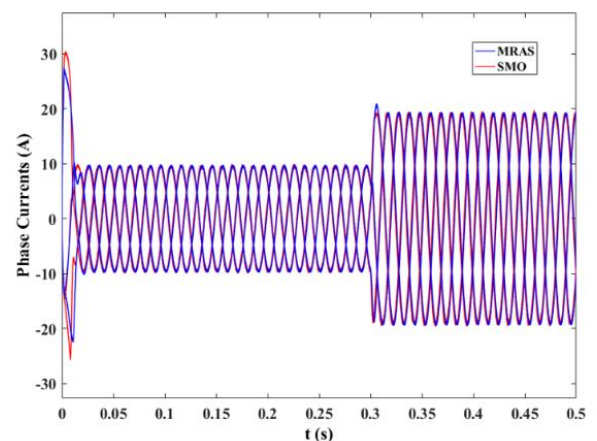
In Fig. 11, reference speed is 1000 rpm and load torque is increased from 5 to 10 Nm at 0.3 s. In Fig. 11, it is shown that speed, torque, phase currents and position error simulation results of SMO and MRAS based models and their comparison.



(a)



(b)



(c)

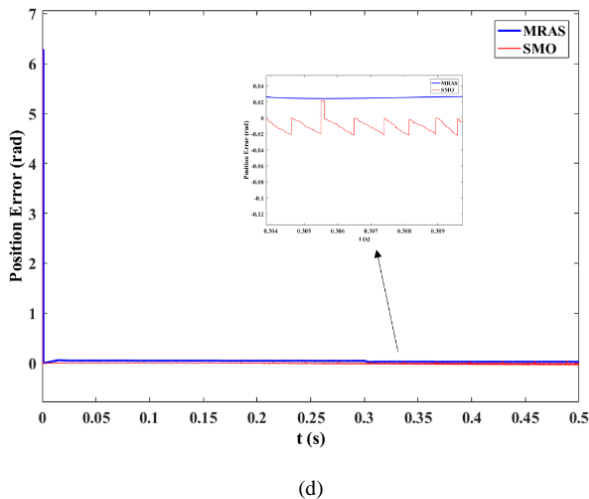


Figure 11. Speed, torque, phase currents and position error graphics of PMSM for 1000 rpm and 5-10 Nm

In Fig. 11.a, MRAS based control method speed response has 5% overshoot and 0.03 s settling time while SMO based control method has 3% overshoot and 0.09 s settling time. In Fig 11.d, position error in MRAS based control is 0.025 rad while in SMO based is 0.02 rad.

5. CONCLUSION

This paper presents a comparison between sensorless FOC of PMSM based on MRAS and SMO methods. Both of the models are able to track the reference values in different speed and load torque operations. But results show that MRAS based method has better dynamic response and higher performance. According to the simulation results in Fig 9.b, 9.c, 10.b, 10.c, 11.b and 11.c, it is observed that initial torque and current values in MRAS based model less than SMO based model. In Fig 9.a, 9.b, 10.a, 10.b, 11.a and 11.b, simulation results also proved that MRAS based model has better performance in terms of settling time and noise than that of SMO based model. As a result, the system is more stable and has less oscillation with the MRAS based method.

REFERENCES

- [1] Blaschke, F., The principle of field-orientation as applied to the transvector closed loop control system for rotating-field machines:Siemens Rev. , vol.34, no.1, pp. 217-220, 1972.
- [2] Pillay, P., Krishnan, R., Modelling, simulation and analysis of permanent magnet motor drives. I. The permanent magnet synchronous motor drive, IEEE Trans. Industry applications, v.40, no.3, pp.265-273, 1989.
- [3] Vas, P., Sensorless vector and direct torque control, Oxford University Press, pp.768., 1998.
- [4] Rahman, M. A. and Slemon, G.R., Promising Applications of NdBFe Iron Magnets in Electrical Machines (Invited), IEEE Trans. On Magnetics, Vol. MAG-21, No. 5., 1985.
- [5] Bojoi, R., Pastorelli, M., Bottomley, J., Giangrande, P., Gerada, C., Sensorless control of PM motor drives - A technology status review, Proc. - 2013 IEEE Work. Electr. Mach. Des. Control Diagnosis, WEMDCD , pp. 168–182., 2013
- [6] Briz, F., Degner, M. W., García, P., and Lorenz, R. D., Comparison of saliency-based sensorless control techniques for AC machines, IEEE Trans. Ind. Appl., vol. 40, no. 4, pp. 1107–1115., 2004.

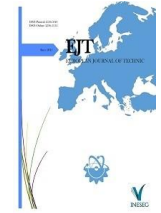
- [7] Yongdong, L., Hao, Z., Sensorless control of permanent magnet synchronous motor - A survey, IEEE Veh. Power Propuls. Conf. VPPC.,2008.
- [8] Holtz, J. Methods for speed sensorless control of AC drives, University of Wuppertal, Germany., 1996.
- [9] Schrödl, M., Sensorless control of AC machines at low speed and standstill based on ‘INFORM’ method, IEEE Industry Applications Conference, IAS’96, vol. 1., 1996.
- [10] Utkin, V., Sliding mode control design principles and applications to electric drive, IEEE Transactions On Industrial Electronics, Vol. 40, No.1., 1993.
- [11] Drakunov, S., Utkin, V., Sliding mode observers tutorial, IEEE, Proceedings of the 34th conference on decision & control, New Orleans., 1995.
- [12] Kılıç, F., Model-free adaptive gain higher order sliding mode speed control of permanent magnet synchronous motor, Ph.D. Thesis, Kocaeli University, Applied Sciences Institutes., 2016.
- [13] Yang, I., Lee, D., Han, D., Designing A Robust Nonlinear Dynamic Inversion Controller for Spacecraft Formation Flying, Mathematical Problems in Engineering Volume., 2014.
- [14] Westin, I., Sensorless Control of a PMSM, MSc. Thesis, KTH Royal Institute of Technology School, Sweden., 2016.
- [15] Kojabadi, H. M. , Ghribi, M., () MRAS-based adaptive speed estimator in PMSM drives, Int. Work. Adv. Motion Control. AMC, no. 1, pp. 569–572, 2006.
- [16] Dursun, M., New model adaptive system design for sensorless speed control of PMSM, Publications Prepared for the Innovations on Intelligent Systems and Applications Symposium ASYU, Sigma J Eng & Nat Sci 8 (2), 117-127., 2017
- [17] Li, W. H. , Chen, Z. Y. , Cao, W. P., Simulation research on optimization of permanent magnet synchronous motor sensorless vector control based on MRAS, Int. Conf. Wavelet Act. Media Technol. Inf. Process. ICWAMTIP, pp. 350–355., 2012.

BIOGRAPHIES

Çağlar Aydın obtained his BSc degree in electrical-electronics engineering from Ondokuz Mayıs University in 2015. He received the MSc. degree in electrical-electronics engineering from the Firat University in 2020. Currently, he is a PhD student at the Department of Electrical-Electronics Engineering of Firat University. His research interests are electrical machines and drive systems.

Şencer Ünal obtained his BSc degree in electrical-electronics engineering from Firat University in 1999. He received the MSc., and PhD. degrees in electrical-electronics engineering from the Firat University in 2002 and 2009, respectively. He is currently Assistant Professor in Electrical and Electronics Engineering Department of Firat University. His research interests are electrical machines, drive systems and power electronics.

Mehmet Özdemir was born in 1958 in Elazığ, Turkey. He obtained his BSc degree in electrical-electronics engineering in 1980. Then he received MSc. and PhD. degrees in Electrical Engineering from Firat University in 1984 and 1993, respectively. He is currently Associate Professor in Electrical and Electronics Engineering Department of Firat University. His research interests are electrical machines and drives.



Numerical Investigation of Fatigue Behaviors of Non-Patched and Patched Aluminum Pipes

Hamit Adin^{1*}, Bilal Yıldız², Mehmet Şükrü Adin³

^{1*}Batman University, Department of Mechanical Engineering, Batman, Turkey. (e-mail: hamit.adin@batman.edu.tr).

² Batman University, Department of Mechanical Engineering, Batman, Turkey. (e-mail: bilyildiz@hotmail.com.tr).

³ Batman University, Department of Mechanical Engineering, Batman, Turkey. (e-mail: mehmet sukru.adin@batman.edu.tr).

ARTICLE INFO

Received: March., 08. 2021

Revised: April., 04. 2021

Accepted: May, 20. 2021

Keywords:

Aluminum

Composite

Patch

Fatigue

Ansys

Corresponding author: Hamit Adin

ISSN: 2536-5010 | e-ISSN: 2536-5134

DOI: <https://doi.org/10.36222/ejt.893327>

ABSTRACT

In this study, the fatigue behaviors of non-patched and patched aluminum pipes were investigated numerically. The Finite Element Method was used for fatigue analysis in the study. Finite Element Method was implemented with Ansys Workbench (15.0) program. Al 6063 type aluminum pipe, DP-460 type adhesive and [0/90]2 reinforced angled glass-epoxy composite patch material were used in the analyzes. As a result of the numerical study, it was observed that patch size is an effective parameter in fatigue strength and that quarter-circle and semi-circular composite patches increase the fatigue life. It was also observed in the analyzes that the quarter-circle patched aluminum pipes achieved higher fatigue strength.

1. INTRODUCTION

The development of materials science has been a very important factor in the progress of technology in the process of history. For this reason, material science needs to be developed for the development of humanity. These two phenomena make up an inseparable whole. Developing materials science offers us solutions that are different, simple, practical, reliable and bring significant cost advantages for businesses when today's conditions are considered. These developments in material science provide cost advantages in the field of industry as well. Nowadays, instead of replacing damaged parts, it is generally preferred to carry out repairs to avoid time and money loss. In choosing repair methods, it is aimed to minimize time and cost. Particularly in tearing and cracking, patching method is preferred by using adhesive [1-6]. Therefore, there is no need for repair with mechanical connection forms such as screws, rivets, and welding. With this method, the destructive damages that may occur in the material can be prevented. In the literature, it is possible to find many studies on patching using adhesives. Some of these studies are presented below:

Lee et al. investigated the effect of different geometric shapes (rectangular, triangular, inverted triangular and parallelogram) on bonding strength [7]. In the study, consistent with the numerical results, they obtained the highest bonding

strength in the inverted triangular patch. Gavgali et al. experimentally and numerically investigated the fatigue and static strengths of single-lap and three-step-lap joints, which were subjected to tensile and four-point bending tests [8]. In the study, they stated that the change in the geometry of the area where the bonding was made had a profound effect on both fatigue and fracture behavior of the joint. Sahin et al. investigated lifetimes of single-lap joints of five different adherend thicknesses obtained using AA2024-T3 aluminum alloy and DP460 structural adhesive under varying tensile fatigue loads [1]. In the study, they stated that the static tensile strength of the joints increased due to the increase in adhesion thickness. Karaman numerically investigated the behavior of double-sided lap joint of AA-5083 aluminum sheets with elliptical holes under bending load [9]. In the analysis, the bending damage loads of the samples were found. From the results, it was revealed that the patched samples carried a higher loads. Erkek experimentally investigated the effects of thermal aging on the buckling behavior of composite sheets repaired with a patch using adhesive from the outer part. In the study, it was observed that temperature and adhesive thickness variations affect the buckling load [10]. Ergün examined AA-5083 aluminum sheets with elliptical holes and glass fiber reinforced composite patches by joining them with DP-460 type adhesive. In the study, experimental and numerical results were found to be close to each other [11]. Adin et al. bonded

the composite material with AA-5083 aluminum material using DP-460 adhesive and examined the tensile strength. As a result of their studies, they stated that lap width and patch width are important [12]. Canbolat examined the repair of aluminum sheets by composite patches in case of damage. In the study, it was observed that damage loads and damage mechanisms converged experimentally and numerically [13]. Zarrinzadeh et al. investigated experimentally and numerically the effects of fatigue on crack growth in a cylindrical aluminum pipe with cracks. In the study, they stated that they approached the realistic behavior of the structure [14]. In another study, Zarrinzadeh et al. examined the fatigue life after patching on a cylindrical cracked aluminum pipe. Different from previous works, glass-epoxy composite material was used as patch material. In addition, they investigated the effect of patch length on fatigue life. As a result of the study, they found a directly proportional relationship between the increase in the number of layers and the fatigue life, and an inversely proportional relationship between the patch length and the fatigue life [15]. Liu et al. investigated the change in fatigue life as a result of patching the cylindrical cracked aluminum pipe with composite material. As a result of the study, they determined that there is a directly proportional relationship between the number of layers of the composite material and their fatigue life [16]. During the use of pipes, damages occur in the form of small cracks due to various internal and external effects [16-18]. In general, cutting out the damaged area and changing it with a new one causes loss of money and time. In this study, aluminum pipes with various cracks were repaired with patches made of glass-epoxy composite material. Later, the draft-pressure fatigue behavior of the patched pipes produced in this way was investigated by the finite element method. On the basis of the studies in the literature, the purpose of the research is to find the effect of the patch on the fatigue life of the structure. Studies in the literature investigate how fatigue life is affected after patching [19]. Although they used different parameters and materials, almost all of them obtained findings on the positive effects of the patch presence.

The tubular Al 6063 aluminum used in our study is a frequently preferred material in the industry. In case of damage of this material, its fatigue behavior was investigated after repair with a composite patch.

2. MATERIAL AND METHOD

In our study, numerical fatigue analyzes were performed using the Finite Element Method. Numerical analyzes were performed using the Ansys Workbench (15.0) finite element package program. In the analyzes, Al 6063 type aluminum pipe base material, [0/90]₂ reinforced angle glass-epoxy patch and DP-460 industrial adhesive were used. In the analyzes, tensile-compression load was applied to the samples, and fatigue was achieved. Samples were modeled in three dimensions. The mechanical properties of Al 6063 type Aluminum pipe, [0/90]₂ reinforced glass-epoxy composite material and DP-460 type industrial adhesive materials used in the analyzes are given in Table 1, Table 2 and Table 3 [11, 20].

TABLE 1

MECHANICAL PROPERTIES OF AL 6063 TYPE ALUMINUM PIPE

Elasticity module	69000 MPa
Poisson ratio	0.33
Tensile strength	150 MPa
Yield strength	90 MPa

TABLE 2

MECHANICAL PROPERTIES OF [0/90]₂ REINFORCED ANGLE GLASS-EPOXY COMPOSITE PATCH

E_1	47902 MPa
$E_2 = E_3$	20395.25 MPa
$G_{12} = G_{13} = G_{23}$	4941 MPa
ν_{12}	0.253
$\nu_{13} = \nu_{23}$	0.106

TABLE 3

MECHANICAL PROPERTIES OF DP-460 TYPE INDUSTRIAL ADHESIVE

Elasticity Module	2077.1 MPa
Poisson's ratio	0.38
Tensile strength	44.616 MPa
Adhesive thickness	0.25 mm
Shear stress	23.99 MPa
Shear strength	33.35 MPa
Shear module	560 MPa

The dimensions of the aluminum pipe used in the study are given in Fig. 1. All dimensions selected in the modeling of pipe samples were determined by considering the industrial uses of aluminum pipes. As seen in Fig. 1, the large diameter (D) of the aluminum pipe is 90 mm, the small diameter (d) is 86 mm, the length is 250 mm, and the pipe thickness is 2 mm. Cracked damaged pipes were examined in the analyzes [21]. The crack lengths in the pipes were taken as 1, 3, 5, 7 and 10 mm. The cracks occurred in the middle of the length of the pipe and perpendicular to the direction where the draft-compression loads were applied. Damaged pipe with a crack length of 10 mm is shown as an example in Fig. 1.

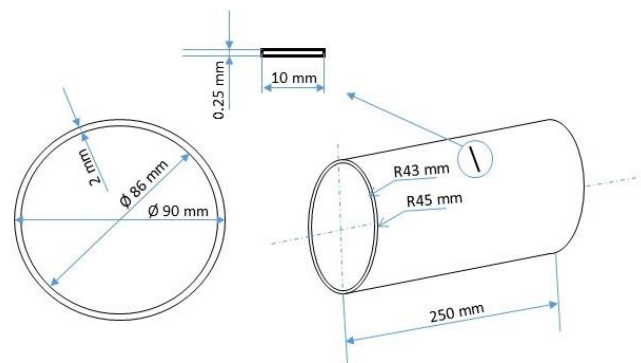


Figure 1. Dimensions of damaged Al 6063 aluminum pipe.

In our study, the repair process was carried out using quarter and semi-circular glass-epoxy patches. The dimensions of the patches used in the repair are shown in Fig. 2a and b. The

length of the glass-epoxy patch material is 50 mm and its thickness is 0.4 mm.

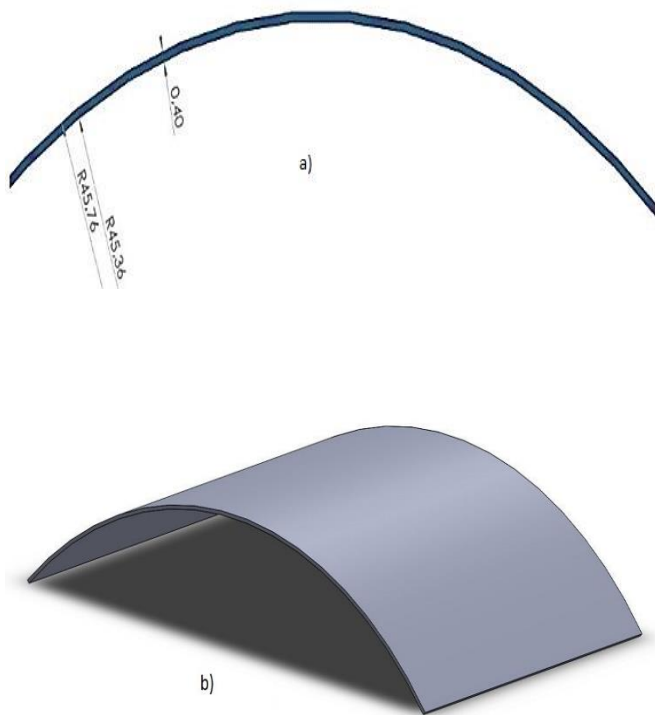


Figure 2. [0/90]₂ reinforced angle glass-epoxy patch; a) front view b) isometric view (Unit: mm).

Analyzes were carried out in three parts as non-patched, quarter-circular and semi-circular patched. In the analyzes, the patches were positioned at the center of the pipe based on the center of the crack zone. Fiber orientation and reinforcement angles of the patches are given in Fig. 3.

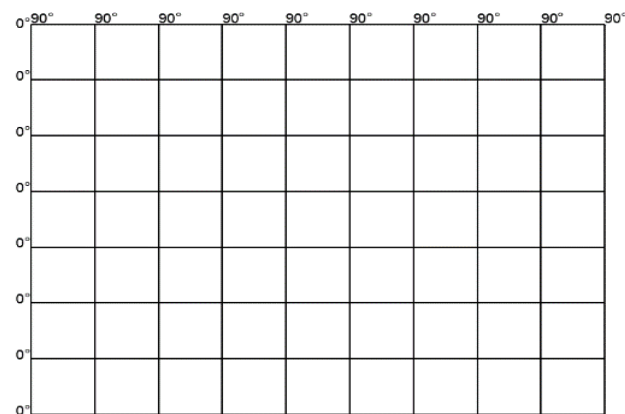


Figure 3. Fiber orientation angles of glass-epoxy composite patches.

2.1. Fatigue analysis

In numerical analyzes, all three-dimensional models were made in the SolidWorks program according to the measurements given in Fig.1, and then finite element analyzes were made in the Ansys Workbench program [22]. Aluminum pipes are modeled as non-patched, quarter-circular and semi-circular composite patches. In addition, in case of three

different patches for each crack length, a total of 15 different modelings was performed using the mechanical values given in Table 1, Table 2 and Table 3, and then numerical analyzes were carried out. In analysis, elasticity module, shear stress and poisson's ratio were introduced to the system respectively, and mesh operation was performed by selecting the mesh structure [23-28]. Then, fatigue analyzes of patched and non-patched pipes were carried out according to five different crack parameters. Fatigue analyzes were performed as tensile-compression [29-34]. When the analysis models were created, one side was accepted as a fixed support, as seen in Fig. 4, and 40.5 MPa, which is 45 percent of the yield strength of Al 6063 Aluminum pipe, was used. All analyzes were made in the case of quarter-circular and semi-circular composite patches with the same pipe sizes, five different crack lengths and two different geometric shapes. In addition, in order to measure the gain, analyzes were made in the non-patched form of the aluminum pipe and a total of 15 different analyzes were carried out. The mesh (mesh structure), which should be used in the finite element separation process, contains a special place that significantly increases the accuracy of the analysis results [35, 36]. Again, taking into account the studies in the literature, 0.25 mm for DP-460 and 1 size for Al 6063 and Glass - epoxy were selected. Other details of the mesh process are like this; three different face-sizing modules for three different materials were added to the Ansys Workbench feature tree section. After selecting individual element sizes and models, the Triangle Surface Mesher method was selected and the program was run.

TABLE 4
NUMBER OF NODE AND ELEMENT

Pipe	Crack length (mm)	Number of nodes	Number of elements
Non-patched	1	1.193.979	651.523
	3	1.198.924	655.243
	5	1.199.661	655.753
	7	1.199.149	655.502
	10	1.199.588	655.129
Quarter-circular patched	1	1.217.890	655.051
	3	1.222.835	658.771
	5	1.225.504	660.683
	7	1.223.090	659.052
Semi-circular patched	10	1.223.499	658.657
	1	1.235.435	657.583
	3	1.240.380	661.303
	5	1.241.117	661.813
	7	1.240.605	661.562
	10	1.241.044	661.189

After the meshing process, data on the nodes and number of elements belonging to different samples divided into finite elements are given in Table 4.

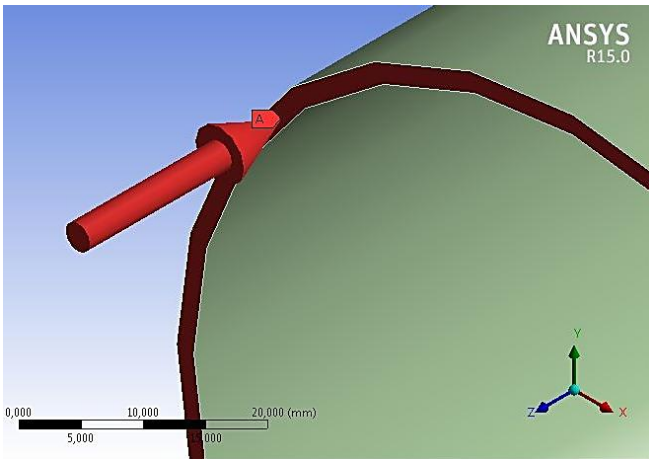


Figure 4. Representation of the 40.5MPa force applied to the analyzed sample.

3. FINDINGS AND DISCUSSION

After repair of aluminum pipes with different crack lengths Non-patched, quarter and semi-circular composite patched, the fatigue life is shown in Table 5 depending on the crack length. Here, N symbolizes the number of cycles.

TABLE 5
FATIGUE LIFES

Crack length (mm)	Non-patched Fatigue Life (N)	Quarter-circular patched Fatigue Life (N)	Semi-circular patched Fatigue Life (N)
1	11333	15365	14746
3	1704	4872	4807
5	1502	6735	5333
7	993	4307	2543
10	521	2944	2337

In the fatigue life calculation of the aluminum pipe made non-patched in Fig. 5a, it can be seen that the fatigue life decreased from 11333 cycles to 521 cycles during the progression of crack length from 1 mm to 10 mm. It was determined that this decrease is due to the crack length. In addition, it was observed from Fig. 5b and Fig. 5c that quarter and semi-circular composite patched aluminum pipes decreased their fatigue life due to the progress of the crack length. In the studies of Zarate and other researchers, the subject of research is the effect of the structure of the patch on the fatigue life [19]. However, it was seen from this study that the shape of the patch is also important.

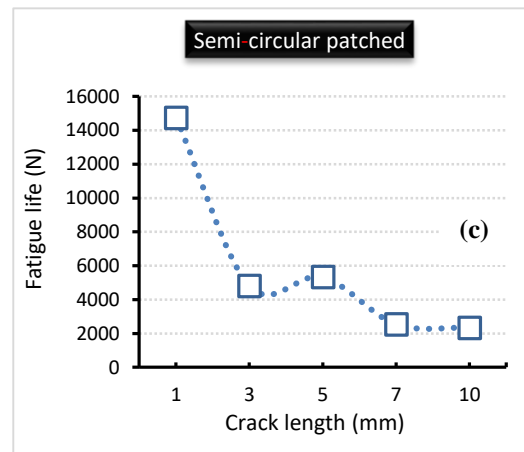
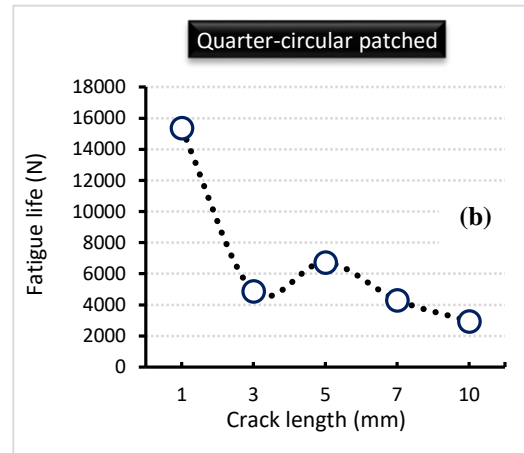
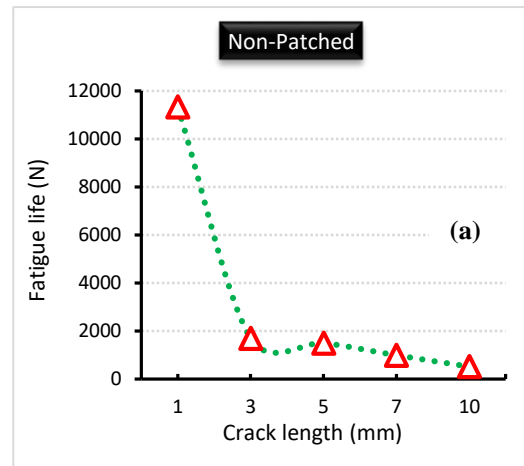


Figure 5. The fatigue lives of (a) non-patched, (b) quarter-circular and (c) semi-circular composite patched aluminum pipes.

Furthermore, it is seen from the comparison of all three cases in Fig. 6 that the fatigue life of the quarter-circular composite patch applied aluminum pipe has a better fatigue life than the semi-circular composite patch applied aluminum pipe. It is thought that the fatigue life increases of the patched specimens with 5 mm long cracks in Figure 5b and c are due to reaching the optimum point.

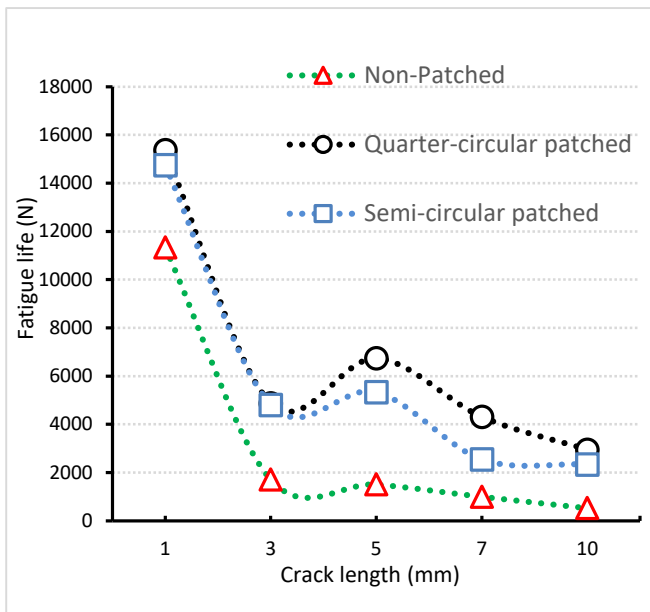


Figure 6. Comparison of fatigue lives of aluminum pipes according to patch shape

When Fig. 5b, c and Fig. 6 are examined, the effect of the patch on fatigue life can clearly be seen. Here, it was found that there is an inversely proportional relationship between the highest fatigue life and crack length. In other words, it was observed that the highest fatigue life was realized in samples with a crack length of 1 mm. When the fatigue life was examined according to the patch condition, the highest cycle number was obtained in the samples patched in quarter-circular form. The findings obtained about the fatigue life of different crack lengths as a result of patch repair and patch repair process seen in Fig. 6, formed by examining Table 5 with the cycle numbers, constitute the first step of the study. The second stage is on the efficiency of the repair process. In order to measure the efficiency, the differences between the fatigue life of the patched and non-patched samples are shown in Table 6 as % ratios. As seen in Table 6, it was determined that the fatigue life increases as a result of repairing the cracked pipe damage with a patch. Here, it was observed that the highest increase in life was in the quarter-circular patched pipe with 10 mm cracks and the increase rate was 565%.

TABLE 6

DIFFERENCES BETWEEN THE FATIGUE LIVES OF THE PATCHED AND NON-PATCHED SAMPLES

Crack length (mm)	Difference in fatigue life of non-patched and quarter-circular patched pipes (%)	Difference in fatigue life of non-patched and semi-circular patched pipes (%)
1	136	130
3	286	282
5	448	355
7	434	256
10	565	449

Fatigue life increase of quarter and semi-circular patched samples compared to non-patched ones are given in Fig. 7. The increases are given as percentages.

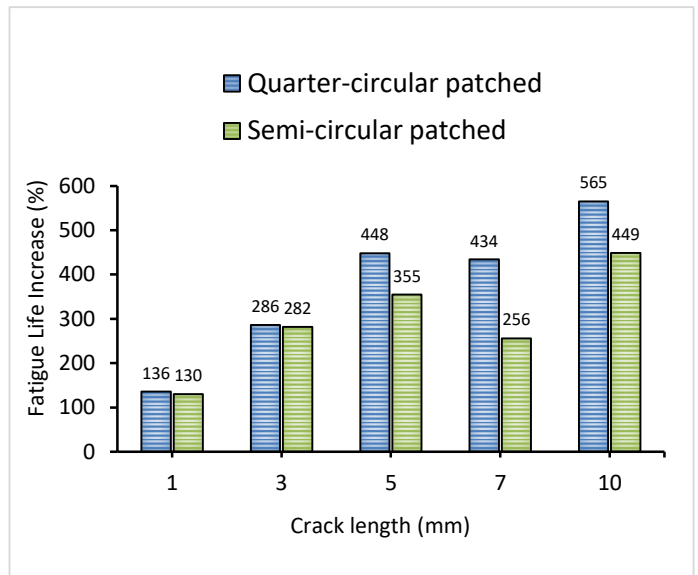


Figure 7. Comparison of the fatigue lives of non-patched and patched samples

As seen in Fig. 7, there is an inverse proportion between fatigue life and crack length. In this comparison, it was seen that the greatest contribution was achieved when the crack length was 10 mm. The reason for this contribution is that the patch coverage area varies. When all the results are examined, it is seen that there is a positive contribution of the patching process to the fatigue life. In addition, it was observed that the fatigue life of the quarter-circular patched pipes was higher than the semi-circular patched pipes.

4. CONCLUSION AND RECOMMENDATIONS

In this study, numerical damage analysis was carried out on non-patched or patched, assuming that 1, 3, 5, 7 and 10 mm long and 0.25 mm high cracks were formed in the center of Al 6063 type aluminum pipes. The patch material used in the study is [0/90]₂ reinforced angled glass-epoxy composite and the adhesive is DP-460. Ansys Workbench (15.0), which is a Finite Element Analysis program, was used in numerical analysis. The following conclusions were drawn from the data obtained on fatigue, stress and deformation.

As a result of patching the samples, it was observed that the fatigue lives increases. The most important point to be considered here is that the patch effect increases with the increase in the length of the crack. Increased fatigue life showed that it is possible to reuse the damaged pipe by patching. Considering the usage areas and costs of aluminum pipes, it is understood that it is more appropriate to patch them instead of replacing the damaged ones. For this reason, the use of pipes repaired with glass-epoxy composite patch will benefit both manufacturers and the national economy. In addition, if the cover area of the patch is patched with an area larger than the quarter-circular form, the patched pipe will have the highest fatigue strength.

REFERENCES

- [1] R. Sahin and S. Akpınar, "The Effects of Adherend Thickness on the Fatigue Strength of Adhesively Bonded Single-Lap Joints," *Int J Adhes Adhes*, p. 102845, 2021.
- [2] S. Bayramoğlu, S. Akpınar, and A. Çalık, "Numerical analysis of elasto-plastic adhesively single step lap joints with cohesive zone models and its experimental verification," *J Mech Sci Technol*, vol. 35, no. 2, pp. 641-649, 2021.
- [3] İ. Saraç, H. Adin, and Ş. Temiz, "A research on the fatigue strength of the single-lap joint joints bonded with nanoparticle-reinforced adhesive," *Weld World*, pp. 1-8, 2021.
- [4] İ. Saraç, H. Adin, and Ş. Temiz, "Experimental determination of the static and fatigue strength of the adhesive joints bonded by epoxy adhesive including different particles," *Composites Part B: Engineering*, vol. 155, pp. 92-103, 2018.
- [5] R. K. Ergün, H. Adin, A. Şişman, and Ş. Temiz, "Repair of an aluminum plate with an elliptical hole using a composite patch," *Mater Test*, vol. 60, no. 11, pp. 1104-1110, 2018.
- [6] Ü. Kurtkan and H. Adin, "The investigation of the tensile behaviors of single L-joint type bonded with adhesive and rivet: Untersuchung der Zugeigenschaften von durch Kleben und Nieten gefügten Einzel-L-Verbindungen," *Materialwiss Werkst*, vol. 49, no. 8, pp. 963-977, 2018.
- [7] H. Lee, S. Seon, S. Park, R. Walallawita, and K. Lee, "Effect of the geometric shapes of repair patches on bonding strength," *The Journal of Adhesion*, vol. 97, no. 3, pp. 207-224, 2021.
- [8] E. Gavgali, R. Sahin, and S. Akpınar, "An investigation of the fatigue performance of adhesively bonded step-lap joints: An experimental and numerical analysis," *Int J Adhes Adhes*, vol. 104, p. 102736, 2021.
- [9] Y. Karaman, "Numerical Investigation of Effect of Bending Behavior On Aluminum Plates With Elliptical Holes Patched By Sticking A Composite Patches," Master thesis, University of Batman, Batman, Turkey, 2017.
- [10] B. Erkek, "Investigation of the Effects of Thermal Aging on the Buckling Behavior of Composite Sheets Repaired Using Patches and Adhesives.," Master thesis, Dicle University, Diyarbakir, Turkey, 2018.
- [11] R. K. Ergün, "Experimental and Numerical Investigation of the Effect of Repairing Elliptical Perforated Aluminum Sheets with Composite Patch on Stress Behavior.," Master's thesis, Kahramanmaraş Sutcu Imam University, Kahramanmaraş, Turkey, 2014.
- [12] M. Ş. Adin and E. Kılıçkap, "Strength of double-reinforced adhesive joints," *Mater Test*, vol. 63, no. 2, pp. 176-181, 2021.
- [13] C. Canbolat, "Repair of 2024 Al plates with Glass-Fiber composite patch.," Master thesis, Kahramanmaraş Sutcu Imam University, Kahramanmaraş, Turkey, 2018.
- [14] H. Zarrinzadeh, M. Z. Kabir, and A. Deylami, "Experimental and numerical fatigue crack growth of an aluminium pipe repaired by composite patch," *Eng Struct*, vol. 133, pp. 24-32, 2017.
- [15] H. Zarrinzadeh, M. Z. Kabir, and A. Deylami, "Crack growth and debonding analysis of an aluminum pipe repaired by composite patch under fatigue loading," *Thin Wall Struct*, vol. 112, pp. 140-148, 2017.
- [16] J. C. Liu, M. J. Qin, Q. L. Zhao, L. Chen, P. F. Liu, and J. G. Gao, "Fatigue performances of the cracked aluminum-alloy pipe repaired with a shaped CFRP patch," *Thin Wall Struct*, vol. 111, pp. 155-164, 2017.
- [17] C. Lam, J. Cheng, and C. Yam, "Finite element study of cracked steel circular tube repaired by FRP patching," *Procedia engineering*, vol. 14, pp. 1106-1113, 2011.
- [18] T. E. Özdemir, "Short Fatigue Cracks Occurring in Welded Steel Constructions.," Master thesis, Celal Bayar University, Manisa, Turkey, 2009.
- [19] B. A. Zarate, J. M. Caicedo, J. G. Yu, and P. Ziehl, "Bayesian model updating and prognosis of fatigue crack growth," *Eng Struct*, vol. 45, pp. 53-61, 2012.
- [20] E. Vatangül, "Determination of Mechanical Properties of Composite Materials and Thermal Stress Analysis with Ansys 10 Program," Master Thesis, Dokuz Eylül University, Izmir, Turkey, 2008.
- [21] V. Eskizeybek, "Fatigue Crack Progression in Stainless Steel Fiber Reinforced Aluminum Composites," Master thesis, Selçuk University, Konya, Turkey, 2006.
- [22] SolidWorks, Solid Works Material Library, Dassault Systèmes, 2020.
- [23] S. H. Pektaş, "Simulation of Brake Mechanism Fatigue Test by FEA Method.," Master thesis, Dokuz Eylül University, İzmir, Turkey, 2006.
- [24] Ö. Sunar, "Fatigue Analysis in Leaf Springs with Finite Element Method.," Master thesis, Celal Bayar University, Manisa, Turkey, 2015.
- [25] S. Roth and M. Kuna, "Prediction of size-dependent fatigue failure modes by means of a cyclic cohesive zone model," *Int J Fatigue*, vol. 100, pp. 58-67, 2017.
- [26] S. Salih, K. Davey, and Z. Zou, "Frequency-dependent cohesive-zone model for fatigue," *Int J Solids Struct*, vol. 152, pp. 228-237, 2018.
- [27] İ. Saraç, "Investigation of the Effect of Using Nanoparticles in Epoxy Adhesive on Static and Fatigue Strength of Single-Action Bonding Joints," PhD thesis, University of Batman, Batman, Turkey, 2018.
- [28] Z. Qian and H. Huang, "Coupling fatigue cohesive zone and magnetomechanical model for crack detection in coating interface," *Ndt&E Int*, vol. 105, pp. 25-34, 2019.
- [29] M. Al-Waily, A. S. Hammood, and A. A. Kamaz, "Effect of Fiber Orientation on Fatigue of Glass-Fiber Reinforcement Epoxy Composite Material," *The Iraqi Journal For Mechanical And Material Engineering*, vol. 11, no. 2, pp. 344-358, 2011.
- [30] M. Z. Kabir and A. Nazari, "The study of ultimate strength in notched cylinders subjected to axial compression," *J Constr Steel Res*, vol. 67, no. 10, pp. 1442-1452, 2011.
- [31] H. Adin and A. Turgut, "Strength and failure analysis of inverse Z joints bonded with Vinylster Atlac 580 and Flexo Tix adhesives," (in English), *J Mech Sci Technol*, vol. 26, no. 11, pp. 3453-3461, 2012.
- [32] M. A. Ghaffari and H. Hosseini-Toudeshky, "Fatigue Crack Propagation Analysis of Repaired Pipes With Composite Patch Under Cyclic Pressure," *J Press Vess-T Asme*, vol. 135, no. 3, 2013.
- [33] M. K. Ghovanlou, H. Jahed, and A. Khajepour, "Cohesive zone modeling of fatigue crack growth in brazed joints," *Eng Fract Mech*, vol. 120, pp. 43-59, 2014.
- [34] B. Günaydın, "Fatigue Behavior of Composite Patch Repaired Surface Notched Filament Winding Tubes," PhD Thesis, Selçuk University, Konya, Turkey, 2010.
- [35] T. Baklacioğlu, "Determination of fatigue life in fractured structures using finite element method.," Master thesis, Anadolu University, Eskişehir, Turkey, 2005.
- [36] S. Demir, "Fatigue Analysis of Single-rotor Driven Flanges with Multiple Screw Connection by Ansys Workbench 13.0 Due to Fatigue Strength Factor and Isotropic Thermal Changes.," Master thesis, Dumlupınar University, Kutahya, Turkey, 2012.

BIOGRAPHIES


Hamit Adin, born in 1972, received his PhD degree from the University of Fırat, Elazığ, Turkey in 2007 and has been Professor of Mechanical Engineering at the University of Batman, Turkey, since 2021. He has done research in the areas of mechanics, composite materials, adhesive, adhesion and finite element analysis. His research includes both theoretical and experimental studies.

Bilal Yıldız received his MSc diploma (Department of Mechanical Engineering) from Batman University in 2019. His research interests are composite materials, adhesive, adhesion and finite element analysis.

Mehmet Şükrü Adin is a PhD candidate of the Department of Mechanical Engineering, University of Batman, Batman, Turkey. He received his master's degree in Mechanical Engineering from the University of Batman in 2016. His research interests include mechanical properties of materials, composite materials, welding, finite element analysis, solid metal forming and alternative fuels.



Dynamic Investigation of a Permanent Magnet Synchronous Motor for Faulty Operations

Muhammed Şeker¹ , Duygu Bayram Kara² 

¹ RWTH Aachen University, Faculty of Electrical Eng. and Inf. Tech., Aachen, Germany. (e-mail: [muhammed.seker@rwth-aachen.de](mailto:m Muhammed.seker@rwth-aachen.de)).

² Istanbul Technical University, Electrical Engineering Department, 34469, Maslak, Istanbul, Turkey. (e-mail: duygu.kara@itu.edu.tr)

ARTICLE INFO

Received: Mar., 05. 2021

Revised: April., 15. 2021

Accepted: May, 24. 2021

Keywords:

Permanent magnet synchronous motor
Mathematical modelling
Condition monitoring
Demagnetization
Winding degradation

Corresponding author: *Duygu Bayram Kara*

ISSN: 2536-5010 / e-ISSN: 2536-5134

DOI: <https://doi.org/10.36222/ejt.891458>

ABSTRACT

Industrial efficacy of electrical energy is an important feature for our daily life. To provide efficient and reliable operation, new types of electrical machines and their condition monitoring have gain importance. In this paper, a model based condition monitoring and fault evaluation application for permanent magnet synchronous motors (PMSM) is presented. Possible fault conditions are realized on mathematical model and their results are discussed. In order to observe the dynamic behavior of PMSM, its mathematical model is implemented into MATLAB / Simulink as a reference. Then, faulty conditions are created by altering specific model parameters to imitate possible faults. The behavior of the motor is observed and compared with the reference output to contribute the dynamic effects of faulty operations.

1. INTRODUCTION

Since electrical machines are the major energy consumer in industry, they should be selected as efficient as possible. Losses of the electrical machines are highly depended on the type and the control equipment for the desired the operation. Therefore, reducing the losses is an important trump to be considered.

In the industry servo motors are well-known for the precise move and transportation applications. To determine which type of electrical machines should be selected, the application should have been well arranged. Commonly used types of electrical machines were conventional DC machines, induction machines and synchronous machines in the last century. Since DC motors need brushes and commutator systems, the maintenance becomes problematic. Consequently, brushless motor drive system is selected for servo motor applications due to their robustness and lower maintenance need. These requirements can be met by AC motors or SRM (switched reluctance motor) [1-2]. If desired output torque is expected to be smooth, then induction machine (IM) or synchronous machine (SM) are the candidates. The use of synchronous motors takes place when the constant speed with high reliability is desired with the line frequency. And also, the variable speed drive is possible with inverter-fed systems. Since the permanent magnets (PM) have their own magnetic

field due to the material property, in PM motors, dc excitation winding does not be there no longer to create rotor magnetic field. If the PMSM is used then the losses decrease because of brushes, slip rings and dc field winding losses are abolished [3]. The PMSM is newly preferred as a workhorse of the industry because of its advantageous over induction machines (IM) such as:

- PMSM has lower inertia due to the absence of rotor cage, therefore the torque to inertia is higher and this makes the machine response faster than IM.
- The PMSM is more efficient than IM because of the ignorance of rotor copper losses.
- The PMSM has its own excitation due to PM but IM needs a magnetization current to being excited.
- In order to provide same output power, the PMSM will have smaller sizes than IM. If the space is an important parameter to be considered, PMSM should be preferred with its higher power density.
- Since rotor losses is mainly copper losses causing the heating then PMSM is a good selection since its rotor is free from windings.

As a result, PMSM becomes a popular type of electrical machine to be applied in industrial application because of its compactness, efficiency, robustness, reliability, and shape adaptation to working environment [4-6]. From another

perspective; the general trend in the industry is to reduce environmental impact and to satisfy that new regulations and standards of International Electro Technical Commission (IEC) [7]. PMSM is a good candidate to meet new standards due to its high efficiency, robustness and reliability.

Thus, condition monitoring and fault diagnostics of PMSMs become more important to evaluate and prevent faults which might interrupt the operation. Also, the importance of the PMSM in aerospace and automotive industry increases due to its high reliability [8], therefore it becomes crucial to model and monitor this machine properly. During the monitoring process it is also vital to understand the reason of the faults and any change on the machine's dynamical response caused by them. Therefore, possible faults should be determined and their effects on the machine should be well studied in order to recognize them. In order to monitor the machine condition, parameters such as stator winding resistance and rotor flux linkages are important to be audited. These quantities are also critical for the controller design. Also, obtaining electromagnetic parameters accurately is necessary for applications such as control system design, online fault diagnosis, and condition monitoring.

Electrical machines are the key components to couple electrical and mechanical power; therefore, their faults can be occurred on both sides. For the electrical side, PMSM has stator windings and rotor magnets. Stator windings can be open circuited due to loss of connection of windings or short circuited due to dysfunctionality of the isolation. According to Reference [9], 35-40% of the PMSM faults are reasoning from the stator faults [10]. The common stator windings faults are because of isolation depreciation causing inter-turn faults. These can lead to huge problems such as phase-to-ground faults. Also Reference [11] indicates that the phase-to-phase or phase-to-ground faults are the ultimate result of undetected turn-to-turn faults, as a general belief. The failure of the insulation is modelled as a resistance, named as fault resistance (r_f) and its value is dependent on the severity of the fault. The value of the resistance changes rapidly from infinity to zero in the cases of short circuit. The resistance is tuned to infinity for no fault operation. For the short-circuit the value of the resistance decreases rapidly to zero by indicating the fault severity through its amplitude [12]. Whenever r_f equals to zero, the windings are assumed to be fully short circuited.

Another fault possibility is the demagnetization which is caused by the stator field. In other words, rotor magnets can be demagnetized due to the high opposite magnetization caused by the stator magnetic field. Another reason for demagnetization in PMSM is the high temperature on magnets. Especially for the surface mounted PMSMs, magnet is exposed to higher flux harmonics causing temperature increase. And also for the super and under synchronous operations rotor is subjected to hysteresis and eddy-current losses resulting additional temperature rise [13]. References [14] and [15] have investigated PMSMs with partially demagnetized magnets at certain rates. Since the demagnetization of the magnets can lead to flux disturbances, unbalanced magnetic pulls (UMP) occurs resulting in the vibration and noise [16].

Additionally, dynamic problems might also occur due to torque pulsations. From the mechanical aspect, bearing damage and eccentricity are the possible faults for PMSM [17-18]. The bearing fault is a common problem for all rotating systems. Another important but not so often confronted rotor fault is the broken or cracked magnets on the rotor.

Lastly, to support line-start ability of PMSMs a cage arrangement can be implemented to rotor. For this case, PMSMs can be supplied directly from the network. This brings a possibility of having some imbalances on the supply side such as frequency and voltage fluctuations.

In this study, mathematical model response two common fault modes are investigated. First, a PMSM model is created on Matlab / Simulink environment and a reference operation is defined for motor. Then failure modes are realized through the intentional manipulations of relevant parameters. The resulting dynamic outputs are compared with the reference case in terms of amplitudes.

2. MATHEMATICAL MODEL FOR PMSM

To model a PMSM dq0 transformation, known as Park's transformation, is used for linear representation of rotating quantities. This transformation fixes the reference frame to the rotor and all electrical quantities are assumed to rotate with the rotor angular speed. This methodology brings simplicity due to decrease 3-phase stator system into 2-phase system which means stator will have only one set of two windings. Since the rotor has only magnets, they can be modelled as current or flux linkage sources. When the transformation is done and fictitious set of direct and quadrature windings are set to represent stator windings, no varying inductance is obtained.

Dynamic model is derived under these assumptions [19].

- The saturation and parameter changes are neglected.
- The inductance versus rotor position is sinusoidal.
- The stator windings are balanced with sinusoidal distributed magneto-motive force.

First, the stator voltages should be transformed into dq0-frame with the transformation matrix given in Eq. 1.

$$\begin{bmatrix} v_q \\ v_d \\ v_0 \end{bmatrix} = \frac{2}{3} \begin{bmatrix} \cos(\theta) & \cos\left(\theta - \frac{2\pi}{3}\right) & \cos\left(\theta + \frac{2\pi}{3}\right) \\ \sin(\theta) & \sin\left(\theta - \frac{2\pi}{3}\right) & \sin\left(\theta + \frac{2\pi}{3}\right) \\ 1/2 & 1/2 & 1/2 \end{bmatrix} \begin{bmatrix} v_a \\ v_b \\ v_c \end{bmatrix} \quad (1)$$

Voltage stator equations presented in rotor reference frame are given in Eq. 2 where R_s is stator resistance, λ_{af} is the mutual flux between armature and field windings, ω_r is the rotor angular speed, L_d and L_q are the direct and quadrature axis inductances, respectively.

$$\begin{bmatrix} v_{qs}^r \\ v_{ds}^r \end{bmatrix} = \begin{bmatrix} R_s + L_q p & \omega_r L_d \\ -\omega_r L_q & R_s + L_d p \end{bmatrix} \begin{bmatrix} i_{qs}^r \\ i_{ds}^r \end{bmatrix} + \begin{bmatrix} \omega_r \lambda_{af} \\ 0 \end{bmatrix} \quad (2)$$

By transferring these equations to Laplace domain, Eq. 3 and Eq. 4 can be obtained;

$$v_{qs}^r = (R_s + L_q s) i_{qs}^r + \omega_r L_d i_{ds}^r + \omega_r \lambda_{af} \quad (3)$$

$$v_{ds}^r = -\omega_r L_q i_{qs}^r + (R_s + L_d s) i_{ds}^r \quad (4)$$

Currents can be derived from the previous equations in well-known Laplace forms in Eq. 5 and Eq. 6.

$$i_{qs}^r = \frac{1}{L_q} \frac{v_{qs}^r - \omega_r L_d i_{ds}^r - \omega_r \lambda_{af}}{(s + R_s/L_q)} \quad (5)$$

$$i_{ds}^r = \frac{1}{L_d} \frac{v_{ds}^r + \omega_r L_q i_{qs}^r}{(s + R_s/L_d)} \quad (6)$$

Flux linkages for direct and quadrature axes calculated through current expressions are given in Eq. 7 and Eq. 8.

$$\lambda_{qs}^r = L_q i_{qs}^r \quad (7)$$

$$\lambda_{ds}^r = L_d i_{ds}^r + \lambda_{af} \quad (8)$$

For these quantities, electromagnetic torque is given in Eq. 9 through mechanical and electrical approaches while J is the moment of inertia, B is the damping coefficient and T_l is the load torque [20].

$$T_e = \frac{3P}{2} [\lambda_{ds}^r i_{qs}^r - \lambda_{qs}^r i_{ds}^r] = \omega_m (Js + B) + T_l \quad (9)$$

3. REFERENCE DYNAMIC MODEL OF PMSM

In order to evaluate dynamic behavior of PMSM with various faults, a reference operation should be defined. For this purpose, a 220V, 50 Hz, 8 poles surface mounted PMSM with stator resistance 2.875 Ω , direct and quadrature inductances 8.8 mH, mutual flux linkage 0.175Wb, 0.0008 kg.m² moment of inertia is observed. First a reference operation is executed to compare with faulty cases. The dynamic answers of chosen PMSM for 10 Nm load torque are given in Fig. 1 - 3.

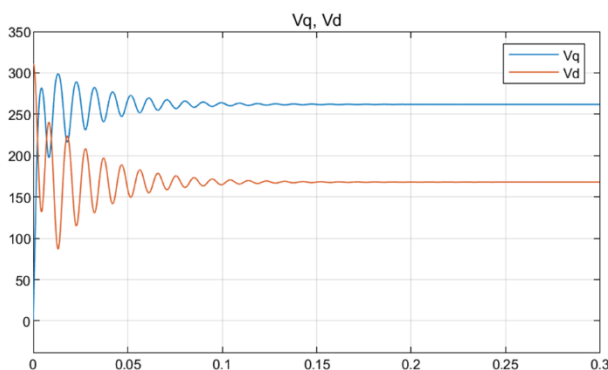


Figure 1. Voltages for direct and quadrature axes.

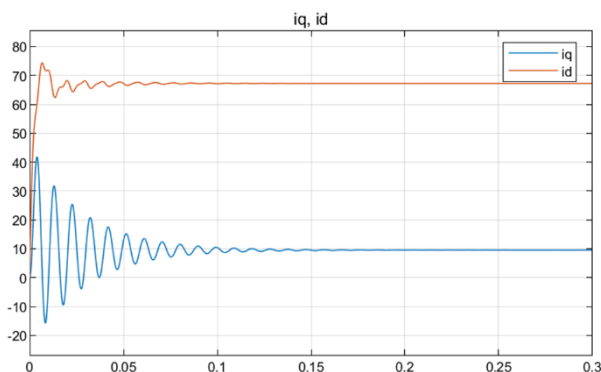


Figure 2. Currents for direct and quadrature axes.

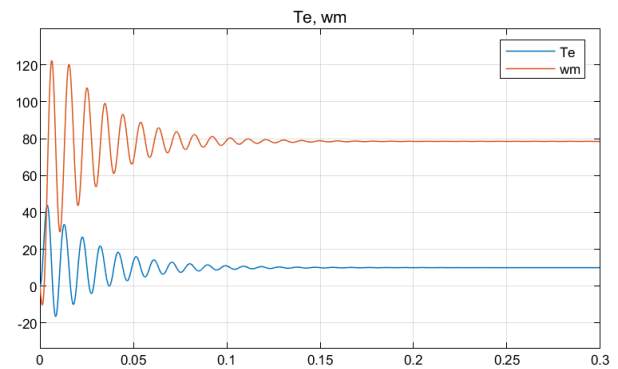


Figure 3. Shaft Torque and speed.

4. IMPLEMENTATION OF FAILURE MODES

It has already been mentioned above that one of the major faults occur on the stator as inter-turn fault and it can be modelled as a drop in the resistances. On the other hand, to imitate the demagnetization, the mutual flux linkage between rotor magnets and stator armature winding λ_{af} can be limited. From that point of view, there are two main parameters to be changed along the simulation. There may be some other results for the aforementioned faults. In other words, some consequences should be taking into account as the side effects of these alterations in experimental studies.

1. Stator resistance has a direct relation with the increase of temperature, and it will affect the system,
2. The magnetic flux linkages variation changes the torque production and also the speed of the machine.

However, in this study these possibilities have been ignored because of the mathematical model limitations.

With the changing of aforementioned parameters, the faulty cases are realized and the machine's dynamical responses are obtained and evaluated regarding the created scenarios. Two different failure modes (FM) are realized and their dynamical behaviors are monitored.

The FMs are listed below:

- Winding degradation: Decrease in the stator resistance to simulate short circuits in various percentages,
- Partial Demagnetization: Decrease in the flux linkage to imitate partial demagnetization resulted from a cracked magnet.

To compare the faulty operations voltage (v_d and v_q) and current (I_d and I_q) are shared for the constant torque and speed (T and ω).

4.1. Failure mode 1: winding degradation

Regarding Table I; with the decrease of stator resistance the current of direct axis increases as an expected result. Also, v_q increases while v_d decreases. In other words, for the higher percentages of short circuit, balance between the voltages of direct and quadrature axis changes while their vector sum converges approximately to the same values. Also, time to reach the steady state strings out with the decreased resistance. As the short circuit percentage augments, the longer time requires to achieve steady state operation. Furthermore, the oscillations enlarge for all parameters.

TABLE I

RESULTS FOR FAILURE MODE 1: DECREASE IN THE STATOR RESISTANCE VALUE

	Case 1	Case 2	Case 3	Case 4	Case 5
Stator Resistance - R_s	2.875	2.15	1.4375	0.71875	0.2875
V_q	261.9	278.7	295.7	308.4	311.1
V_d	167.9	138.2	96.78	40.98	1.8
I_d	67.25	76.12	85.02	92.35	94.88
I_q	9.524	9.524	9.524	9.53	9.569

4.2. Failure mode 2: partial demagnetization

Table II shows that current components elevate with the decreasing rotor mutual flux linkage to satisfy required magnetic coupling and to induce defined electromagnetic torque. There is no significant alteration on the voltage values since the relevant modification is not defined on the electrical circuit as the previous one.

TABLE II

RESULTS FOR FAILURE MODE 2: CHANGE IN THE FLUX LINKAGE OF ROTOR AS DEMAGNETIZATION

	Case 1	Case 2	Case 3	Case 4	Case 5
Rotor Mutual Flux Linkage (λ_{af})	0.175	0.1575	0.14	0.1225	0.105
V_q	261.9	262	262.6	264.1	266.7
V_d	167.9	167.8	166.8	164.5	160.2
I_d	67.25	68.19	69.07	69.84	70.45
I_q	9.524	10.58	11.9	13.61	15.87

5. CONCLUSION

In this study, the dynamical modelling of a PMSM is achieved and its fault evaluation is executed. The rotor reference frame is employed for the modelling to calculate d- and q- axes voltage. Different failure modes are presented and their dynamic results are compared with the reference model. Deliberate manipulations of parameters cause the dynamic model to respond different to satisfy torque and speed which are hold constant.

In order to imitate short circuit failure, stator resistance value is decreased in different percentages. For this fault mode, the oscillation interval and damping time increases during the start, by the augmented winding degradation. To simulate the demagnetization or broken magnet failure, rotor flux λ_{af} is decreased gradually. The torque and speed characteristics do not show a noticeable difference but the higher damping times are observed. Also the stator current components raise to provide the required coupling field.

These findings lead the researcher of diagnosing;

1. Winding degradation fault while monitoring longer time to reach steady state operation and larger oscillations with unexpected increase in the direct axis current.

2. Demagnetization fault while monitoring increasing current components with slightly lengthened out time to reach steady state.

As the contribution, dynamic investigation of faulty operations is guiding for the condition monitoring purposes. A condition monitoring list is possible to be presented by creating different scenarios through the manipulations of relevant machine parameters. As the future work, authors are planning

on correlating the dynamical model result with the experimental observations.

REFERENCES

- [1] M. Yıldırım and H. Kurum, "Influence of Stator Embrace on Torque of In-Wheel Switched Reluctance Motor," *European Journal of Technique (EJT)*, vol.7, no.2, pp. 78-84, 2017.
- [2] E. Kılıç, S. Şıt, H. Özçalık and A. Gani, "An Efficient Adaptive Controller Design for Three Phase Induction Motors based on RBF Neural Network.," *European Journal of Technique (EJT)*, vol. 7, no. 1, pp. 69-77, 2017.
- [3] R. Krishnan, "Application Characteristics of Permanent Magnet Synchronous and Brushless dc Motors for Servo Drives," *IEEE Trans. Ind. Appl.* vol. 27, pp. 986-996, 1991.
- [4] M. A. Rahman and P. Zhou, "Analysis of Brushless Permanent Magnet Synchronous Motors," *IEEE Trans. on Ind. Electronics*, vol. 43, no.2, pp. 256-267, 1996.
- [5] H. Yetiş, and T. Göktaş, "Comparative Design of Permanent Magnet Synchronous Motors for Low-Power Industrial Applications," *Balkan Journal of Electrical and Computer Engineering*, vol. 8, no. 3, pp. 218-224, 2020.
- [6] A. Consoli, G. Scarcella, and A. Testa, "Industry application of zero-speed sensorless control techniques for PM synchronous motors," *IEEE Trans. Ind. Appl.*, vol. 37, pp. 513-521, 2001.
- [7] D. Gatt, C. Yousif, M. Cellura and L. Camleri, "An Innovative Approach to Manage Uncertainties and Stock Diversity in the Epbid Cost-Optimal Methodology," *European Journal of Technique (EJT)*, vol. 8, no.1, pp. 35-49, 2018.
- [8] S. Bolognani, M. Zordan, and M. Zigliotto, "Experimental fault-tolerant control of a PMSM drive," *IEEE Trans. Ind. Electron.*, vol. 47, pp. 1134-1141, 2000.
- [9] S. S. Kulkarni and A.G. Thosar, "Mathematical Modeling and Simulation of Permanent Magnet Synchronous Machine," *Int. J. Electron. Electr. Eng.*, vol. 1, pp. 66-71, 2013.
- [10] Z. Doğan and R. Selçuk, "A Diagnosis of Stator Winding Fault Based on Empirical Mode Decomposition in PMSMs.," *Balkan Journal of Electrical and Computer Engineering*, vol. 8, no. 1, pp. 73-80, 2020.
- [11] G. B. Kliman, W. J. Premerlani, R. A. Koegl and D. Hoeweler, "A new approach to on-line turn fault detection in AC motors," presented at 1996 IEEE Industry Applications Conference 31st IAS Annual Meeting, San Diego, CA, USA, 2002.
- [12] B. Vaseghi, N. Takorabet, B. Nahid-Mobarakeh and F. Meibody-Tabar, "Modelling and study of PM machines with inter-turn fault dynamic model-FEM model," *Electr. Power Syst. Res.*, vol. 81, pp. 1715-1722, 2011.
- [13] D. D. Reigosa, F. Briz, P. García, J. M. Guerrero and M. W. Degner, "Magnet temperature estimation in surface PM machines using high-frequency signal injection," *IEEE Trans. Ind. Appl.*, vol. 46, pp. 1468-1475, 2010.
- [14] Z. Yang, X. Shi and M. Krishnamurthy, "Vibration monitoring of PM synchronous machine with partial demagnetization and inter-turn short circuit faults" presented at IEEE Transportation Electrification Conference and Expo (ITEC), Detroit, MI, USA, 2014.
- [15] W. Le Roux, R. G. Harley, and T. G. Habetler, "Detecting rotor faults in low power permanent magnet synchronous machines," *IEEE Trans. Power Electron.*, vol.22, pp. 322-328, 2007.
- [16] M. Zafarani, T. Goktas and B. Akin, "A Comprehensive Magnet Defect Fault Analysis of Permanent-Magnet Synchronous Motors," *IEEE Transactions on Industry Applications*, vol. 52, no.2, pp. 1331-1339, 2016.
- [17] M. Riera-Guasp, J. A. Antonino-Daviu, and G. A. Capolino, "Advances in electrical machine, power electronic, and drive condition monitoring and fault detection: State of the art," *IEEE Trans. Ind. Electron.*, vol. 62, pp. 1746-1759, 2015.
- [18] J. Hong et al., "Detection and Classification of Rotor Demagnetization and Eccentricity Faults for PM Synchronous Motors," *IEEE Transactions on Industry Applications*, vol. 48, no. 3, pp. 923-932, 2012.
- [19] Krishnan, R. Permanent magnet synchronous and brushless DC motor drives, CRC press, USA, 2009.
- [20] M. Döşoğlu and M. Dursun, "Response and Analysis of Permanent Magnet Synchronous Motor According to Different Reference Signals," *Balkan Journal of Electrical and Computer Engineering*, vol. 6, pp. 18-22, 2018.

BIOGRAPHIES

Muhammed Şeker obtained his BSc degree in electrical engineering from Istanbul Technical University (ITU) in 2019. He is currently studying as Master Student in the RWTH Aachen University in the Faculty of Electrical Engineering and Information Technology. He is pursuing his master's in Electrical Power Engineering. His research interests are electrical drive systems and their control and monitoring, energy storage systems and their applications.

Duygu Bayram Kara obtained her B.Sc., M.Sc., and Ph.D. degrees from the Electrical and Electronics Faculty of Istanbul Technical University (ITU), in 2006, 2009, and 2015, respectively. She worked as Research Assistant in ITU between 2007 and 2015. She joined University of Tennessee Knoxville, Nuclear Engineering Department and Maintenance and Reliability Centre, as a Visiting Researcher, for induction motor diagnostic studies in 2013. She is currently working as Assistant Professor in the Electrical Engineering Department, ITU. Her research interests include technical design and dynamics of electrical machines, additionally their condition monitoring and fault detection through signal processing and soft computing algorithms.

Modeling the Ca²⁺/CaMKII network of LTP in the JigCell Environment

Onur Alptürk 

Istanbul Technical University, Department of Chemistry, 34469, Maslak, Istanbul, Turkey. (e-mail: onur.alpturk@itu.edu.tr).

ARTICLE INFO

Received: Feb.,22.2021
Revised: Apr.,19.2021
Accepted: May,11.2021

Keywords:

Memory formation
Long-term potentiation
Mathematical model
JigCell
Calcium
CaMKII

Corresponding author: O. Alptürk

ISSN:2536-5010 | e-ISSN: 2536-5134

DOI: <https://doi.org/10.36222/ejt.962475>

ABSTRACT

Since their initial discovery, long-term potentiation (LTP), and long-term depression (LTD) are accepted as the main biomolecular mechanism that controls memory acquisition. In doing this, both mechanisms are fairly complex and involve specific triggers and many cascades reactions that cross-talk and communicate with others. Thus, they are very complex. To reveal how these mechanisms operate and instruct the brain to remember and forget, one judicious approach is developing the mathematical models of processes. However, this notion requires some basic knowledge regarding ordinary differential equations and writing codes. To this respect, it can be postulated that tools, which can be utilized rather by everyone, would certainly facilitate the formulation of such models. With this rationale in mind, we demonstrate that JigCell offers the perfect platform to develop such models for LTP. The choice for this tool originates from the fact that it is designed to simulate complex biological systems with ease. Thus, this manuscript is crafted to illustrate how the Ca²⁺/CaMKII network in LTP was constructed in the JigCell environment and to give an idea of how this tool works.

1. INTRODUCTION

The question of how we code information in our memory has remained a scientific puzzle, that is inherited from one generation to the next one. However, it should not be interpreted as no progress has been made. On the contrary, so much is known from Hebb's early work. With his theory summarized as "Cells that fire together wire together", Hebb postulates that activation of pre-and postsynaptic cells strengthens the connection between neurons [1]. To communicate more, the synapses of neurons are observed to change, as a result of which their synaptic strength is enhanced. This observation is synaptic plasticity, which depicts the capacity of synapsis to strengthen or weaken in time [2]. Presently, our view of memory formation is dominated by these long-term changes in synaptic communication, which are bidirectional; long-term potentiation (LTP) as a long-lasting increase in signal transmission between two neurons and long-term depression (LTD), in which case the extent of transmission between neurons is weakened. In summary, LTP and LDP are accepted as the biomolecular mechanism that underlies memory acquisition [3].

The structure of how LTP operates starts up with specific triggers. Under the resting condition, the pores of NMDA (N-

methyl-D-aspartate) receptors are occupied with Mg²⁺ ions. Upon depolarization, Mg²⁺ is removed from the pore, which culminates in the influx of Na⁺, K⁺ and Ca²⁺ [4]. Of them, calcium influx triggers a postsynaptic cascade of reactions that alters the density of AMPA receptors at the post-synapsis. In this process, the frequency in calcium dictates the fate of memory formation by impacting the direction on the alteration of AMPA receptors; high-frequency calcium influx results in LTP, whereas low-frequency calcium influx actuates LTD. Thus, calcium influx has a bidirectional role in deciding whether we remember or we forget [5].

There is no need to mention that in reality, the process of how the brain remembers is far more perplexing than what is described. For this reason, one way to fully grasp and study this process requires composing mathematical models regarding biochemical events behind memory acquisition. With this motivation, many groups (including ours) have developed models that cover either all or a certain fraction of LTP (for instance, see [6-10]).

Conspicuously, such mathematical models could only be formulated by researchers who are familiar with solving ordinary differential equations (ODE) or writing codes. To this respect, software that can be utilized by everyone without requiring a background in mathematics and computer science will assuredly expedite progress in this field. For this reason,

the JigCell Model Connector was introduced to the scientific community [11]. This software is specially devised to construct molecular network models which are inherently complex. By design, JigCell allows hierarchical model composition; that is to say, a complex network is engineered as a combination of smaller models. In the JigCell environment, these smaller models are named “modules” and each one represents a well-defined fragment of the model. Once the modules are connected through the so-called “interface ports”, the overall network is obtained. This way, one can understand how a certain part of the model behaves and interacts with others. From standpoint of user-friendliness, JigCell is very advantageous; the ordinary differential equations are written through a panel without demanding a code to solve them. Thus, it can be used by anyone.

Given the complexity of the mechanism underlying memory formation, it is reasoned that this software offers the perfect platform to elucidate the dynamics in LTP. To address the applicability of JigCell in this context, a model that covers the Ca²⁺/CaMKII network in LTP is formed as an illustration, with the use of differential equations reported in the literature. Ultimately, this manuscript is crafted to discuss how this model is formed in the JigCell environment and more importantly, to give the reader a feel about the basics of this software.

2. MATERIAL AND METHODS

JigCell and COPASI (analysis environment for JigCell) can be downloaded for free from the link given in [12]. In the JigCell environment, the model designed to simulate the Ca²⁺/CaMKII network is envisioned to harbor two modules; Module 1 and Module 2. In this model, Module 1 relates to the chemistry of calcium, which serves as the well-established initiation signal of LTP. On the other hand, Module 2 deals with the dynamics of CaMKII, a protein kinase known to activate the following downstream reactions in memory formation.

Before discussing the content of each module, this section of the manuscript is crafted to provide some insight into how this software works. In general, the JigCell environment offers two rationales to implement rules for dynamic changes. The first one is through the “species” menu; the dynamics of reactants and variables (collectively coined as “species”) are given through ordinary differential equations. To illustrate, this rationale was utilized in Module 1, wherein the calcium influx is delineated by the ODE given in the box “expression” (Figure 1).

Reactions	Species	Module quantities	Functions	Events	Compartments	Equations	Model properties	Ports
#	Name	Initial quantity	Type	Compartment	Expression	Notes		
1	Ca	0.01	ODE	cell	-5*Ca+a*(1+Ca1)			
2	Ca1	0.1	ODE	cell	100*Ca2			
3	Ca2	0.1	ODE	cell	-100*Ca1			

Figure 1. A screenshot of the menu “Species”.

The second one involves the representation of these dynamic changes in terms of chemical reactions, as in Module 2. This one is more suited to the cases with multiple species reacting in the form of a cascade (such as phosphorylation/dephosphorylation reaction of CaMKII subunits). For this one, the components of each reaction are predefined in the menu “Functions”, wherein the left column is utilized to itemize the components of each reaction in the form of reactants (“MOD”) or rate-constants (“VAR”).

Subsequently, the right column sets the reaction rules that combine the stoichiometric coefficients, and the rate constants with the reactants (Figure 2).

Reactions	Species	Module quantities	Functions	Events	Compartments	Equations	Model properties	Ports
#	Name					Equation		
1	Rxn1(MOD A1,VAR c1,VAR c3)					-c1+c3*A1		
2	Rxn2(MOD A1,MOD A2,VAR c1,VAR c2,VAR c3)					c1-c3*A1-c2*A1+2*c3*A2		
3	Rxn3(MOD A1,MOD A2,MOD A3,VAR c2,VAR c3)					c2*A1-2*c3*A2-1.8*c2*A2+3*c3*A3		
4	Rxn4(MOD A2,MOD A3,MOD A4,VAR c2,VAR c3)					1.8*c2*A2-3*c3*A3-2.3*c2*A3+4*c3*A4		
5	Rxn5(MOD A3,MOD A4,MOD A5,VAR c2,VAR c3)					2.3*c2*A3-4*c3*A4-2.7*c2*A4+5*c3*A5		
6	Rxn6(MOD A4,MOD A5,MOD A6,VAR c2,VAR c3)					2.7*c2*A4-5*c3*A5-2.8*c2*A5+6*c3*A6		
7	Rxn7(MOD A5,MOD A6,MOD A7,VAR c2,VAR c3)					2.8*c2*A5-6*c3*A6-2.7*c2*A6+7*c3*A7		
8	Rxn8(MOD A6,MOD A7,MOD A8,VAR c2,VAR c3)					2.7*c2*A6-7*c3*A7-2.3*c2*A7+8*c3*A8		
9	Rxn9(MOD A7,MOD A8,MOD A9,VAR c2,VAR c3)					2.3*c2*A7-8*c3*A8-1.8*c2*A8+9*c3*A9		
10	Rxn10(MOD A10,MOD A8,MOD A9,VAR c2,VAR c3)					1.8*c2*A8-9*c3*A9-c2*A9+10*c3*A10		
11	Rxn11(MOD A10,MOD A9,VAR c2,VAR c3)					c2*A9-c3*10*A10		

Figure 2. A screenshot of the menu “functions”.

With the rate constants and reactants defined once again as “species” (Figure 1), the kinetic law for each reaction is then formulated through the menu “Reactions” (Figure 3).

Reactions	Species	Module quantities	Functions	Events	Compartments	Equations	Model properties
#	Name (opt)	Reaction	Kinetic Type	Kinetic Law			
1	"1"	-> P0; P1	User Defined	Rxn1_1(P1,v1,v3)			
2	"2"	-> P1; P1 P2	User Defined	Rxn2_1(P1,P2,v1,v2,v3)			
3	"3"	-> P2; P1 P2 P3	User Defined	Rxn3_1(P1,P2,P3,v2,v3)			
4	"4"	-> P3; P2 P3 P4	User Defined	Rxn4_1(P4,P2,P3,v2,v3)			
5	"5"	-> P4; P3 P4 P5	User Defined	Rxn5_1(P4,P5,P3,v2,v3)			
6	"6"	-> P5; P4 P5 P6	User Defined	Rxn6_1(P4,P5,P6,v2,v3)			
7	"7"	-> P6; P5 P6 P7	User Defined	Rxn7_1(P5,P6,P7,v2,v3)			
8	"8"	-> P7; P6 P7 P8	User Defined	Rxn8_1(P6,P7,P8,v2,v3)			
9	"9"	-> P8; P7 P8 P9	User Defined	Rxn9_1(P7,P8,P9,v2,v3)			
10	"10"	-> P9; P10 P8 P9	User Defined	Rxn10_1(P8,P9,P10,v2,v3)			
11	"11"	-> P10; P9 P10	User Defined	Rxn11_1(P9,P10,v2,v3)			

Figure 3. A screenshot of the menu “Reactions”.

To obtain the model, Module 1 (Figure 4) and Module 2 are connected through Ca port, whereby the chemical information is conveyed from Module 1 to its partner, Module 2 (as an example, a layout of Module 1 and the model are shown in Figure 4 and 5, respectively). Then, the model is exported in the SBML extension and is imported into the COPASI environment. Finally, the simulation is run from the “Time Course” menu, after its parameters are entered (in this paper, they are: duration is 10 s, intervals is 100, and interval size is 0.01 s). COPASI also has an interface to visualize the results of simulations. As a note, the files of this model are available from GitHub [13].

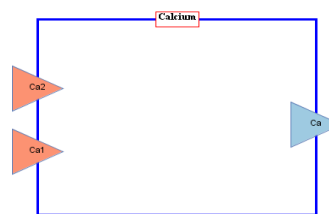


Figure 4. The layout of Module 1. Note that the inputs and the output of Module 1 are marked in red and blue, respectively.

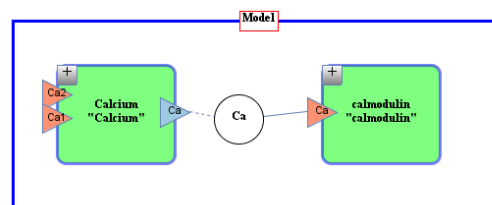


Figure 5. The layout of the model designed to simulate the Ca²⁺/CaMKII network in the JigCell environment.

3. RESULTS AND DISCUSSION

This section will elaborate on the nature of the modules, as well as the differential equation utilized in each one. Then, the results from the simulation will be discussed.

3.1. Module 1: Calcium Module

Serving as the initiation signal for LTP, the calcium module aims at simulating the dynamics of calcium uptake. Commonly, mathematical models consider the influx of calcium to post-synaptic neurons as the sole stimulant to LTP, whilst the roles of calcium from other intracellular sources (such as nuclear calcium) are very much omitted. Hence, calcium (Ca^{2+}) in Module 1 stands for synaptic calcium in this manuscript. Of paramount importance is the notion that the model presented hereby doesn't consider any event prior to the calcium influx to post synapsis (for instance, membrane depolarization or displacement of Mg^{2+} from NMDA receptors). Thus, the oscillatory calcium influx given in Module1 functions as "the trigger" in this model.

Conventionally, the calcium influx is expressed as an instant elevation, followed by an exponential decay, as tabulated in equation 1 [14].

$$[Ca^{2+}] = [Ca^{2+}]_{rest} + A \sum_{i=1}^n \exp\left(-\frac{i}{f\tau}\right) \quad (1)$$

where $[Ca^{2+}]_{rest}$ is the resting concentration of calcium, A is the amplitude of a single Ca^{2+} pulse, f is the frequency of excitation, τ is the relaxation time of Ca^{2+} decay, and n is the number of pulses in the tetanic stimuli (i.g., high-frequency sequence of individual stimulations), with frequency varying from 5 Hz to 100 Hz. In constructing module 1, the formulation of equation 1 in the JigCell environment posed a challenge, as such that this software doesn't recognize summation or exponential function. For this reason, this equation was redevised as a set of ordinary differential equations, wherein equation 2 describes the calcium influx, whilst equations 3 and 4 effectuate characteristic periodicity in the equation 2 with a frequency of 100 Hz (therein, variables Ca_1 and Ca_2 don't have biological meaning). The kinetics of oscillatory calcium influx described by equations 2-4 is shown in Figure 6 (parameters in these equations are described in Table 1).

$$\frac{d[Ca](t)}{dt} = -\tau[Ca](t) + \alpha\{1 + (Ca_1)(t)\} \quad (2)$$

$$\frac{d(Ca_1)(t)}{dt} = \omega(Ca_2)(t) \quad (3)$$

$$\frac{d(Ca_2)(t)}{dt} = -\omega(Ca_1)(t) \quad (4)$$

TABLE 1
PARAMETERS IN EQUATIONS 2-4

Parameters	Description	Value
α	Strength of signal	50 $\mu\text{mol/L}$
Ω	Frequency	100 Hz
Θ	Time-constant	5 s^{-1}

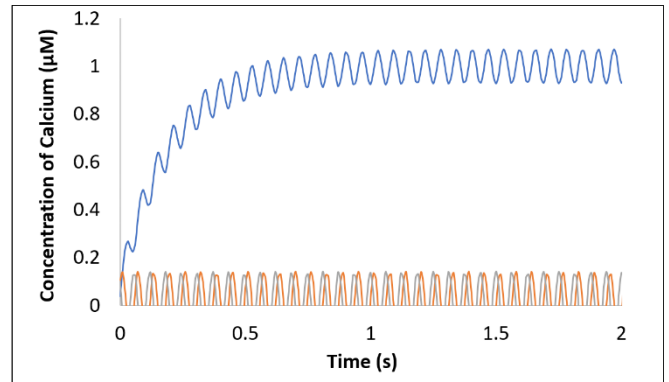


Figure 6. The kinetics of calcium influx defined by the set of equations (2-4) (the basal concentration of calcium is 10 nM and the initial values of Ca_1 and Ca_2 are 0.1).

Unsurprisingly, this approach fails to reflect the exponential decay in equation 1. To engineer this behavior, the equation 2 was revised to the equation 5, by expressing the strength of the signal in the form of a time-dependent variable. In doing this, the prediction was that it would stimulate the calcium influx when initially equal to 50, whereas it would actuate the exponential decay, once set to 0.

$$\frac{d[Ca](t)}{dt} = -\tau[Ca](t) + \alpha(t)\{1 + (Ca_1)(t)\} \quad (5)$$

$$\frac{d(Ca_1)(t)}{dt} = \omega(Ca_2)(t) \quad (6)$$

$$\frac{d(Ca_2)(t)}{dt} = -\omega(Ca_1)(t) \quad (7)$$

$$\alpha(t) = \begin{cases} 50 & \text{if } 0 \leq t \leq 5 \text{ secs,} \\ 0 & \text{otherwise.} \end{cases} \quad (8)$$

In the JigCell environment, discontinuity in functions is arranged from the menu "events" that stipulates two entries: "actions" to specify the nature of the triggered event and "delay" to indicate the trigger time for the event (Figure 7). With this menu, the variable α was programmed to switch from 50 to 0 after 5 seconds, whereupon it would serve as a turn-off signal for the calcium uptake, initiating the exponential decay in the equation 5 (Figure 8).

Reactions		Species	Module quantities	Functions	Events	Compartments	Equations	Model properties	Ports
#	Name (opt)	Trigger expression	Actions	Delay	DlyCalc	Notes			
1	Calcium trigger	$Ca > 0.04$	$a=0$	5	<input checked="" type="checkbox"/>				
2					<input type="checkbox"/>				

Figure 7. A screenshot of the menu "events" to introduce an exponential decay in the equation.

Once completed, Module 1 is of 2-inputs/1-output configuration, wherein Ca_1 and Ca_2 are the inputs as Ca is the output that stimulates the phosphorylation of Ca^{2+} /calmodulin-dependent protein kinase II (CaMKII) in Module 2 (vide infra).

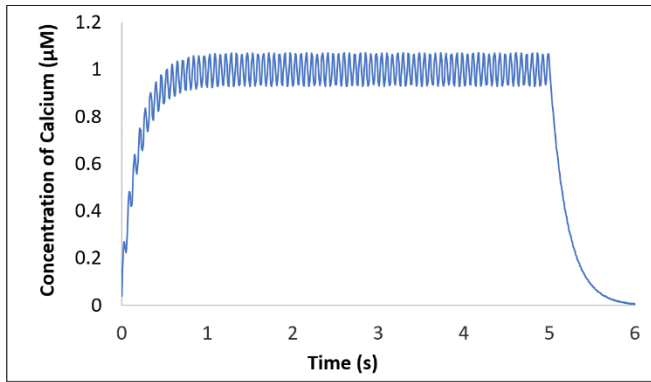


Figure 8. The kinetics of oscillatory calcium influx described by the set of equations 5-8.

3.2. Module 2: Calmodulin Module

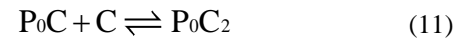
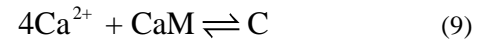
Module 2 is devoted to the chemistry of CaMKII, on the grounds that this kinase is believed to impact the fluctuations of the size and strength of neuronal connection [15]. In the context of LTP, such fluctuations are referred to as “synaptic plasticity”, which controls the extent of communication amongst neurons [16,17].

Being a determinant of how we remember, CaMKII is a serine/threonine kinase, which mediates Ca^{2+} -dependent phosphorylation of many neuronal targets. The crystal structure of this enzyme reveals that the holoenzyme is made up of 8-10 of two subunits, 52-kDa α and 60-kDa β . These subunits are arranged in the form of two rings, which pivot between an active and inactive conformation [18]. Under basal conditions, the kinase activity of CaMKII is blocked by the binding of the autoinhibitory domain to the catalytic domain. With the calcium transient, calcium/calmodulin (Ca^{2+}/CaM) binds to the autoinhibitory domain and restores the kinase activity of CaMKII by removing it. Later on, this induces autophosphorylation of Thr-286 and phosphorylation of other numerous targets in downstream reactions, which eventually leads up to LTP [19].

Given its significance, many models have been proposed to accurately express and understand how this kinase responds to intracellular calcium [20-23]. Amongst them, the one developed by Zhabotinsky is particularly intriguing as it reported a rather simple one to elucidate the mechanism of autophosphorylation of CaMKII in the presence of a calcium-dependent phosphatase [20]. Therefore, this model was of choice for the design of Module 2.

To make the mechanism of this enzyme more intelligible, Zhabotinsky made certain assumptions. For instance, this model fully ignores any difference between α and β subunits, treating CaMKII as a decamer of a single type of subunits. Then, the activation of subunits by calcium obeys the Hill equation, and the binding of Ca^{2+}/CaM and the phosphatase to a subunit is independent of the phosphorylation state of other subunits.

Quite naturally, this manuscript will manifest certain key aspects of this model; for further details, the reader should refer to the original paper. To begin with, CaMKII is portrayed as a single ring of subunits, in which the cascade of phosphorylation propagates in one direction, as originally proposed by Hanson and Schulman [24]. In the initiation step of phosphorylation reactions, $(Ca^{2+})_4CaM$ binds to two neighbor subunits. Then, the first subunit phosphorylates the second one in the clockwise direction, as shown by reactions 9-12.



where C represents $(Ca^{2+})_4CaM$ complex. P_0 and P_1 are unphosphorylated and 1-fold phosphorylated haloenzyme, respectively.

Next is the incorporation of the dephosphatase activity. There are four protein phosphatases known to act upon CaMKII-P [25], however; this model solely deals with PP1, given that this is the only protein that dephosphorylates CaMKII in the postsynaptic densities [25,26]. In this regard, it was demonstrated that the activity of PP1 is regulated by Ca^{2+}/CaM via inhibitor 1, calcineurin (CaN), and cAMP-dependent protein kinase A (PKA). Of note, inhibitor 1 (I1) is phosphorylated by PKA and dephosphorylated by Calcineurin; once phosphorylated, I1 deactivates PP1 [27,28]. In terms of LPT, I1 is crucial as its role renders this element a regulatory factor that links the calcium influx to synaptic plasticity [29]. Overall, the model of autophosphorylation of CaMKII in the presence of PP1 is given with the following equations 13-25 (the constants c_1 - c_4 and the parameters therein are defined in Table 2, and Table 3, respectively).

$$\frac{dP_0(t)}{dt} = -v_1 + v_3P_1 \quad (13)$$

$$\frac{dP_1(t)}{dt} = v_1 - v_3P_1 - v_2P_1 + c_1v_3P_2 \quad (14)$$

$$\frac{dP_2(t)}{dt} = v_2P_1 - c_1v_3P_2 - c_2v_2P_2 + c_3v_3P_3 \quad (15)$$

$$\frac{dP_3(t)}{dt} = c_1v_2P_2 - c_2v_3P_3 - c_3v_2P_3 + c_4v_3P_4 \quad (16)$$

$$\frac{dP_4(t)}{dt} = c_1v_2P_3 - c_2v_3P_4 - c_3v_2P_4 + c_4v_3P_5 \quad (17)$$

$$\frac{dP_5(t)}{dt} = c_1v_2P_4 - c_2v_3P_5 - c_3v_2P_5 + c_4v_3P_6 \quad (18)$$

$$\frac{dP_6(t)}{dt} = c_1v_2P_5 - c_2v_3P_6 - c_3v_2P_6 + c_4v_3P_7 \quad (19)$$

$$\frac{dP_7(t)}{dt} = c_1v_2P_6 - c_2v_3P_7 - c_3v_2P_7 + c_4v_3P_8 \quad (20)$$

$$\frac{dP_8(t)}{dt} = c_1v_2P_7 - c_2v_3P_8 - c_3v_2P_8 + c_4v_3P_9 \quad (21)$$

$$\frac{dP_9(t)}{dt} = c_1v_2P_8 - c_2v_3P_9 - v_2P_9 + c_3v_3P_{10} \quad (22)$$

$$\frac{dP_{10}(t)}{dt} = v_2P_9 - c_1v_3P_{10} \quad (23)$$

$$\frac{de_p(t)}{dt} = -k_3Ie_p + k_4(e_{p0} - e_p) \quad (24)$$

$$\frac{dI(t)}{dt} = -k_3 I e_p + k_4 (e_{p0} - e_p) + v_{PKA} I_0 - \frac{V_{CaN} ([Ca] / K_{H2})^3 I}{1 + ([Ca] / K_{H2})^3} \quad (25)$$

where the rate constants v_1 , v_2 , and v_3 are:

$$v_1 = \frac{10k_1([Ca] / K_{H1})^8 P_0}{(1 + ([Ca] / K_{H1})^4)^2} \quad (26)$$

$$v_2 = \frac{k_1([Ca] / K_{H1})^4 P_1}{(1 + ([Ca] / K_{H1})^4)} \quad (27)$$

$$v_3 = \frac{k_2 e_p}{K_M + \sum_{i=1}^{10} iP_i} \quad (28)$$

TABLE 2
THE CONSTANTS C1-C4 IN EQUATIONS (13-23)

Equation	c ₁	c ₂	c ₃	c ₄
21	2	-	-	-
22	2	1.8	3	-
23	1.8	3	2.3	4
24	2.3	4	2.7	5
25	2.7	5	2.8	6
26	2.8	6	2.7	7
27	2.7	7	2.3	8
28	2.3	8	1.8	9
29	1.8	9	10	-
30	10	-	-	-

3.3. The Model

The results of the simulation indicate that this cascade proceeds as a response to calcium, which concurrently orchestrates phosphorylation and dephosphorylation reactions. In this regard, it is observed that when Ca^{2+} firstly triggers *n-fold* phosphorylation reactions of CaMKII, as a result of which unphosphorylated holoenzyme (P_0) is fully consumed and evokes the synthesis of holoenzyme with a higher degree of phosphorylation. Mechanistically, the kinetics of each reaction exhibit bell-curve-like behavior in that each signal sequentially reaches its maximum, and then, undergoes “dephosphorylation”, forming the cascade of “*n-fold* dephosphorylation”. Thus, this model consists of two series of reactions merged to form a cascade; *n-fold* phosphorylation reactions ($P_0 \rightarrow P_1 \rightarrow P_2 \dots P_8 \rightarrow P_9$), and *n-fold* dephosphorylation reactions ($P_{10} \rightarrow P_9 \rightarrow P_8 \dots P_1 \rightarrow P_0$).

From standpoint of LTP, the phosphorylation of holoenzymes and kinase activity in post-synapsis come to mean the signal, which is essential to catalyze the other downstream events in LTP. After fulfilling its role, this signal is shut down through dephosphorylation of holoenzymes, as discussed before. However, it is worth noting that according to this model, the concentration of subunits doesn't fully return to their initial values, indicating partial dephosphorylation, rather than a complete one. This may stem from the dynamic of phosphatase and inhibitor-1 cycle, which governs the turn-off signal. To elaborate, calcium accumulating in the post-synapsis yields the concurrent synthesis of free inhibitor 1 (I1, Figure 10) and phosphatase

(E_p , Figure 11). Consequently, phosphatase activity is temporarily inhibited, sustaining the *n-fold* phosphorylation cascade (Figure 9). When the calcium influx begins to decay at $t=5$ s, however; one would expect that the balance in E_p /I1 should have favored phosphatase activity, whereby CaMKII holoenzymes are thoroughly dephosphorylated. In contrast, it appears that the extent of phosphatase activity tends to decrease beyond $t=5$ s. Thus, the lack of sufficient phosphatase activity may be responsible for CaMKII holoenzymes preserving their phosphorylated states and not fully turning the kinase activity off at $t>5$ s.

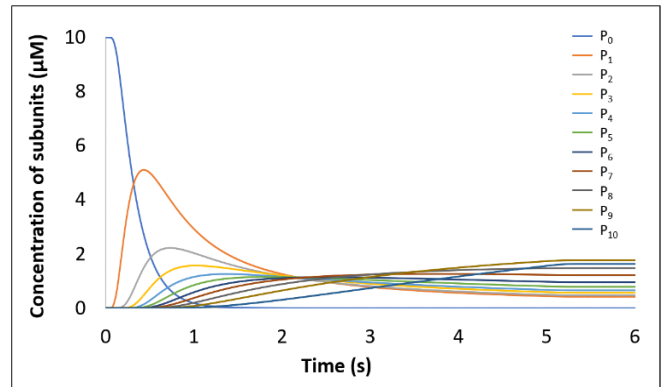


Figure 9. Kinetics of CaMKII subunit phosphorylation in response to calcium influx (the initial concentration of P_0 is $10 \mu M$ whereas that of other subunits is assumed to be 0. K_m and K_{H2} are $10 \mu M$, $0.6 \mu M$, respectively) [20].

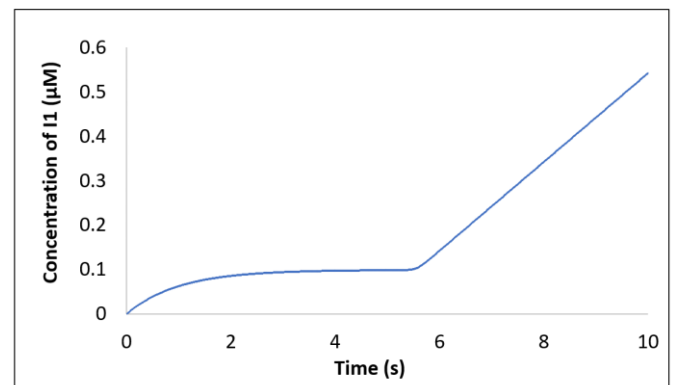


Figure 10. Kinetics of I1 in the response to calcium influx.

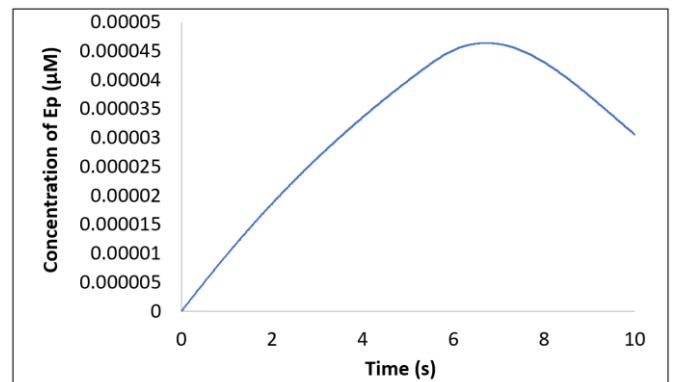


Figure 11. Kinetics of E_p in the response to calcium influx (E_{p0} is $0.6 \mu M$) [20].

4. CONCLUSION

In summary, the results reveal that the model formulated hereby is an avenue to study the Ca^{2+} /CaMKII network in the JigCell environment. Needless to say, this model and the similar ones may serve as a theoretical experimental environ-

TABLE 3.
PARAMETERS OF MODULE-2

Parameter	Description	Value	Unit	Reference
e_k	Total concentration of CaMKII	0.1–30	μM	25
ep_0	Total concentration of protein phosphatase	0.01–1.2	μM	20
I_0	Concentration of free inhibitor 1	0.0, 0.1	μM	20
V_{CaN}	Activity of calcineurin divided by its Michaelis constant	1.0	s^{-1}	20
V_{PKA}	Activity of PKA divided by its Michaelis constant	1.0	s^{-1}	20
K_M	The Michaelis constant of protein phosphatase	0.4–20	μM	20
K_{H1}	The Ca^{2+} activation Hill constant of CaMKII	4.0	μM	[30,31]
K_{H2}	The Ca^{2+} activation Hill constant of calcineurin	0.3–1.4	μM	32
k_1	The catalytic constant of autophosphorylation	0.5	s^{-1}	33
k_2	The catalytic constant of protein phosphatase	2.0	s^{-1}	20
k_3	The association rate constant of the PP1•I1P complex	1.0	μM	[20,28]
k_4	The dissociation rate constant of the PP1•I1P complex	1×10^{-3}	s^{-1}	[20,28]

ment, in which one can study the impact of any parameter on the process. Of course, the next step should be the validation and fine-tuning of such models through some experimental results; once done, a better understanding of memory formation will be obtained. In long term, more accurate models that are composed this way will aid the scientific community to understand how we learn but also, how our brain fails us, as in neurodegenerative diseases.

One final remark concerns JigCell and COPASI. To this date, these tools have been utilized to analyze many complex systems [34]. However, their use in the context of LTP has not been precedented, to the best of our knowledge. Thus, this study will expand the repertoire of their applications. Within this scope, the development of more elaborative models is currently in progress, in our laboratories (see: <https://onuralpturk8.wixsite.com/projectcerebra>).

5. ACKNOWLEDGEMENT

This study was carried out in the Chemistry Department of Istanbul Technical University (Bioorganic and Biochemistry Laboratory). The author kindly acknowledges Prof. Dr. Neslihan S. Şengör for the valuable suggestions she provided throughout the preparation of this manuscript.

REFERENCES

- [1] Hebb, D. O. (1949). *The Organization of Behavior*. New York, NY: Wiley & Sons.
- [2] Hughes, J. R. (1958). Post-tetanic potentiation. *Physiological reviews*, 38(1), 91-113.
- [3] Bliss, T. V., & Lomo, T. (1973). Long-lasting potentiation of synaptic transmission in the dentate area of the anaesthetized rabbit following stimulation of the perforant path. *The Journal of Physiology*, 232(2), 331-356.
- [4] Baltacı, S. B., Mogulkoc, R., & Baltacı, A. K. (2019). Molecular mechanisms of early and late LTP. *Neurochemical Research*, 44(2), 281-296.
- [5] He, Y., Kulasiri, D., & Samarasinghe, S. (2016). Modelling bidirectional modulations in synaptic plasticity: A biochemical pathway model to understand the emergence of long-term potentiation (LTP) and long term depression (LTD). *Journal of Theoretical Biology*, 403, 159-177.
- [6] Alptürk, O., & Şengör, N. S. (2019). A Model for the Effect of Glia on the Communication Amongst Neurons. 2019 27th Signal Processing and Communications Applications Conference (SIU), pp. 1-4.
- [7] Lisman, J. E., & Zhabotinsky, A. M. (2001). A model of synaptic memory: a CaMKII/PP1 switch that potentiates transmission by organizing an AMPA receptor anchoring assembly. *Neuron*, 31(2), 191-201.
- [8] Tewari, S., & Majumdar, K. (2012). A mathematical model for astrocytes mediated LTP at single hippocampal synapses. *Journal of Computational Neuroscience*, 33(2), 341-370.
- [9] Ohadi, D., Schmitt, D. L., Calabrese, B., Halpain, S., Zhang, J., & Rangamani, P. (2019). Computational modeling reveals frequency modulation of calcium-cAMP/PKA pathway in dendritic spines. *Biophysical Journal*, 117(10), 1963-1980.
- [10] Smolen, P., Baxter, D. A., & Byrne, J. H. (2006). A model of the roles of essential kinases in the induction and expression of late long-term potentiation. *Biophysical Journal*, 90(8), 2760-2775.
- [11] Jones Jr, T. C., Hoops, S., Watson, L. T., Palmisano, A., Tyson, J. J., & Shaffer, C. A. (2018). JigCell Model Connector: building large molecular network models from components. *Simulation*, 94(11), 993-1008.
- [12] http://copasi.org/Projects/JigCell_Model_Connector/
- [13] The files (the model – ETJ.jmc and the model – ETJ.xml) can be downloaded from <https://github.com/oalptul/Cerebra.git>
- [14] He, Y., Kulasiri, D., & Samarasinghe, S. (2016). Modelling bidirectional modulations in synaptic plasticity: A biochemical pathway model to understand the emergence of long term potentiation (LTP) and long term depression (LTD). *Journal of Theoretical Biology*, 403, 159-177.
- [15] Zalcman, G., Federman, N., & Romano, A. (2018). CaMKII isoforms in learning and memory: localization and function. *Frontiers in Molecular Neuroscience*, 11, 445.
- [16] Kennedy, M. B. (2016). Synaptic signaling in learning and memory. *Cold Spring Harbor perspectives in Biology*, 8(2), a016824.
- [17] Citri, A., & Malenka, R. C. (2008). Synaptic plasticity: multiple forms, functions, and mechanisms. *Neuropsychopharmacology*, 33(1), 18-41.
- [18] Hoelz, A., Nairn, A. C., & Kuriyan, J. (2003). Crystal structure of a tetradecameric assembly of the association domain of Ca^{2+} /calmodulin-dependent kinase II. *Molecular Cell*, 11(5), 1241-1251.
- [19] Magupalli, V. G., Mochida, S., Yan, J., Jiang, X., Westenbroek, R. E., Nairn, A. C., Scheuer, T., & Catterall, W. A. (2013). Ca^{2+} -independent activation of Ca^{2+} /calmodulin-dependent protein kinase II bound to the C-terminal domain of CaV2.1 calcium channels. *Journal of Biological Chemistry*, 288(7), 4637-4648.
- [20] Zhabotinsky, A. M. (2000). Bistability in the Ca^{2+} /calmodulin-dependent protein kinase-phosphatase system. *Biophysical Journal*, 79(5), 2211-2221.
- [21] Pharris, M. C., Patel, N. M., VanDyk, T. G., Bartol, T. M., Sejnowski, T. J., Kennedy, M. B., Stefan, M. I., & Kinzer-Ursem, T. L. (2019). A multi-state model of the CaMKII dodecamer suggests a role for calmodulin in maintenance of autophosphorylation. *PLoS Computational Biology*, 15(12), e1006941.
- [22] Lisman, J. E., & Goldring, M. A. (1988). Feasibility of long-term storage of graded information by the Ca^{2+} /calmodulin-dependent protein kinase molecules of the postsynaptic density. *Proceedings of the National Academy of Sciences*, 85(14), 5320-5324.

- [23] Michelson, S., & Schulman, H. (1994). CaM kinase: a model for its activation and dynamics. *Journal of Theoretical Biology*, 171(3), 281-290.
- [24] Hanson, P. I., & Schulman, H. (1992). Neuronal Ca²⁺/calmodulin-dependent protein kinases. *Annual Review of Biochemistry*, 61(1), 559-601.
- [25] Strack, S., Choi, S., Lovinger, D. M., & Colbran, R. J. (1997). Translocation of autophosphorylated calcium/calmodulin-dependent protein kinase II to the postsynaptic density. *Journal of Biological Chemistry*, 272(21), 13467-13470.
- [26] Yoshimura, Y., Sogawa, Y., & Yamauchi, T. (1999). Protein phosphatase 1 is involved in the dissociation of Ca²⁺/calmodulin-dependent protein kinase II from postsynaptic densities. *FEBS Letters*, 446(2-3), 239-242.
- [27] Shenolikar, S., & Nairn, A. C. (1991). Protein phosphatases—recent progress. *Adv. Sec. Mess. Phosphoprot. Res.* 23:1–121.
- [28] Endo, S., Zhou, X., Connor, J., Wang, B., & Shenolikar, S. (1996). Multiple structural elements define the specificity of recombinant human inhibitor-1 as a protein phosphatase-1 inhibitor. *Biochemistry*, 35(16), 5220-5228.
- [29] Allen, P. B., Hvalby, Ø., Jensen, V., Errington, M. L., Ramsay, M., Chaudhry, F. A., Bliss, T. V. P., Storm-Mathisen, J., Morris, R. G. M., Andersen, P., & Greengard, P. (2000). Protein phosphatase-1 regulation in the induction of long-term potentiation: heterogeneous molecular mechanisms. *Journal of Neuroscience*, 20(10), 3537-3543.
- [30] Fährmann, M., Möhlig, M., Schatz, H., & Pfeiffer, A. (1998). Purification and characterization of a Ca²⁺/calmodulin-dependent protein kinase II from hog gastric mucosa using a protein-protein affinity chromatographic technique. *European Journal of Biochemistry*, 255(2), 516-525.
- [31] De Koninck, P., & Schulman, H. (1998). Sensitivity of CaM kinase II to the frequency of Ca²⁺ oscillations. *Science*, 279(5348), 227-230.
- [32] Stemmer, P. M., & Klee, C. B. (1994). Dual calcium ion regulation of calcineurin by calmodulin and calcineurin B. *Biochemistry*, 33(22), 6859-6866.
- [33] Hanson, P. I., Meyer, T., Stryer, L., & Schulman, H. (1994). Dual role of calmodulin in autophosphorylation of multifunctional CaM kinase may underlie decoding of calcium signals. *Neuron*, 12(5), 943-956.
- [34] The list of publications regarding the use of COPASI could be accessed from <http://copasi.org/Research/>

BIOGRAPHIES

Onur Alptürk obtained his BSc degree in chemistry with a focus on biochemistry from Middle East Technical University (METU) in 1998. Then, he received the MSc. diploma from the biochemistry program of Middle East Technical University in 2001. In the same year, he was accepted to the graduate school of Louisiana State University (Baton Rouge). After receiving his Ph.D. degree in chemistry, he worked as a post-doctoral researcher at the University of Pittsburgh, School of Medicine for two years. In 2012, he moved back to Turkey and started working as an assistant professor in the chemistry department of Istanbul Technical University.

His current research interests involve biochemistry, bioorganic chemistry, and system biology, where he investigates the dynamics of protein networks.



Classification of Analyzable Metaphase Images by Extreme Learning Machines

Abdulkadir Albayrak

¹Dicle University, Department of Computer Engineering, 21280, Sur, Diyarbakır, Turkey. (e-mail: kadir.albayrak@dicle.edu.tr).

ARTICLE INFO

Received: Oct., 29. 2020
Revised: Dec., 21. 2020
Accepted: March, 10. 2021

Keywords:

Karyotyping
Metaphase detection
Extreme learning machines
Gray level co-occurrence matrix

Corresponding author: *Abdulkadir Albayrak*

ISSN: 2536-5010 / e-ISSN: 2536-5134

DOI: <https://doi.org/10.36222/ejt.818160>

ABSTRACT

A chromosome is a DNA molecule that contains the genetic material of an organism. Possible defects in chromosomes can cause structural and functional disorders in living things. Identifying the metaphase stages of cells is a critical step to identify problems in chromosomes. In this proposed study, the discriminative features of possible metaphase images were extracted with Gray level co-occurrence matrix and classified with the Extreme Learning Machines classification method. When the results were evaluated, it was observed that the proposed method was as successful as the deep learning methods in the literature. Especially in recent years, when online learning has become important, the need for re-training of deep learning-based algorithms after each validation will increase the importance of the proposed method in this field. The rapid increase in unlabelled data from each patient every day affects the duration of training and creates time and resource constraints. Fast and accurate modelling of such data with alternative machine learning methods will contribute to the studies in this area.

1. INTRODUCTION

Cytogenetics is a branch of genetics which concerned with the study of number, structure and function of chromosomes. A healthy individual has a total of 46 chromosomes, 23 of which are genetically inherited from the mother and 23 from the father. Anomalies in these chromosomes may cause the presence of various syndromes called congenital (Down syndrome, Edward syndrome, etc.). Experts try to detect the anomaly by analyzing genes obtained by sampling special tissues such as bone marrow, blood, amniotic fluid or placenta in order to detect possible congenital syndromes. This process performed in the expert's cytogenetics laboratory is called karyotyping. In karyotyping, chromosome analyzes are performed based on the division of cells in the metaphase stages of the samples taken from the patient. Scanning of chromosomes on the specimen slide is done at the metaphase stage, since the chromosomes have the best morphological features while in the metaphase stage and are suitable for imaging. At least 8 to 10 glass slide samples should be prepared for each individual in order to obtain an adequate analyzable metaphase spread image. Each glass slide typically contains about 10-20 metaphase formations. Of the approximately 200 metaphases prepared, approximately 20 of the "best" (based on the subjective opinion of an experienced cytogenetics expert) are selected for karyotyping. Optical microscopes are used for image selection and analysis. The lens of the microscope are the apparatus that determines the

quality of the image obtained, since it controls the illumination and the angle of entry of the light into the front lens. It has been observed that by adjusting the aperture of the lenses, more analyzable chromosome images can be obtained. The karyotyping process, which is quite tiring for the expert, also affects the performance of the expert in the process, and misdiagnosis may be made due to fatigue and lack of performance. In recent years, especially with the development of imaging technology and digital image processing methods, it is aimed to develop secondary decision support systems that will help the expert by making the karyotyping process, which is difficult and time-consuming by the expert with the help of computer-aided diagnosis systems. There are various studies proposed in the literature to handle this purpose. These approaches can generally be divided into two groups as rule-based and deep learning-based image processing methods [1]. When the studies in the literature are examined in rule-based methods, it can be observed that the rates of false positive are quite high [2]. In recent years, It has been observed that the deep learning methods give accurate results in many areas such as object recognition, target tracking, natural language processing, voice recognition [3].

The number of images used in previous studies are presented comparatively in Table 1 [3-16]. Difficulties in preparing data and the high false positive rates of the achieved achievements prevented the creation of a data set that can be considered as a reference in this area. The number of images

used in this area is expected to increase due to the following reasons: Especially in recent years, devices with high imaging technology used for this purpose in hospitals' genetic laboratories and existence of high-performance devices, especially using up-to-date digital image processing methods. After deep learning-based metaphase detection methods such as GoogleNet, VGG16, Inception, LeNet, which were quite successful in our previous study in the literature and we suggested before, experts were provided to present metaphase images with higher success.

TABLE I

THE NUMBER OF IMAGES USED IN THE LITERATURE AND IN THIS PROPOSED METHOD

Proposed study	# of images
Castleman 1992 [4]	-
Garza Jinich et. al. 1992 [5]	1,196
Vroluk et. al. 1994 [6]	150
Mclean and Johnson1995 [7]	100
Corkidi et. al. 1998 [8]	177
Cosio A et. al. 2001 [9]	909
Wang et. al. 2008 [10]	170
Ravi Uttamatin 2013 [11]	200
Yucehn Q et. al. 2014 [12]	200
Yucehn Q et. al. 2016 [13]	150
Tanvi Arora, RenuD 2017 [14]	200
Yilmaz and Turan 2017 [15]	3018
Yilmaz and Turan 2018 [16]	3018
Moazen et. al. [3]	50,000
Proposed	50,000

2. MATERIALS AND METHODS

This proposed study consists of two stages: Detection of metaphase candidates and classification of metaphase candidates in order to identify possible metaphases.

2.1. Detection of Metaphase Candidates

The imaging system used in the study consists of the following components: Zeiss Imager M2 motorized microscope with 0.3 numerical aperture, 10x objective and 0.63x trinocular camera adapter. 1.4 megapixel (1360 x 1024) CCD camera with Marzhauser scan and 2/3 inch for 8 X - Y motorized stages. The first stage, which determines the possible metaphases in this proposed study, consists of 5 basic sub-steps.

In the first step, the system performs noise removal pretreatment using a low pass filter to reduce the noise ratio of the scanned image. In the second step, the gradient amplitude of the pixels is found by the Sobel method in order to detect the edges of the cells and objects in the image. In the third step, the Otsu method is used to determine and reduce the color levels of the gray levels [17]. In the fourth step, irrelevant objects such as spots and undivided cells are eliminated from the image. The system performs this step by using the morphological properties of these objects such as their circularity and pixel information. Finally, using the morphological dilation process, neighboring chromosomes of the metaphase cells are linked and the cell regions (region of interest) that have fully metaphase spread are recorded to the computer. In order to verify the steps performed at this stage, it scans the 100x zoomed image of the regions of interest obtained and provides performance improvement by eliminating the regions that are thought to have background information. Figure.1 obtains a whole image obtained from the data set and the metaphase and non-metaphase image

sections obtained from this image. Figure 1 represents the first step of the proposed method, which is the detection of metaphase candidates.

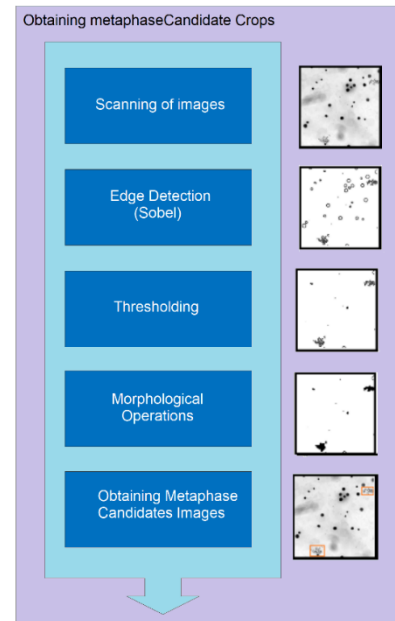


Figure 1. Basic operation steps of the first stage of the proposed method.

2.2. Classification of Metaphase Candidates

After obtaining the possible metaphase sections highlighted in the previous section, it is necessary to obtain distinctive features in order to perform high-performance classification. Traditional methods are used to obtain shape, color and textural features in the image that is desired to be distinguished in the region of interest. Depending on the characteristics of the object to be classified, features such as the longest side, the shortest side, the ratio of these edges to each other, concave and convexity define the shape information; the red, green and blue pixel brightness values describe the color information. In some images where shapes and colors are not distinctive, tissue information (such as a change in the pattern of a cancerous region due to cell density) is tried to be obtained with textural information descriptors. These highlighted methods are defined specific to the problem and implemented manually to solve the current problem.

2.2.1 Gray Level Co-Occurrence Matrix(GLCM)

Feature vectors of possible metaphase image sections included in the data set were extracted using the gray level co-occurrence matrix (GLCM). GLCM is a texture descriptor algorithm proposed by Robert Haralick [18]. The algorithm basically tries to obtain a distinctive feature between images by calculating the number of sequences of certain successive pixels. This method takes a gray level image as input. In an input image, the values of consecutive pixels are computed and thus the GLCM features are extracted. Then, specific vectors are taken from this GLCM and given as input to the classification method. In order to obtain features by using GSEM in color images, the features can be obtained by applying the algorithm to each color band separately. One of the important parameters used in the algorithm is at what angles the method will be applied. For example, if it is desired to be applied at 45 degrees in the whole image, the number of the central pixel and the other pixels adjacent to that pixel at

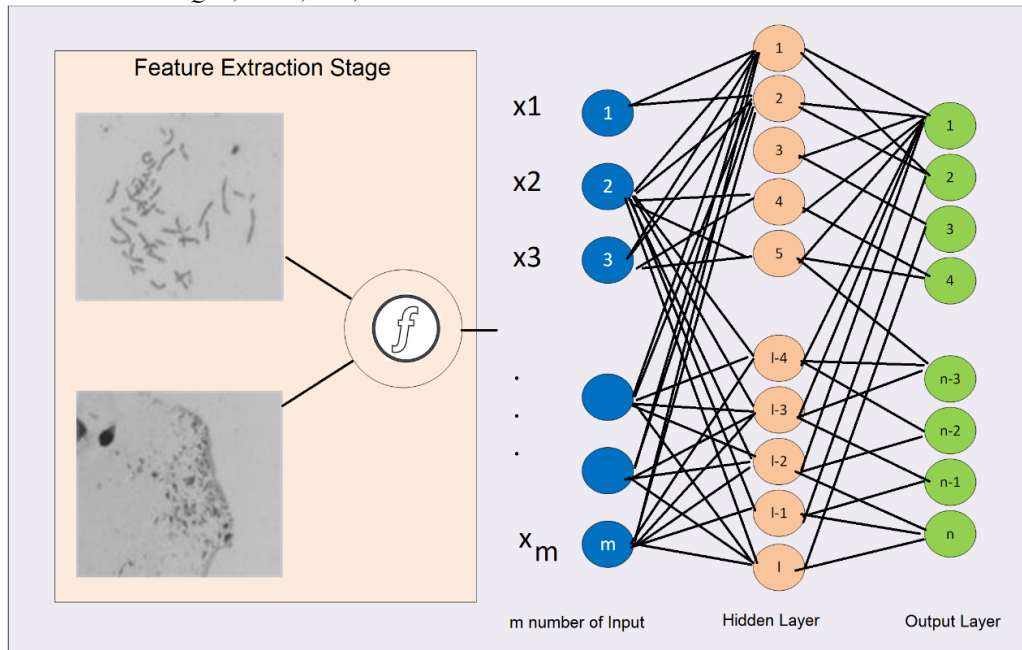


Figure 2. Classification stage of the proposed study

45 degrees are kept in the formation matrix. After applying Figure 2: Classification stage of the proposed study this process to all pixels in the image, the resulting co-occurrence matrix is then used for feature extraction. In this study, GLCM. was calculated by counting the sequences of pixels in 4 neighborhoods in one direction and 10 feature vectors related to each image were obtained.

2.2.2 Extreme Learning Machines (ELM)

Extreme Learning Machine (ELM) is a machine learning method that consists of a single feed-forward neural network and classifies objects based on their distinctive properties. [19]. ELM was first designed to consist of a total of 3 layers, as an input layer, a hidden layer and an output layer. Unlike convolutional neural networks, weights connecting hidden nodes to outputs can be trained very quickly. It can be said that it has only one hidden layer and the fast results are obtained with vector products. When the experimental studies in the literature are examined, it has been shown that ELMs can produce acceptable predictive performance and the computation costs are much lower than the networks trained by the back propagation algorithm. Figure 2 shows the process steps followed in metaphase classification in this proposed study.

$$X = x_t \in R^p \quad t = 1, \dots, n \quad (1)$$

In Eq. 1, let R^p be a dataset to which ELM will be applied, with n number of samples and p features. The outputs to be obtained with ELM can be expressed in Eq. 2.

$$O_i(x_t) = m_i(x_t)h(x_t) \quad (2)$$

where m_i indicates the weight vector connecting the latent neurons to the i th output neuron. $h(t)$ represents the vector of the outputs of hidden neurons for a given input model x_t . Then $h(t)$ can be written as:

$$h(t) = f(w_1^T x(t) + b_1), f(w_2^T x(t) + b_2), \dots, f(w_q^T x(t) + b_k) \quad (3)$$

Here, b_k indicates the bias of the k 'th latent neuron, w_k represents the weight vector of the k 'th latent neuron and $f(\cdot)$ indicates a sigmoidal activation function. An important point to note here is that the values of the weight vectors w_k and the bias b_k are randomly generated from a Gaussian distribution.

3. EXPERIMENTS

The digital images used in this proposed study were first published by Moazzen et. al. [3]. There are 55000 possible metaphase image sections obtained from a total of 26000 images with a width and height of 1360x1024 to create the data set. The location of possible metaphases in these images has been precisely marked by a sitogenetic expert.

In Table 2, the comparison of true positive rate (TPR) and false positive rate (FPR) values of previous studies were compared with the proposed study. According to the table, while the FPR in the results obtained with traditional methods such as SVM, decision trees and k-NN is quite high, the FPR of deep learning methods remained quite low. In addition, the TPR in the table have yielded more successful results in deep learning approaches. It has been observed that the proposed method gives more successful results than traditional methods, but relatively less successful than deep learning-based methods. Considering the FPR values, it can be said that the proposed method has a low error rate. In the proposed method, the training and classification phase is completed in 239 seconds in total, while in our previous study [3], where the data set was shared, it can take hours for deep learning methods. Considering the rapid increase in data, the need to train the system over and over again for each new data requires the development of alternative methods to deep learning algorithms.

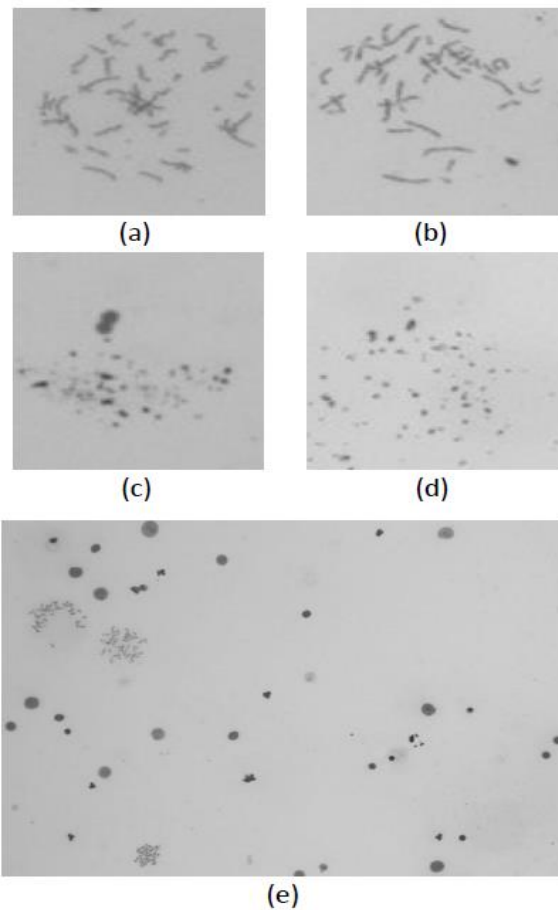


Figure 3. (a) and (b) represent metaphase images obtained from dataset; while (c) and (d) represent non-metaphases images. (e) represents whole image which includes metaphases and non-metaphase image crops.

Table 2. Comparison of TPR and FPR values of the proposed method with the methods in the literature

TABLE 2
THE NUMBER OF IMAGES USED IN THE LITERATURE AND IN THIS PROPOSED METHOD

Approaches	TPR	FPR
SVM based	%88	%69
Decision Trees	%89	%71
k-NN based	%90	%72
AlexNet	%99	%0.76
GoogleNet	%98	%0.52
ResNet	%99	%0.74
Inception	%99	%0.55
Castlemen	%80	%0.73
MetaSel	%90	%4.6
proposed	%97,6	%2.2

It is a known fact both in this study and in the literature that deep learning methods are more successful than traditional methods. However, it is a known fact that the training phase of deep learning algorithms in large-scale data is very slow if the graphics processing unit is not used. With the graphic processing unit, the training phase is very fast, but the repetitive training of the data obtained from patients, such as the data set used in this study, and increasing day by day, can make deep learning algorithms inefficient in terms of time. It is an undeniable fact that the training phase gain importance as the amount of data increases.

4. CONCLUSION

In this proposed study, the feature vectors of the possible metaphase images were extracted with the GLCM algorithm and classified with the ELM algorithm. When the results were evaluated, it was observed that performance of the proposed method has more accurate than results obtained with rule-based algorithms. In our first study where the dataset was introduced, a very high success was achieved with deep learning-based algorithms. It is clear that algorithms based on deep learning have the best results in classifying metaphase images. However, the long duration of the training phase of deep learning algorithms and the need for retraining, especially after the verification of data such as online learning, caused the need to examine alternative methods. ELM differs from deep learning algorithms in this respect. With the GLCM and single layer Basic-ELM algorithm, the training and classification phase of the data takes in 239 seconds in total. It is clear that this approach, which is quite fast in this respect, will be a good alternative by increasing the classification performance. In future studies, testing algorithms such as kernel-based ELM (Kernel ELM), multilayer ELM (Multilayer ELM), which can be alternative to Basic-ELM in classification of metaphase images, with different feature extraction algorithms may increase the performance. In addition, the training processes will be accelerated by examining transfer learning and fine tuning processes. It is planned to focus on these methods in future studies.

ACKNOWLEDGEMENT

The Author would like to thank Argenit Co. for their contribution in providing and marking the data.

REFERENCES

- [1] X. Wang, B. Zheng, M. Wood, S. Li, W. Chen, & H. Liu, "Development and evaluation of automated systems for detection and classification of banded chromosomes: current status and future perspectives," *Journal of Physics D: Applied Physics*, 38(15), 2536, 2005.
- [2] T. Arora, & R. Dhir, "A review of metaphase chromosome image selection techniques for automatic karyotype generation," *Medical & Biological Engineering & Computing*, 54(8), 1147-1157, 2016.
- [3] Y. Moazzen, A. Çapar, A. Albayrak, N. Çalık, & B. U. Töreyn, "Metaphase finding with deep convolutional neural networks," *Biomedical Signal Processing and Control*, 52, 353-361, 2019.
- [4] K. R. Castleman, "The PSI automatic metaphase finder," *Journal of radiation research*, 33(Suppl_1), 124-128, 1992.
- [5] M. Garza-Jinich, C. Rodriguez, G. Corkidi, R. Montero, E. Rojas, & P. Ostrosky-Wegman, "A Microcomputer-Based Supervised System for Automatic Scoring of Mitotic Index in Cytotoxicity Studies," In *Advances in Machine Vision: Strategies and Applications* (pp. 301-311), 1992.
- [6] J. Vrolijk, W. C. R. Sloos, F. Darroudi, A. T. Natarajan, & H. J. Tanke, "A system for fluorescence metaphase finding and scoring of chromosomal translocations visualized by in situ hybridization," *International journal of radiation biology*, 66(3), 287-295, 1994.
- [7] J. R. N. McLean & F. Johnson, "Evaluation of a metaphase chromosome finder: Potential application to chromosome-based radiation dosimetry," *Micron*, 26(6), 489-492, 1995.
- [8] G. Corkidi, L. Vega, J. Márquez, E. Rojas, & P. Ostrosky-Wegman, "Roughness feature of metaphase chromosome spreads and nuclei for automated cell proliferation analysis," *Medical & Biological Engineering & Computing*, 36(6), 679-685, 1998.
- [9] F. A. Cosío, L. Vega, A. H. Becerra, R. P. Meléndez, & G. Corkidi, "Automatic identification of metaphase spreads and nuclei using neural networks," *Medical & Biological Engineering & Computing*, 39(3), 391-396, 2001.

- [10] X. Wang, S. Li, H. Liu, M. Wood, W. R. Chen, & B. Zheng, "Automated identification of analyzable metaphase chromosomes depicted on microscopic digital images" *Journal of Biomedical Informatics*, 41(2), 264-271, 2008.
- [11] R. Uttamatani, P. Yuvapoositanon, A. Intarapanich, S. Kaewkamnerd, R. Phuksaritanon, A. Assawamakin, & S. Tongsima, "MetaSel: a metaphase selection tool using a Gaussian-based classification technique," *BMC bioinformatics*, 14(16), 1-13, 2013.
- [12] Y. Qiu, J. Song, X. Lu, Y. Li, B. Zheng, S. Li, & H. Liu, "Feature selection for the automated detection of metaphase chromosomes: performance comparison using a receiver operating characteristic method," *Analytical Cellular Pathology*, 2014.
- [13] Y. Qiu, X. Lu, S. Yan, M. Tan, S. Cheng, S. Li, ... & B. Zheng, "Applying deep learning technology to automatically identify metaphase chromosomes using scanning microscopic images: an initial investigation," *International Society for Optics and Photonics*(Vol. 9709, p. 97090K), 2016.
- [14] Arora, T., & Dhir, R. (2017). An automatic human chromosome metaspread image selection technique. *Knowledge and Information Systems*, 52(3), 773-790.
- [15] H. Yilmaz, & M. K. Turan, "FahamecV1: A Low Cost Automated Metaphase Detection System," *Engineering, Technology & Applied Science Research*, 7(6), 2160-2166, 2017.
- [16] H. Yilmaz, & M. K. Turan, "Filter development for automatic detection of analyzable metaphases," In *2018 26th Signal Processing and Communications Applications Conference (SIU)* (pp. 1-4), 2018.
- [17] X. Xu, S. Xu, L. Jin, & E. Song, "Characteristic analysis of Otsu threshold and its applications," *Pattern recognition letters*, 32(7), 956-961, 2011.
- [18] R. M. Haralick, & L. G. Shapiro, "Computer and robot vision" Reading: Addison-wesley, (Vol. 1, pp. 28-48), 1992.
- [19] G. B. Huang, Q. Y. Zhu, & C. K. Siew, "Extreme learning machine: theory and applications," *Neurocomputing*, 70(1-3), 489-501, 2006.

BIOGRAPHIES

Abdulkadir Albayrak completed BSc, MS and PhD in computer science. He is a Research Assistant at the Department of Computer Engineering, Dicle University, Turkey. He studies machine learning, computer vision and biomedical image analysis.

Effects of Partial RCCI Application of LPG on Performance, Combustion and Exhaust Emissions in a Diesel Engine Powered Generator

Ahmet Aydin^{1*} , Hüseyin Aydin² 

¹Batman University, Mechanical Engineering Department, Batman, Turkey. (e-mail: g.ahmetaydinn@gmail.com).

²Batman University, Mechanical Engineering Department, Batman, Turkey. (e-mail: husayyinaydin@gmail.com).

ARTICLE INFO

Received: Nov., 18. 2019

Revised: Sep., 10. 2020

Accepted: Feb, 01. 2021

Keywords:

Diesel engine

Dual-Fuel system

Emission

LPG

Performance

Corresponding author: *Ahmet Aydin*

ISSN: 2536-5010 / e-ISSN: 2536-5134

DOI: <https://doi.org/10.36222/ejt.647912>

ABSTRACT

In this study, engine performance, combustion and emissions of a diesel engine used for driving an electrical generator was investigated with LPG fumigation into the manifold of the engine as secondary fuel. Tests were carried out in 4 cylinders, 4 strokes water-cooled and direct-injection diesel engine generator. According to the test results; cylinder pressure, average gas temperature and peak values of heat release rate were increased as amount of LPG was increased. However, brake specific fuel consumption and mass fuel consumption were higher as well. Generally, with LPG addition, CO and HC emissions were found higher. Up to 40% LPG addition, CO₂ emissions were lowered and over 40% LPG addition, CO₂ emission increased. With increasing LPG ratio, there was a decrease in NO_x emission values. On the other hand, generally, as LPG content was increased, O₂ emissions were decreased significantly. Generally, the LPG usage of certain levels were found to be possible as secondary fuel in diesel engines. However, its usage in the engine up to certain levels resulted in considerable negative changes in performance, combustion and emissions changes. Over 55% LPG fumigation resulted in quite high flame velocity and propagation which eventually resulted in the accelerated cylinder pressure for per crank angle. This condition may be accepted as the starting of the knock. Therefore, only certain low amounts of LPG usage as secondary nonreactive fuel in diesel engine were found to be possible.

1. INTRODUCTION

Petroleum supplies most of the energy needs so as to be used as fuel in the world. As a result of extreme use of petroleum, the oil reserves are reducing. Due to gradual increase in reserve usage and exhaust emissions, it is forced humanity to face with air pollution and the scarce of the existing energy resources. Therefore an attempt has been made to discover the alternative fuels [1,2]. Besides, the extreme usage of fuels in the world lead to considerable levels of smoke and particulate emissions to the atmosphere. Also, the increased number of diesel engines has led to alternative fuel searches.

Liquefied Petroleum Gas (LPG), which significantly reduces emissions in internal combustion (IC) engines, may also be used in diesel engines. LPG cannot be used alone in diesel engines because it has a low reactivity fuel and has a low cetane number and will need a combustion start. In diesel engines, LPG can be used with auxiliary methods to ignite. These methods include cetane number enhancer additives, LPG can be used together with pilot injections of high reactivity fuel with high cetane number such as diesel fuel [3].

Low-cost production, storage, easy to obtain, and low exhaust emissions of LPG make it possible to use as an alternative fuel for internal combustion engines [4].

In the literature, some studies related LPG usage in diesel engines as follows;

Kannan et al. [5] This study investigated the performance of LPG fueled Homogeneous charge compression ignition (HCCI) of inlet air preheating at different loads. Experiments were carried out using LPG as the primary fuel with a single cylinder 1500 rpm constant engine speed. According to the results; HC emissions at full load were higher in LPG fuel compared to diesel fuel. CO emissions for LPG were higher when compared to diesel. Especially under low load and no load conditions. Less NO_x emissions were observed in LPG compared to diesel fuel. When compare to pure diesel, the brake thermal efficiency of LPG was found lower at all loads. A decrease of approximately was 20% detected in the exhaust gas temperature in all combustion modes compared to diesel. Although peak pressures were better in LPG compared to diesel fuel. It was observed that the peak cylinder pressure decreased. Anye Ngang and Ngayihi Abbe [6] In this study the performance and emission characteristics of a dual fuel

(diesel-LPG) engine were investigated by changing the LPG mass fraction. The four-cylinder engine was tested at different loads and at different speeds. It was observed that the maximum in-cylinder pressure increased with the increase in engine speed. In addition, with the increase in the LPG mass fraction the cylinder pressure and temperature increased as well as the fuel consumption. It has been observed, when the LPG mass ratio is increased from 50% to 60% that there is a decrease in HC and NO_x emissions and an improvement in engine performance (torque, efficiency, power). Vinoth et al. [7] In this study were the use of diethyl ether (DEE) as an ignition enhancer and LPG as a primary fuel in a direct injection single-cylinder, water-cooled and four-stroke diesel engine investigated. They found that knocking decreased with the addition of diethyl ether. In addition, it was observed that CO and NO_x emissions decreased with a higher percentage of Diethyl ether compared to LPG. Brake thermal efficiency increased in the range of 2% to 10% at all loads for all LPG rate of flow, while the brake thermal efficiency decreased by approximately 5% with the addition of diethyl ether. The best performance, the highest efficiency and the least noisy situation were observed with the addition of 15% DEE and LPG flow rate of 0.221 kg/h. Guan et al. [8] In this study, pilot waste cooking oil biodiesel (WCOB) or pilot diesel and fumigated LPG were carried out with a 4-cylinder diesel engine operated at three different loads. With the addition of LPG, LPG is expressed as a percentage of power expression (LPSP), which varies between 10% and 30% at each load. According to the results; They found a slight decrease in peak heat release rate (HRR) and peak in-cylinder pressure in dual fuel compared to single fuel operation at low load. The effect of LPSP on brake thermal efficiency and brake specific fuel consumption improved at high load for both pilot fuel types, but worse at low load. They found that LPG-WCOB was better at reducing particulate emissions, while LPG diesel operation was better at reducing NO_x emissions. Rimkus et al. [9] In this study was the effect of LPG on environmental, energy performance and combustion in a compression ignition (CI) engine working on a diesel fuel investigated. By adding LPG to diesel fuel are reduced CO₂ emissions. There was a decrease in NO_x emission observed, while CO and HC emissions increased with LPG additive. Irgin et al. [10] In this study were the effects of dual fuel (diesel/LPG) on emissions and engine performance investigated. According to the test results; There was a slight increase in NO_x emission compared to diesel fuel, while a decrease in HC and CO emissions was detected. It also observed improvement in effective efficiency and specific fuel consumption. Nugroho et al. [11] In this study was dual fuel used in C223 diesel engine as LPG as secondary fuel. The experiments were carried out at different engine speeds and different LPG concentrations (35%, 45% and 75%). According to the results; They observed that brake specific fuel consumption, brake thermal efficiency and power were better in dual fuel compared to single fuel. Improvements were seen in brake thermal efficiency (BTE) with 45% LPG. Ünal et al. [12] In this study were cost and energy analyzes carried out according to the results obtained with different drying air inlet temperatures for heating the drying air in the drying chamber of the LPG-fueled horizontal type corn drying plant. According to the results; It has been observed that when the drying inlet air temperature is increased, fuel consumption, unit drying cost increase and energy efficiency decreases. They observed that while the relative humidity of the heater

inlet air increased, the energy efficiency decreased, while the unit drying cost and fuel consumption increased. Aliustaoğlu and Ayhan [13] They investigated in this study the effects of diesel-LPG fuel mixture on emissions and performance in a single-cylinder direct injection diesel engine. According to the test results; It has been observed that the 20% LPG-80% diesel fuel mixture provides superiority in terms of specific fuel consumption and cost without causing any negative effects on performance. It has been observed in addition, that they provide very important improvements in emissions. Sendilvelan and Sundarraj [14] In this study was LPG used as a secondary fuel in a direct-injection, single-cylinder, four-stroke, water-cooled and constant speed (1500 rpm) diesel engine under all loading conditions. According to the test results; Brake thermal efficiency slightly decreased due to the use of LPG. Significant reduction in diesel fuel consumption was observed. A slight increase was observed in CO and HC emissions at low loads, while a decrease was observed with increasing load. With the use of LPG was a reasonable reduction in smoke density and NO_x emissions observed. Aktaş and Doğan [15] made an investigation on the effect of diesel and LPG fuels on emission and performance in a direct injection single cylinder diesel engine was investigated. Brake specific fuel consumption was increased for the fuel mixture including LPG above 40%. It has been observed that NO_x emissions were decreased and CO and HC emissions were increased. Another research on diesel engine with a single-cylinder air-cooled direct injection was made by Yiğit [16]. According to his results, the use of LPG at 25% and 20% load was increased engine power and torque. CO emissions have been increased by a certain amount and then tended to decrease. As the amount of LPG increased, the increase in smoke emissions was observed. In addition, an increase in NO_x and HC emissions has been observed. Different LPG ratios with different butane/propane ratios were used in the dual fuel diesel engine by Saleh [17]. According to the test results as the propane ratio increased and the CO emissions decreased but the NO_x emission decreased as the butane ratio increased. The best results in terms of performance and emissions are ensured when using 40% LPG and 60% diesel fuel with 70% propane and 30% butane ratio. Another work was carried out on the experiments on a four-cylinder, four-stroke, water-cooled engine by Aydın and Acaroğlu [18]. The tests were firstly made with gasoline, followed by LPG. The engine emissions and performance values were compared. The results of the tests showed that LPG does not led decrease in performance with respect to gasoline fuel. Abd Alla et al. [19] converted the single-cylinder Ricardo E6 compression ignition engine into a dual-fuel engine with pilot injection. They used methane and propane fuels as the secondary fuel. As the amount of the pilot injection was increased while CO, NO_x and HC emissions were decreased, thermal efficiency was increased. Çarman et al. [20] studied in a diesel engine using 70% diesel fuel with 30% LPG and pure diesel fuel to examine for the emissions and performance characteristics. Test results were showed an increase of 5.8% in engine power and torque during dual fuel operation, a decrease in smoke emissions and a decrease in NO_x of 5.9%. In the general conclusions, they observed that dual fuel mode was shown better than the single-fueled operation. Jothi et al. [21] used LPG and diethyl ether (DEE) in a four-stroke, direct injection and water-cooled diesel engine. The test results showed that the thermal efficiency was decreased at full load compared to diesel fuel and NO_x emissions were decreased. Slight

increases in HC and CO emissions were observed when a decrease in smoke density and PM emissions were observed. Qi et al. [22] performed their experiments at different loads and speeds on a direct injection engine with pure diesel and LPG-diesel mixture. In the test results, it was observed that the increase in the LPG ratio in the mixture led to the increase in the ignition delay, with the maximum cylinder pressure. Compared with diesel, NO_x emission and smoke density were decreased. There was a slight increase in CO emissions at low loads. HC emissions were increased with the increase of the mass of LPG in the mixture.

In this study, the effects of LPG fumigation into the intake manifold as a secondary fuel in a diesel engine generator engine performance, combustion and exhaust emissions were experimentally investigated.

2. METHODOLOGY

2.1. Experimental materials and method

For the experiments, a generator connected to a water cooled, 4 cylinders, NWK22 model diesel engine with the power output of 18 kW was used. A schematic diagram of the experimental setup is given in Figure 1. A precision scale with digital indicator was used to calculate fuel consumption. The temperature was measured by means of a non-contact infrared digital thermometer.

CAPELEC CAP 3200 model diesel and gasoline emission measurement device was used for analyzing exhaust emissions in the experiments. The device is complying OIMLR99, ISO 3930 and BAR 97 standards. The commercial LPG supplied from a fuel station. Conveniently, the LPG fumigation system was mounted in the intake manifold. The FEBRIS combustion analysis software was used to analyze performance and combustion data in the experiments. Signals from a cylinder pressure sensor and crank angle encoder mechanism was used in experiment to analyze the combustion parameters. The cylinder pressure sensor records pressure data for every crank angle (1 °CA) and average of 100 cycles were used for drawing the curves. The data received from the signals through the FEBRIS program were simultaneously seen on the computer screen and recorded. The experimental data obtained during the experiments were observed and recorded through the FEBRIS software. By means of this it is possible to calculate many data, such as mean gas temperature, mean effective pressure, heat release rate, knock density and total heat release for each of crank angles.

Table 1 shows the physical properties and combustion characteristics of butane propane and mixture LPG fuels. The standards of the diesel fuel are shown in Table 2. The technical specifications of the engine used in the experiment are shown in Table 3. The fuel blends and their abbreviations used are shown in Table 4.

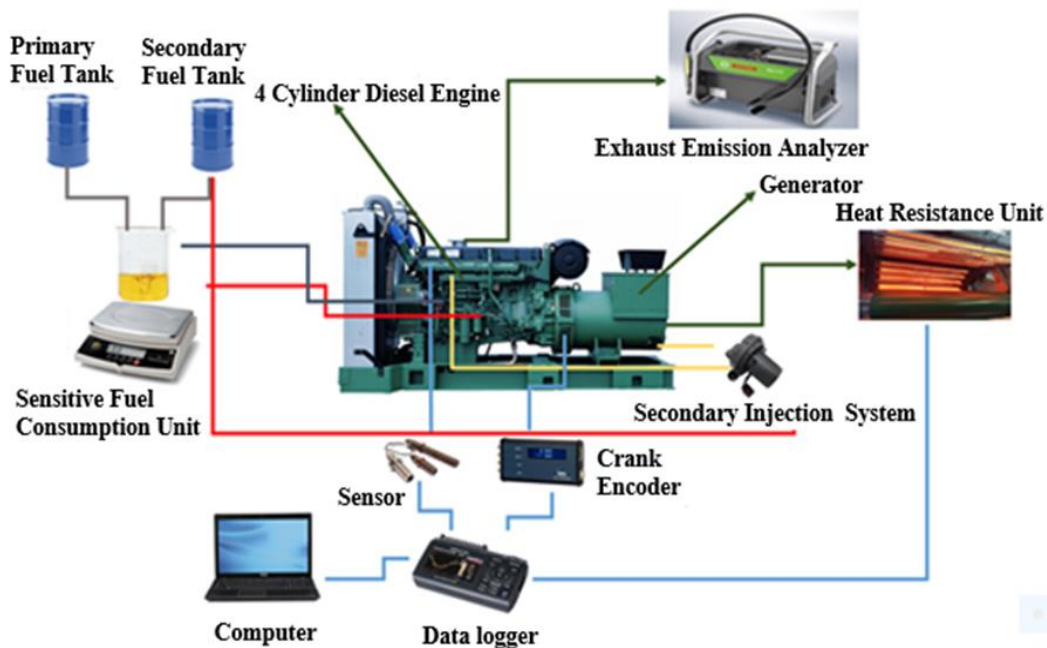


Figure 1. Experiment mechanism figure

TABLE I
TECHNICAL SPECIFICATION OF PROPANE, BUTANE AND LPG [23]

Properties	Unit	Propane	Butane	Blends
Closed Chemical Formula	-	C ₃ H ₈	C ₄ H ₁₀	% 30 C ₃ H ₈ + % 70 C ₄ H ₁₀
Molecular weight	gr /mol	44,09	58,12	53,91
Liquid Form				
Normal Boiling Point	°C	-42	-0,5	-13
Normal Melting Point	°C	-190	-138	-154
Normal Flashing Point	°C	-105	-60	-74
Specific Mass (at 15 °C)	kg /lt	0,508	0,584	0,560

TABLE II
THE STANDARDS OF THE DIESEL FUEL ACCORDING TO DINN 51601 [24]

Properties	Values	The experiment norms
Volumetric water content	%0,1	DIN 51777
Density at 15 °C	0.820-0,860 g/ml	DIN 51757
Distilled part up to 360 °C min.	%90	DIN 51752
Kinematic viscosity at 20 °C	1.8-10 mm ² /s	DIN 51550
Filtration	Summer 0 °C/ Winter -12°C	DIN 51770
Max mass sulphur percentage	%1,0	DIN 51768
Max mass percentage of carbon residue	%0,1	DIN 51551
Ash quantity, max ash percentage	%0,02	DIN 51575

TABLE III
TECHNICAL FEATURE OF THE ENGINE USED IN THE EXPERIMENT

Model	NWK22
Power output @1500 rpm	18 kW
Cooling system of the engine	Water cooled
The model of the engine	4DW81-23D
Bore x stroke (mm)	85x100
Cylinder volume (cm ³)	2400
Number of cylinders	4
Ignition system	Direct
Pressurizing rate	17:1

TABLE IV
THE FUEL BLENDS AND THEIR ABBREVIATIONS

The name of the mixture	LPG (%)	Diesel (%)
D100	-	100
D80 & LPG20	20	80
D70 & LPG30	30	70
D60 & LPG40	40	60
D55 & LPG45	45	55
D45 & LPG55	55	45
D35 & LPG65	65	35

2.2. Calculated Parameters

Febris software was used to analyze combustion parameters. Cylinder gas pressure values, cylinder volume, piston acceleration, average piston speed and crankshaft position were determined through the program. Thanks to the pressure sensor, the cylinder gas pressure data is accessed. Parameters were calculated for each crank angle by means of the equations given below.

2.2.1. Heat release rate

According to the calculations of the ideal gas law and the first law of thermodynamics in closed systems, the heat release rate was found using the equation.

$$\frac{dQ}{d\theta} = \frac{\gamma}{\gamma-1} P \frac{dV}{d\theta} + \frac{1}{\gamma-1} V \frac{dP}{d\theta} \quad (1)$$

2.2.2. Total heat release

The integral of the heat release rate was prepared as the total heat release. The equation in 1 is used to calculate the accumulated heat release.

$$\int dQ = \int \left(\frac{\gamma}{\gamma-1} \right) p(dV) + \int \left(\frac{1}{(\gamma-1)} \right) V(dP) \quad (2)$$

Here is γ a particular temperature ratio taken as 1.32, θ is the crank angle, P is the cylinder gas pressure, and V is the cylinder volume. The pressure data is separated from the

pressure sensor and the terms V and $dV/d\theta$ are calculated using the equation below.

$$V = V_c + A \cdot r \left\{ 1 - \cos \left(\frac{\pi A}{180} \right) + \frac{1}{\lambda} \left(1 - \sqrt{1 - \lambda^2 \sin^2 \left(\frac{\pi \theta}{180} \right)} \right) \right\} \quad (3)$$

$$\frac{dV}{d\theta} = \left(\frac{\pi A}{180} \right) \times r \left\{ \sin \left(\frac{\pi \theta}{180} \right) + \frac{\lambda^2 \sin^2 \left(\frac{\pi \theta}{180} \right)}{2\lambda \sqrt{1 - \lambda^2 \sin^2 \left(\frac{\pi \theta}{180} \right)}} \right\} \quad (4)$$

$$\lambda = \frac{l}{r} \text{ ve } A = \frac{\pi D^2}{4} \quad (5)$$

Here is r is the crank radius =H/2, l is the length of the rod connecting rod, D is the cylinder diameter and Vc is the stroke volume. The heat transfer coefficient (J) is calculated from the cylinder wall based on the Hohenberg equation.

$$\frac{dQ_w}{d\theta} = hA(T - T_w) \quad (6)$$

The following equation gives the ratio of specific heats based on the average gas temperature.

$$\gamma = 1,338 - 60 \times 10^{-5} T + 10^{-8} T^2 \quad (7)$$

The Hohenberg heat transfer coefficient is used in combustion analysis with the equation given below.

$$h_c = C_1 V^{-0.06} P^{0.8} T^{-0.4} [C_m + C_2]^{0.8} \quad (8)$$

Here is h is the heat transfer coefficient, V instantaneous cylinder volume, P instantaneous cylinder pressure, T average gas temperature, C_m average piston speed, and C_1 and C_2 values are experimentally found constants of 13×10^{-3} and 1.4 respectively.

The knock intensity analysis is calculated with the following equation.

$$dp(\theta) = \frac{[86(p_{i-4}-p_{i+4})+142(p_{i+3}-p_{i-3})+193(p_{i+2}-p_{i-2})+126(p_{i+1}-p_{i-1})]}{1118d\theta} \quad (9)$$

Here is γ is the specific temperature coefficient, Q is the apparent heat release rate calculated by the experimental equation (J). P is the cylinder pressure (bar), V is the instantaneous volume of the cylinder (m^3) and Q_w is the temperature transfer coefficient and J is calculated from the cylinder wall based on the Hohenberg equation.

2.2.3. Average gas temperature

Average gas temperature results are taken from the regional environments of the gas temperature in the combustion chamber. The expansion stroke is considered to be polytropic and the average gas temperature is calculated by the following equation.

$$T_i = P_i V_i \frac{T_{ref}}{P_{ref} V_{ref}} \quad (10)$$

Here is T_i ; average gas temperature, P_i and V_i simultaneous pressure and cylinder volume; T_{ref} , P_{ref} and V_{ref} are reference parameters at any point on the polytropic expansion curve.

3. EXPERIMENTAL RESULTS AND DISCUSSION

Figure 2 shows the variation of the cylinder pressure values of the test fuels with respect to the crank angle of at 1500 rpm at 10.8 kW load. The highest cylinder pressure was observed for D35LPG65 fuel. The lowest cylinder pressure was observed for D100, pure diesel fuel. Generally, as the rate of LPG used increases, the pressure curve changes almost proportionally. This is considered to be due to the increase in ignition delay. At the same time, the amount of fuel burned during the uncontrolled combustion period also increased, and resulted to an increased peak pressure. As a result, the formation of the pressure curve for the D35LPG65 fuel is quite different from the other fuels and it can be said that this curve constitutes a diesel knock limit in the use of LPG. The reasons for this situation, which are accompanied by an increase in the LPG ratio; it that the LPG is a gasoline-like fuel with low cetane number, high auto ignition temperature and high flame speed after burning.

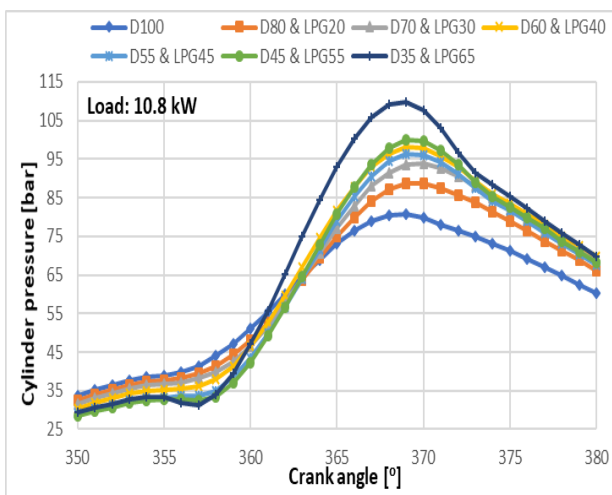


Figure 2. Cylinder pressure change with crank angle for test fuels

As can be seen in Figure 3, the highest heat release rate was observed for the D35LPG65 fuel. The lowest heat release rate was observed for pure diesel fuel D100. The formation of the heat release curve for D35LPG65 fuel is considerably different compared to the other fuels. This situation is due to the characteristics of LPG as mentioned above. As it can be seen in Figure 3, the combustion process of the D35LPG65 fuel is delayed, and after the combustion starts, there is an uncontrolled and rapid combustion that lead to excessive heat release in the combustion chamber. This can be attributed to the prolonged ignition delay period and

the accumulated amount of fuel and flame speed, which is high after combustion starts.

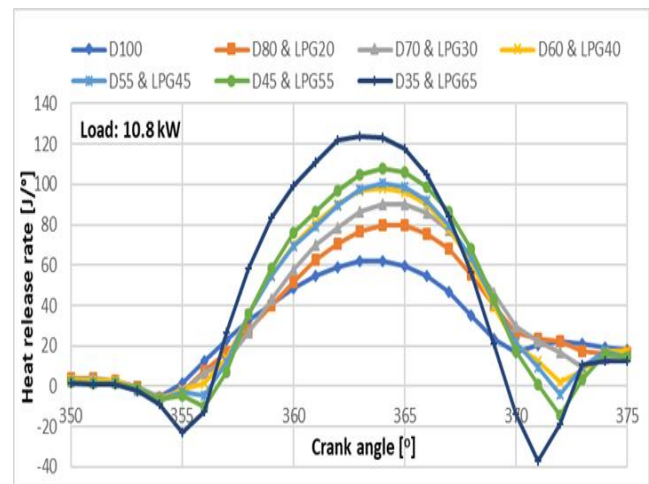


Figure 3. Change in rate of heat release rate for test fuels

As can be seen in Figure 4, the highest total heat release was observed for D35LPG65 fuel. The lowest total heat release was observed for pure diesel fuel D100. Total heat release curves differed from the diesel fuel with increased LPG amount. The total heat release curve due to the use of D35LPG65 fuel is quite different and the reasons of these are due to the characteristics of LPG as mentioned earlier.

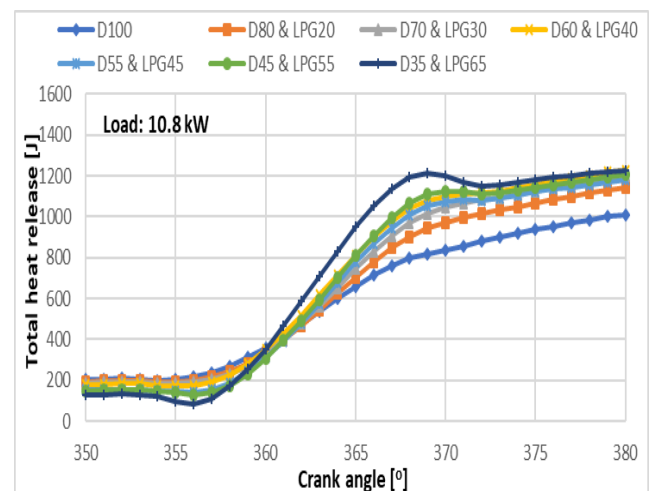


Figure 4. Crank-related change in total heat release rate

As can be seen in Figure 5, the highest average gas temperature was observed for D35LPG65 fuel. The lowest average gas temperature was observed for pure diesel fuel D100. The use of D35LPG65 fuel resulted in very high cylinder temperatures. All of the combustion results mean that 50% of LPG usage can be allowed. But above the mentioned reasons that the combustion can be classified as a diesel knock. The increase in exceeding heat transfer zones created by the turbulent flame zones in the combustion chamber during the diesel knock causes an increase in the overall hot combustion chamber. For this reason, the average cylinder gas temperatures are maximized in the case of D35LPG65.

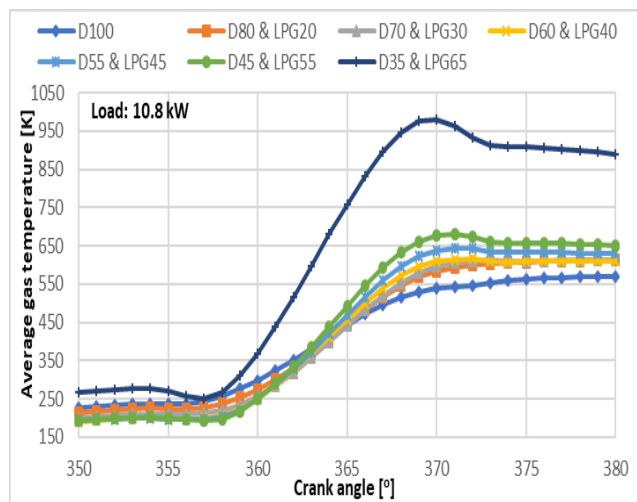


Figure 5. Crank-related change in average gas temperature

In Figure 6, burning of D35LPG65 fuel which also can be supported by the figures given above is classified as the knock as mentioned earlier. In the case of the D35LPG65, the knock intensity values were maximized. In general, the increase in the LPG ratio has increased the tendency to knock.

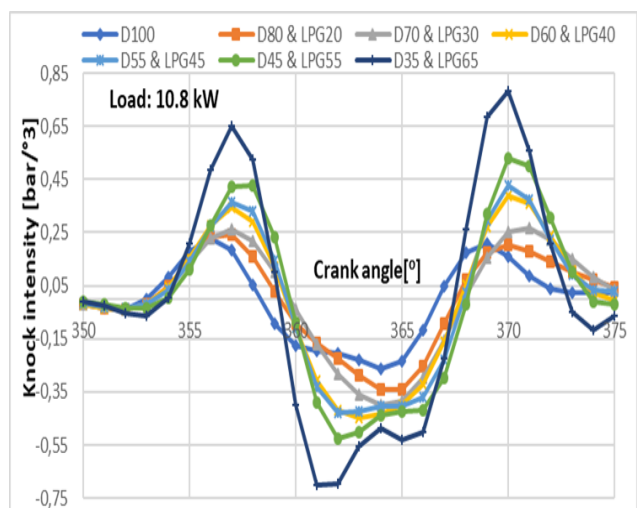


Figure 6. The change of the knock intensity due to cranking

Figure 7 graphically shows the amount of specific fuel consumption for each fuel at full load. When the figure was examined, the lowest specific fuel consumption was observed for pure diesel (D100). This ratio was increased significantly when using 45% and 55% LPG. The highest specific fuel consumption was observed for the D35LPG65. In fact, the unsteadiness in the engine operation was increased when the LPG ratio was increased. Therefore, the specific fuel consumption was reduced due to the cyclic changes and reduced engine speed along with knocking. Reduction in engine speed resulted in reduced specific fuel consumption in the case of D35LPG65. This was reduced engine power as well. As a result, specific fuel consumption was increased. However, the use of LPG up to approximately 50% did not adversely affect the engine's excessive specific fuel consumption and unsteady engine operation.

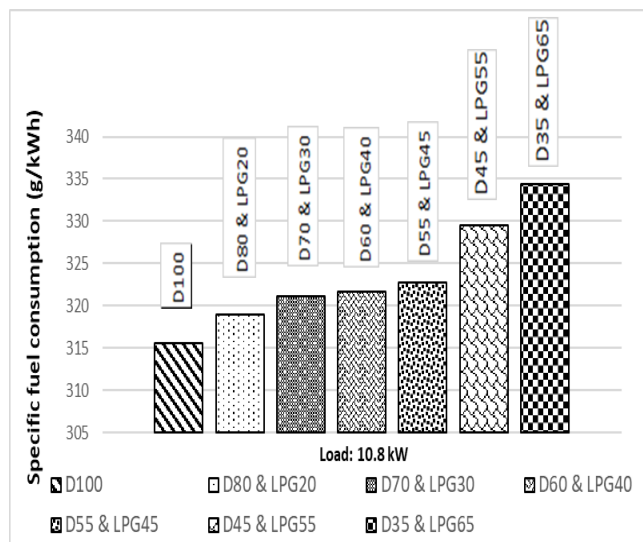


Figure 7. Changes in specific fuel consumption with LPG ratio

Figure 8 represents thermal efficiency values that symbolize the ratio of heat energy generated by combustion of the fuel to the engine converting rate of this energy into useful work. According to the obtained graphical results, the highest thermal efficiency was observed for pure diesel (D100). In general, thermal efficiency drops due to the use of LPG. The lowest thermal efficiency was observed for the D35LPG65 operating mode. Since the use of LPG is limited by knocking, it is not possible to calculate and interpret the thermal efficiency for D35LPG65.

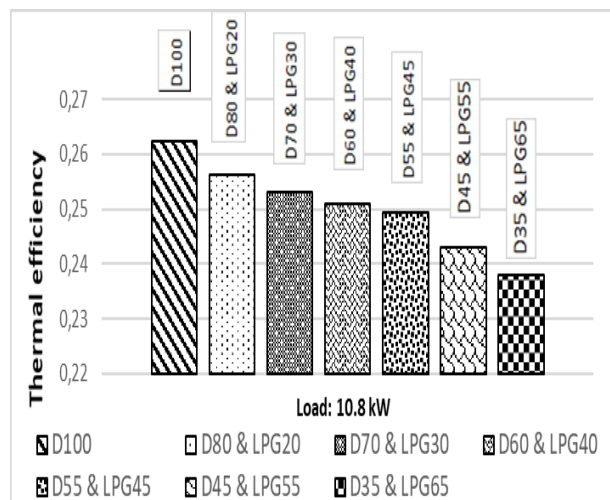


Figure 8. Variation of thermal efficiency values according to LPG ratio

Figure 9 shows the temperature of the gases passing through the exhaust manifold. The lowest exhaust gas temperature according to the graphs was observed for pure diesel fuel D100. Besides, as the LPG addition was increased, there was a steady increase in the overall exhaust gas temperature. The highest exhaust gas temperature was observed for D35LPG65 fuel.

The exhaust gas temperature of the dual fuel operation is higher than the single fuel operation. This is probably due to the fact that the end-of-combustion temperatures in the cylinder during the dual-fuel operation are higher than the end-of-combustion temperatures for single-fuel operation.

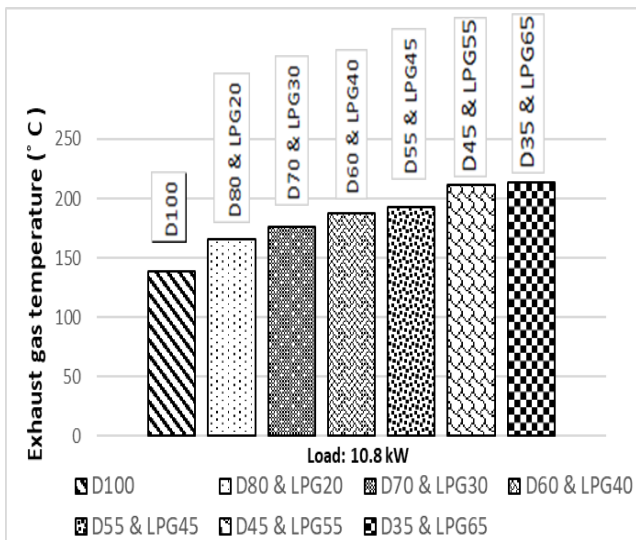


Figure 9. Variation of exhaust manifold temperature according to LPG ratio

The exhaust gas temperature is also increasing with the increase of the temperature inside the cylinder. The increase in exhaust gas temperature is indirectly related to nitrogen oxide emissions [16].

Figure 10 shows the mass fuel consumption for the test fuels. The highest mass fuel consumption according to the graphs was observed in the D35LPG65 operation. The lowest mass fuel consumption was observed for pure diesel fuel D100. Namely, fuel consumption was increased when the LPG ratio was increased. However, with the use of excessive LPG, the mass fuel consumption was reduced due to the change in speed caused by the unsteady operation of the engine together with the formation of the engine knock. The decline in engine speed resulted in a reduction in mass fuel consumption after the D35LPG65. Actually, it can be said that mass fuel consumption was also increased. However, the use of LPG until approximately 50% did not have a negative effect on engine operation.

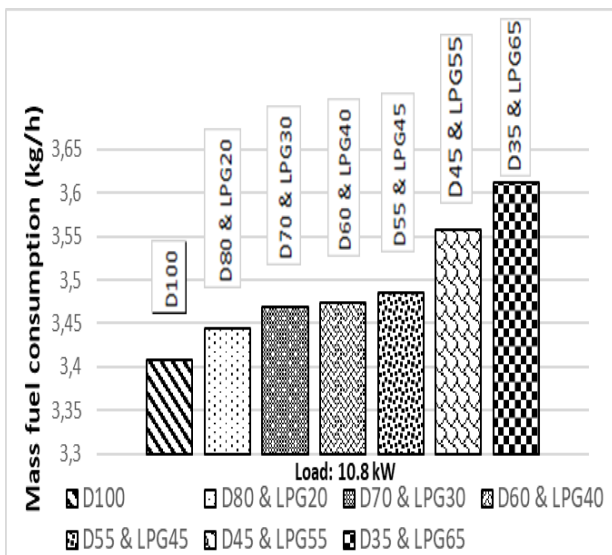


Figure 10. Change of mass fuel consumption by LPG ratio

Figure 11 shows the changes in CO emissions of fuels. The lowest amount of CO emissions was observed for pure diesel fuel D100. As the amount of LPG increased, the

in-cylinder charge was enriched and increased the CO emissions.

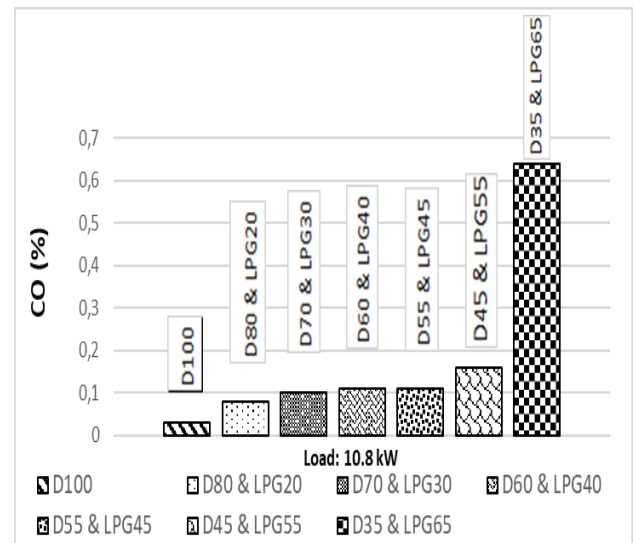


Figure 11. Change of CO emission according to LPG ratio

The main reason for the presence of CO in combustion products is the inadequate oxygen amount. Considering the combustion chamber as, oxygen may generally be inadequate, but if the mixture is not completely homogeneous, the oxygen may also be inadequate at a certain place in the combustion chamber. As a main reason, CO formation varies as a strong function of the air excess factor. The fact that the distribution of fuel in the combustion chamber is not the same prevents the combustion to occur in a uniform condition. For this reason, there will be an increase in the incomplete reaction and incomplete combustion of hydrocarbons. Namely, the CO formation is due to reasons such as heterogeneous distribution of air in the combustion chamber, insufficient oxygen and low reaction temperature [25].

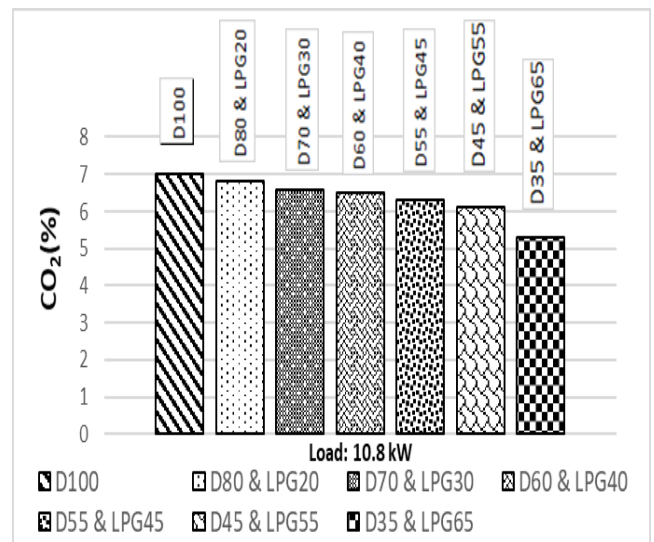


Figure 12. Change of CO2 emission according to LPG ratio

The changes in CO₂ emissions of the fuels used in the experiment are shown in Figure 12. When the graphs are analyzed, it is observed that the use of LPG-added diesel fuel according to D100, which is the CO₂ emission change pure diesel fuel, shows a steady decrease to the 40% LPG ratio

and a significant decrease in the CO₂ level in the mixture with more than 40% LPG. The lowest CO₂ emission by graph was observed for D35LPG65 fuel. In the cases of D45LPG55 and D35LPG65, as the amount of fuel entering increased, a rich mixture formed and CO emission increased, thus leading to a decrease in CO₂ emissions.

In flame fronts, reactions reach equilibrium when high temperatures are reached. However, good mixing of the blend and turbulent burning tend to increase the CO₂ ratios as the CO in the flame zone is converted to CO₂. The amount of CO₂ was lower in all LPG percentages than in the pure diesel fuel D100 fuel. This is thought to be due to the fact that the combustion temperature of LPG usage is lower that result in in-complete combustion. Another reason may be the rich fuel-air ratio of the burning charge with the use of LPG [26].

In Figure 13, the lowest HC release was for pure diesel (D100). The highest HC emissions were observed for D35LPG65 fuel.

With the addition of LPG, there was an increase in HC emissions in general. Increasing the amount of LPG reduces the amount of diesel fuel in dual-fuel experiments. The reduction in diesel fuel also causes a decrease in the heat energy that will increase the LPG usage. The increase in the amount of HC emissions in the LPG usage may be caused in-complete combustion due to the fuel rich zones in the combustion chamber. It is thought that the rapid increase of HC amount is due to the beginning of irregular burning [16]. In addition, with the use of LPG, HC emissions are seen to increase considerably. This can be interpreted as the deterioration of the air fuel ratio and the lack of oxygen in the combustion chamber.

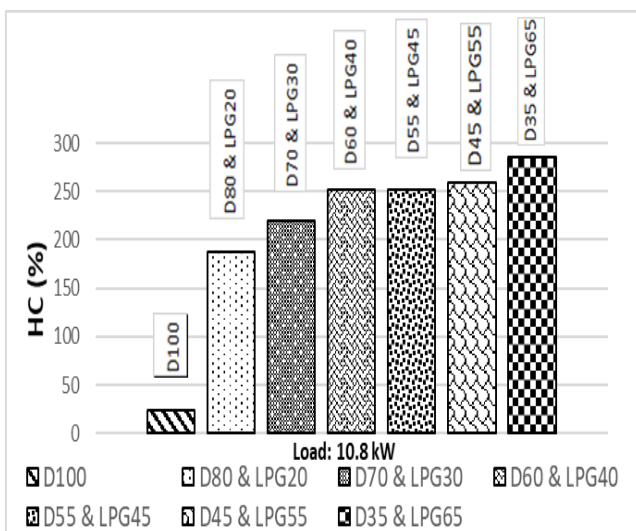


Figure 13. Change of HC emission according to LPG ratio

As seen in Figure 14, the O₂ measurements of pure diesel fuel (D100) and dual fuel D80LPG20 and D70LPG30 were almost similar. D45LPG55 decrease was about 6%, while there was a decrease of about 19% in D35LPG65 usage.

A reduction in the amount of air in the cylinder reduces the amount of oxygen released from the exhaust. Because LPG-homogeneous mixture with air causes more air around the fuel particles during the combustion, it also causes decrease of oxygen amount. In addition, in dual fuel

experiments, the amount of air in the cylinder is as low as the amount of LPG taken into the cylinder, resulting in a low amount of oxygen due to the relatively rich fuel-air mixture [26].

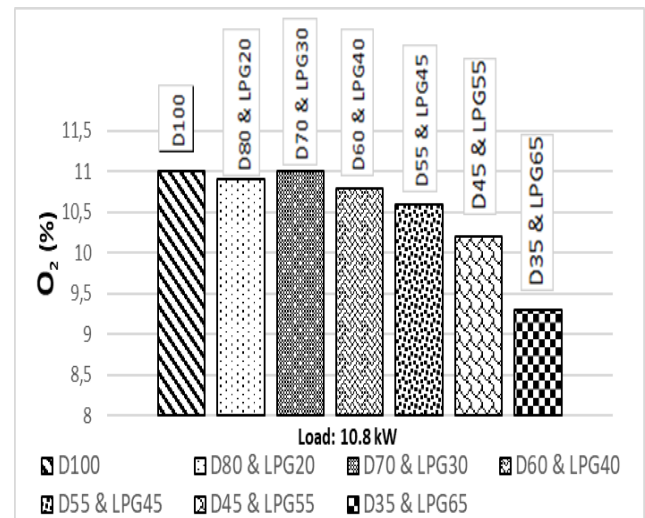


Figure 14. Change of O₂ emission according to LPG ratio

As shown in Figure 15, initially the NO_x values of pure diesel fuel (D100) and LPG RCCI modes were similar. The highest NO_x value was observed for D35LPG65 fuel. With increasing LPG ratio, there was usually a decrease in NO_x emission values. However, there were increases in NO_x emissions for LPG55 and LPG65 modes. This may be attributed to the increased uncontrolled combustion phase due to the increased combustion chamber temperatures and knock formation. In general, it is observed in the graph that there was a decrease in NO_x emissions as the LPG content increases.

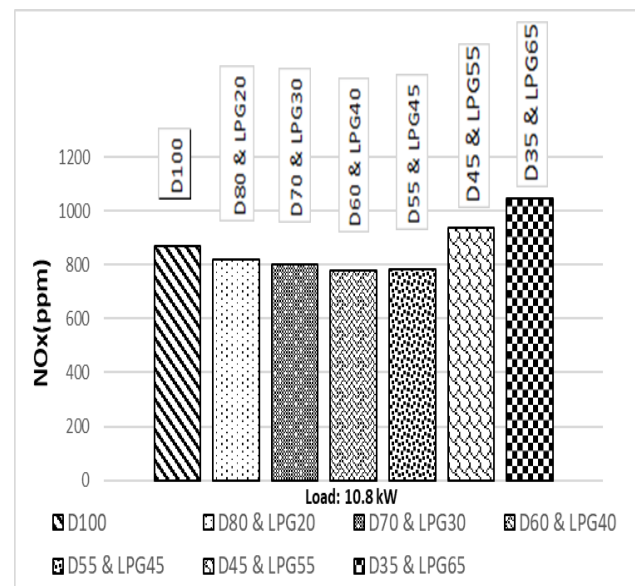


Figure 15. Change of NO_x emission according to LPG ratio

The density of the smoke values according to the LPG ratio is shown in Figure 16. As can be seen, the increase in the pilot LPG ratio reduced the density of exhaust gases, so the amount of smoke. However, after a certain LPG rate, the deterioration of the combustion caused the smoke density

values to increase again. The ideal smoke density values were observed in the D55LPG45 mode.

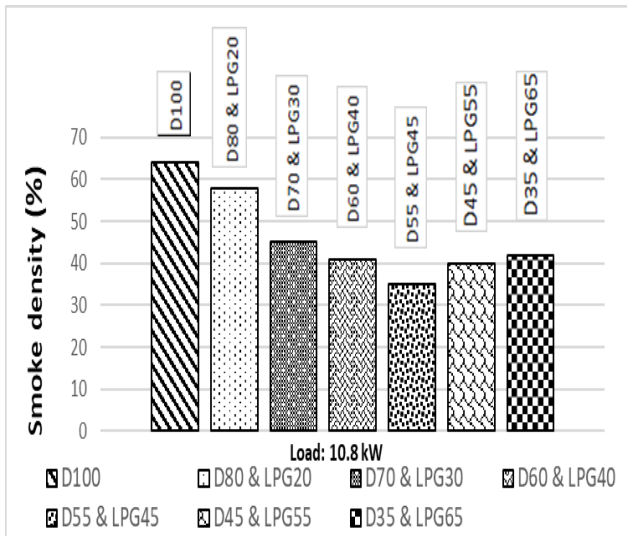


Figure 16. Change of smoke density values according to LPG ratio

4. CONCLUSIONS

In this study, engine performance, combustion and emissions a diesel engine used for driving an electrical generator was investigated with LPG fumigation into the manifold of the engine as secondary fuel. Briefly the following results were obtained.

According to the results obtained from the experiments; an increase in cylinder pressure was observed with increase in the LPG ratio in general and it was seen as the tendency of knocking when the LPG ratio was excessively high. Exhaust gas temperatures were deteriorated up to 54% with amount of LPG. It can also be said that specific fuel consumption and mass fuel consumption were also increased up to %12 while the mixture of high amount LPG with diesel is decreased 3%. Over 55% LPG fumigation resulted in quite high flame velocity and propagation which eventually resulted in the accelerated pressure increase for per crank angle. This condition may be accepted as the starting of the knock. Therefore only certain low amounts of LPG usage as secondary nonreactive fuel in diesel engine were found to be possible.

When examining emission test results; up to 2033% increase was observed for CO emission and up to 1088% of HC emission was increased as well. CO and HC emission values were increased with the addition of LPG. With increasing LPG, there was a decrease in the NO_x emission values. That decrease was up to 16%. As can be seen, the increase in the pilot LPG ratio reduced the density of exhaust gases, so the amount of smoke. However, after a certain LPG rate, the deterioration of the combustion caused the smoke density values to increase again. The ideal smoke density values were observed in the D55LPG45 mode.

In general, experiments have shown that the use of LPG as a secondary fuel in diesel engines makes it possible to use LPG at certain rates instead of diesel fuel in terms of similar combustion, performance and emission values.

Usage of LPG in engine improve exhaust emissions better than existing fuels and in order to increase efficiency along improved emissions, some additives for LPG can be tested. Additionally, the effect of LPG usage on engine parts should be evaluated for a long term. In the future study, cost analysis and current resources of LPG can be made to demonstrate its position in market. Lastly, the impact of advanced injection technologies such as pilot injection is needed to demonstrate and compare with this paper.

REFERENCES

- [1] Ögüt, H., and R. Kus. (1999). Alternative fuel usage in motor vehicles, II. Transportation and traffic congress report book, TMMOB, *Mechanical Engineering Publishing*. 149-162.
- [2] Ünal, F. (2021). Energy and exergy analysis of an industrial corn dryer operated by two different fuels. *International Journal of Exergy*, 34(4), 475-491.
- [3] Sertcelik, N. Effects of using LPG in dual fuel diesel engine on performance and emission, Master's thesis, Gazi university, Ankara, TR, 2010.
- [4] Gümüş, M. (2009). The effect of LPG using ratio on performance and emission characteristics in a spark ignition engine with dual fuel injection, *The Journal Of The Engineering And Architecture Faculty Of Gazi University*, Vol. 24, No. 2, 265-273.
- [5] S. Kannan, S. Mahalingam, S. Srinath, M. Sivasankaran, and S. Kannan, "An experimental study in HCCI combustion of LPG in diesel engine," *Mater. Today Proc.*, vol. 37, pp. 3625–3629, 2021, doi: <https://doi.org/10.1016/j.matpr.2020.09.774>.
- [6] E. Anye Ngang and C. V. Ngayihi Abbe, "Experimental and numerical analysis of the performance of a diesel engine retrofitted to use LPG as secondary fuel," *Appl. Therm. Eng.*, vol. 136, pp. 462–474, 2018, doi:<https://doi.org/10.1016/j.applthermaleng.2018.03.022>.
- [7] T. Vinoth, P. Vasanthakumar, J. Krishnaraj, S. K. ArunSankar, J. Hariharan, and M.Palanisamy, "Experimental Investigation on LPG + Diesel Fuelled Engine with DEE Ignition Improver," *Mater. Today Proc.*, vol. 4, no. 8, pp. 9126–9132, 2017, doi: <https://doi.org/10.1016/j.matpr.2017.07.268>.
- [8] G. Guan, C. S. Cheung, Z. Ning, P. K. Wong, and Z. Huang, "Comparison on the effect of using diesel fuel and waste cooking oil biodiesel as pilot fuels on the combustion, performance and emissions of a LPG-fumigated compression-ignition engine," *Appl. Therm. Eng.*, vol. 125, pp. 1260–1271, 2017, doi:<https://doi.org/10.1016/j.applthermaleng.2017.07.17>.
- [9] A. Rimkus, M. Melaika, and J. Matijošius, "Efficient and Ecological Indicators of CI Engine Fuelled with Different Diesel and LPG Mixtures," *Procedia Eng.*, vol. 187, pp. 504–512, 2017, doi: <https://doi.org/10.1016/j.proeng.2017.04.407>.
- [10] A. IRGIN, M. AYDIN, and M. B. ÇELİK, "Tek Silindirli Bir Dizel Jeneratörde Dizel/LPG Çift Yakıtının Performans ve Emisyonlara Etkisi," 2017.
- [11] A. Nugroho, N. Sinaga, and I. Haryanto, "Performance of a compression ignition engine four strokes four cylinders on dual fuel (diesel-LPG)," in *AIP Conference Proceedings*, 2018, vol. 2014, no. 1, p. 20166.
- [12] F. Ünal, H. Bulut, and A. KAHRAMAN, "Lpg Yakıtlı Endüstriyel Yatay Tip Mısır Kurutma Tesisinin Enerji ve Maliyet Analizi," *DÜMF Mühendislik Derg.*, vol. 11, pp. 161–170, Mar. 2020, doi: [10.24012/dumf.452540](https://doi.org/10.24012/dumf.452540).
- [13] S. Aliustaoglu and V. Ayhan, "Direk Enjeksiyonlu Bir Dizel Motorda Lpg-Dizel Çift Yakıt Karışımının Performans Ve İş Emisyonlarına Etkileri," *İleri Teknol. Bilim. Derg.*, vol. 8, no. 2, pp. 109–116. 2019.
- [14] S. Sendilvelan and C. Sundarraj, "Performance and emission study on a dual fuel engine with modified gas inlet," *Int. J. Heat Technol.*, vol. 34, no. 3, pp. 545–550, 2016.
- [15] Aktaş, A., and O. Doğan. (2010). Effect of LPG percentage to performance and exhaust emissions in a dual fuel engine, *The Journal Of The Engineering And Architecture Faculty Of Gazi University*, Vol. 25, No. 1, 171-178.
- [16] Yiğit, A. The usage of LPG in a diesel engine and the observation of the effects of different kinds of pilot diesel fuel on the

- performance of the engine and emission, Master's thesis, Karabuk university, Karabuk, Tr, 2008.
- [17] Saleh, H.E. 2008. Effect of variation in LPG composition on emissions and performance in dual fuel diesel engine, *Fuel*, Vol.87, No.(13-14), 3031–3039. doi:10.1016/j.fuel.2008.04.007.
- [18] Aydın, F., and M. Acaroğlu, (2009). Investigation of vehicle performance and exhaust in sequential gas phase LPG injection system, 10. Combustion Symposium.
- [19] Alla, G.A., H. Soliman, and O. Badr, M.A. Rabbo, (2000). Effect of pilot fuel quantity on the performance of a dual fuel engine, *Energy Conversion and Management*, Vol. 41, No. 6, 559-572. doi:10.1016/S0196-8904(99)00124-7.
- [20] Çarman, K., S. Salman, and M. Ciniviz. (2001). Effects on performance and emissions using diesel fuel and LPG on the diesel engines, *Technical Online Journal Faculty Of Selçuk University*, Vol. 2, No. 1, Issn, 1302-6178
- [21] Jothi, N.M., G. Nagarajan, and S. Renganarayanan. (2007). Experimental studies on homogeneous charge CI engine fueled with LPG using DEE as an ignition enhancer, *Renewable Energy*, Vol.32, No.9, 1581–1593. doi:/10.1016/j.renene.2006.08.007.
- [22] Qi, D., Y. Bian, Z. Ma, C. Zhang, and S. Liu. (2007). Combustion and exhaust emission characteristics of a compression ignition engine using liquefied petroleum gas–Diesel blended fuel, *Energy Conversion and Management*, Vol. 48, No. 2, 500–509. doi:/10.1016/j.enconman.2006.06.013.
- [23] LPG System. Accessed November 20, 2017. <http://www.ipragaz.co/brosurler/dokmegaz/araci-firma-segmentasyon-katalogu.pdf>
- [24] Borat, O., M.A. Balcı, and A. Sürmen. 1994. Internal Combustion Engines, G.U. Technical Education Foundation Publications-2.
- [25] Koca, D. Ö. The experimental investigation of the diesel and LPG fuels together diesel engine, Master's thesis, Yıldız technical university, İstanbul, TR, 2013.
- [26] Ciniviz, M. Effect on performance and emission of using diesel fuel and LPG on diesel engines, Master's thesis, Selçuk university institute of science and technology, Konya, TR, 2001.

BIOGRAPHIES

Ahmet Aydın graduated from Department of Mechanical Engineering at University of Batman at 2014. He gained her MSc. degree at the same university at 2017. His main research fields are energy and internal combustion engines.

Hüseyin Aydın graduated from Department of Mechanical Education at University of Dicle at 2004. He gained his Ph.D. degree at the Firat university at 2011. He is working as Professor at University of Batman, department of Mechanical Engineering since 2011. His main research fields are combustion, automotive and energy.

Designing a Control Interface and PID Controller of CUK Converter

Davut Sevim^{1*} , Veysel Gider² 

^{1*} Batman University, Electrical and Electronics Engineering Department, Batman, Turkey. (e-mail: davut.sevim@batman.edu.tr).

² Batman University, Electrical and Electronics Engineering Department, Batman, Turkey. (e-mail: vyslgdr@gmail.com).

ARTICLE INFO

Received: Nov., 04. 2020

Revised: May, 20. 2021

Accepted: May, 26. 2021

Keywords:

CUK Converter
PID Controller
Transfer function

Corresponding author: *Davut Sevim*

ISSN: 2536-5010 / e-ISSN: 2536-5134

DOI: <https://doi.org/10.17694/ejt.821257>

ABSTRACT

The system of CUK converter, which is controlled by PI controller, is unstable due to excessive oscillations caused by excessive integrations. To remove this instability, a converter controlled with a proportional-integral-differential (PID) controller is used. The dynamic model of the system is found by the mathematical analysis of the converter. In this article, PID design and control of CUK converter has been implemented. A fourth-order parametric transfer function is obtained here. The converter is simulated in virtual environment by using the obtained parameters. To find the control parameters of the system, an interface design is carried out. The control parameters (P, PI and PID) of the system are obtained by using the Ziegler-Nichols method. The results were evaluated by simulating the system as uncontrolled, PID controlled and Regulated PID controlled. The performance of CUK converter at different values of parameters by using PID controller is found more effective than PI controller.

1. INTRODUCTION

Maximum power point tracking technique (MPPT) is used to make the most of solar cells and solar panels [1-2]. In order to obtain the maximum efficiency, the solar panel is wanted (required) to be operated at maximum power. This situation is only possible if the system remains at a certain voltage and current level. It also determines the MPP tracking performance of DC-DC (Direct Current - Direct Current) converter topologies [3].

The CUK converter topology allows the dc voltage source to be stepped up or stepped down through a single switching control. A variety of classical control methods have been applied to the CUK converter including PI/PID [25], linear state feedback [4-5], fuzzy-logic [6], and sliding mode control [7-8].

DC-DC CUK converter is one of the power converters used in many studies. The static and dynamic properties of CUK converters have been widely discussed in the literature, where powerful tools for analysis, modeling and design are available [9-14]. CUK converters feature excellent properties (capacitive energy transfer, integrity of magnetic components and use of full transformers) and good steady-

state performances (wide conversion ratio, smooth input and output currents).

In this study, the design and control of the CUK converter has been carried out. Mathematical analysis of the CUK converter has been done. Then, the state-space averaging technique has applied to find the dynamic model. A fourth-order parametric transfer function has been obtained here. Using the obtained parameters, the CUK converter was simulated in virtual environment and the results were evaluated. The transfer function has been done by using the Graphical User Interface (GUI) editor in the virtual environment. Here, an interface has been designed to find out the necessary control parameters of the system. The transfer function was created by entering the parameters of the converter with the designed interface. The control parameters (P, PI and PID) of the system were obtained by using the Ziegler-Nichols method. Uncontrolled and PID controlled simulation of the system was made and the results were evaluated. Finally, the effects based on the PID controller performance at different values of parameters of the CUK converter were examined. Optimal control values for the system were observed.

In order to control the fourth order system of the CUK converter, it must be reduced to the second-order [15]. With

the designed interface, control parameter values were calculated very quickly without reducing the degree of the system. In addition, the user can adjust the input parameters of the circuit to the desired values and display the results numerically and graphically on the same interface. The results obtained from the simulation are presented to the user in a short time and in integrity. Thus, it is thought that it will be beneficial to a certain extent in eliminating problems such as time constraints encountered in converter applications. In addition, the output of this study has the potential to make an important contribution to the electric vehicles, industry, communication and renewable energy sectors [16].

Excessive integration, which is one of the disadvantages of PI controller in previous studies, leads the system to instability. PID controller is most widely used in power converter control [17]. With the derivative factor and filter coefficient in PID control, it has been found to be more suitable for eliminating unwanted oscillations and instability. This study emphasizes filtering one of the disadvantages of PID's sensitivity to noise at the most appropriate value. In the study, the situations at different values of the switching frequency, which is one of the important parameters in converter design, were observed and system analysis was made.

2. CUK Converter

The CUK converter circuit is shown in Figure 1. The output voltage can be greater or smaller than the input voltage. There is a reverse polarity at the output. Here, the converter works according to the open and closed state of the switch. It can be applied where very low input and output noise is required [18].

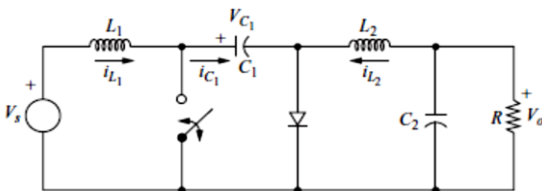


Figure 1. CUK Converter Circuit

The open state matrix (A_1) and the closed state matrix (A_2) of the switch are shown in Equation (1).

$$A_1 = \begin{bmatrix} 0 & 0 & 0 & 0 \\ 0 & 0 & \frac{1}{L_2} & -\frac{1}{L_2} \\ 0 & -\frac{1}{C_1} & 0 & 0 \\ 0 & \frac{1}{C_1} & 0 & -\frac{1}{RC_2} \end{bmatrix} \quad A_2 = \begin{bmatrix} 0 & 0 & -\frac{1}{L_2} & 0 \\ 0 & 0 & 0 & -\frac{1}{L_2} \\ \frac{1}{C_1} & 0 & 0 & 0 \\ 0 & \frac{1}{C_2} & 0 & -\frac{1}{RC_2} \end{bmatrix} \quad (1)$$

The transfer function calculated from the state-space equation in Equation (2) is shown below parametrically.

2.1. PID Control

The PID controller has optimum control dynamics such as zero steady-state error, fast response (short rise time), minimum oscillation and higher stability. The necessity to use a derivative gain component in addition to the PI controller is to eliminate overshoots and oscillations that occur in the output response of the system. One of the main

advantages of PID controller is that it can be used with higher-level processes involving more than single energy storage [19].

PID controllers are considered as the best controllers in the control system family. Nichols Minorsky has published a theoretical analysis paper on the PID controller. The operating signal for PID control consists of the proportional error signal added by the derivative and integral of the error signal [20].

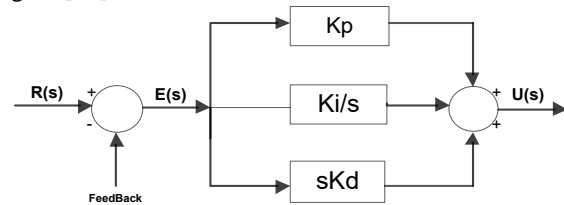


Figure 2. PID Control Block Diagram

Equation (3) contains the mathematical representation of the relationship between the input and output of the PID controller.

$$\frac{Eo(s)}{Ei(s)} = \left(Kp + \left(\frac{Ki}{s} \right) + sKd \right) = Kp \left(1 + \left(\frac{Ki}{sKp} \right) + \left(s \frac{Kd}{Kp} \right) \right) \quad (3)$$

2.2 Interface Design to Control and Calculate the Control Parameters

In this study, a graphical user interface was designed to simulate the CUK converter circuit from DC-DC converters by using the Graphical User Interface (GUI) editor included in the MATLAB program [21]. The transfer function of the system in the designed interface and the critical gain and critical time period of the transfer function created by using the Ziegler-Nichols method were calculated. The required control parameter values (P, PI, PID) for controlling the system were calculated with the calculated critical gain and critical time period.

In the system, the user will be able to adjust the input parameters of the circuit to the desired values and display the results numerically and graphically on the same interface. Thus, the simulation process and the results obtained will be presented to the user in a short time and in integrity, and it is thought that it will be beneficial in solving the problems such as time constraints encountered in converter circuit applications. The designed interface is shown in Figure 3.

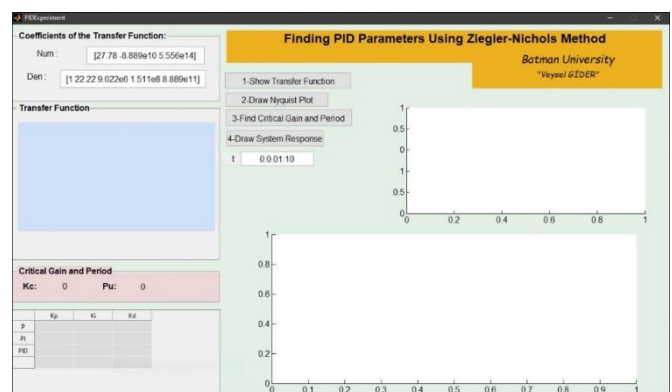


Figure 3. Interface created with MATLAB GUI

In the design, the transfer function is created automatically by writing the desired parameters in the code section. D (operation) ratio required for the system is

automatically calculated according to the input / output voltage value.

2.3. Ziegler-Nichols Method

PID controller is faster and less oscillating than PI controller. But with small changes in the input set point, the PID controller tends to be more unstable than PI controller even in the case of distortion. The Ziegler-Nichols Method is one of the most effective methods to increase the use of PID controllers. First, it is checked whether the desired proportional control gain is positive or negative [22]. This critical Kp value is reached as "Critical Gain", Kc, and the period in which the oscillation occurs is called Pu "Critical Time Period". As a result, the whole process depends on two variables and other control parameters are calculated according to Table 1. Ziegler-Nichols method values used in the calculation for control parameters are shown in the table below.

TABLE 1.
ZIEGLER-NICHOLS METHOD

Control Type	Kp	Ki	Kd
P	0.5 * Kc	-	-
PI	0.45 * Kc	1.2 * Kp/Pu	-
PID	0.6 * Kc	.2 * Kp/Pu	Kp / Ku/8

3. Analysis And Results Of The Simulation System

The parameters in Table 2 below were used for the CUK Converter. First, the mathematical analysis of the converter was done. Then the CUK converter was simulated and the results were observed. In order to control the designed interface transfer function and the system, necessary control parameters have been calculated.

TABLE 2.
CUK CONVERTER SYSTEM PARAMETERS

Parameters	V _i	L ₁	C ₁	L ₂	C ₂	R	V ₀	f _s	Duty
Values	25V	1mH	100µF	1mH	450µF	100Ω	100V	5kHz	0,8

The output voltage and current values of the system are found as follows. The output voltage, the output current on the load resistor and the output power on the load are calculated by putting the values into the Equation (4), Equation (5) and Equation (6).

$$V_0 = -V_s \cdot \frac{D}{1-D} = -25 \cdot \frac{0,8}{0,2} = -100V \tag{4}$$

$$I_0 = \frac{-V_0}{R} = \frac{-100V}{100} = -1A \tag{5}$$

$$P_0 = I_0^2 R = 1^2 100 = 100W \tag{6}$$

The currents on the L1 and L2 coils are calculated by putting the values into the Equation (7) and (8). Here, the average power supplied by the source should be the same as the average power dissipated by the load [18].

$$I_{L1} = \frac{P_s}{V_s} = \frac{100w}{25V} = 4A \tag{7}$$

$$I_{L2} = \frac{P_o}{-V_0} = \frac{100w}{-100V} = -1A \tag{8}$$

3.1. Uncontrolled Simulation Results of CUK Converter

At this stage, uncontrolled system analysis of the CUK converter was made.

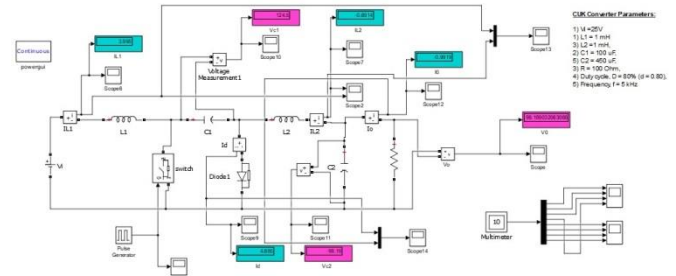


Figure 4. Uncontrolled CUK converter simulation of the created system

The output voltage and current values of the system were found as follows.

$$\begin{aligned} V_0 &= -99.189V \\ I_{L1} &= 3.995A \\ I_{L2} &= -0.6914A \\ I_0 &= -0.9919A \end{aligned}$$

Here, the average power (Ps) provided by the source and the power (Po) consumed by the load were calculated.

$$P_s = I_{L1} * V_s \tag{9}$$

$$P_s = 3.995A * 25V = 99.875W$$

$$P_o = I_{L2} * (-V_0) \tag{10}$$

$$P_o = -0.6914A * 99.189V = -68.57W$$

The current and voltage output graphs of the uncontrolled system of the CUK converter are as follows.

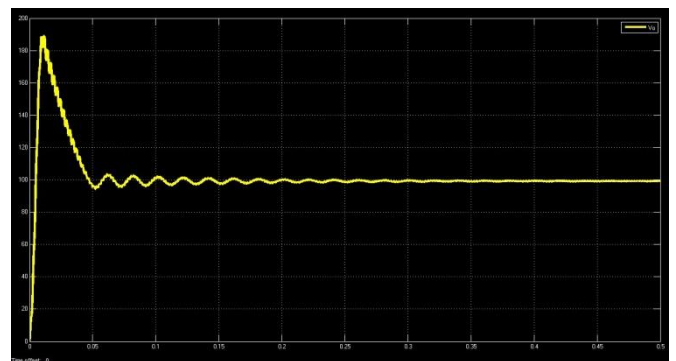


Figure 5. Output voltage (Vo) of uncontrolled CUK converter

Results of the mathematical analysis of the CUK converter and uncontrolled simulation are shown in Table 3, and power values are shown in Table 4.

TABLE 3.
Mathematical Analysis and Uncontrolled CUK Converter Results

	Mathematical Analysis	Uncontrolled Result
I _{L1} (A)	4	3.995
I _{L2} (A)	-1	-0.6914
I _o (A)	-1	-0.9919
V _o (V)	-100	-99.189

TABLE 4.

Mathematical Analysis and Uncontrolled CUK converter Power values

	Mathematical Analysis	Uncontrolled Result
$P_s(W)$	100	99.875
$P_o(W)$	-100	-68.57

As seen in Figure 5, the output voltage of the uncontrolled CUK converter value is 99.189 with a large amount of percentage (approximately more than 90%). This is also an undesirable and oscillating situation. A Control design is needed to eliminate overshoots and oscillations [23].

3.2. Finding the Transfer Function, Control Parameters and Their Results from the Interface

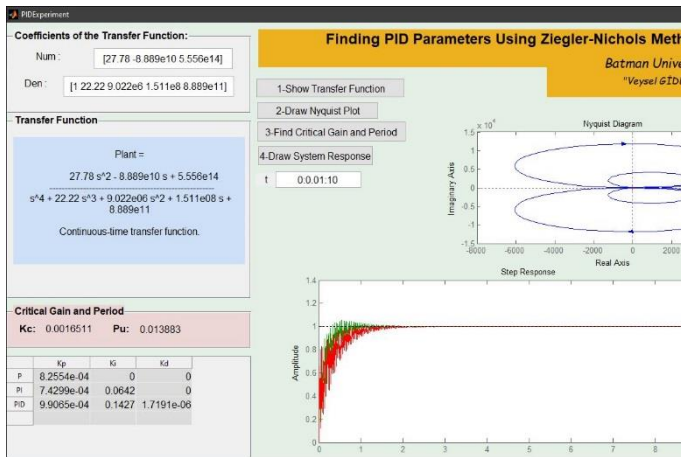


Figure 6. Finding the transfer function and control parameters from the interface

The transfer function of the system of which parameters are given in Equation (11) as seen below.

$$\frac{V_o(s)}{d(s)} = \frac{27.78s^2 - 8.889 \times 10^{10}s + 5.556 \times 10^{14}}{s^4 + 22.22s^3 + 9.022 \times 10^6s^2 + 1.511 \times 10^8s + 8.889 \times 10^{11}} \quad (11)$$

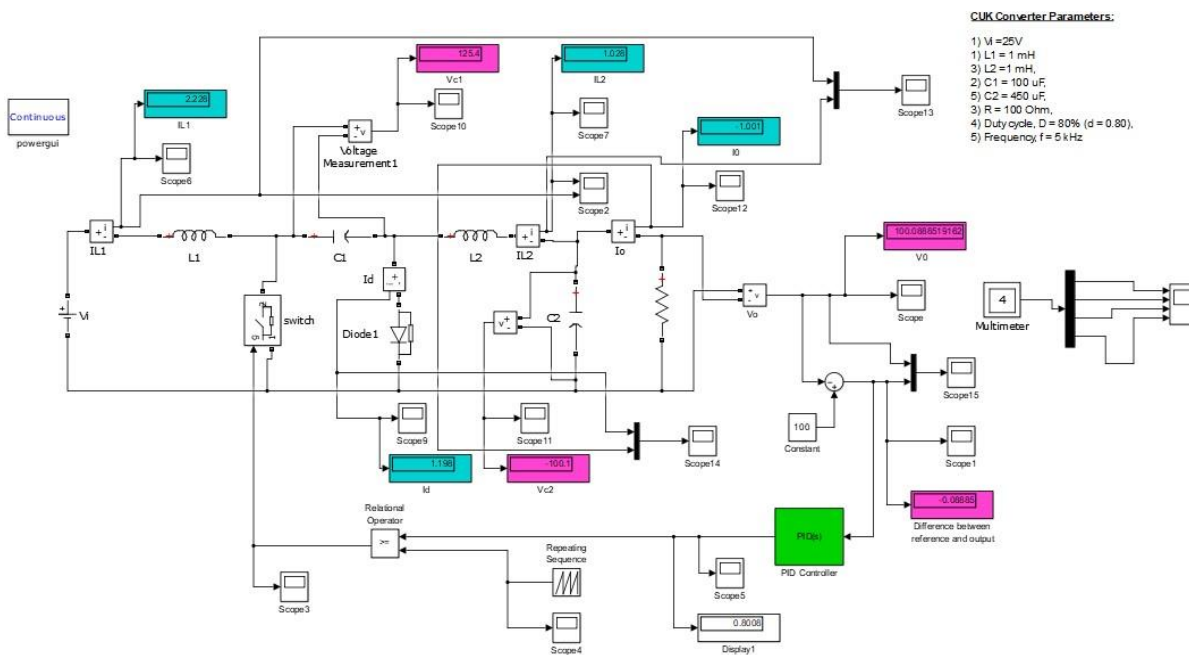


Figure 7. The CUK converter circuit with PID controller

The transfer function of the system is calculated in the designed interface. The critical gain of the transfer function generated by using the Ziegler-Nichols method was calculated as (Kc) = 0.0016511, critical time period (Pu) = 0.013883. The required control parameter values (P, PI, PID) for system control were calculated with the critical gain and critical time period calculated before. The values of PID controller parameters were selected as Proportional gain (Kp) = 0.00099065, Integral gain (Ki) = 0.1427, Derivative gain (Kd) = 0.0000017191, Filter coefficient (N) = 1000.

3.3. Simulation Results of CUK Converter with PID Controller

As seen in Figure 7, the system has been analyzed by performing the PID control process with the calculated Kp, Ki, Kd and N values of the CUK converter. The output voltage of the PID controlled circuit of the CUK converter is V0 = 100.089 V, current values IL1 = 2.228 A, IL2 = 1.029 A, IO = 1.001 A.

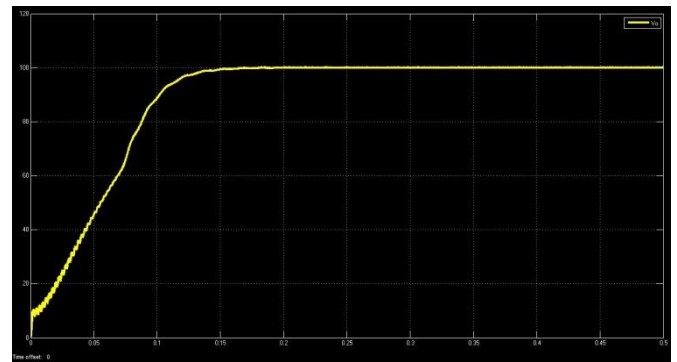


Figure 8. Output voltage (Vo) graph of PID controlled CUK converter

The output voltage (Vo) graph of the PID controlled CUK converter is shown in Figure 8.

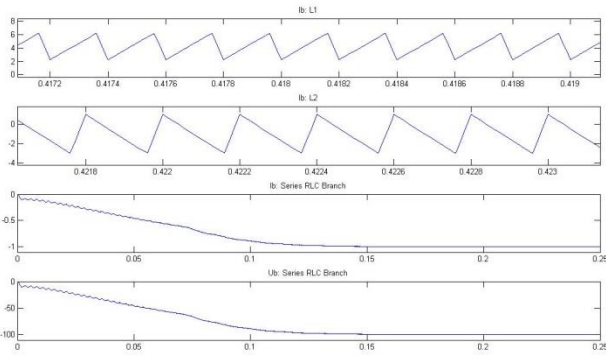


Figure 9. Graphs of current and output voltage (V_o) on L_1 , L_2 , R (I_{L1} , I_{L2} , I_o) of PID controlled CUK converter

Mathematical analysis results of CUK converter, uncontrolled and PID controlled results are compared in table 5.

TABLE 5.

Mathematical Analysis and Uncontrolled and PID Controlled		
Mathematical Analysis	Uncontrolled Result	PID Controlled Result
$I_{L1}(A)$	3.995	2.228
$I_{L2}(A)$	-0.6914	1.029
$I_o(A)$	-0.9919	1.001
$V_o(V)$	99.189	100.1

The purpose of designing a controller for the CUK converter is to both ensure the stability of the system and achieve a less steady-state error with minimal overshoot despite distortions in the input voltage. It is to regulate the output voltage by monitoring the set point value [24].

In the PID Controller block, the Filter coefficient (N) is the bandwidth of the low pass filter on the derivative. Pure derivatives are practically avoided as they increase the measurement noise. This low pass filter made by the PID controller block should be used. In order to get as close to the pure derivative as possible, the default filter coefficient values from 100 to 10000 are given.

In CUK converter with PI controller, the system is unstable due to the high oscillation caused by excessive integration. During system analysis with variables such as K_p , K_i , K_d in PID control, the filter coefficient that affects the K_d factor should be selected at the most appropriate value. One of the disadvantages of PID controller is that it is very sensitive to noise. The filter coefficient affects the steady-state error (e) of the system. The steady-state error is the difference between the reference input value and the output value. This difference is desired to be zero.

Figure 10-15 shows the comparison of the PID Tuner values in Simulink and the PID control parameters of the converter calculated at the interface. Here, how the different filter coefficient affects the system is examined.

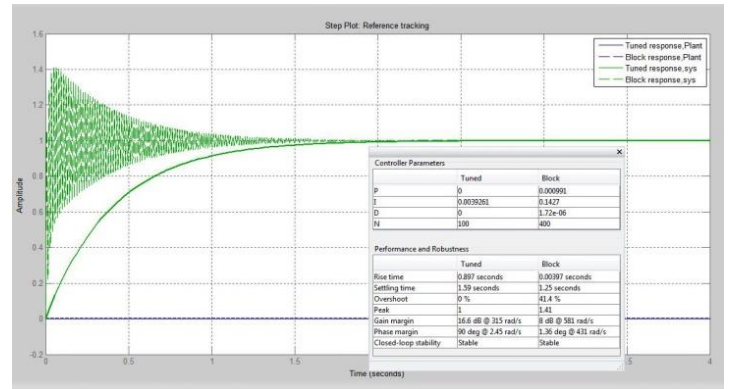


Figure 10. For filter coefficient N = 400

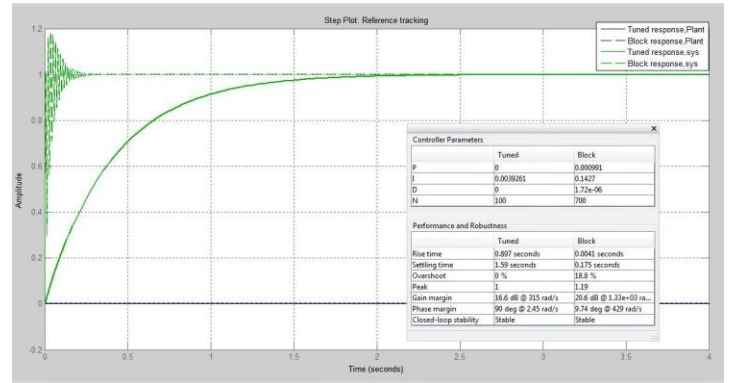


Figure 11. For filter coefficient N = 700

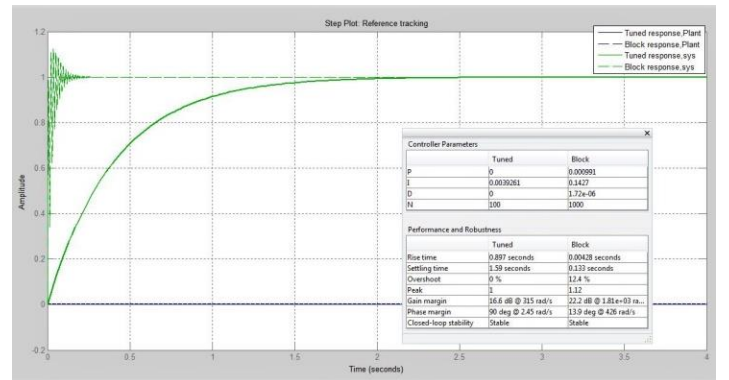


Figure 12. For filter coefficient N = 1000

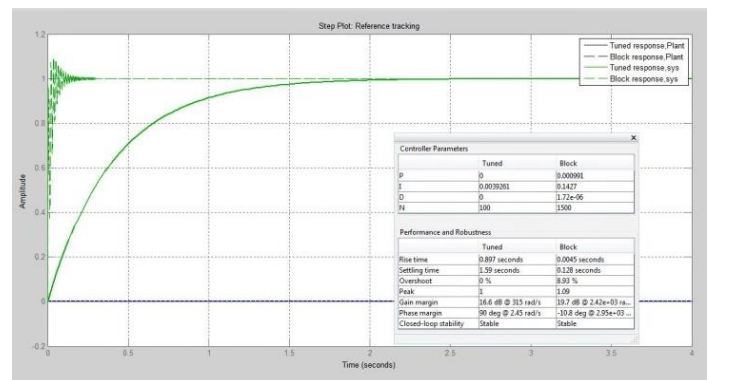


Figure 13. For filter coefficient N = 1500

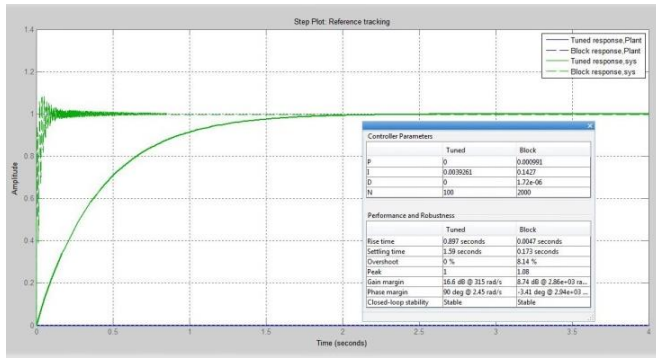


Figure 14. For filter coefficient N = 2000

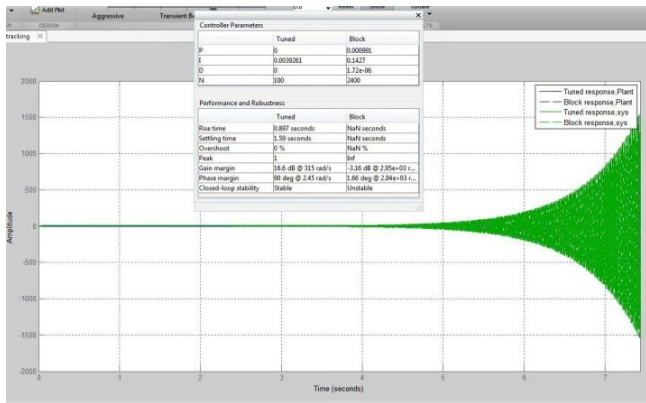


Figure 15. For filter coefficient N = 2400

The comparison of settlement time, rise time and overshoot values for different filter coefficients formed in Table 6 is included.

TABLE 6.

The Comparison of settlement time, rise time and overshoot values for different filter coefficients

Filter Coefficient N	Kp	Ki	Kd	Settlement time(sn)	Rise Time (sn)	Overshoot%
400	0,000991	0,1427	0,00000172	1,25	0,00397	41,4
500	0,000991	0,1427	0,00000172	0,343	0,004	29
600	0,000991	0,1427	0,00000172	0,22	0,00405	22,9
700	0,000991	0,1427	0,00000172	0,175	0,0041	18,8
800	0,000991	0,1427	0,00000172	0,155	0,00416	15,9
900	0,000991	0,1427	0,00000172	0,141	0,00422	13,9
1000	0,000991	0,1427	0,00000172	0,133	0,00428	12,4
1500	0,000991	0,1427	0,00000172	0,128	0,0045	8,93
2000	0,000991	0,1427	0,00000172	0,173	0,0047	8,14
2200	0,000991	0,1427	0,00000172	0,733	0,00474	8,37
2300	0,000991	0,1427	0,00000172	Unstable	Unstable	Unstable
2400	0,000991	0,1427	0,00000172	Unstable	Unstable	Unstable

Displayed in red are the reference parameter results used for system analysis.

When Table 6 and Figure 10-15 are examined; as the filter coefficient increases from N = 400 to N = 2000, the settlement time decreases, the rise time increases and the overrun decreases. At N = 2200, the rise time increases, although the overrun decreases, the sitting time increases. The system becomes unstable after N = 2300.

3.4. Input-Output Power Values for Different Switching Frequency Values (fs)

Table 7 shows the effects of different switching frequencies on coil currents. As the switching frequency increases, the "switching" losses of the switch also increase. In the study, the optimum switching frequency value can be selected from the table so that the average power value supplied by the source and the average power value consumed by the load are the closest values to the power values in the mathematical analysis results. According to the chart, it is the value where the power supplied by the source and the power consumed by the load are closest to each other, fs = 6.7 kHz.

TABLE 7.

The effect of different switching frequency (fs) values on input and output powers

Frequency fs(kHz)	Vi (V)	IL1 (A)	Input Power (W) (Vg * IL1)	Vo (V)	IL2 (A)	Output Power (W) (Vo * IL2)
1	25	2.117	52.295	101.376	-0.4669	-47.332
2	25	1.633	40.825	99.764	1.653	164.909
3	25	5.791	144.775	99.873	-2.682	-267.859
4	25	1.725	43.125	100.139	1.547	154.915
5	25	2.228	55.700	100.089	1.029	102.991
6	25	3.399	84.975	99.968	-0.164	-16.394
6.7	25	3.994	99.850	99.9977	-0.976	-97.597
7	25	4.233	105.825	99.954	-1.008	-100.7536
7.5	25	3.737	93.425	100.056	-0.4918	-49.2075
8	25	2.982	74.550	100.034	0.2607	26.0788
9	25	1.412	106.525	100.262	-3.646	-365.555

Displayed in red are the reference parameter results used for system analysis.

3.5. New System Regulated with Analysis

According to the study, many observations were made to select the system parameters at the most appropriate values. As a result of the observations, the organized state of the system parameters and PID controller parameter values has shown in the chart. Looking at Table 8, different from the previous system parameter, L1, L2 coil values and fs switching frequency values selected as a result of the analyzes have been changed. The system was analyzed again according to the changed values and results close to the desired values were obtained.

TABLE 8.

The parameters of the regulated CUK Converter system

Parameters	Vi	L1	C1	L2	C2	R	V0	fs	D
Values	25V	5mH	100µF	50mH	450µF	100Ω	100V	6.7kHz	0,8

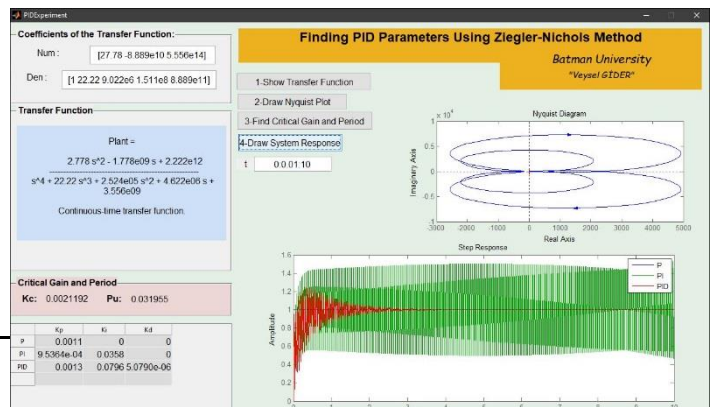


Figure 16. Finding the Transfer function and control parameters of the system regulated from the interface

The transfer functions and control parameter values of this regulated system are calculated from the designed interface.

The transfer function of the regulated system whose parameters are given is as in equation (12) below.

$$\frac{V_o(s)}{d(s)} = \frac{2.778s^2 - 1.778x10^9s + 2.222x10^{12}}{s^4 + 22.22s^3 + 2.524x10^5s^2 + 4.622x10^6s + 3.556x10^9} \quad (12)$$

PID values calculated from the interface of the regulated system were found to be Proportional gain (K_p) = 0.0013, Integral gain (K_i) = 0.0796, Derivative gain (K_d) = 0.0000050790, Filter coefficient (N) = 350. CUK converter circuit made with PID controller with regulated system parameters and its results are shown in Figure 16 below.

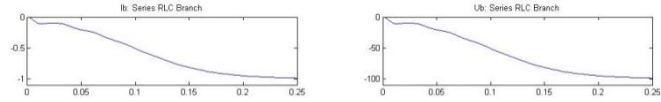


Figure 19. Graph of output current and voltage on the load resistance (I_o , V_o) of the PID controlled CUK converter of the regulated system

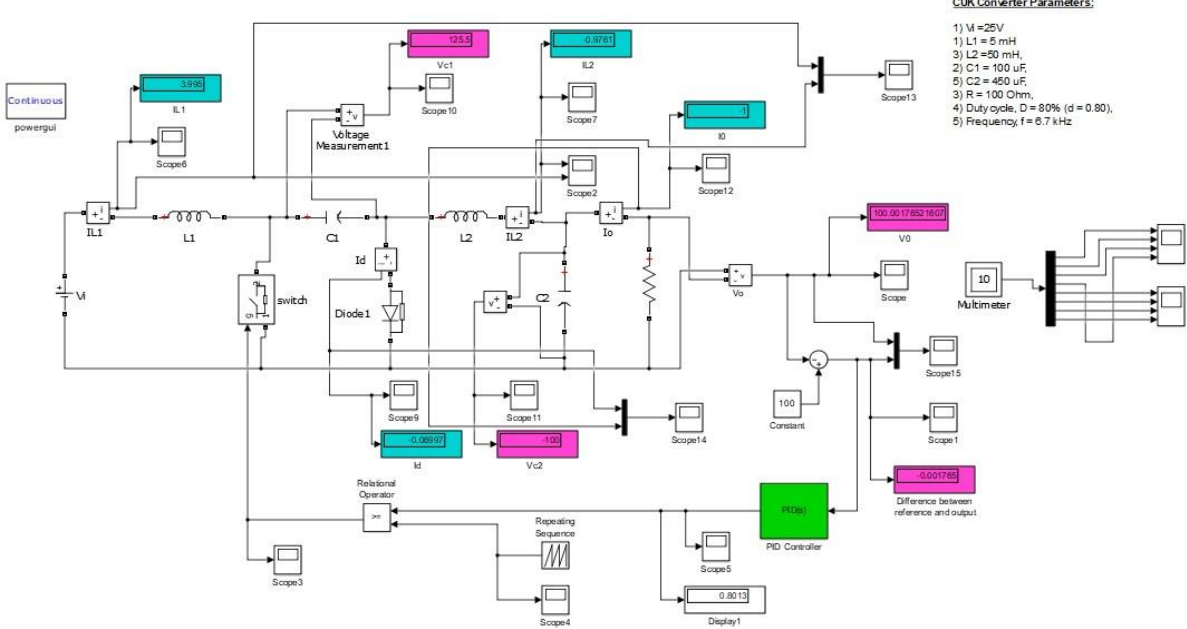


Figure 17. PID controlled circuit of the regulated system of the CUK converter.

The output voltage and current values of the PID controlled circuit of the regulated system of the created CUK converter were found as follows.

$$\begin{aligned} V_o &= 100.001772 V \\ I_{L1} &= 3.995 A \\ I_{L2} &= -0.9761 A \\ I_o &= -1 A \end{aligned}$$

Here, the average power P_s supplied by the source and the power P_o consumed by the load are calculated.

$$P_s = I_{L1} \cdot V_s \quad (13)$$

$$\begin{aligned} P_s &= 3.995 A \cdot 25 V = 99.875 W \\ P_o &= I_{L2} \cdot (-V_o) \quad (14) \\ P_s &= -0.9761 A \cdot (100.001772 V) = -97.612 W \end{aligned}$$

The output voltage (V_o) graph of the PID controlled CUK converter of the regulated system is shown in Figure 18.

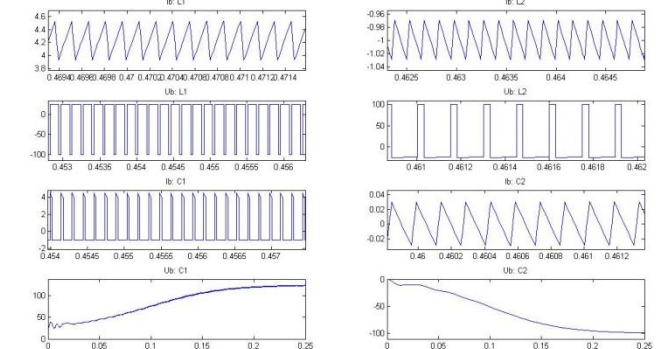


Figure 20. L_1 of the regulated system's PID controlled CUK converter Current and voltage graph on L_2 and $C_1, C_2, (I_{L1}, I_{L2}, V_{C1}, V_{C2})$

Mathematical analysis results, uncontrolled, regulated system PID controlled CUK converter current, voltage and power results are compared in Table 9 below.

TABLE 9. Mathematical Analysis, Uncontrolled, Regulated System and PID Controlled CUK Converter Results

	Mathematical Analysis	Uncontrolled Result	Regulated System PID Control Result
$I_{L1}(A)$	4	3.995	3.995
$I_{L2}(A)$	-1	-0.6914	-0.9761
$I_o(A)$	-1	-0.9919	-1
$V_o(V)$	-100	-99.189	-100
$P_s(W)$	100	99.875	99.875
$P_o(W)$	-100	-68.57	-97.612

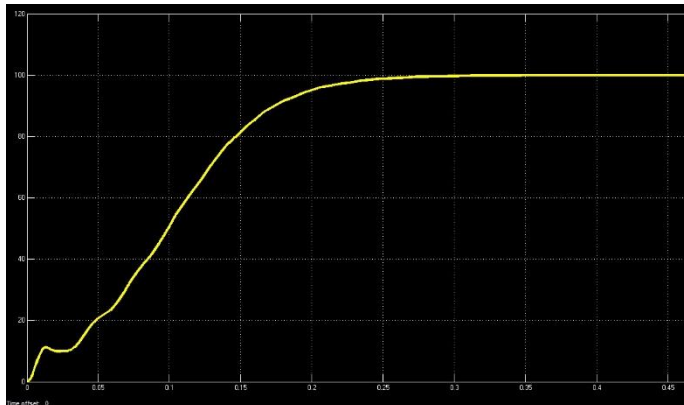


Figure 18. Output voltage graph of the PID controlled CUK converter of the regulated system

4. CONCLUSION

In PI-controlled CUK converter, the system is unstable due to excessive integration. In this article, proportional-integral-differential (PID) controller is used to eliminate the instability of the CUK converter. By simulating the converter in a virtual environment, the interface design was realized to find the control parameters of the system. The effect of CUK converter on PID control parameters is observed according to different component values. With these varying parameters, the effect of the system on rise time, residence time, overrun value, current and voltage values were investigated. In addition, different values of the filter coefficient in PID control and its effect on the controller have been observed. Comparisons of the PID control block diagram of the transfer function with the PID-controlled result and steady-state error of the CUK circuit were also made. It has been found that PID control performance is more effective than the PI control at different parameter values of CUK converter.

References

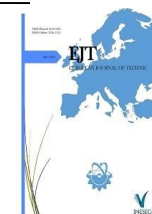
- [1] Safari, A., & Mekhilef, S. (2010). Simulation and hardware implementation of incremental conductance MPPT with direct control method using cuk converter. *IEEE transactions on industrial electronics*, 58(4), 1154-1161.
- [2] Diab-Marzouk, A., & Trescases, O. (2015). SiC-based bidirectional Cuk converter with differential power processing and MPPT for a solar powered aircraft. *IEEE Transactions on Transportation Electrification*, 1(4), 369-381.
- [3] A. Mizani and A. Shoulaie, (2020), "A New Non-isolated High Gain DC-DC Converter for Grid-Connected Photovoltaic Systems", doi: 10.1109/PEDSTC49159.2020.9088387.
- [4] Poudeh, M.B.; Eshtehardiha, S.; Ershadi, M.H., "Optimizing the Classic Controllers to Improve the Cuk Converter Performance Based on Genetic Algorithm," *Smart Manufacturing Application*, 2008. ICSMA 2008. International Conference on, pp.329-334, 9-11 April 2008.
- [5] Amato, F.; Cosentino, C.; Fiorillo, A.S.; Merola, A., "Stabilization of Bilinear Systems via Linear State-Feedback Control," *Circuits and Systems II: Express Briefs*, IEEE Transactions on, vol.56, no.1, pp.76-80, January 2009.
- [6] Rakshit, Saptarshi, and Jayabrata Maity. "Fuzzy logic controlled cuk converter." *International Conference on Communication and Signal Processing (ICCS)*. IEEE, 2018.
- [7] T. L. Skvarenina; *The Power Electronics Handbook*, Industrial Electronics Series; 2002, CRC Press LLC, G. Spiazzi; P. Mattavelli; Chap 8.
- [8] Chen, Zengshi. "PI and sliding mode control of a Cuk converter." *IEEE Transactions on Power Electronics* 27.8 (2012): 3695-3703.
- [9] Sahu, Tekeshwar Prasad, and T. V. Dixit. "Modelling and analysis of Perturb & Observe and Incremental Conductance MPPT algorithm for PV array using Cuk converter." *2014 IEEE Students' Conference on Electrical, Electronics and Computer Science*. IEEE, 2014.
- [10] Hanif, Omar, Zeeshan Rayeen, and Shipra Tiwari. "Design and comparative analysis of fractional order controllers for cuk converters." *2018 IEEE 8th Power India International Conference (PIICON)*. IEEE, 2018.
- [11] Tiwari, Shipra, Zeeshan Rayeen, and Omar Hanif. "Design and analysis of fractional order PID controller tuning via genetic algorithm for cuk converter." *2018 IEEE 13th International Conference on Industrial and Information Systems (ICIS)*. IEEE, 2018.
- [12] S. Choudhary, Piyush, and Som Nath Mahendra. "Feedback control and simulation of DC-DC Cuk converter for solar photovoltaic array." In *Electrical, Computer and Electronics Engineering (UPCON)*, 2016 IEEE Uttar Pradesh Section International Conference on, pp. 591-596. IEEE, 2016.
- [13] Huang, H. Xu, and Y. Liu, "Sliding mode controlled Cuk switching regulator with fast response and first-order dynamic characteristic," in *PESC 1989*, Milwaukee, WI, pp. 124-129.
- [14] P. Maranesi, L. Pinola, V. Varoli, and G. F. Volpi, "Analysis of the cuk converter in delta-V mode by charge and flux balances." in *ESPC 1989*. Madrid, Spain, pp. 409-414.
- [15] K. M. Smedley and S. Cuk, "One-cycle control of switching converters," in *PESC 1991*, Cambridge, UK, pp. 888-896.
- [16] Suguna S. ve Kumar M.S., (2017), "Design of Controller for CUK Converter Using Evolutionary algorithm via Model Order Reduction", *International Journal of Pure and Applied Mathematics Volume 114 No.8*, 297-307.
- [17] Adnan M.F., Oninda M.A.M., Nishat M.M. ve Islam N., (2017), "Design and Simulation of a DC-DC Boost Converter with PID Controller for Enhanced Performance", *International Journal of Engineering Research Technology (IJERT)* Vol. 6 Issue 09.
- [18] Ibrahim, O., Yahaya, N. Z. B., & Saad, N. (2016). "PID Controller Response to Set-Point Change in DC-DC Converter Control". *International journal of power electronics and drive systems*, 7(2), 294.
- [19] M. H. Rashid, *Power Electronics: Circuits, Devices and Applications*, 3rd ed., New Jersey: Prentice-Hall, 2003.
- [20] Temel, S., Yağlı, S. ve Gören, S. (2013). P, PD, PI, PID kontrolörleri. *Orta Doğu Teknik Üniversitesi, Elektrik ve Elektronik Mühendisliği Bölümü*.
- [21] Bennett, S. (1993). "PID kontrolörünün geliştirilmesi". *IEEE Kontrol Sistemleri Dergisi*, 13(6), 58-62.
- [22] MATLAB-MathWorks. (2014), *GUIDE Kullanarak Arayüz Oluşturma, Bilgisayar Programı*.
- [23] Ziegler, J.G. and Nichols N.B. (1942). Optimum Settings for Automatic Controllers, *Transactions of the A.S.M.E.*, 759-768.
- [24] Priyadarshini, D. ve Rai, S. (2014). "Düşürücü (Buck)-Yükseltici (Boost) and CUK Converter için bir PID Denetleyicisi Tasarımı, Modellemesi ve Simülasyonu". *Uluslararası Bilim ve Araştırma Dergisi (IJSR)*, 3(5).
- [25] A. F. Algamluoli. (2019), "Novel Controller for DC-DC Cuk Converter", doi: 10.1109/GPECOM.2019.8778545.

BIOGRAPHIES

Davut Sevim obtained his B.Sc. degree from Marmara University in 2001. In 2010, he started to work as a lecturer at Batman University. He received his M.Sc. degree from Firat University in 2009 and Ph.D. degree from Gazi University in 2017 respectively. He has been working at Batman University since 2010.

He works in the fields of circuits and systems and control systems.

Veysel Gider obtained his B.Sc. degree from Batman University in 2017. In 2019, he started to work as an Electrical-Electronic teacher at Batman Boğaziçi Collage. He received his M.Sc. degrees from Batman University in 2020. He has been Ph.D. at Diyarbakır Dicle University since 2020. He works in the fields of Electrical-Electronic engineering and Biomedical on artificial intelligence, machine learning and deep learning.



Modeling and Analysis of Pitch Angle Control on Variable Speed Wind Turbines

Hasan Bektas Percin¹ , Abuzer Caliskan² 

¹Firat University, Electrical, and Electronics Engineering Department, Elazig, Turkey. (e-mail: hbpercin@firat.edu.tr).

²Firat University, Electrical and Electronics Engineering Department, Elazig, Turkey. (e-mail: acaliskan@firat.edu.tr).

ARTICLE INFO

Received: Nov., 09. 2020

Revised: Apr., 05. 2021

Accepted: May, 06. 2021

Keywords:

Wind energy

Modeling

Matlab/Simulink

Pitch angle

Permanent magnet synchronous generator

Corresponding author: *Hasan Bektas Percin*

ISSN: 2536-5010 / e-ISSN: 2536-5134

DOI: <https://doi.org/10.17694/ejt.823439>

ABSTRACT

Nowadays, due to the increasing demand for electrical energy, investments in renewable energies are a satisfactory solution to meet this demand. Wind energy, which is one of these renewable energies, has many advantages such as low environmental impact, renewable structure, and decreasing system costs with developing technology. However, the instant changes of the wind, affect the sustainability of the system and the production efficiency negatively.

Maximum efficiency, stable and long-lasting operation is aimed at wind energy conversion systems with permanent magnet synchronous generators (PMSG). In line with these objectives, systems should be used with appropriate control structures. Modeling studies in the computer environment allow analyzing the different controls to be used in energy conversion, which can be difficult and costly to work on the real system. These studies provide analysis, comparison of various control parameters, and adjustments before system installation. Thus, the problems can be prevented before the installation, higher performance and less costly designs can be achieved.

In this study, the basic components and parameters of the wind energy system were explained and mathematical models of these parameters were obtained. The working principle of the control structures for the system was explained through these models. The general system modeling, which includes pitch angle control for higher wind speeds, was designed in Matlab/Simulink environment, and graphical analysis of the control structure was performed based on various system parameters. As a result, the control structure ensured stable operation of the system at higher wind speeds.

1. INTRODUCTION

Wind energy conversion systems (WECS), used to generate electrical energy, are structures created by the integration of mechanical and electrical components. Turbines and generators used in energy conversion are the most crucial parts of these systems. Commercially, three-bladed, speed and pitch angle-controlled turbines are commonly used. For generators, permanent magnet synchronous generators (PMSG) have come to the fore due to their characteristics such as direct connection to wind turbines, compatibility with variable speeds, and higher efficiency due to permanent magnets in their rotors. Different control methods are used for higher production efficiency, preventing mechanical and less electrical stress to the system and increasing the service life of the system. Before applying different control methods to the system, simulation of a WECS through a computer program such as Matlab/Simulink provides dynamic and steady-state performance of the system by selecting appropriate control

methods and analyzing different system parameters. Thus, more efficient systems can be installed at lower costs.

In the literature, Different control simulations have been conducted based on the mathematical models of the system components. Furthermore, graphical analysis based on system parameters for different techniques is presented in [1-3]. In other studies; based on reference frame conversion, PMSG and electronic interface simulations are presented in [4-6]. There are many different studies on the analysis of the pitch angle control used for WECS in [7-10]. Comparative analysis of these control techniques allows appropriate control selection and design as presented in [11-14]. There are also studies using soft computing methods such as fuzzy logic and neural networks used for the pitch angle control in [11, 15-18].

In this study, the main components of a WECS and its basic controls, such as maximum power point tracking (MPPT) and pitch angle control techniques were explained theoretically. Simulation of the system in Matlab-Simulink

environment was carried out and system parameters were analyzed based on the pitch angle control.

2. MATERIAL AND METHOD

Figure 1 shows the main components of a WECS and energy conversion stages.

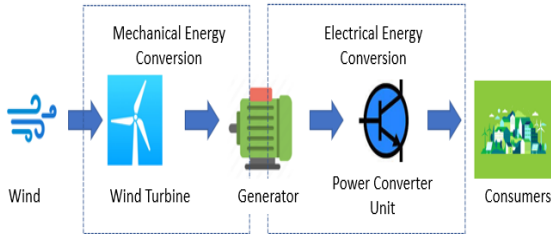


Figure 1. Basic conversion scheme for REDS

Criteria in the selection of WECS components are

- Size
- Design and Maintenance costs
- Control designs ensuring stable and efficient operation

The main objective for a WECS is to create a system where efficient and ergonomic components are used to design a control for high efficiency, according to instant winds. As for the working principle of the system, the kinetic energy of the wind is converted into mechanical energy by the wind turbine. Then, this energy is transferred to the generator through the drive system between the turbine and generator. Finally, produced electrical energy is supplied to the grid or a standalone load by the power converter unit, which is used as an intermediate link structure and used to control the efficiency and quality of the produced energy [19,20].

In the earlier designs, 3-bladed fixed-speed turbines were commonly used. Due to the low efficiency and power quality of the fixed types, variable speed, pitch angle-controlled turbines with PMSG, whose rotor speed can be adjusted according to instant wind speed, have been widely used at present.

For a variable speed WECS, there are two main control structures. The first is to control the speed of the system below the rated wind speeds, the latter is to control the pitch angle of the turbine for protecting the system components above the rated wind speeds [21,23]. WECSs can be operated at wider range wind speeds without exceeding the rated power through pitch angle control.

Computer simulations can be used for selecting and designing proper control structures. For this purpose, Basic models of the system components are needed. These models explain the energy efficiency and conversion process.

2.1. Wind turbine model

The mechanical power transferred to the generator from the turbine is expressed as shown in Equation (1) [3, 24-26].

$$P = \frac{1}{2} \times C_p \times \rho \times A \times V_w^3. \quad (1)$$

In this equation, P is the power extracted from the wind (W), ρ is the air density, which is equal to 1.225 kg/m^3 , C_p is the power coefficient, V_w is the wind speed (m/s), and A is the area swept by the rotor (m^2). The power coefficient, showing

the ratio of power extracted from wind energy, can be defined based on two parameters as shown in Equation (2).

$$C_p(\lambda, \beta) = C_1 \left(\frac{C_2}{\lambda_i} - C_3 \times \beta - C_4 \right) e^{-(C_5/\lambda_i)} + C_6 \times \lambda. \quad (2)$$

Coefficients C_{1-6} are characteristic values for turbines. β (pitch angle) is kept at a minimum value below the rated wind speeds, and it can be adjusted to prevent the turbine from damage especially at higher wind speeds. The tip speed ratio λ and λ_i parameters are defined as shown in Equation (3,4).

$$\lambda = \frac{w \times R}{V}. \quad (3)$$

$$\frac{1}{\lambda_i} = \frac{1}{\lambda + 0.08\beta} - \frac{0.035}{\beta^3 + 1}. \quad (4)$$

In Equation (3), w is the angular velocity of the rotor (rad/s), R is the rotor radius (m) and V is the wind speed (m/s).

Figure 2 shows the power coefficient C_p as a function of the tip speed ratio (λ) and pitch angle (β).

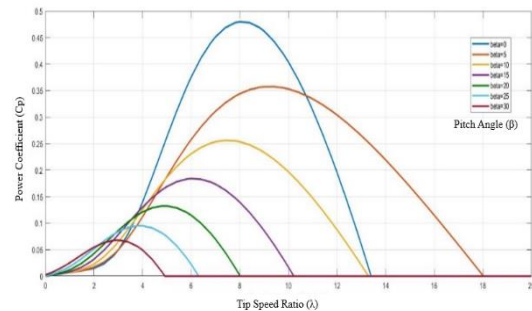


Figure 2. C_p curves as a function of λ and β

According to Figure 2, obtaining the optimum mechanical energy, according to instantly changing wind speed, depends on keeping the power coefficient at the maximum value. Furthermore, keeping the power coefficient at the maximum value for any wind speeds is related to keeping the pitch angle value at the minimum and the tip speed ratio at an appropriate value. As shown in Equation (3), the optimum value of the tip speed ratio can be obtained by adjusting the rotor speed according to the instant wind speed. This adjustment composes the main principle of speed control and MPPT. Another feature shown in Figure 2, the power coefficient is decreased by increasing the value of the pitch angle. This guarantees that excessive power can be limited above the rated wind speeds by adjusting the pitch angle.

2.2. Generator and drive system model

Obtaining the mathematical model of a generator is very important to understand which parameters can be used for control. For machines operating at synchronous speeds, the transformation from a 3-phase (a-b-c) stator reference frame to a 2-phase (d-q) reference frame provides convenient control design and analysis as in direct current (DC) machines. This reference frame transformation can be used for the mathematical model of a PMSG and controller designs [26-27].

As a result of reference frame transformation, the following equations are used to express the model of the PMSG as shown in Equation (5-6).

$$\frac{di_q}{dt} = \frac{1}{L_q} [-(R_s * i_q) + w_E(L_d i_d + \lambda r) + V_q]. \quad (5)$$

$$\frac{di_d}{dt} = \frac{1}{L_d} [-(R_s * i_d) + w_E(L_q i_q) + V_d]. \quad (6)$$

Where subscripts d and q refer to the physical quantities that have been transformed into the d-q reference frame, R is stator resistance (Ω), L_d and L_q are q and d axis inductances (H) of the generator, $V_{d,q}$ and $i_{d,q}$ are d and q axis voltages and currents consecutively, λr is the permanent magnetic flux w_E , the electrical angular velocity of the generator, as expressed in Equation (7).

$$w_E = \frac{P}{2} \times w_R. \quad (7)$$

Where P is the number of poles of the generator, w_R is the mechanical angular velocity of the generator. The electromagnetic torque produced by the generator (T_E) can be expressed based on (d-q) quantities as shown in Equation (8).

$$T_E = \frac{3p}{2} ((L_d - L_q) * i_d i_q) + i_q * \lambda r. \quad (8)$$

For a non-salient-pole PMSG, L_d and L_q inductances are approximately equal. In this case, the equation of electromagnetic torque can be expressed in the following form.

$$T_E = \frac{3p}{2} (i_q * \lambda r). \quad (9)$$

In Equation (9), it is seen that the torque equation obtained in the reference frame is similar to the torque equation of DC machines. This similarity proves that reference frame transformation provides ease of control and analysis. Equation (9) also shows that the generator torque can be controlled by the q axis current of the generator [26-28].

The drive system ensuring energy transfer from the turbine to the generator can be treated as a one-lumped mass model. The mathematical model of the drive train presents the motion equation of the system. The equation is defined as in Equation (10).

$$\frac{dW_R}{dt} = \frac{T_M - T_E}{J} - \frac{B}{J} * W_R. \quad (10)$$

Where J is the total moment of inertia, B is the coefficient of viscous friction. T_E and T_M are electromagnetic and mechanical torques respectively. W_R is the mechanical angular velocity of the generator. This equation shows that the rotor speed can be controlled by adjusting the electromagnetic torque. This torque can be adjusted by the q-axis current of the generator based on Equation (8). This adjustment forms the basis of MPPT control for a WECS below the rated wind speeds.

2.3. Power converter unit

The main purpose of these units is to produce energy with high efficiency and transfer the produced energy properly. They can also be used as an energy buffer for the power

fluctuations caused by the wind turbine and for the transients coming from the load side. There are two common converter types for WECSs. The first configuration is designed as a back-to-back converter connected to the grid or load, the second configuration is a diode-bridge rectifier, a boost converter, and an inverter connected to the grid or load. Designed controllers aim to regulate the operation of the power converter unit for various purposes based on the control variable. For example, adjusting the switching signals in a back-to-back configuration or regulating the duty cycle for a boost converter can be used as control variables for MPPT control [28-31].

2.4. Pitch angle control

In this control, the controller, which is activated above the rated wind speeds, provides the opportunity to work at higher wind speeds and mechanical protection [7-8]. Pitch angle control is an essential and useful controller to enhance the efficiency of a WECS and improve the stability of power conversion. Pitch systems are classified into two types, hydraulic and electrical pitch controls. Electrical controls provide more efficient and faster operation [21]. For a PID-based pitch angle control, different parameters (rotor speed, power, torque, etc.) are compared with their rated values. The error between these values could be used as inputs for pitch angle actuators. Figure 3 shows the working principle of a classical PI controller used for a pitch angle control with various input parameters.

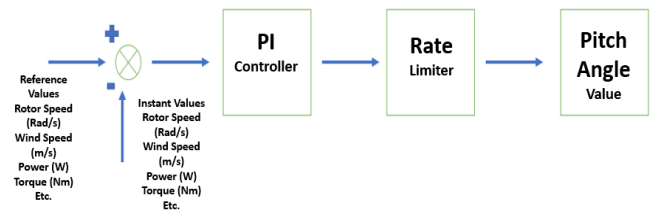


Figure 3. PI controller as a pitch angle control

A rate limiter can be used for adjusting the rate of change of the pitch angle. Furthermore, it adjusts the operating range of the controller. The angle value can also be adjusted to a value that can stop the turbine operation by the used controller in conditions where the wind speed is very high or low [11,16].

3. FINDINGS AND DISCUSSION

Figure 4 shows the general WECS model designed in Matlab/Simulink environment.

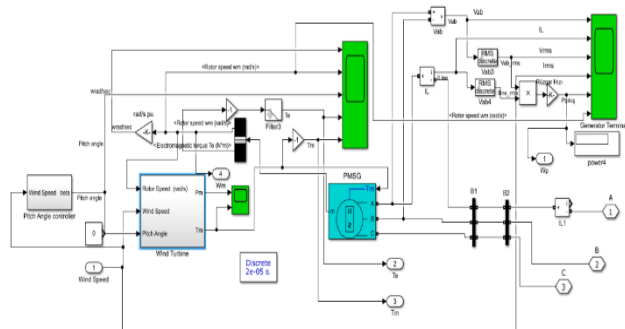


Figure 4. WECS system model

According to Figure 4, the mechanical torque obtained by the turbine is given as input to PMSG by the wind turbine. The mechanical power and torque are obtained based on the mathematical models of the wind turbine. The sign of the torque applied to the PMSG determines whether the machine works as a motor or a generator. The negative torque enables it to work as a generator. The detailed model of the wind turbine is shown in Figure 5.

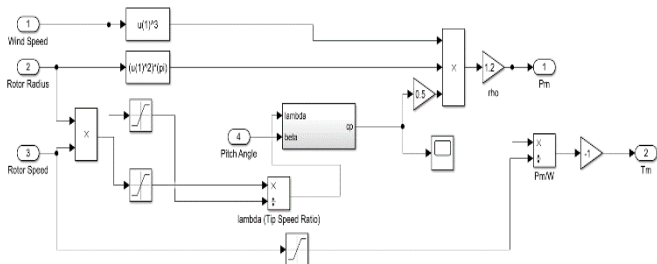


Figure 5. The detailed model of the wind turbine

In the pitch angle control, which is adjusted to activate above the rated wind speed (12 m/s defined in this model). The general system can be operated at the rated values through this control. The Pitch angle is adjusted to change between 0°-45°. Figure 6 shows the detailed model of the pitch angle control, working based on instant wind speed.

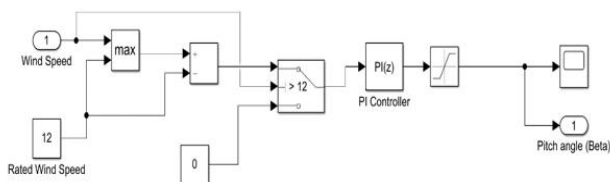


Figure 6. Pitch angle control model

According to the model shown in Figure 6, the control limits the power capturing capacity of WECS to the rated value, if the wind speed is greater than the rated wind speed (12 m/s). During lower wind speed, the pitch angle of the turbine is adjusted to the minimum value to rotate the rotor at a higher speed thus increasing the power capacity of the generator.

Control analysis will be carried out for a 1 kW WECS based on a wind profile as shown in Figure 7.

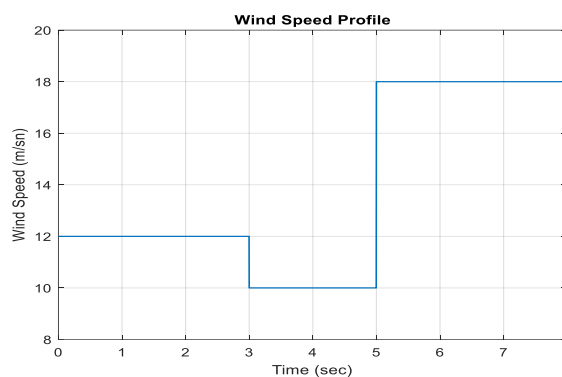


Figure 7. Wind speed profile

When pitch angle control is not applied throughout the simulation period, Figure 8 shows the variation of rotor speed and output power.

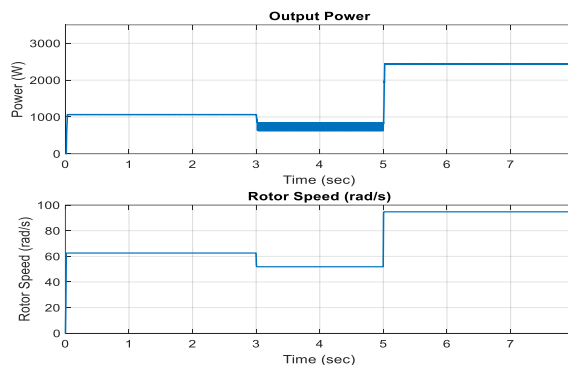


Figure 8. Variation of output power and rotor speed (pitch angle control not applied)

For a 1 kW system, when the pitch angle control is not applied, the output power increases to a 2.5 kW level at the fifth second. Power level is higher than the rated value, so this power can damage the system. This problem shows that a pitch angle control is required to limit the output power to the rated value at higher wind speeds.

When the pitch angle control is applied, the angle value starts to increase from the fifth second. Figure 9 shows the variation of the pitch angle.

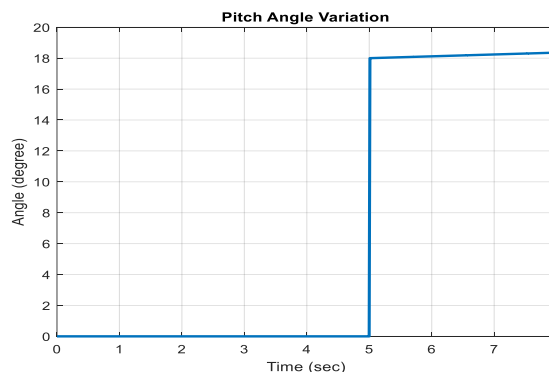


Figure 9. Pitch angle variation

This variation proves that the controller activates only when wind speed above the rated value (12 m/s). Figure 10

shows the variation of rotor speed and output power when the controller is applied.

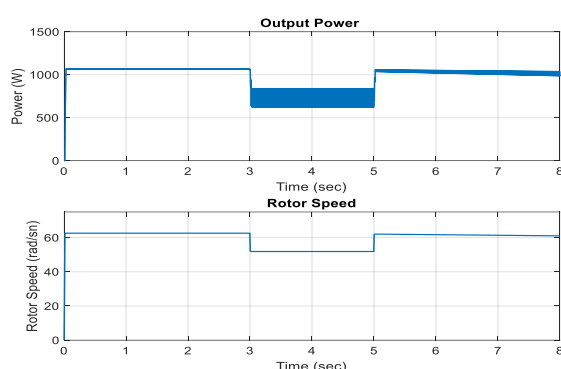


Figure 10. Variation of output power and rotor speed (with pitch angle controller)

The activation of the pitch angle control at the fifth second enables safe energy production at higher wind speeds by limiting the power and rotor speeds to the rated values. This control also enables energy production at higher wind speeds as well as safe operation. Overall efficiency is also improved in this way.

Figure 11 shows the variation of generator output voltage and current according to the pitch angle control

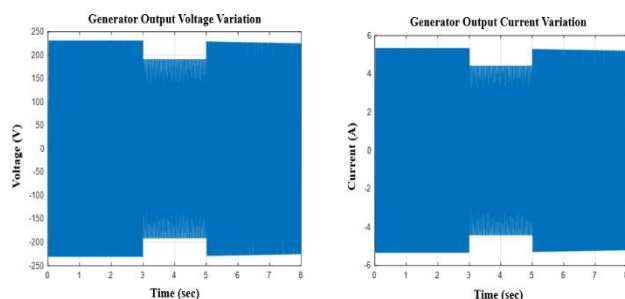


Figure 11. Variation of output voltage and current of the PMSG

When the wind speed exceeds the rated value, the voltage and current values can be limited to the rated values, which indicates that the pitch angle control of the system works properly.

4. CONCLUSION

In this study, the working principles of a WECS, mathematical models of the system parameters, and the control methods were explained theoretically. The simulation, conducted in Matlab/Simulink environment, gave detailed information about pitch angle control. Graphical analysis of the system parameters was conducted based on this simulation. It was observed that the system continued to operate without exceeding the rated power at higher wind speeds throughout the simulation period and the output current and voltage remained at the desired value. As used in this study, simulation is an important tool to see the effects of a control structure and make required regulations before the production process. For future studies, instead of PID controller, soft computing techniques such as fuzzy logic, artificial neural networks, and optimization methods can be used for pitch angle control. Simulation studies also allow comparative analysis of different control techniques.

REFERENCES

- [1] Naama, F. Z., Zegaoui A., Benyessad Y., Kessaissia F.Z., Djahbar A., and Aillerie M., "Model and simulation of a wind turbine and its associated permanent magnet synchronous generator", *Energy Procedia*, vol. 157, no. 2018, pp. 737–745, 2019.
- [2] Wang, C.N., Lin W.C., Le X.-K., "Modelling of a PMSG Wind Turbine with Autonomous Control", *Math. Probl. Eng.*, vol. 2014, pp. 1–9, 2014. J. S. Turner, "New directions in communications," *IEEE J. Sel. Areas Commun.*, vol. 13, no. 1, pp. 11–23, Jan. 1995.
- [3] Karakaya, A., Karakaş, E., "Küçük Güçlü Rüzgar Enerji Dönüşüm Sisteminin Benzetimi, Modellemesi ve Uygulaması, *Karadöğül Science and Engineering Journal*, pp 377-386, 2016.
- [4] Kokate, A., Khandagale, H., George, J., Koli, A., & Nair, S. Modeling and Simulation of Standalone Wind Energy Conversion System. In *2019 3rd International Conference on Trends in Electronics and Informatics (ICOEI)*, pp. 1295-1297, 2019.
- [5] Kumar, P., Kumar, R., Verma, A., Kala, M.C., "Simulation and Control of WECS with Permanent Magnet Synchronous Generator (PMSG)", in *2016 8th International Conference on Computational Intelligence and Communication Networks (CICN)*, 2016, pp. 516–521.
- [6] Vadi, S., Gurbuz, F.B., Bayindir, R., and Hossain E., "Design and Simulation of a Grid-Connected Wind Turbine with Permanent Magnet Synchronous Generator", in *2020 8th International Conference on Smart Grid (icSmartGrid)*, 2020, pp. 169–175.
- [7] Rashid, T. H. M. S., Routh A. K., Rana R., I. Ferdous, and R. Sayed, "A Novel Approach to Maximize Performance and Reliability of PMSG Based Wind Turbine: *Bangladesh Perspective American Journal of Engineering Research (AJER)*," no. 6, pp. 17–26, 2018
- [8] Bhanu Chandra, M. E., "The pitch angle control of variable speed wind turbine using PID controller", *International Journal of scientific research and management (IJSRM)*, vol. 3, no. 11, pp. 3728–3734, 2015.
- [9] Chauhan, S., Sameeullah, M., and Dahiya, R. "Maximum power point tracking scheme for variable speed wind generator", in *2014 IEEE 6th India International Conference on Power Electronics (IICPE)*, 2014, pp. 1–5.
- [10] Mohd, M., Shadab, A. and Mallick, M. "Simulation and Control of 20 kW Grid Connected Wind System", *International Journal of Electrical and Electronics Engineering Research (IJEEER)*, vol. 3, no. 3, pp. 275–284, 2013.
- [11] Biswal, G.S., Mohapatra, A., "A Grid Integrated PMSG Using Wind Energy Conversion System with Various Pitch Angle", *International Journal of Innovative Research in Science, Engineering and Technology*, pp. 5101–5109, 2018.
- [12] Devashish, Thakur, A., "A comprehensive review on wind energy system for electric power generation: Current situation and improved technologies to realize future development", *Int. J. Renew. Energy Res.*, vol. 7, no. 4, pp. 1787–1805, 2017.
- [13] Tiwari, R., and R. B. N., "Comparative Analysis of Pitch Angle Controller Strategies for PMSG Based Wind Energy Conversion System," *Int. J. Intell. Syst. Appl.*, vol. 9, no. 5, pp. 62–73, May 2017
- [14] Slah, H., Mehdi, D. and Lassaad, S., "Advanced Control of a PMSG Wind Turbine", *Int. J. Mod. Nonlinear Theory Appl.*, vol. 05, no. 01, pp. 1–10, 2016.
- [15] Hassan, S.Z., Li, H., Kamal, T., Abbas, M.Q, Khan, M.A. and Mufti G.M., "An intelligent pitch angle control of wind turbine", in *2017 International Symposium on Recent Advances in Electrical Engineering, RAEE 2017*, 2017, vol. 2018, pp. 1–6.
- [16] Van, T.L., Nguyen, T.H. and Lee, D.C., "Advanced Pitch Angle Control Based on Fuzzy Logic for Variable-Speed Wind Turbine Systems", *IEEE Trans. Energy Convers.*, vol. 30, no. 2, pp. 578–587, 2015
- [17] Yilmaz, A.S., Özer, Z., "Pitch angle control in wind turbines above the rated wind speed by multi-layer perceptron and radial basis function neural networks," *Expert Syst. Appl.*, vol. 36, no. 6, pp. 9767–9775. 2009.
- [18] Civelek, Z., Çam, E., Lüy, M., & Görel, G., "A new fuzzy controller for adjusting of the pitch angle of the wind turbine.", *The Online Journal of Science and Technology*, vol. 6, no 3, 2016.
- [19] B. Wu, Y. Lang, N. Zargari, and S. Kouro, *Power Conversion and Control of Wind Energy Systems*. John Wiley & Sons, Inc., New York, 2011.
- [20] Anaya Lara, O., Jenkins, N., and Ekanayake, J, *Wind Energy Generation Systems: Modelling and Control*, John Wiley & Sons., New York, 2011

- [21] Tiwari, R., Babu, N.R., "Recent developments of control strategies for wind energy conversion system," *Renew. Sustain. Energy Rev.*, vol. 66, pp. 268–285, 2016
- [22] Yin, M., Li, G., Zhou, M and Zhao, C., "Modeling of the Wind Turbine with a Permanent Magnet Synchronous Generator for Integration", in *2007 IEEE Power Engineering Society General Meeting*, pp. 1–6, 2007
- [23] Gajewski, P., Pieńkowski, K., "Advanced control of direct-driven PMSG generator in wind turbine system," *Arch. Electr. Eng.*, vol. 65, no. 4, pp. 643–656, 2016.
- [24] Rolan, A., Luna, G., Vazquez, D., Aguilar, and Azevedo, G., "Modeling of a variable speed wind turbine with a Permanent Magnet Synchronous Generator", in *2009 IEEE International Symposium on Industrial Electronics*, pp. 734–739, 2009
- [25] Priya, G. J., "Modelling and performance analysis of grid-connected PMSG based wind turbine.", *International Journal of Advanced Research in Electrical, Electronics and Instrumentation Engineering*, 3(2), pp 155-165, 2014
- [26] Patil K., Mehta, B. "Modeling and simulation of variable speed wind turbine with direct drive permanent magnet synchronous generator", in *2014 International Conference on Green Computing Communication and Electrical Engineering (ICGCCEE)*, pp. 1–6, 2014.
- [27] Gencer, A., "Modelling of operation PMSG based on fuzzy logic control under different load conditions", in *2017 10th International Symposium on Advanced Topics in Electrical Engineering (ATEE)*, 2017, pp. 736–739
- [28] Ackermann, T., *Wind Power in Power Systems*, John Wiley & Sons, Chichester, UK, 2005.
- [29] Hussein, M. M., Orabi, M., Ahmed, M. E., Sayed, M. A., "Simple sensorless control technique of permanent magnet synchronous generator wind turbine," *PECon2010 - 2010 IEEE Int. Conf. Power Energy*, pp. 512–517, 2010
- [30] Jafari, H. K. . "Effect of Turbulence on Fixed-Speed Wind Generators", *Advances in Wind Power*, 31,2012.
- [31] Yaramasu, V., Wu, B., Sen, P. C., Kouro, S. and Narimani, M., "High-power wind energy conversion systems: State-of-the-art and emerging technologies," *Proc. IEEE*, vol. 103, no. 5, pp. 740–788, 2015.

BIOGRAPHIES

Hasan Bektas Percin obtained his BSc degree in electrical and electronics engineering from Firat University in 2011. He has been studying on MSc degree in electrical and electronics engineering at Firat University. His research interests are renewable energy, energy efficiency, smart control modelling.

Abuzer Caliskan obtained his BSc degree in electrical and electronics engineering from Firat University in 1997. He received the MSc., and PhD. diploma in Electrical and Electronics Engineering from the Firat University in 2004 and 2011 respectively. His research interests are power electronics drive circuits, electric machines, renewable energy, energy efficiency and their modeling. In 2002 he joined the Faculty of Electrical and Electronics Faculty, Firat University as a research assistant, where he is presently working as an assistant professor.